LBNL-41283
UC-404

ERNEST ORLANDO LAWRENCE
BERKELEY NATIONAL LABORATORY

Extreme Ultraviolet Interferometry

Kenneth A. Goldberg
Materials Sciences Division

December 1997
Ph.D. Thesis

97

LBNL-41283
UC-404

Extreme Ultraviolet Interferometry

Kenneth Alan Goldberg
Ph.D. Thesis

Department of Physics
University of California, Berkeley

and

Materials Sciences Division
Ernest Orlando Lawrence Berkeley National Laboratory
University of California
Berkeley, CA 94720

December 1997

This work was supported by the Director, Office of Energy Research, Office of Basic Energy Sciences, Materials Sciences Division, of the U.S. Department of Energy under Contract No. DE-AC03-76SF00098.

Extreme Ultraviolet Interferometry

by

Kenneth Alan Goldberg

A.B. (University of California, Berkeley) 1992
M.A. (University of California, Berkeley) 1994

A dissertation submitted in partial satisfaction of the

requirements for the degree of

Doctor of Philosophy

in

Physics

in the

GRADUATE DIVISION

of the

UNIVERSITY of CALIFORNIA, BERKELEY

Committee in charge:

Professor Roger W. Falcone, Chair
Professor Jeffrey Bokor
Professor Joseph Orenstein

1997

Extreme Ultraviolet Interferometry

by

Kenneth Alan Goldberg

Abstract

Extreme Ultraviolet Interferometry

by

Kenneth Alan Goldberg

Doctor of Philosophy in Physics

University of California, Berkeley

Professor Roger W. Falcone, Chair

EUV lithography is a promising and viable candidate for circuit fabrication with 0.1-micron critical dimension and smaller. In order to achieve diffraction-limited performance, all-reflective multilayer-coated lithographic imaging systems operating near 13-nm wavelength and 0.1 NA have system wavefront tolerances of 0.27 nm, or 0.02 waves RMS. Owing to the highly-sensitive resonant reflective properties of multilayer mirrors and extraordinarily tight tolerances set forth for their fabrication, EUV optical systems require at-wavelength EUV interferometry for final alignment and qualification.

This dissertation discusses the development and successful implementation of high-accuracy EUV interferometric techniques. Proof-of-principle experiments with a prototype EUV point-diffraction interferometer for the measurement of Fresnel zoneplate lenses first demonstrated sub-wavelength EUV interferometric capability. These experiments spurred the development of the superior phase-shifting point-diffraction interferometer (PS/PDI), which has been implemented for the testing of an all-reflective lithographic-quality EUV optical system. Both systems rely on pinhole diffraction to produce spherical reference wavefronts in a common-path geometry. Extensive experiments demonstrate EUV wavefront-measuring precision beyond 0.02 waves RMS. EUV imaging experiments provide verification of the high-accuracy of the point-diffraction principle, and demonstrate the utility of the measurements in successfully predicting imaging performance.

Complementary to the experimental research, several areas of theoretical investigation related to the novel PS/PDI system are presented. First-principles electromagnetic field simulations of pinhole diffraction are conducted to ascertain the upper limits of measurement accuracy and to guide selection of the pinhole diameter. Investigations of the relative merits of different PS/PDI configurations accompany a general study of the most significant sources of systematic measurement errors.

To overcome a variety of experimental difficulties, several new methods in interferogram analysis and phase-retrieval were developed: the Fourier-Transform Method of Phase-Shift Determination, which uses Fourier-domain analysis to improve the accuracy of phase-shifting interferometry; the Fourier-

Transform Guided Unwrap Method, which was developed to overcome difficulties associated with a high density of mid-spatial-frequency blemishes and which uses a low-spatial-frequency approximation to the measured wavefront to guide the phase unwrapping in the presence of noise; and, finally, an expedient method of Gram-Schmidt orthogonalization which facilitates polynomial basis transformations in wavefront surface fitting procedures.

Dedicated to Hector Medecki, my teacher, mentor, and inspiration.
With deeper understanding than I shall ever have, he intuits light.

Table of Contents

Acknowledgements

This research reflects the considerable effort of a team of scientists, engineers, and technicians. Foremost among them have been those who have steadfastly guided this project forward through several often difficult years of keeping it afloat: Jeffrey Bokor, David Attwood, and Keith Jackson, whose constant hard work, faith, and belief in the importance of this project are reflected in its every accomplishment.

It is beyond argument that the successes of this project would never have been realized were it not for the creative vision and sincere dedication of Hector Medecki, the primary inventor of the phase-shifting point-diffraction interferometer, the *Medecki Interferometer*, whose clever and insightful approach daily brings the joy of experimental research to light.

The ingenuity of Chief Engineer Philip Batson and his team, including Drew Kemp and Senajith Rekawa, is evident in every flexural-pivot, window flange, and high-resolution stage. On a shoestring budget, they designed and built the system to succeed, then re-designed it to excel.

Special acknowledgment must be given to Paul Denham, whose unique electronic and mechanical contributions and tireless efforts play an indispensable role in the facility with which these experiments are performed.

The intuitive and rapid computer interface through which the numerous translational stages are controlled is largely due to the persistence and considerable skill of undergraduate computer scientist Joshua Cantrell. Additional technical computer support essential for the present and continued development and improvement of the experimental interface is provided by Shane Cantrell. Numerous computer and electronic systems were installed and are maintained by Ron Tackeberry, Everett Harvey, and Jos Polman, whose responsive support is greatly appreciated.

The most critical components of the interferometers are the tiny reference pinholes. For their contributions to the fabrication of these essential components, gratitude is due to James Spallas, Ralph Hostetler, Charles Fields, and Richard Livengood. Special thanks are also due to Erik Anderson for his continuing support with pinhole fabrication and other exceptionally challenging tasks, including the fabrication of the high-resolution EUV Fresnel zoneplates used in the first-round of interferometry experiments.

EUV imaging experiments could not have been performed without the skillful contributions of Avijit Ray-Chaudhuri and Kevin Krenz of Sandia National Laboratories.

Two other graduate student researchers working on this project share credit for its every success and deserve recognition for their essential contributions to this team effort: Edita Tejnil, whose often

shaky hands were always steady enough to place sub-micron pinholes to within 10 μm of their target; and SangHun Lee, who, as a first-year graduate student faced with a steep learning-curve, met every challenge with enthusiasm.

My sincere gratitude is also due to Gary Sommargren, who was involved with the EUV PDI research from its inception. His always-open door has led to many interesting discussions and has shaped my understanding of the important issues in interferometry.

This research would not have been possible without the generous sponsorship of Intel Corporation, the EUV LLC, and the Virtual National Laboratory, SRC contract no. 96-LC-460, DARPA Defense Advanced Lithography Program, Office of Basic Energy Sciences, U. S. Department of Energy under Contract No. DE-AC03-76SF00098, and NCSA.

I am grateful for the support I have received from my thesis committee members, especially Professor Roger Falcone, whose encouragement for my work outside of the Physics Department precipitated my involvement in this rewarding research, and Professor Joseph Orenstein, who encouraged me to reflect on the opportunities I have been presented.

Separate from this experimental work but no less essential to its completion has been the constant love and support I have received from my parents, Sandra and Joseph Goldberg, whose steadfast guidance has kept *me* afloat through several often difficult years. Sincere thanks and appreciation are also due to Naomi Leite, who although far outside of her own academic discipline, way beyond the call of duty, and significantly past the side-effects of a strong pot of coffee, patiently proofread and diligently edited every word of this dissertation. From its first draft awash in a sea of green ink, she helped to make the text as readable and sound as it now is. Any remaining deficiencies or excesses (mistakes) in punctuation are clearly present only because I chose not to take her advice.

Thank You.

Introduction

EUV lithography is a promising and viable candidate for circuit fabrication with 0.1-micron critical dimension and smaller. To achieve this end at 13-nm wavelength, nearly diffraction-limited, multilayer-coated, near-normal-incidence reflective optical systems with 0.1 numerical aperture are required (Himel 1993). The suggested wavefront aberration tolerance for these sophisticated, all-reflective systems, composed of aspherical elements, is only 0.02 waves RMS, or 0.27 nm (Williamson 1994). This places extremely high demands on the fabrication of EUV mirror substrates and multilayer coatings and even higher demands on the metrology tools required to characterize them.

The EUV wavefront is determined by the geometric figure of the mirror surfaces and by the properties of the multilayer coatings, which are deposited across mirror areas of several square centimeters. While advanced visible-light interferometric techniques possessing the required measurement accuracy are being developed (Sommargren 1996a, 1996b), optical aberrations arising from multilayer coating defects and thickness errors are measurable only at the EUV operational wavelength. Furthermore, it is widely agreed in the lithography community that final alignment and qualification must be performed *at-wavelength* in order to successfully predict the imaging performance of an optical system. These factors motivate the development of high-accuracy EUV wavefront-measuring interferometry.

This thesis is devoted to the development of EUV interferometry capable of achieving the highest wavefront-measuring accuracy and precision. Early proof-of-principle experiments with a prototype EUV point-diffraction interferometer (PDI) for the measurement of Fresnel zoneplate lenses (Goldberg 1995a, 1995b) demonstrated sub-wavelength EUV interferometric capability, and revealed the very high quality of the lithographically-fabricated zoneplate optics. Experience and the limitations of the conventional PDI spurred the development of the superior *phase-shifting point-diffraction interferometer* (PS/PDI) (Medecki et al. 1996). The implementation and development of this novel tool at EUV wavelengths is now in progress on an undulator beamline at Ernest Orlando Lawrence Berkeley National Laboratory's Advanced Light Source synchrotron radiation facility (Goldberg et al. 1995b, 1997; Tejnil et al. 1996a, 1997).

The prototype PS/PDI is being used to test lithographic-quality multilayer-coated 10× Schwarzschild objectives. While extensive experiments with one such objective have revealed its nearly diffraction-limited performance, the more important data comprise a wealth of information about the performance of the interferometer itself.

Evaluation of the interferometer's performance has revealed significant progress toward the accuracy and precision targets set by the wavefront measurement requirements of EUV lithography. In tens of separate trials performed on a 0.07 NA sub-aperture of the 10× Schwarzschild objective, a wavefront-measuring precision better than 0.02 waves (0.27 nm, or $\lambda/50$) has been observed. Accuracy verification with imaging experiments has shown excellent agreement between predicted and measured performance. Additionally, the interferometer has been used in the first direct quantitative measurement of chromatic aberrations related to the isolated properties of multilayer reflective coatings.

Accompanying the discussion of development of the experimental system and its prototypical components, theoretical and empirical investigations of the systematic and random error sources are presented in this thesis. The studies are presented in a very general manner and are intended to serve as a framework for the investigation of the most significant error sources in the PS/PDI measurement of arbitrary optical systems. Special attention is given to the EUV optical systems of interest to this research. The theoretical studies feed back into the experimental methods and have improved the quality and reliability of the measurements.

Experimental difficulties have complicated many aspects if this research, and have necessitated the creation of new general methods of interferogram analysis. Several techniques developed by the author and described herein overcome the limitations of the optical system under test and problems associated with the experimental system. Emphasis is placed on the practical implementation of robust and efficient analysis methods, and many examples of varying complexity are presented.

The investigation of the measurement precision has identified the individual contributions of the interferometer's components to the measurement uncertainties. It appears clear that even with the high performance demonstrated to date, there are several areas in which improvements are possible; and specific recommendations for such are made.

EUV interferometry research and experiments were performed between May 1993 and November 1997 using facilities of the Lawrence Berkeley National Laboratory and the University of California, Berkeley. EUV Imaging experiments were conducted at Sandia National Laboratory, in Livermore, California.

OVERVIEW

This thesis is organized into four main sections, covering both theoretical investigations and the results of experimental research. Part I presents a detailed investigation of the most critical physical component of any point-diffraction interferometer: the pinhole responsible for the point-diffraction that generates the spherical reference wavefront. Here, a highly detailed vector model of the electromagnetic field in the vicinity of the tiny pinholes is illuminated with EUV light and investigated to predict the upper limits of reference wavefront accuracy.

Part II describes the research conducted with an EUV point diffraction interferometer (PDI) used to evaluate the wavefront diffracted by high-resolution Fresnel zoneplate lenses. This research paved the way for the development of the more sophisticated *phase-shifting point diffraction interferometer* (PS/PDI). All of the research related to the EUV PS/PDI is presented in Part III. Chapter 4, which provides a description of several PS/PDI designs, is followed in Chapter 5 by a mathematical investigation of systematic error sources and measurement issues. The interferometer configuration for the measurement of a Schwarzschild objective is described in Chapter 6, and the measurements themselves are presented in Chapter 7. Chapter 8 contains the results of numerous experiments conducted to evaluate the performance of the interferometer. Finally, Chapter 9 records an investigation of chromatic aberrations and the wavelength-dependent behavior of the Schwarzschild objective related to the properties of the multilayer coatings.

The six chapters of Part IV all describe practical aspects of interferogram analysis, including detailed procedural descriptions of the individual methods. Following a general overview in Chapter 10, Chapters 11 and 12 provide a description of the two major classes of phase-recovery methods, single interferogram techniques and multiple interferogram phase-shifting techniques, respectively. Chapter 12 also includes a novel phase-shifting analysis method developed by the author to overcome phase-shift calibration errors, the *Fourier-Transform Method of Phase-Shift Determination.* This method eliminates problems associated with phase-step uncertainties and fringe print-through in situations where it may be applied.

The critically important and challenging subject of phase-unwrapping is addressed in Chapter 13. Here, following a discussion of conventional methods, a new unwrapping procedure developed by the author is described. This method combines highly-filtered phase-information with raw phase data to perform what is called *Fourier-Transform Guided Unwrapping.* This robust method was designed to overcome the presence of numerous invalid data regions found in the measurement of the EUV Schwarzschild objective. It preserves all of the phase information present in the raw *wrapped* phasemap without suffering the complications from invalid points that plague all other unwrapping methods.

Analysis in terms of a convenient set of aberration polynomials, such as the familiar Zernike circle polynomials, is essential for the accurate description and interpretation of the measured data. Chapter 14 describes some important properties of the Zernike polynomials and presents practical issues of how these functions may be most effectively represented on a computer. Chapter 15 describes general methods of wavefront surface fitting, including the very important Gram-Schmidt method of orthogonalization which is extremely useful for minimizing uncertainties associated with polynomial fitting. A modification made by the author to the published method streamlines the fitting procedure and reduces uncertainties by eliminating the need to perform a matrix inversion in the transformation between two polynomial basis sets.

Following the concluding remarks of Chapter 16, the seven appendices cover several auxiliary topics important to this research. These include EUV optical properties, EUV optical systems, EUV multilayer behavior, and Fresnel zoneplate lenses. Also given are the definition of fringe contrast, followed by a Fourier-domain method of fringe contrast determination implemented by the author. Finally, there is a note regarding the conventions used in plotting the coefficients of the Zernike polynomials when representing a wavefront surface.

I. PINHOLE DIFFRACTION SIMULATIONS

2

EUV Pinhole Diffraction

2.1 INTRODUCTION

The central principle of the EUV point diffraction interferometers is the generation of the reference wavefront by pinhole diffraction. Both accuracy and precision rely on the spherical quality of the diffracted wavefront across the numerical aperture of measurement. A broad assumption may be made that for a sufficiently small pinhole, a spherical wavefront of arbitrary quality may be achieved over a given numerical aperture. However, such an assumption is difficult to justify for an experimental, and necessarily imperfect, pinhole in a highly absorptive, thick membrane subject to a plane-polarized incident electric field of non-uniform intensity.

In principle, detailed knowledge of the electromagnetic field emerging from the pinhole membrane would enable the prediction of non-spherical components in the diffracted wavefront phase and allow estimation of the measurement accuracy limits. The goal of this section is to assess the results of a first-principles simulation of the pinhole-diffracted reference wavefront, to guide the selection of the appropriate pinhole size and characteristics of the experimental interferometer.

While the simplifying assumptions of this simulation do overlook several experimental conditions (non-ideal pinhole shapes, spatial variation of the incident electric field, etc.), this work lays the foundation for further research and more detailed analysis performed utilizing the rapidly increasing capacity and availability of computing power. These early results may portray an optimistic view of the minimum required pinhole size for EUV interferometry: only careful experimental research can truly establish a maximum allowable pinhole size or qualify an individual pinhole for a given application and desired accuracy.

2.1.1 *Motivation of the Numerical Simulation*

Several methods have been developed to study diffraction from a variety of aperture shapes with various boundary conditions (Cerjan 1994, Born and Wolf 1980), yet no general analytical treatment addresses diffraction through pinholes in a highly absorptive medium with the range of non-ideal shapes that serve as reasonable physical models for the experimental pinholes used in EUV point diffraction interferometry near 13 nm wavelength (Goldberg et al. 1996). The introduction of the three-dimensional pinhole structure and inclusion of the polarization of incident light motivate the use of numerical solutions based on detailed simulations of the vector electromagnetic field in the vicinity of the pinhole. This in itself presents an especially difficult challenge owing to the relatively large diameter of the pinholes in question (3-15 λ) and the polarization-dependent absorptive boundary conditions at the membrane interfaces.

Beyond rigorous numerical solution of Maxwell's equations in the domain containing the pinhole, no analytic treatment is sufficiently versatile to accommodate the irregular pinhole shape models that serve as approximations to the actual shape of the experimental pinholes. Determination of the complete electromagnetic field in the vicinity of the pinhole was performed in this study for a variety of pinhole

geometry models using TEMPEST 3D (Wong and Neureuther 1995). Several pinhole models with cylindrical and elliptical cross-sections were considered in the studies described in this chapter. These calculations set an upper limit to the allowable pinhole diameters necessary to achieve a reference wavefront of a given quality in an ideal system.

All of the TEMPEST 3D calculations were performed in 1995 on a CM-5 connection machine. Typically, these simulations utilized 128 parallel processors and 870 MB of RAM, requiring approximately five minutes of CPU time. At the time these simulations were performed, the large simulation domains necessitated the use of a super-computer and restricted the simulations to a narrow cross-sectional area containing the open pinholes. The author notes that at present such computing power (aside from the number of processors) is becoming available on desktop workstations.

2.2 MODELING THE ELECTROMAGNETIC FIELD

Pinholes with diameters ranging from 50-150 nm (~3-11 λ, at $\lambda \approx 13$ nm), fabricated by electron beam lithography in a highly absorptive cobalt membrane approximately 90 nm (~7 λ) thick (Spallas et al. 1995), are considered in this study because they are suitable for testing optical systems with NA around 0.1 near 13 nm wavelength. The three-dimensional electromagnetic field in the vicinity of the pinhole was calculated using TEMPEST 3D, a time-domain, vector electromagnetic field simulation computer program. Once the field has been calculated at the exit-side of the pinhole membrane, the reference wavefront is calculated using a simple vacuum-propagation model incorporating the Fresnel-Kirchoff approximation for far-field diffraction.

2.2.1 *Calculating the Field in the Vicinity of the Pinhole*

Calculations are performed on a range of pinhole geometry models, including cylindrical and conical pinholes and elliptical pinholes of uniform cross-section. Figure 1 shows the four pinhole-bore models studied here. To simplify the models, variations of the field incident on the pinhole are neglected: across the small simulation domain, uniform, normally incident plane-wave illumination with linear polarization along the x-axis is assumed. Experimentally, however, the electric field may vary over an extremely small

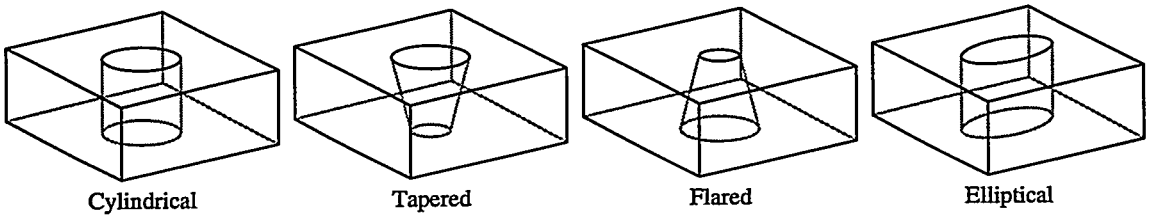

Figure 1. A representation of the four pinhole shape models used in the TEMPEST 3-D simulations. The pinholes range from 50 — 150 nm diameter. The walls of the sloped pinholes (tapered and flared) are angled at 10° to the vertical. The two-fold symmetry of these models is exploited to increase the simulation domain size.

Table 1. Parameters of the pinhole simulations

wavelength	$\lambda = 13.55$ nm (91.5 eV)
illumination	uniform plane wave, normal incidence, plane polarized
simulation domain size	230.6 nm × 230.6 nm × 115.2 nm = 17 λ × 17 λ × 8.5 λ, periodic in x and y
simulation nodes	uniform, λ/15 spacing, 2×10^6 total nodes, exploiting two-fold symmetry
pinhole diameters	50 nm – 150 nm
cobalt membrane	thickness, 90 nm = 6.64 λ; density, 8.9 g/cm^3
index of refraction	$n \equiv 1 - \delta + i\beta = 1 - 0.0659 + 0.0657i = 0.9341 + 0.0657i$

spatial scale, rendering suspect the uniform-illumination assumption. This is especially true for large pinholes, and for those displaced significantly from the center of the focal pattern. Thus the pinhole size conditions described herein set a *lower limit* for the magnitude of aberrations that should be expected from ideal plane-wave illumination.

Parameters of the simulation are listed in Table 1. The simulation domain, which exploits the two-fold symmetry of the pinhole models, contains a cobalt membrane in vacuum with a thin free-space layer above and below. TEMPEST 3D uses periodic boundary conditions in the x and y directions, thereby forming an infinite square array of *virtual* pinholes with center-to-center spacing of 230.6 nm for the parameters of interest. This periodicity is represented in Fig. 2(a). If the pinhole itself is symmetric about both the x- and y-axes, defined from the center of the pinhole (as is always the case in these simulations), then the domain size may be reduced by a factor four, as shown in Fig. 2(b). (It should be noted that recent versions of TEMPEST under development do not impose periodic boundary conditions. These advances were not available at the time this research was undertaken.)

The propagation of EUV light in cobalt is characterized by *rapid* extinction: the $1/e$ intensity transmission depth is 16.4 nm (1.21 λ) at 13.55 nm wavelength, and the relative transmission through 90 nm is 4.1×10^{-3}. This rapid extinction is important to the separation distance between the pinholes of the peri-

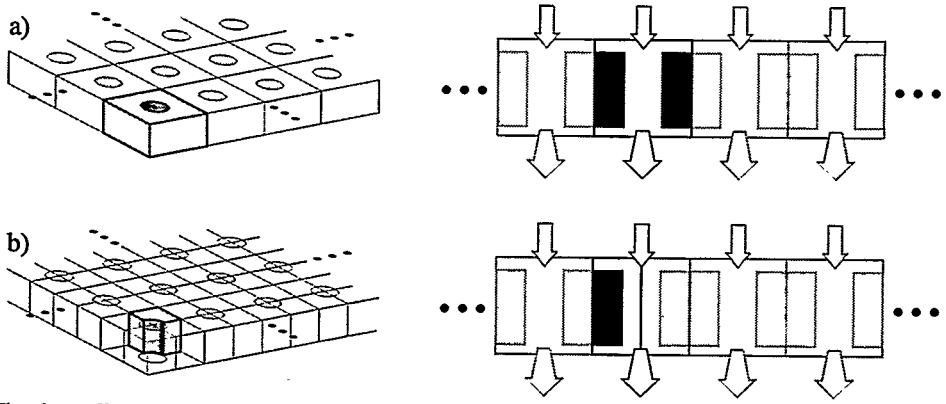

Figure 2. The three-dimensional TEMPEST simulation domain. (a) The inherent periodic boundary conditions create a virtual lattice containing the simulation domain. On the right is a cross section containing the pinhole axis. The limits of the simulation domain are outlined in black. (b) The simulations performed here exploit the two-fold symmetry of the pinhole models to enable the simulation of larger domains.

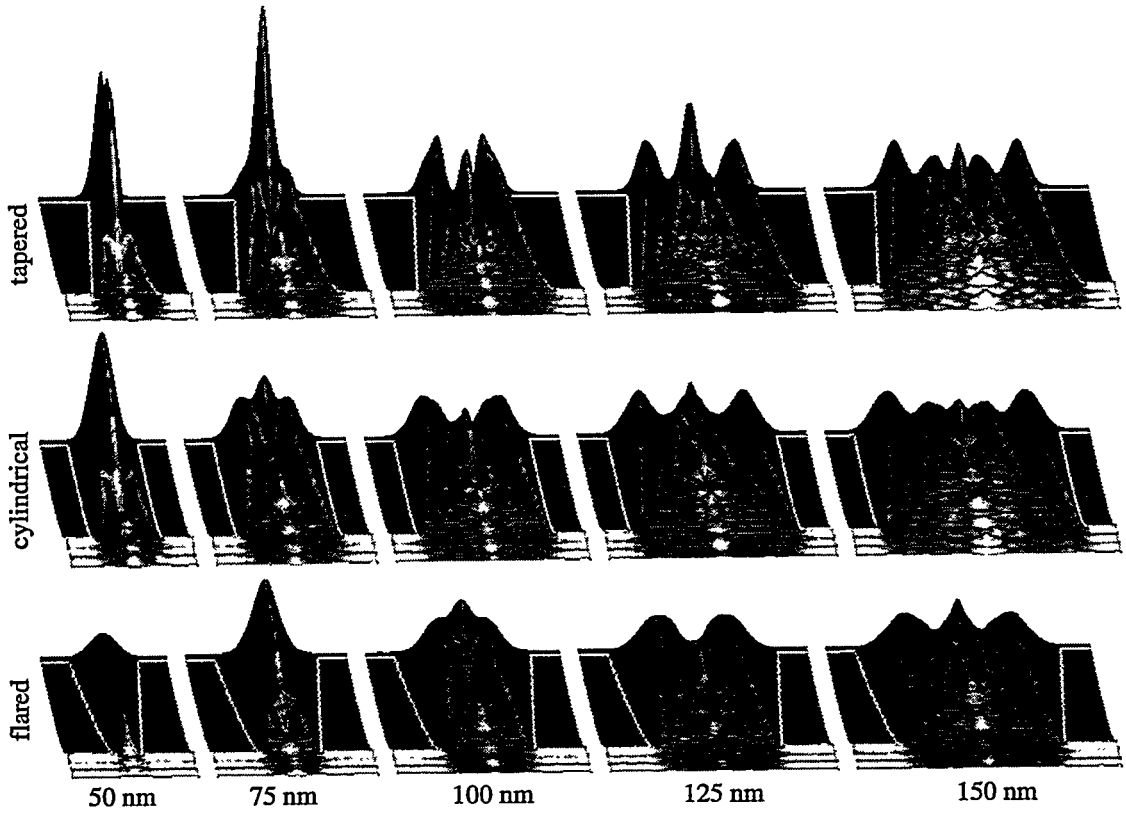

Figure 3. Calculated electric field intensity patterns showing diffraction within the pinhole and attenuation in the cobalt membrane. Surface heights represent the electric field intensity in a plane containing the axis of the pinhole and the direction of the electric field polarization. The light propagates from the bottom of each image to the top. White lines on the surfaces represent the boundaries of the cobalt.

odic domain. In order to consider the individual pinholes as isolated structures, the separation must be great enough to substantially reduce the contribution of overlapping fields from the neighboring *virtual* pinholes. Hence the rapid extinction makes this simulation possible.

A short distance away from the pinhole, light propagates through the material with characteristic exponential extinction:

$$I(x) = I_o e^{-x/16.4\ \mathrm{nm}}. \tag{1}$$

Within the open pinhole, a stationary diffraction pattern is formed. For pinholes of circular cross-section and various radii, the electric field is shown in Fig. 3. The figure shows only the cross section taken in the plane parallel with the polarization.

Polarization affects the propagation of light in the pinhole, and breaks the rotational cylindrical symmetry of the study. Along the walls of the pinhole (i.e. the interface), the electric field satisfies different boundary conditions in the different directions. The electric field polarized *parallel* to the boundary must be continuous across the interface, with a continuous first derivative in the direction normal to the boundary. Since the field inside the absorber is rapidly attenuated, this continuity requirement forces the parallel electric field to become nearly zero along the pinhole walls. The field polarized *perpendicular* to

the interface may be discontinuous, and is not necessarily small at the boundary.

This polarization dependence illustrates one main difference between scalar and vector solutions to pinhole diffraction. While it is true that for pinhole diameters many times larger than the wavelength, the contributions from the boundaries of the pinhole become negligible, this is certainly not the case for the pinholes of interest here. The difference between the parallel and perpendicular boundary orientations establishes a 2θ-dependence in the diffracted wavefront manifested as a small amount of *astigmatism* (the lowest-ordered 2θ-dependent aberration).

2.2.2 *Propagation to* Far-Field

Once the fields have been calculated and the field at the exit of the pinhole is known, the diffracted wavefronts are calculated by numerical propagation of the calculated electric field to a spherical surface, 10 cm away. Experimentally, this distance represents diffraction to the *far-field* and corresponds to the position of the detector in the EUV point diffraction interferometer and phase-shifting point diffraction interferometer described in this thesis. The x-polarized component of the electric field, calculated 2.7 nm ($\lambda/5$) below the cobalt membrane, is used as the *initial field* for the numerical propagation. In the absence of a y-polarized component, the x-polarized component of the electric field across the initial x-y plane is sufficient to completely and uniquely describe the propagated field (Clarke and Brown 1980). Furthermore, for relevance to interferometry the interference fringe pattern is generated by the interaction of like-polarized electric field components of the test and reference beams. The test wave here contains only x-polarized light, and therefore the presence of any y-polarized light in the reference beam would contribute only to the stationary background intensity. The propagation is performed with a two-dimensional Fourier transform that approximates the Fresnel-Kirchoff diffraction formula for far-field diffraction (Born and Wolf 1980).

In the pinhole simulation domain, the propagated *emergent* field may be described as thelinear superposition of the *diffracted* field and the incident *uniform* field transmitted through the cobalt membrane. To isolate the diffracted field, a uniform (constant) component representing only the attenuated transmitted field is subtracted before the propagation was performed. This superposition and subtraction is illustrated in Fig. 4. Isolation of the diffracted field enables the imposition of the boundary condition that

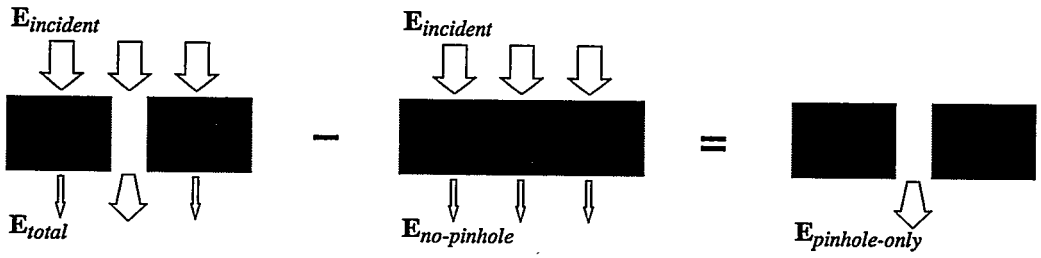

Figure 4. Strategy for the calculation of the diffracted wavefront from TEMPEST simulations. Superposition is used to isolate the diffracted wave from the wave transmitted in the absence of the pinhole. This subtraction is necessary to eliminate the contribution of the finite, square simulation domain cross-section.

the diffracted field becomes arbitrarily small away from the pinhole. As mentioned previously, the rapid extinction of all light not transmitted *through* the open pinhole allows the use of a relatively small domain size in these calculations.

2.3 THE DIFFRACTED WAVEFRONT

The Kirchoff model of scalar diffraction theory (Born and Wolf 1980) provides a first approximation to the far-field wavefront diffracted from the experimental pinhole.

2.3.1 *Simple Theory — The Airy Pattern*

Consider the diffraction of uniform, plane-wave illumination from a simple circular aperture in a planar screen. For a small aperture, in the far-field this is referred to as *Fraunhofer diffraction* (Goodman 1988:62). This simplified model predicts a spherical reference wavefront that covers the central portion of a diffracted *Airy pattern,* bounded by the first diffraction minimum.

A highly simplified model of the field emergent from a circular pinhole of diameter d is

$$t(\mathbf{r}) = \begin{cases} 1, & |\mathbf{r}| \le d/2 \\ 0, & |\mathbf{r}| > d/2 \end{cases} . \tag{2}$$

Following Goodman (1988:48-54), the angular spectrum of the diffracted wavefront when the system is illuminated by a normally incident, monochromatic plane wave is calculable via Fourier-transform. Let $\boldsymbol{\alpha} \equiv (\alpha_x, \alpha_y)$ be direction cosines of the field in the x and y directions. The angular spectrum is

$$U(\boldsymbol{\alpha}/\lambda) = \int_{dA} t(\mathbf{r}) \exp\left[-\frac{2\pi i}{\lambda}\boldsymbol{\alpha}\cdot\mathbf{r}\right] d\mathbf{r} . \tag{3}$$

Taking advantage of the cylindrical symmetry of the problem, Eq. (3) can be solved using the Fourier-Bessel transform. The result is the familiar *Airy pattern,* named after its discoverer, G. B. Airy.

$$U(\alpha/\lambda) = 2\pi \int_0^{\infty} t(r) J_0\left(\frac{2\pi}{\lambda}\alpha r\right) r\,dr = 2\pi \int_0^{d/2} J_0\left(\frac{2\pi}{\lambda}\alpha r\right) r\,dr = \frac{\lambda d}{2\alpha} J_1\left(\frac{\pi\alpha d}{\lambda}\right). \tag{4}$$

The intensity is proportional to the aperture area:

$$I(\alpha/\lambda) \propto \left(\frac{\lambda d}{2\alpha}\right)^2 J_1^2\left(\frac{\pi\alpha d}{\lambda}\right). \tag{5}$$

The first diffraction minimum corresponds with the first zero of the Bessel function $J_1(x)$ at $x \approx 1.22\,\pi \approx 3.83$. Hence, with θ as the polar angle,

$$\alpha \approx 1.22\ \lambda/d \ \rightarrow\ \sin\theta \approx 1.22\ \lambda/d . \tag{6}$$

To compare the *phase* of Eq. (4) with an ideal, spherical wavefront, notice that the expression is purely real. Changes in sign correspond to a π change of phase. Thus, by inspection, the phase of the Airy

Table 2. Maximum measurement NA based on an ideal Airy diffraction pattern producing a spherical reference wavefront within the first diffraction minimum.

d [nm]	50	75	100	125	150	175
NA	0.33	0.22	0.17	0.13	0.11	0.094

pattern relative to an ideal spherical wave ϕ_{Airy} is

$$\phi_{Airy} = \begin{cases} 0, & J_1(\pi\alpha d/\lambda) \geq 0 \\ \pi, & J_1(\pi\alpha d/\lambda) < 0 \end{cases}. \tag{7}$$

In this simple treatment, the phase of the diffracted wavefront is *perfect* over the central region of the pattern. The NA that is filled by this central region is

$$\mathrm{NA}_{filled} \approx \sin\theta \approx 1.22\ \lambda/d\ . \tag{8}$$

Calculations based on Eq. (8) are shown in Table 2.

In each TEMPEST simulation case, the phase of the diffracted wavefront is fit to a series of Zernike polynomials (see Chapter 15) over a range of NA angles. The four lowest-order polynomials that describe the displacement of the coordinate system from the wavefront center of curvature are removed from this analysis. Pinholes from which the remaining peak-to-valley (P-V) wavefront aberration is larger than 0.15 λ are rejected from consideration in this study. This includes all pinholes larger than 150-nm in diameter.

2.3.2 *Cylindrical and Conical Bore*

In addition to a simple cylindrical bore, two conical bore models, tapered (narrower at the exit) and flared (wider at the exit), are studied in this chapter. For both of the conical models, the cone half-angle is 10°. The five pinhole diameters studied here are 50, 75, 100, 125, and 150 nm. Conical pinholes are labeled by their *maximum* diameters.

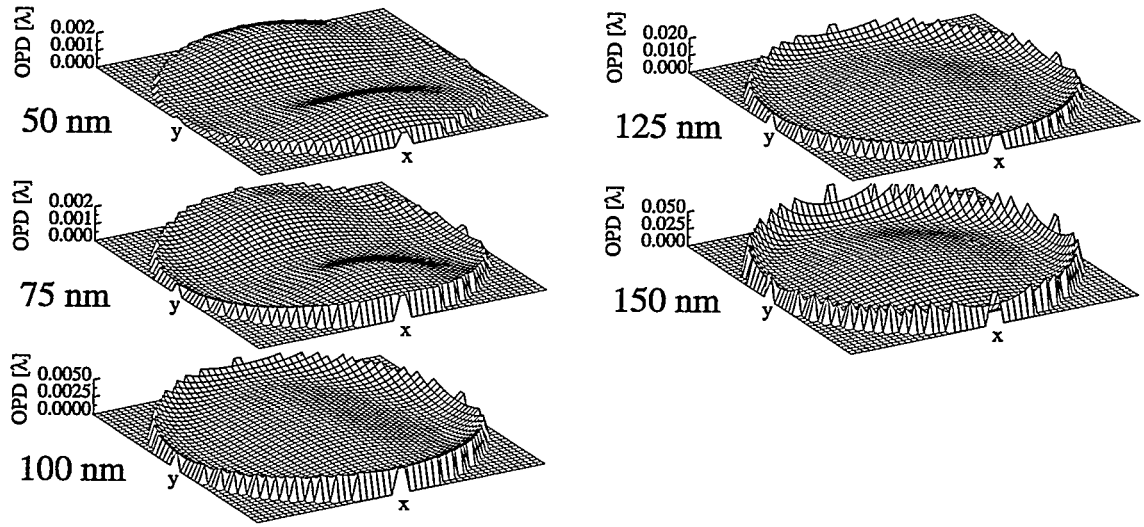

Figure 5. Calculated wavefronts diffracted by cylindrical pinholes. The optical path difference (OPD) between the diffracted wavefront and an ideal spherical wavefront is shown. The incident illumination is *x*-polarized. Note the changes in the *z*-axis scaling.

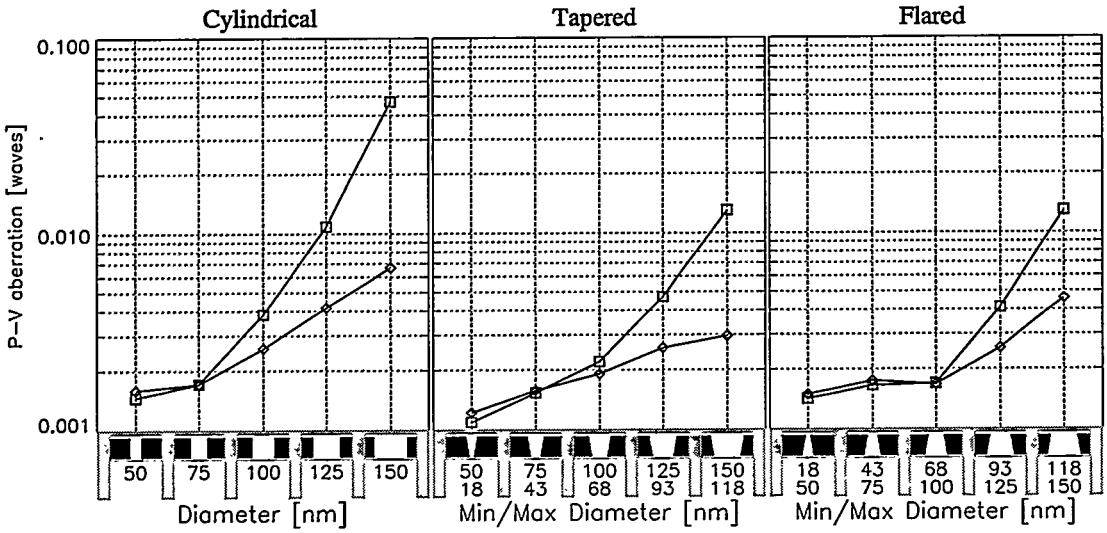

Figure 6. Calculated P-V wavefront aberrations within 0.08 (diamond symbol) and 0.1(square symbol) NA for three pinhole bore shape models and five different diameters. Pinhole cross-sections, parallel to the polarization vector, are shown above the *x*-axis labels: black represents the cobalt membrane, white is empty space. Anomalous behavior is seen in the 50-nm-diameter pinholes where the astigmatic aberrations dominate the diffracted wavefronts and the 0.08 NA wavefront has a larger peak-to-valley error than the 0.1 NA wavefront when the defocus terms are subtracted.

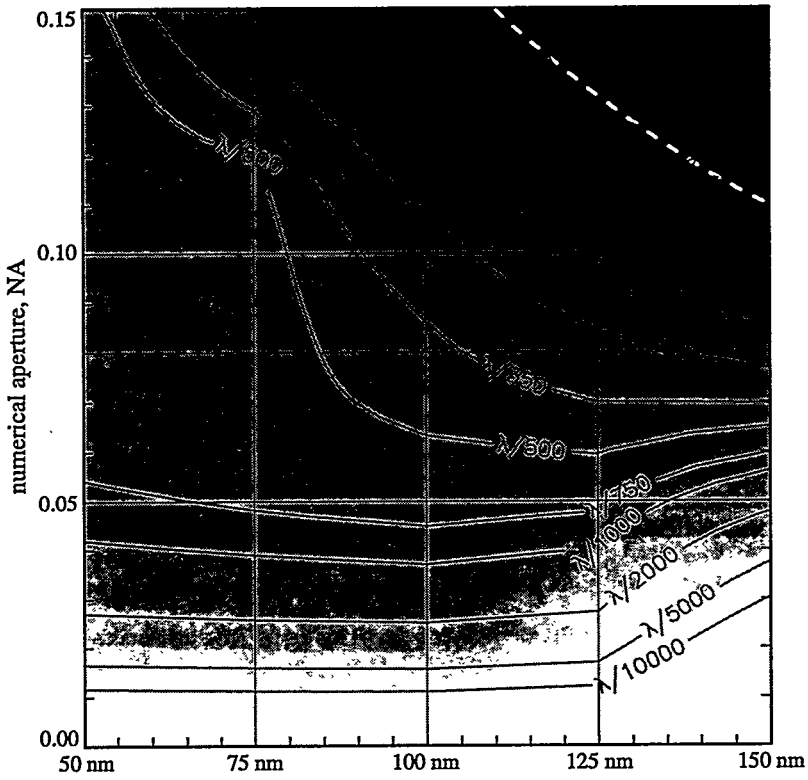

Figure 7. Calculated reference wavefront P-V aberration magnitude plotted as a function of pinhole diameter and numerical aperture for pinholes in the cylindrical bore model. Wavefronts are only calculated for the five labeled pinhole diameters; bi-cubic interpolation is used to generate the contours in the intermediate regions. The expected behavior of wavefront quality improving with reduction in pinhole size is demonstrated; however, anomalous behavior occurs where the pinholes are greater than 100 nm and NA is below 0.08. The cross-section for 0.08 NA is indicated by a dark dashed line. The dashed white line indicates the maximum NA of the spherical wavefront predicted by the simple Airy diffraction formula, NA = 1.22 λ/d.

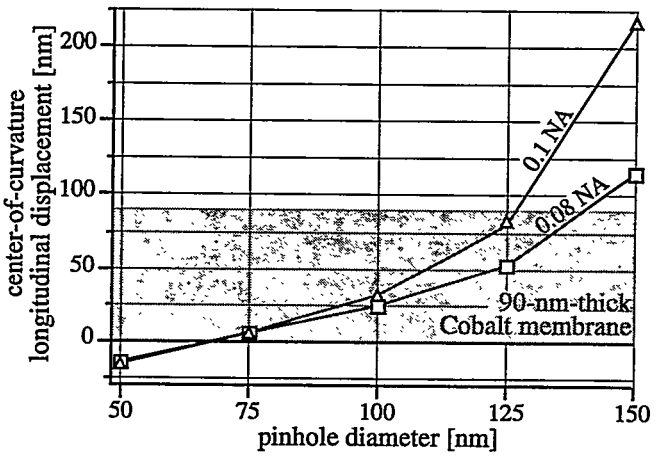

Figure 8. Longitudinal change in the center-of-curvature of the wavefront diffracted by cylindrical pinholes of five different diameters. The center-of-curvature is determined from the defocus term in a best-fit Zernike polynomial series representation of the reference wavefront. The presence of higher-ordered aberrations creates a dependence of the defocus on the NA of measurement; this is especially evident for the 150-nm-diameter pinhole. Longitudinal position is measured from the bottom (exit-side) of the cobalt membrane; positive position values indicate that the center-of-curvature lies *within* the pinhole.

Calculated wavefronts diffracted by the cylindrical pinholes are plotted in Fig. 5 with the piston, tilt, and defocus components removed. Wavefronts diffracted by the two smallest pinholes reveal a small astigmatic component, while the largest pinholes diffract wavefronts dominated by rotationally symmetric aberrations.

The calculated P-V wavefront aberration magnitudes are plotted in Figs. 6 and 7 for each of the pinhole bore shapes and diameters studied. Within this range, the P-V aberration magnitude is an increasing function of the pinhole size. The dominant wavefront aberration components for the larger pinholes are rotationally symmetric (spherical aberration). However, a small astigmatic ($\cos 2\theta$) component, less than 0.02 λ P-V, is present in each diffracted wavefront.

There is no significant qualitative difference between the wavefronts diffracted by the cylindrical and the conical pinhole models. In general, each conical pinhole diffracts a reference wavefront that is similar to a wave diffracted from a cylindrical pinhole of diameter between the minimum and maximum conical diameter.

As the raw wavefront data is analyzed, defocus, a rotationally-symmetric aberration component of order r^2, is typically the dominant aberration component. Defocus, however, arises from the arbitrary position of the origin of the coordinate system (just below the pinhole membrane) used in the calculation. Experimentally, the defocus is determined by the relative longitudinal positions of the test beam and the membrane containing the reference pinhole. There exists one point along the axis of symmetry which may be called the center-of-curvature of the diffracted wavefront. This point, for which the best-fit defocus is identically zero, occurs somewhere in the vicinity of the reference pinhole. The next-higher rotationally-symmetric aberration component is spherical aberration, of order r^4. Due to the r^2 dependence of the defocus magnitude and presence of higher-order aberrations, the best-fit amount of defocus in an arbitrary reference wavefront depends strongly on the NA of measurement.

One characteristic observable in the data is a shift of the longitudinal position of the center-of-curvature with changing pinhole size, shown in Fig. 8. This effect is an important contributor to the astigmat-

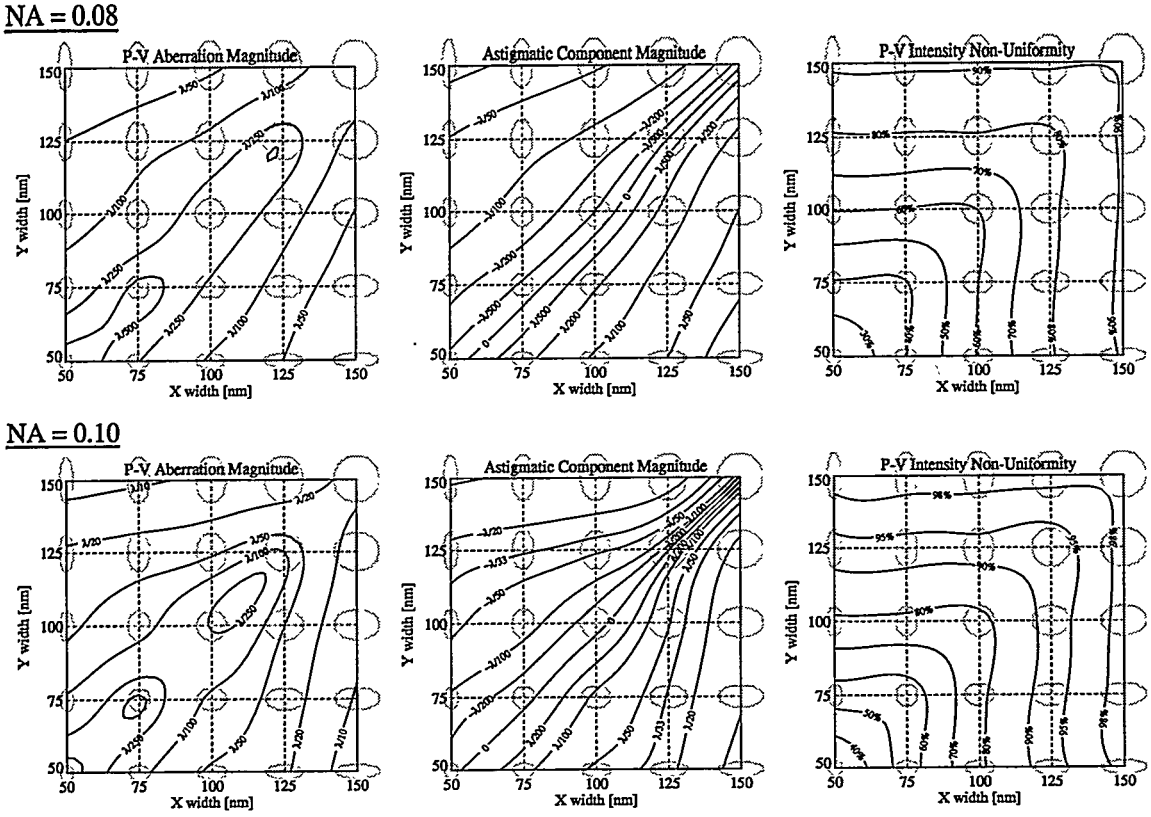

Figure 9. Calculated characteristics of the reference wavefronts diffracted from elliptical pinholes into 0.08 and 0.10 NA. With the position-dependent wavefront components removed, the residual P-V wavefront aberrations, the amplitude of the astigmatic (cos 2θ) components, and the intensity non-uniformity are shown. The 25 pinhole shapes are shown in grey behind the appropriate locations on the plots; intermediate points are based on a minimum-curvature surface interpolation and are thus not verified by the simulation. Pinhole ellipticity and the *x*-direction polarization of the incident light both introduce a small amount of astigmatism into the diffracted wavefronts. Note that in the top-center plot, the unlabeled contours are λ/33. In the bottom-center plot, the unlabeled contour is λ/10.

ic wavefront found from *elliptical* pinholes, discussed in the following section.

The asymmetric wavefront components in diffraction from *circular* pinholes come from the polarization of the incident field. As stated earlier, electric field components parallel and perpendicular to the vertical walls of the pinhole satisfy different boundary conditions. The field emerging from the pinhole is not rotationally symmetric, but contains *astigmatic* components.

2.3.3 *Elliptical Bore*

A series of simulations was conducted to investigate the effect of elliptical pinhole cross-sections on the diffracted wavefront. Several of the relevant reference wave parameters are shown in Fig. 9, for 25 width and ellipticity combinations at 0.08 and 0.1 NA.

From elliptical pinholes, the diffracted reference wavefront can contain a significant amount of astigmatism. In the previous section, the dependence of the longitudinal position of the center-of-curvature with respect to the pinhole size was discussed; this effect is manifest in the rotationally-symmetric defocus term. Here, where the pinholes are elliptical, the horizontal and vertical *centers-of-curvature*

occur at different longitudinal positions; the r^2 defocus term then takes on a 2θ dependence and astigmatism is introduced into the diffracted wavefronts. Furthermore, regarding the higher-ordered aberrations, the elliptical pinhole wavefronts show greater aberration magnitudes in the direction of the pinholes' major-axis, leading to an additional source of astigmatism. Figure 9 shows the P-V aberration magnitude and the magnitude of these astigmatic components, in addition to the intensity non-uniformity discussed in the following section. Since the astigmatic term depends on cos 2θ, a negative sign of the coefficient simply indicates rotation by 90°.

2.4 INTENSITY UNIFORMITY

Separate from the wavefront phase, an important consideration for the quality of the reference wavefront is the intensity uniformity across the NA of measurement. In an ideal Airy pattern, for example, although the wavefront *phase* is that of an ideal spherical wavefront, the *intensity* varies monotonically from its peak at the center of the pattern to zero at the first diffraction minimum. Since the signal-to-noise of the measurement is related to fringe contrast, and fringe contrast depends on the relative intensities of the test and reference waves, the uniformity of the reference wave must be taken into consideration in the selection of the appropriate reference pinhole diameter.

To evaluate the uniformity of the pinhole-diffracted reference wave, define a non-uniformity

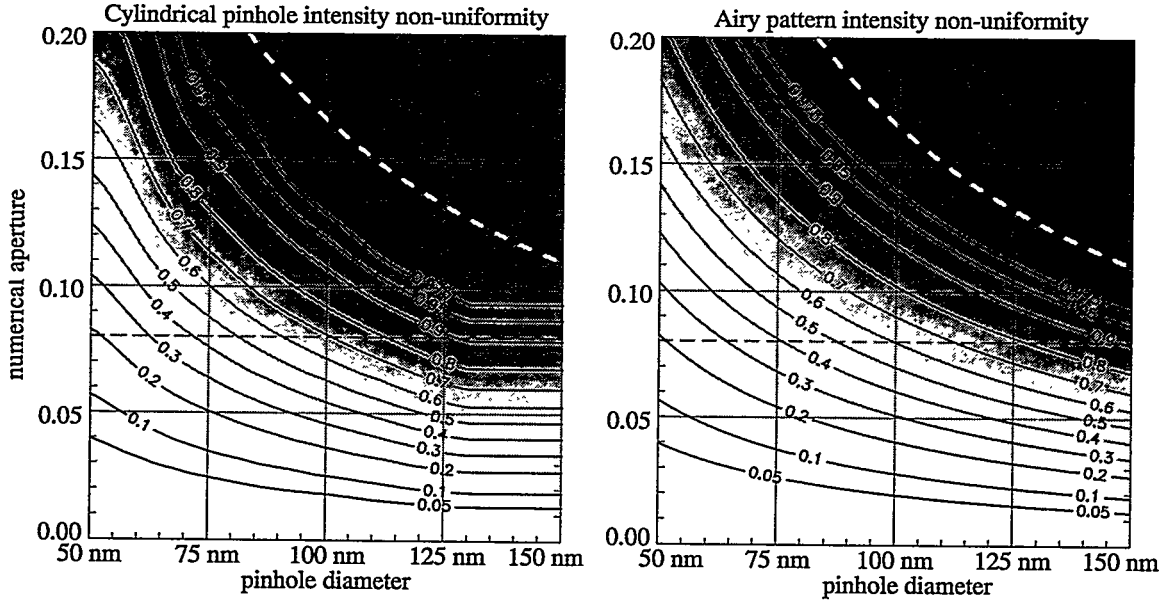

Figure 10. The intensity non-uniformity of the diffracted wavefronts in the cylindrical bore model, calculated for a range of pinhole diameters and numerical apertures and compared with the features of the Airy pattern. Pinhole-diffracted reference waves cannot uniformly illuminate arbitrarily large apertures. Non-uniformity from the radial decrease in intensity ultimately affects interferogram fringe contrast. The dashed dark line indicates 0.08 NA. The dashed white line indicates the angle of the first Airy diffraction minimum where, in the simple theory, the non-uniformity is one.

parameter ν as

$$\nu \equiv 1 - \frac{I_{min}}{I_{max}}. \tag{9}$$

By this definition, when the reference wavefront is perfectly uniform, I_{min} equals I_{max}, and ν is zero. On the other hand, if the reference wave intensity falls to zero within the NA, then I_{min} equals zero, and ν is one.

Based on the TEMPEST 3D calculations for the cylindrical-bore pinhole model, discussed in Section 2.3.2, Fig. 10 shows the reference wave intensity non-uniformity as a function of pinhole diameter and NA. The TEMPEST compares very closely with the simple Airy model, also shown. The calculation reveals that a reasonable reference wave non-uniformity of 30% at 0.08 NA requires a sub-75-nm-diameter pinhole, and at 0.1 NA requires a sub-50-nm pinhole. These are very challenging requirements.

2.5 ERROR ANALYSIS

The uncertainty of the phase or intensity of the diffracted waves can be estimated using information about the simulation method and separately, using data from the calculations. The simulation convergence requirements, the electric-field data, and a separately calculated secondary data set are here used to place upper limits on the magnitude of the uncertainties.

One cause of uncertainty is the finite lateral size of the simulation domain. An estimate of the total power *outside* of the simulation domain provides an upper-limit to this uncertainty. Based on the field magnitude at the edge of the domain and the rate of field attenuation away from the pinhole, the uncertainty upper-limit in the diffracted field is estimated to be not more than 10^{-4} based on a unit amplitude incident field. This field uncertainty translates to 10^{-4} radians or $\sim 2\times10^{-5}$ waves of phase uncertainty. Attenuation in the membrane makes the contributions from the adjacent virtual pinholes in the periodic simulation domain even smaller than this level. Further study is required to fully characterize the uncertainty introduced by the small domain size.

The TEMPEST 3D electromagnetic-field simulation utilizes an iterative approach to compute the fields within the domain. Convergence or *steady-state* is achieved when three successive iterations agree to within a given *absolute* tolerance ε. Only a small subset of the domain points are used in the convergence testing. An alternate convergence scheme using the *relative* field magnitude may be more appropriate for simulations such as this, where the field magnitude varies substantially from one region to the next. Furthermore, convergence tests across the entire domain or a full cross-section of it would improve confidence in the results. Such strategies were not implemented in this version of the TEMPEST program.

With a unit amplitude input electric field, the convergence parameter ε is set equal to 0.01. Smaller values require much longer processing time, making their use infeasible for the breadth of experiments

performed. Yet this value of ε renders the uncertainty in each point to be as large as 0.01. With the calculation of the first-quadrant field *unfolded* to all four quadrants, there are 255 × 255 or 65,025 lateral nodes in the domain. Since the diffracted wave is calculated via discrete Fourier-transform, the errors propagate linearly into the wavefront measurement. That is, any component of the Fourier-spectrum is calculated by a simple summation of the field in the image-plane. The maximum uncertainty (without any scaling coefficient) in that measurement is 65,025*ε ≈ 650. The figure of merit is the ratio of this maximum uncertainty to the amplitude of the diffracted wave: this value dictates the *maximum* phase error. For the five pinhole sizes ranging from 50 to 150 nm {50, 75, 100, 125, 150 nm} the unscaled peak amplitudes of the diffracted waves are {5503, 8222, 12044, 17460, 23013}, making the maximum uncertainty at the peaks {11%, 8%, 5.4%, 3.7%, 2.8%}. Following this argument, the uncertainties increase away from the peak because of the decrease in the diffracted wave's amplitude with angle.

Uncertainty in the complex field amplitude translates directly into maximum uncertainties in the phase. Based on the vector addition of the peak calculated field amplitude with the uncertainty (having unknown phase), the maximum net phase error is {0.11, 0.08, 0.054, 0.037, 0.028} radians, or {0.018, 0.013, 0.009, 0.006, 0.004} waves or {λ/56, λ/77, λ/116, λ/170, λ/224}.

In practice, these maximum uncertainty values are *much* larger than the actual errors in the calculation. Because of the absorptive membrane, most of the field amplitudes at the exit-side of the simulation domain are smaller than 0.01, the error tolerance, yet the fields are well-behaved and are reliable to a much higher accuracy.

One secondary estimate of the uncertainties comes from consideration of the *y*-polarized field. The illuminating electric field is polarized only in the *x*-direction and the material contains no polarization-rotating bi-refringence. The presence of a *y*-polarized field comes from very small glancing-incidence reflections within the pinhole and from numerical errors accrued during the calculation of various vector field curls and divergences. For this reason, the errors should not be larger than the amplitude of the *y*-polarized components.

Similar to before, since a discrete Fourier-transform is used to calculate the diffracted wave, the sum of the absolute values of the *y*-polarized field amplitudes at the exit-side of the domain can be used to estimate the error. Here, the field totals for the three smallest pinholes are {60, 34, 19}, meaning uncertainties at the peaks of {0.3%, 0.4%, 0.5%} relative to the peak amplitudes stated previously. Because of the intensity fall-off, uncertainties at the maximum angles within the diffracted wavefront are on the order of twice these values. The amplitude uncertainties relate to phase uncertainties of {4.8×10^{-4}, 6.4×10^{-4}, 8.0×10^{-4}} waves, or {λ/2100, λ/1570, λ/1260}.

It is difficult to judge the accuracy or reliability of these calculations well below λ/100 or λ/500.

Further research could be used to clarify some outstanding issues: how do the diffracted waves depend on the domain size, the number of nodes per wavelength, the absolute error tolerance ε, single- versus double-precision calculations, etc.? In the absence of such tests, these results must stand as they are, awaiting further verification.

2.6 CONCLUSION

Calculated EUV wavefronts diffracted into 0.08 and 0.1 NA by 50 to 150-nm pinholes in a cobalt membrane show aberrations that increase as a function of pinhole size. Even in the presence of a slightly conical bore or an elliptical cross-section, the diffracted wavefronts are spherical to within 0.01 waves (λ/100) from 125-nm pinholes and within 0.002 waves (λ/500) from sub-75-nm circular pinholes. Both polarization and pinhole ellipticity introduce astigmatic components into the diffracted wavefront. Polarization contributes astigmatism due to the rotational-symmetry-breaking boundary conditions. Since the longitudinal center-of-curvature varies as a function of pinhole diameter, elliptical pinholes with different diameters along the major and minor axes generate astigmatism by a different mechanism.

The intensity uniformity of the diffracted waves is an essential consideration for evaluating the quality of the reference wavefront. Experimentally, the desire for intensity uniformity places a separate restriction on pinhole size from the phase-uniformity requirement. Within these simulations it is shown that the sub-75-nm pinholes are capable of producing non-uniformities below 30% for 0.08 NA measurements, while sub-50-nm pinholes are required for the same non-uniformity at 0.1 NA. These results closely follow the predictions of the simple Airy-pattern from the Kirchoff diffraction model.

To the extent that these pinhole models correctly represent experimental conditions, measurements of aberrated spherical wavefronts using EUV point diffraction interferometry may be limited to an accuracy of a few thousandths of a wavelength when pinholes as small as 50 nm are used — substantially smaller than the diffraction-limited resolution of the test optics.

II. THE CONVENTIONAL PDI

3

The Point Diffraction Interferometer

3.1 INTRODUCTION

The first prototype implementation of the EUV point diffraction interferometer (PDI) was dedicated to the development of high-accuracy EUV interferometric capability, and to the investigation of high-resolution Fresnel zoneplate lenses. The experiments and measurements described in this chapter detail the progress made toward those goals.

Experiments related to the investigation of zoneplate aberrations were conducted between August 1994 and August 1995. These experiments revealed the nearly diffraction-limited quality of the low-spatial-frequency wavefront aberrations (Goldberg et al. 1995a, 1995b). Mid- and high-spatial frequency aberrations were observable in the measured intensity profiles (Tejnil et al. 1996b).

As a demonstration experiment, the EUV interferometry performed on Fresnel zoneplate lenses was the first critical step toward the development of more sophisticated measurement techniques. Ultimately, the uncertainties in the measurements were on the same order as the wavefront aberrations that were found, and the success of the measurements was limited by a range of experimental issues. However, a great number of concrete lessons were learned; the significant problems were identified and later overcome.

This chapter details the theory and use of the EUV PDI and describes the experimental system. The characterization of a Fresnel zoneplate lens is presented. Development of this prototype EUV interferometer led to a superior interferometer design concept, the PS/PDI, which is the subject of Part III of this thesis. Before the measurement goals for the zoneplate lenses could be achieved, the PS/PDI was applied to the measurement of lithographic reflective optical systems.

3.2 THE CONVENTIONAL PDI

The PDI was first described by Linnik (1933) and later by Smartt and Steel (1975) as a simple, common-path, wavefront-splitting interferometer well-suited for applications in X-ray optics, where conventional amplitude-splitting interferometer designs are not easily implemented. The PDI has previously been used successfully in a number of short wavelength applications (Speer et al. 1979, Mrowka and Speer 1981). The interferometer, shown in Fig. 1, consists of a small *reference pinhole* in a semi-transparent membrane, placed near the focus of a coherently illuminated optical system under test. The illuminating beam is often generated by a suitable *object pinhole spatial filter* to ensure a coherent, spherical wavefront.

A single beam passes through the test optical system, acquiring the aberrations of interest here. This may be considered as the linear superposition of two beams transmitted through the pinhole membrane. One beam passes through the membrane undiffracted and forms the interferometer's *test beam.* Light diffracted through the tiny pinhole forms the *reference beam*, and overlaps the test beam across the

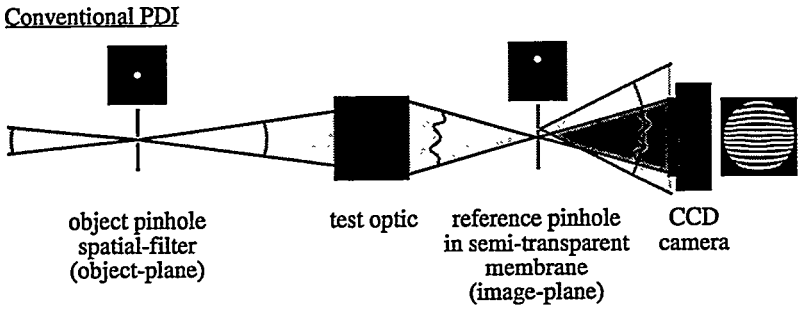

Figure 1. A schematic representation of the essential components of the Conventional PDI. A tiny pinhole in a semi-transparent membrane is placed near the focus of a coherently illuminated optical system. Light diffracted from the pinhole forms a reference wave that overlaps the test wave over the numerical aperture of interest.

measurement NA. In principle, the reference beam consists of a nearly perfect, spherical wavefront, and the test beam contains the aberrations of the optical system. Where the overlap occurs, interference fringes appear in a measurable pattern that reveals the path-length difference between the two beams.

The reference pinhole size must be chosen to balance two opposing concerns: throughput and reference wavefront quality. The pinhole should be significantly smaller than the diffraction-limited focal spot size of the optic under test to ensure a high-quality diffracted reference wavefront across the NA of measurement. Reducing its size decreases the amount of light diffracted into the reference beam. Because interference fringes are required for analysis, the pinhole often must be displaced significantly from the focus into a region where the light intensity is low. This further reduces the amount of light in the reference beam. From the balance of these considerations, the transmission of the semi-transparent membrane is chosen to provide nearly equal intensity in the two interfering beams, ensuring high fringe contrast. The optimum number of fringes required for analysis is strongly dependent on the power spectrum of the test optic. Analysis issues are addressed in Part IV.

3.3 EXPERIMENTAL COMPONENTS

This section presents a description of the key components of the EUV PDI system configured for the measurement of Fresnel zoneplate lenses. The key elements are shown schematically in Fig. 2.

3.3.1 *EUV Fresnel Zoneplates*

A number of zoneplates were prepared and examined with the EUV PDI. Because of experimental limitations, the wavefront aberrations were carefully investigated in only one zoneplate.

A series of similarly prepared zoneplates was fabricated by Erik Anderson and Dieter Kern (1992) for testing with the EUV PDI. The binary zoneplates used in these experiments were fabricated in electroplated nickel on a silicon-nitride membrane. The zone plates have a diameter of 200 μm, an outer zone width of 75 nm, and a *primary* or *first-order* focal length of 1.2 mm at 13.5-nm wavelength. The zone

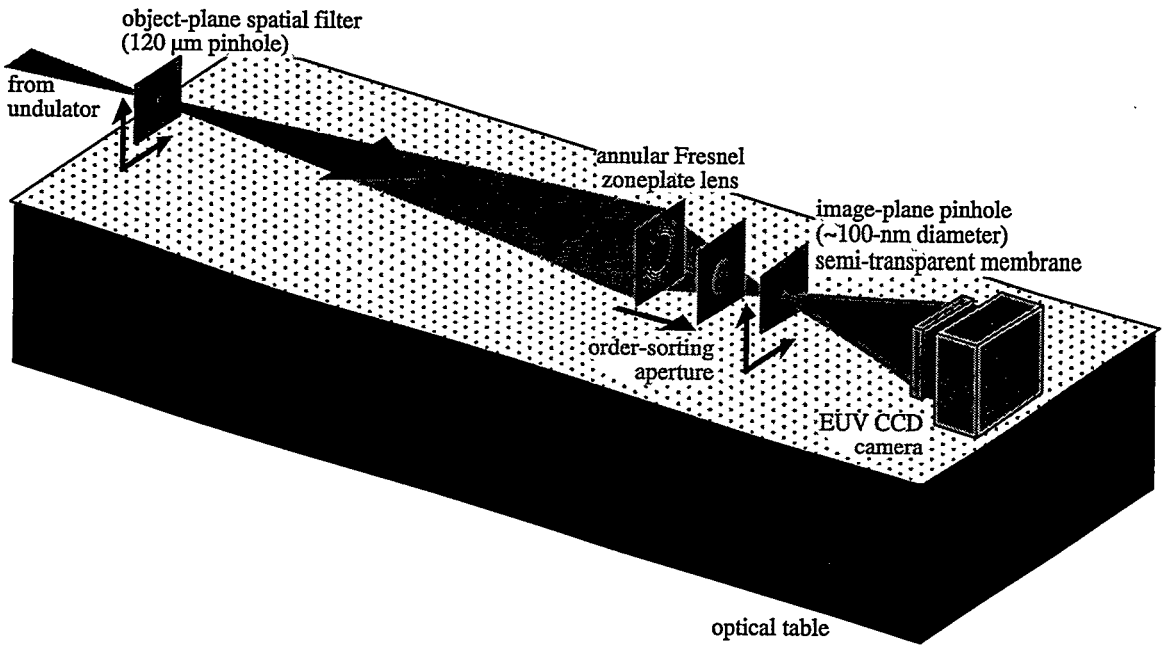

Figure 2. The arrangement of the PDI components configured for EUV Fresnel zoneplate measurement, 1994-5. The arrows indicate the degrees of freedom of the five translation stages. Measurements were performed at Beamline 9.0.1 at the Advanced Light Source.

plates contain an opaque *central stop* of 60-μm diameter, which gives them an annular pupil. Without the central stop, the zoneplate design calls for approximately 640 transparent and opaque zone pairs.

As discussed in Appendix 4, EUV light is diffracted by the zoneplate into a series of converging and diverging diffractive orders, each with a unique real (converging) or virtual (diverging) focal point. In addition to the diffracted orders, there is a strong "undiffracted" zeroth-order component that propagates forward without focusing.

Wavefront measurements are based on the focused first-diffractive order. Overlapping light from the other orders is blocked by an essential, appropriately-located aperture stop, called an *order-sorting aperture* (OSA). Of primary concern are the overlapping zeroth-order and negative-first-order beams. If not adequately blocked, the strong zeroth-order beam is capable of causing damage to a sensitive detector. Although it contains only (roughly) twice as much flux as the first-order, it propagates in a comparatively narrow angle. The negative-first-order beam is of equal strength as the first-order beam and propagates past the focus with the same divergence angle. Because these beams originate from the comparatively small zoneplate lens and propagate over a large distance, their overlap in the detector plane is nearly complete.

The OSA is placed in a position where it takes advantage of the opaque central stop of the annular pupil. This is shown in Fig. 3. It is necessary to place the OSA far enough away from the zoneplate that the first-order beam is narrower than the diameter of the OSA pinhole while maintaining enough working distance in the vicinity of the focus to allow the PDI membrane room to operate. The position of the OSA

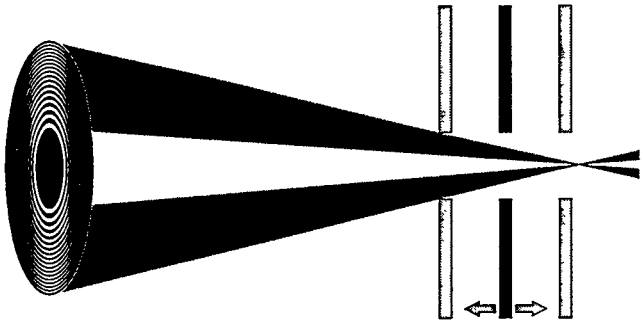

Figure 3. Position of the order-sorting aperture to transmit only the focused, first diffracted-order from a Fresnel zoneplate. With a 60 μm central stop in the 200-μm-diameter annular zoneplate and a 50-μm OSA pinhole, the OSA must be placed more than 3/4 of the distance to focus from the zoneplate; yet the OSA must not project so far as to limit access to the focal plane by the PDI pinhole membrane.

determines the range of wavelengths that can be used without obstruction. Some of the data in this chapter show the effects of the OSA encroachment on the first-order beam. With a first-order beam of 200-μm diameter at the zoneplate, and an OSA of 50-μm diameter, the OSA must be placed beyond 3/4 of the distance to focus. Here, with a focal length of 1.2 mm, the OSA must be placed beyond 0.9 mm from the zoneplate, leaving less than 0.3 mm of working distance.

The OSA is mounted to the zoneplate membrane and positioned in the following way. The OSA pinhole exists at the center of a thin, circular metal foil. Using an appropriately-sized ball-bearing, the foil is forced to conform to a spherical shape by firmly pressing the ball-bearing and foil into a thick piece of rubber. The foil then forms the shape of a spherical cap, with the pinhole at the center. The target height of the cap is around 1 mm, but not less than 0.9 mm. Using a microscope to observe the back-illuminated zoneplate, the cap is carefully positioned with the OSA pinhole above the zoneplate center. It is then held in place using a drop of epoxy.

3.3.2 *Light Source Description*

The light source used in these experiments is an undulator beamline operating at the Advanced Light Source (ALS) at Ernest Orlando Lawrence Berkeley National Laboratory. The beamline incorporates a spherical grating monochromator with a resolving power of $\lambda/\Delta\lambda \approx 3000$ (FWHM) at 13-nm wave-

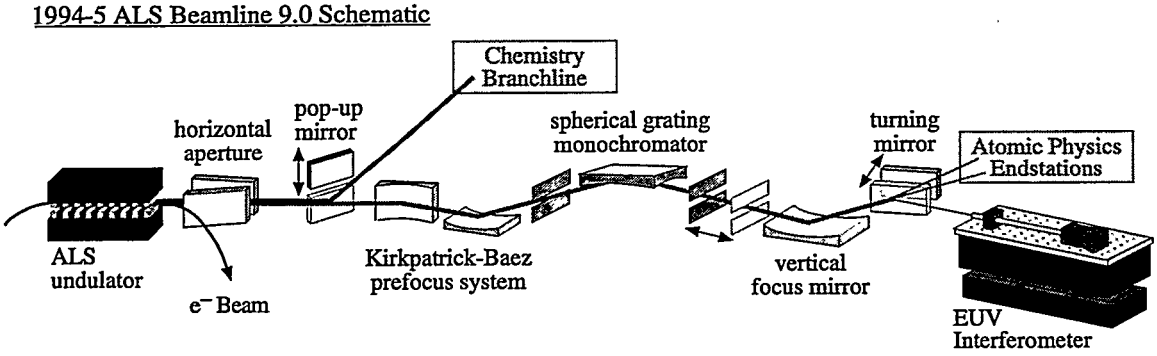

Figure 4. Schematic representation of the shared 8-cm-period undulator beamline 9.0 at the Advanced Light Source, c. 1994-5. A spherical grating monochromator provides a resolution of $\lambda/\Delta\lambda \approx 3000$ and a flux of 10 mW through a 120-μm pinhole. In the horizontal direction, the source is imaged onto the interferometer's object plane, 1:1. A bendable focusing mirror vertically re-images the beam from the monochromator's exit slit onto the interferometer's object plane.

length. Glancing incidence beamline optics, shown schematically in Fig. 4, focus the beam both horizontally and vertically onto an entrance pinhole spatial filter located 2.4 meters from the zone plate. The entrance pinhole diameter, which determines the spatial coherence of the zoneplate illumination, was chosen as 120 μm to maximize throughput without sacrificing illumination uniformity. This diameter is small enough that the zoneplate produces a diffraction-limited focal spot with a central Airy disk diameter of approximately 170 nm in the plane of the primary (first-order) focus. Flux through the entrance pinhole is in the range of 10^{11}–10^{12} photons per second, or ~10 μW at 13.0-nm wavelength, depending on experimental conditions, including wavelength and other beamline settings.

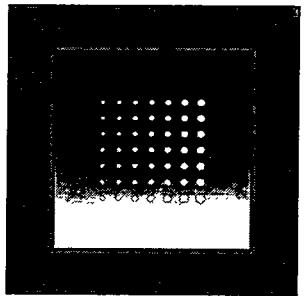

Figure 5. The PDI pinhole array provides a range of pinhole diameters and absorber thicknesses for various working conditions. The pinholes, spaced by 40 μm, are used one-at-a-time.

3.3.3 *Pinhole Descriptions*

A variety of image-plane reference pinholes were fabricated for use in the first EUV PDI experiments. As this was a prototypical system, the optimal pinhole membrane configuration was not known before the experiments were conducted. Special membranes were fabricated (Spallas et al. 1995) containing an array of pinhole sizes and with a graded absorber thickness, according to the prescription of Sommargren and Hostetler (1993). These arrays were intended to cover a range of testing situations and also to identify the optimum experimental combination of attenuation and pinhole size. The original design of this membrane, shown in Fig. 5, consisted of a 200-nm-thick silicon-nitride membrane and a graded cobalt film of approximately 40 to 70-nm in thickness as the absorber layer. The pinholes, patterned by electron beam lithography, ranged in size from 150 to 400-nm in diameter. The pinholes were etched completely through the silicon-nitride membrane prior to the cobalt deposition. This thermal evaporation process was done using care to achieve highly anisotropic deposition, which maintains the open pinholes through both the cobalt absorber and the silicon-nitride membrane.

Initial PDI interferometric tests (Goldberg et al. 1994, 1995a, 1995b) revealed that to improve the reference wavefront quality and fringe contrast, smaller pinholes and increased attenuation were required. Both objectives were satisfied by an additional deposition step. Approximately 2.4 nm of chromium, followed by 24 nm of gold, were deposited by thermal evaporation. The effective pinhole diameters were determined before and after deposition by observation of the diffraction pattern, including angles beyond the angle of the first diffraction minima, under plane-wave illumination conditions. Pinhole diffraction data is described in Section 3.5.

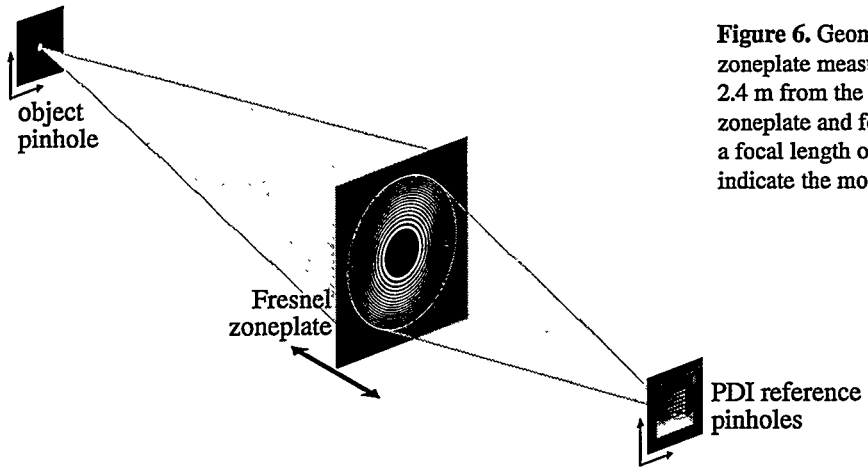

Figure 6. Geometry of the PDI Fresnel zoneplate measurement. The object pinhole, 2.4 m from the zoneplate, is imaged by the zoneplate and forms a first-order focus with a focal length of 1.2 mm at 13 nm. Arrows indicate the motions of the five stages.

3.3.4 *Stages*

Alignment of the essential components of the interferometer is achieved using five translation stages, shown in Fig. 6. The object pinhole spatial filter sits on a kinematic rotation stage, allowing it to be easily removed and replaced. This is mounted to a two-axis lateral translation stage, controlled by hand using two micrometers. The system demagnification of 2000 and the relatively large pinhole size (120-μm) make hand-positioning possible. Positioning the reference pinhole near the zoneplate focus requires three degrees of freedom. Here the zoneplate is mounted to the end of a cylindrical tube that attaches snugly into an axial mount maintaining a constant polar-angular orientation. Through a pair of bellows, this mount is coupled to a longitudinal-direction stage outside of the vacuum chamber. The PDI pinhole membrane attaches kinematically to a mount that is also coupled through a bellows to a high-resolution lateral motion stage. Using a pair of dc-motors and a two-dimensional Heidenhein scale, this critical stage is capable of 0.01-μm resolution and stability over an approximate area of 8 mm × 2 mm.

3.3.5 *Other Components*

At a distance of several centimeters beyond focus, the light from the zeroth-order beam is hundreds of times more intense than that of the first diffracted order. While the first-order beam diverges to a diameter of 2 cm at the CCD detector plane, the zeroth-order beam remains approximately 200 μm wide. Hence the intensity per unit area is 10,000 times higher in the zeroth-order than the first. To protect the sensitive CCD detector from accidental misalignment of the OSA, a small circular beam-stop is placed before the CCD detector. This beam-stop, often referred to as *the lollipop,* is held by two thin, adjustable wires. Its shadow is visible as a grey disk in the center of each image.

The CCD detector used in these experiments is a Princeton Instruments 1024 × 1024 pixel, back-thinned, back-illuminated, 1-square-inch area, 16-bit detector. At 13.4-nm wavelength, the CCD sensitivity is approximately 0.8 measured counts per photon (measured by Patrick Naulleau). This value is based on measurement of the statistical distribution of measured intensity values at various illumination levels. To

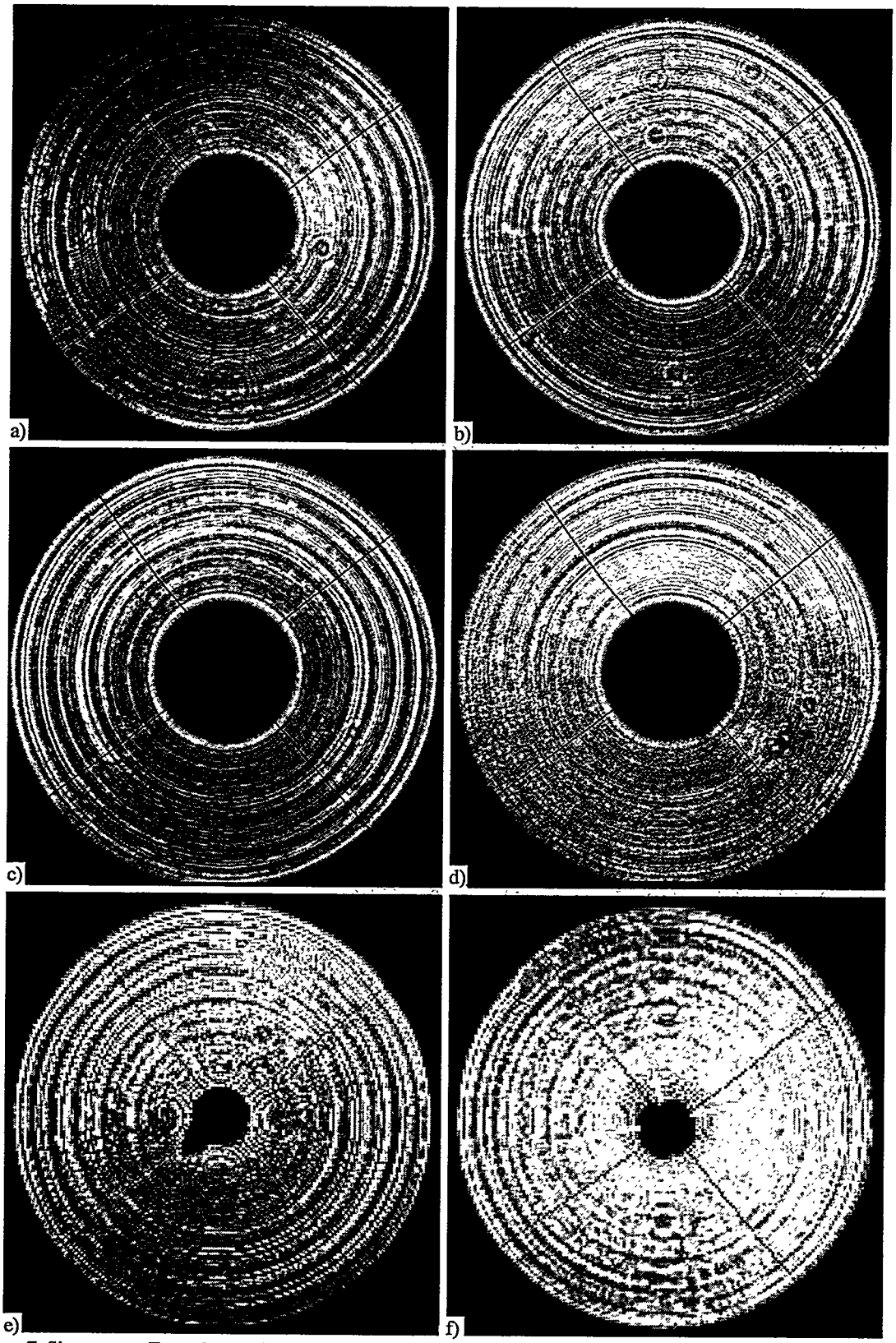

Figure 7. Six separate Fresnel zoneplates were inspected with EUV light. (a) through (d) are made of the same annular design, while (e) and (f) are made with no central stop region. The inspection wavelength is as follows: (a) 12.4 nm (100 eV); (b) through (e) 13.48 nm (92.0 eV); (f) 11.64 nm (106.5 eV). Only zoneplate (a) was used extensively in wavefront measurements.

reduce the contribution of *dark noise*, the detector is cooled to temperatures below –30°C during the experiments. To protect the CCD from contamination, a square-ring cryo-pump *cold-finger* in thermal contact with a liquid nitrogen bath is placed in close proximity to the detector.

A differential ion pump separates the interferometry endstation from the vacuum system of the beamline. Turbo pumps are used to maintain pressures below 1×10^{-5} torr.

3.4 THE TEST WAVE: FRESNEL ZONEPLATE DIFFRACTION PATTERN

Under uniform illumination conditions, the stationary test wavefront measured in the detector plane (far-field) resembles the illumination pattern of the pupil. A 120-μm-diameter pinhole spatial filter placed 2.4 m from the annular Fresnel zoneplate lens provides coherent illumination of acceptable uniformity: at 13.0-nm wavelength, the first Airy-null in the pupil plane has a radius of approximately 300 μm. The radius of the zoneplate is only 100 μm.

The diffraction patterns from a number of similar zoneplates were inspected. Figure 7 shows six of these images. In each case, mid- and high-spatial-frequency errors are clearly visible as circular and radial features in the images. These effects are the result of small fabrication errors, either in zone-placement or in the line-to-space ratio (Tejnil et al. 1996b).

3.5 THE REFERENCE WAVE

The accuracy of the PDI is primarily determined by the quality of the spherical reference wavefront, which is largely determined by the size of the reference pinhole. Size is the most critical aspect of the PDI reference pinholes: they must be small enough to diffract a high-quality spherical wavefront overlapping the entire NA of the zoneplate. Open pinholes on the order of 100-nm diameter in a thick, absorptive membrane are extremely difficult to fabricate, and more challenging to procure. Often the pinholes used in these experiments were slightly larger than the target size range.

Using EUV light, the pinhole quality was established in three ways: first, by inspection of a sampling of pinholes with electron-beam microscopy; second, by observation of the independent pinhole dif-

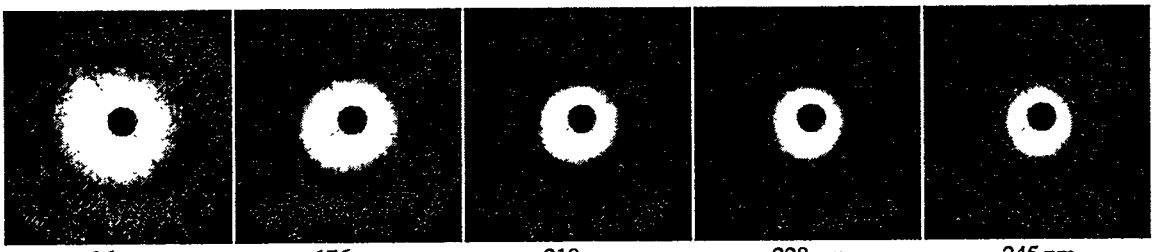

Figure 8. Measured pinhole diffraction patterns from five adjacent reference pinholes of different size. The circular Airy-like diffraction minima enable estimation of the pinhole diameters, as shown below each pattern. The shadow of a small, round beamstop suspended close to the CCD detector is visible as a dark disk in the center of each image.

fraction pattern; and third, by inspection of the measured interferograms. The following sections describe these observational procedures and enumerate the most important experimental difficulties. The issues discussed here are the critical size of the reference pinhole and the inadvertent contamination of the semi-transparent membrane during experiments.

3.5.1 *Pinhole Diffraction*

One way to characterize the pinholes and the reference wavefront *in situ* is to perform pinhole diffraction experiments in which isolated reference pinholes are uniformly illuminated and the far-field diffraction pattern is observed. In order to perform this experiment, a 50-μm diameter circular aperture was placed within 5 mm of the pinhole membrane. In this configuration, with no optical system (zoneplate) in place, the diffraction pattern from each reference pinhole of the 7×7 array was measured at 12.4-nm wavelength.

Five diffraction patterns representing one row of pinholes with increasing diameter and constant absorber thickness are shown in Fig. 8. These pinholes were located in the thickest part of the absorber substrate. The approximate effective pinhole sizes are calculated from diameters of the first minimum ring of the Airy-like diffraction patterns.

3.5.2 In Situ *Pinhole Size Assessment*

It is important to develop inspection criteria to distinguish unacceptable pinholes *in situ*. There are several rapidly identifiable clues in the data which serve as warnings of poor pinhole quality. Usually the interference fringe pattern reveals a clear signature of the reference wavefront. Under uniform plane-wave illumination conditions, the expected diffraction pattern of the reference wave is the well-known Airy-pattern of concentric circular rings surrounding a bright central lobe, and separated by circular intensity nulls. A uniform wavefront phase in each of these rings is shifted by π radians from the neighboring rings. When the pinhole is placed in the outer regions of the focal pattern of the test optic, where the reference pinhole illumination is rapidly-varying, the pinhole diffraction pattern can no longer be described simply as an Airy pattern; yet it does contain many of the same features.

Note: a common practice during the zoneplate experiments is to perform a *background subtraction* to improve the fringe visibility. Here, an image of the test beam alone is acquired with the reference pinhole located very far from the focused beam. By subtracting the test beam pattern from subsequent measurements, the average intensity is close to zero and even faint fringes became clearly visible. The images in Fig. 9 have all undergone background subtraction.

3.5.2.1 ***Zeros of Fringe Visibility.*** Bringing the reference-pinhole-containing membrane out of the focal plane yields an interference pattern of concentric rings. These *defocus* rings result from the mismatched radii-of-curvature of the test and reference beams. It is easily shown from the Fresnel diffraction integral (Goodman 1988:59-60) that for a small longitudinal displacement z, the number of waves of defo-

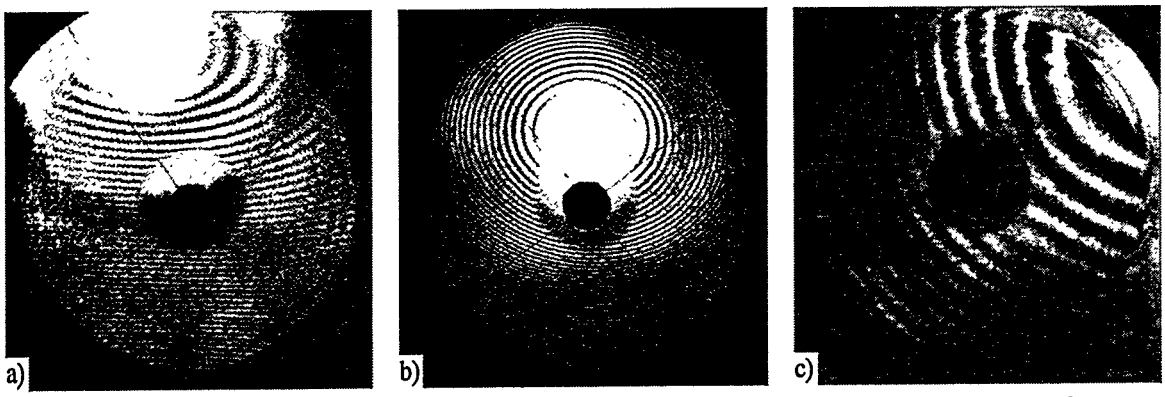

Figure 9. (a) and (b) Interferograms from over-sized reference pinholes show clear evidence of reference wavefront intensity minima within the NA of measurement. When the system is out of focus, the broad reference wave intensity patterns are clearly visible as a modulation in the fringe contrast. (c) Although less pronounced here, the loss of fringe contrast is from this same effect.

cus (equivalent to the number of fringes observed) is

$$n = \frac{(NA)^2 z}{2\lambda} \Rightarrow 4.1\ \mu\text{m / fringe at } 0.08\ \text{NA},\ \lambda = 13.0\ \text{nm}. \tag{1}$$

With a high-density of defocus fringes, reference wave intensity nulls are easily observable as circular bands of zero fringe contrast. This is evident in Fig. 9. Here the images are a combination of multiple patterns: the slowly-varying bands of contrast modulation due to the large pinhole size, the rapidly-varying defocus-fringes due to the longitudinal displacement of the pinhole, the annular pupil of the zoneplate, and the shadow of the beam-stop. Wherever the reference wavefront amplitude nulls occur, the fringe contrast becomes zero. The displaced center of the ring pattern is due to a lateral displacement of the reference pinhole from the test-beam axis.

3.5.2.2 ***Fringe forking.*** An abrupt reference wavefront phase shift of π radians produces a rapid change in the fringe pattern, from bright to dark or vice-versa. This effect is here referred to as *fringe forking*. Several examples of this behavior are shown in Fig. 10.

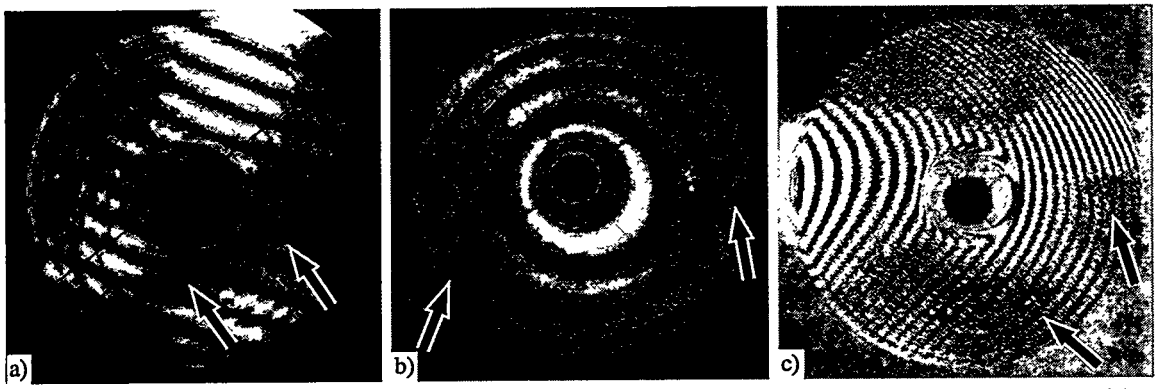

Figure 10. The presence of "forked" fringes, as indicated by the arrows, gives clear evidence for over-sized pinholes. The pinhole diffracted wavefront undergoes an abrupt half-cycle phase-shift as it crosses a diffraction minimum. This causes a point or contour of zero fringe visibility bordered by *forked* fringes one-half-cycle out of phase.

3.5.2.3 ***Contrast variation.*** Even when the pinhole is small enough that there are no regions of zero fringe visibility and no forked fringes, it may still be too large. A properly-sized pinhole behaves as a good spatial filter and creates a uniform reference wave. When an interference pattern contains any regions of reduced fringe visibility, the pinhole is still too large. Often observed are bright regions aligned in the direction perpendicular to the fringes. Most likely this is caused by the directionally-dependent illumination pattern in the focal plane: the pinhole samples a small region in a pattern of rings, causing a directionally-dependent diffracted wave to result. This effect is present in Fig. 10(c).

3.5.2.4 ***Contamination.*** One major experimental difficulty facing EUV interferometry is the issue of hydrocarbon contamination. Although it has not been well characterized, this contamination is frequently observed in varied experiments involving EUV light (Alastair MacDowell, Avijit Ray-Chaudhuri, Werner Meyer-Ilse, personal communication). Hydrocarbon contamination on otherwise clean surfaces apparently occurs at a rate which is dependent both on the density of hydrocarbons in the vacuum system, and on the local intensity of EUV light impinging on a surface.

Because it relies on diffraction from a tiny object in the image-plane, the PDI is *very sensitive* to imperfections in the semi-transparent pinhole membrane — especially those that are close to the reference

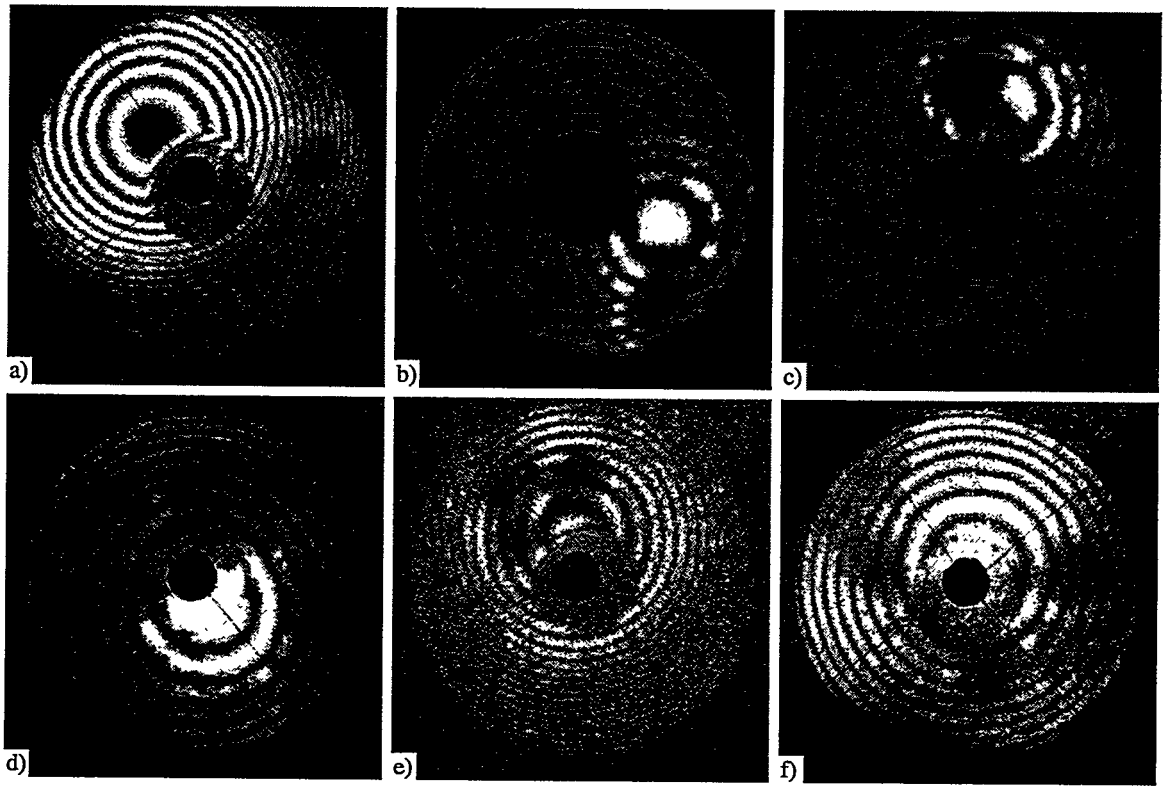

Figure 11. Mask contamination, damage, or defects greatly impair the proper use of the EUV PDI. System alignment and interferogram-recording with long, continuous exposure times inadvertently damaged the mask in the vicinity of the reference pinhole. (d) through (f) Damage is often concentrated along the vertical and horizontal directions because efforts were made to record interferograms with horizontal and vertical fringe patterns. Evidence of this damage is pronounced in the defocused interferogram patterns shown here.

pinholes. Any non-uniformity, transparent or opaque, behaves as an additional point-diffractor corrupting the quality of the reference wavefront. The most sensitive component of the PDI, the pinhole membrane, also receives the most strongly focused EUV light, making it highly vulnerable to contamination. Long, continuous exposures during the interferometry experiments and the inspection of reference pinholes severely damaged many of the membrane pinholes used in these experiments.

Evidence of this damage is clearly visible in the interferograms shown in Fig. 11. In many of the interferometry experiments an attempt was made to align the fringes with either a horizontal or vertical orientation. To do so implies that the reference pinhole must be displaced horizontally or vertically from the center of the focal pattern. Many of the observed damage patterns (especially Figs. 11(c) through (e)) display a "+" pattern consistent with the deposition of hydrocarbons along the two axes. When the pinhole membrane is displaced from the focal plane by several microns in the longitudinal direction, a larger area of the membrane is illuminated. Hence, contamination features that are (relatively) far from the reference pinhole contribute to the interference pattern.

More evidence of contamination in the mask can be seen in the interferogram data of Section 3.6. When, because of contamination, there is more than one point-diffractor, and thus more than one "filtered" reference beam, the multiple beams combine to form an interference pattern of their own, separate from the test wavefront. For example, in the center of the annular aperture where the test beam intensity is nearly zero, a fringe pattern is often observed. Because these multiple "reference beams" are spatially filtered, they typically cover the entire measurement NA, and their interference is most noticeable in the dark regions of the pattern. When image subtraction is used to remove the unmodulated portion of the intensity pattern, these separate, fainter patterns of reference wave interference are most visible.

Two successful, proven ways to combat the build-up of carbon contamination are, first, to clean the experimental and vacuum system components to remove latent sources of hydrocarbons (finger-prints, grease, etc.), and second, to introduce a small pressure of oxygen gas. Although the introduction of oxygen to the PDI system through a thin capillary aimed directly onto the pinhole membrane made no noticeable difference to the contamination issue, the beneficial effects of oxygen have been dramatically demonstrated in the PS/PDI system that followed.

3.6 PDI EXPERIMENTS

During the course of the EUV PDI experiments with the Fresnel zoneplate test optic, several data sets were collected. The limited scope of these experiments results from the narrow experimental window of opportunity that existed between the fabrication of adequately small reference pinholes and the contamination of the pinhole membrane.

Table 1. Measurement of a Fresnel zoneplate test optic in three data sets.

Data Set	Series A	Series B	Series C
Photon Energy	96.0 eV	96.0 eV	96.0 eV
Wavelength, λ	12.9 nm	12.9 nm	12.9 nm
# of images	5	5	4
Orientation	0°	139.5°	139.5°
Exposure Time	60 s	120 s	120 s
Spatial Filter	*none*	120 μm	120 μm
Fringe orientation	horizontal	vertical	horizontal

Among the interferometric data are three sets in particular, A, B, and C, described here and shown in Fig. 12. Each separate set represents a sequential series of images recorded with the same experimental conditions, differing only in the lateral position of the reference pinhole. In principle, an entrance pinhole spatial filter *must* be used to ensure the coherent illumination of the zoneplate test optic. However, to increase the photon flux (reduce the exposure time) and investigate the effect of the spatial filtering, interferograms were occasionally recorded without a spatial filter. Series B and C were recorded using the 120-μm-diameter object pinhole spatial filter. For Series A, no spatial filter was used. Between Series B and C the reference pinhole was translated laterally by several microns to change the fringes from horizontal to vertical; otherwise all other experimental conditions were maintained. The parameters of each series are given in Table 1.

Wavelength. The wavelength was chosen based on the fixed position of the OSA with respect to the zoneplate lens. Outside of a narrow wavelength range, the edge of the first-order beam becomes clipped by that aperture.

Intensity. The input photon flux is measured using a detector placed a few centimeters beyond the object plane. The use of an object pinhole spatial filter guarantees the coherence of the illumination at the expense of flux. Using the pinhole filter, the flux is reduced in two ways: first, the spatial filter directly limits the amount of light passing through the object plane, and second, the increased diffraction angle generated by the use of smaller pinholes sends more of the remaining light out to large angles not collected by the zoneplate. By this simple argument, the usable flux depends on the diameter as d^{-4}. In one typical measurement, a 120-μm object pinhole reduced the photon flux to 15% of its unfiltered strength. Separately, when using the 120-μm pinhole, the measured flux collected by the zoneplate was 25.3% of the unfiltered strength; it was 2.2% of the unfiltered amount when using a 50-μm pinhole.

Orientation. Following Series A, the zoneplate was removed and reinstalled with a different azimuthal orientation. Based on the easily-recognizable and measurable positions of the imperfections in this particular zoneplate, the rotation angle is known to be 139.5°±0.5° (estimated uncertainty). This rotation is appropriately re-introduced into the wavefront data to facilitate comparison of the three sets.

Exposure Time. The exposure time was chosen to achieve more than 100 detected counts in the

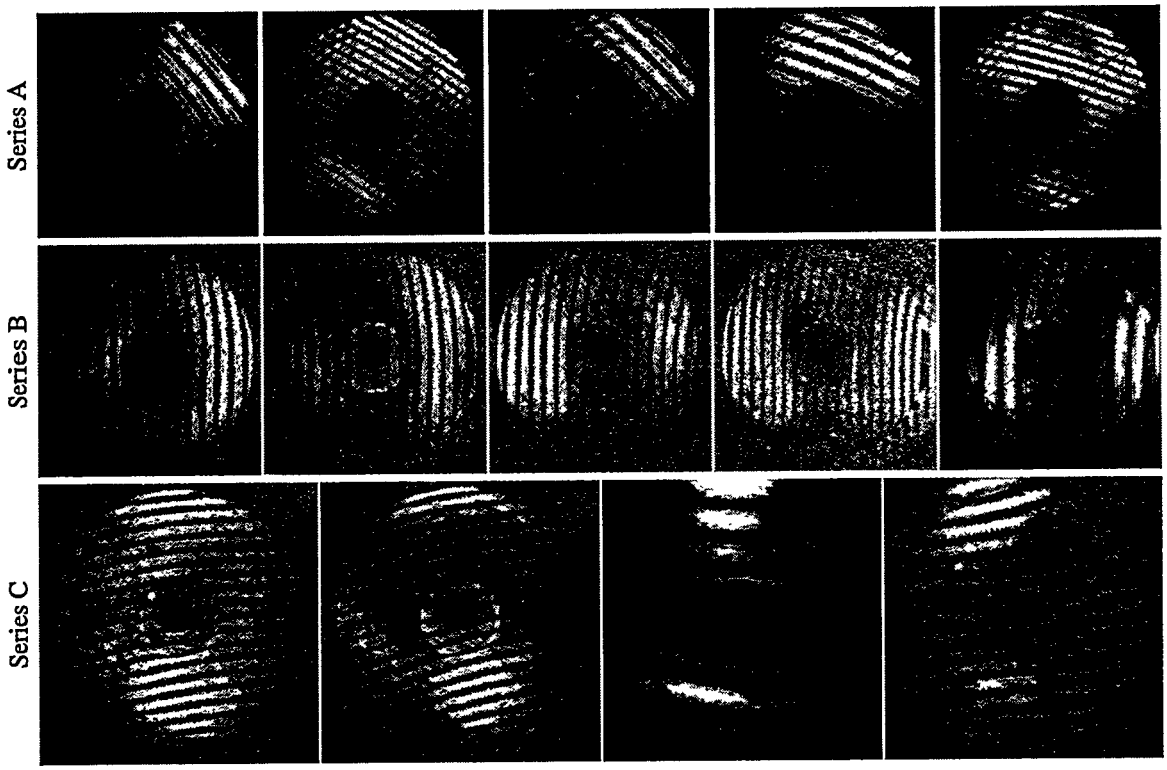

Figure 12. Three EUV interferogram data series from measurements of one annular Fresnel zoneplate lens. Series A was recorded first, when the pinhole membrane was relatively clean. Although in Series B and C the effects of pinhole membrane damage are clearly evident (non-uniform fringe contrast, fringe patterns in the dark regions of the zoneplate, etc.), the interferograms are analyzable and the wavefront may be studied.

peak-to-valley fringe modulation. This arbitrary level is a compromise between the measurement accuracy, the rate of membrane contamination, and the limited beam-time allocated for the experiments. Alignment was performed using continuously updating exposures, each of less than two seconds in duration. To record data for future analysis, exposure times between one and two minutes were typical.

3.6.1 *Raw Data*

To improve the fringe visibility during system alignment and pinhole positioning, the zoneplate data were recorded using background subtraction, as described previously. The test wave images used for subtraction were recorded with the reference pinhole placed far from the focus (20 μm away, laterally). These images are "subtracted" from subsequent images to enhance the fringe visibility during alignment and data collection.

By collecting several similar measurements in series, each analyzed individually, an attempt is made to quantify and reduce random measurement errors. Analysis methods are discussed in Part IV. In the analysis of each image, the wavefront is fit to a set of 37 Zernike annular polynomials, based on a central obscuration of 35% (chosen slightly larger than 30% to reduce the contribution of diffraction effects at the edge) (Melozzi and Pezzati 1992). The arbitrary piston and the position-dependent tilt and defocus terms are subtracted from the wavefront. Using the known measurement NA, a systematic coma

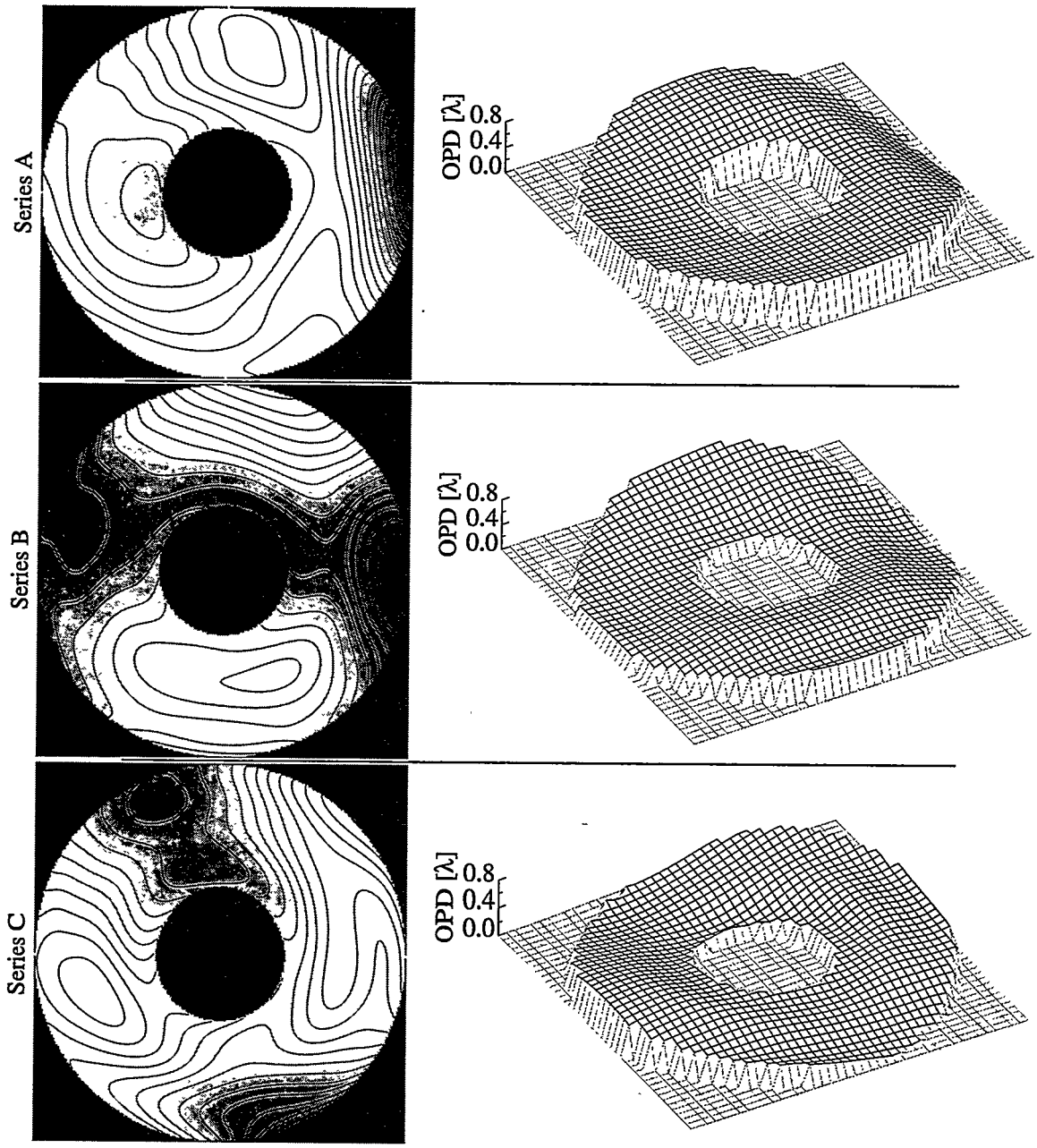

Figure 13. Contour and surface reconstructions of the averaged wavefronts from the three measurement series. Contours represent 0.05 waves, or λ/20. The azimuthal rotation angle of the Series A wavefront has been adjusted to match the angle of Series B and C.

Table 2. Global wavefront statistics for the three measurement series.

Series	RMS			P-V	
A	0.133 λ	1.72 nm	λ/7.5	0.731 λ	9.43 nm
B	0.134 λ	1.73 nm	λ/7.5	0.727 λ	9.38 nm
C	0.147 λ	1.90 nm	λ/6.8	0.753 λ	9.71 nm

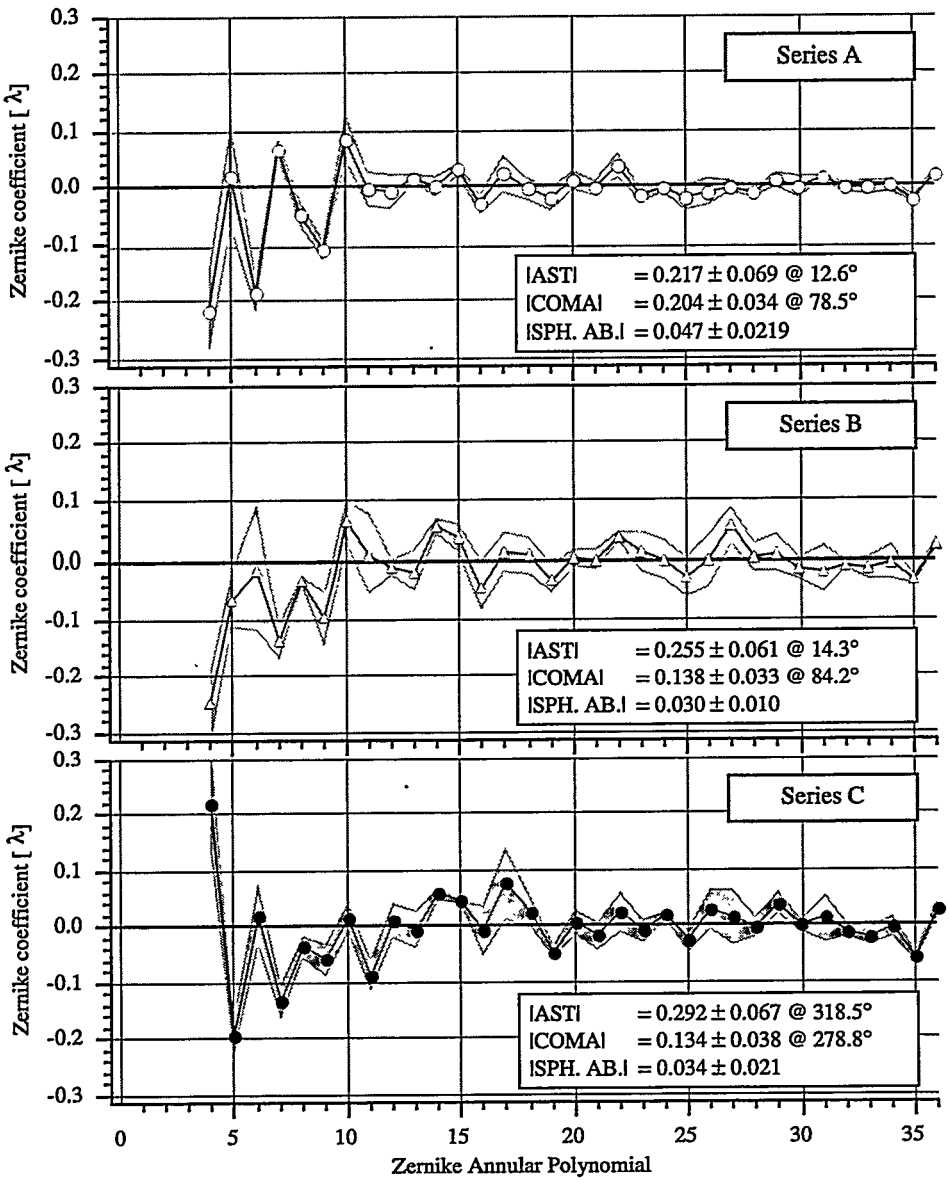

Figure 14. Zernike annular polynomial representations of the Series A, B, and C average wavefronts. The position-dependent piston, tilt, and defocus terms are not shown. The grey band behind the plot values indicates the measurement uncertainty based on the standard deviations of the data. With each plot the magnitudes and directions of the astigmatism, coma, and spherical aberration components are shown.

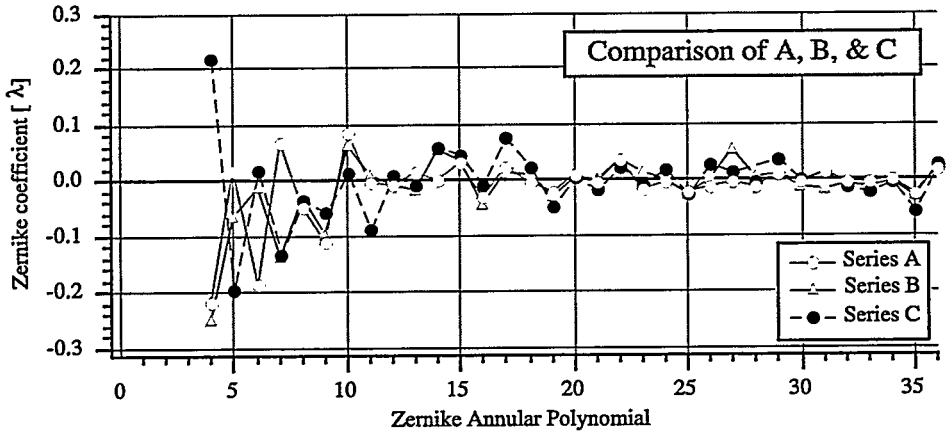

Figure 15. A comparison of the Zernike coefficients of the three measurement series. By inspection, the agreement between Series A and B is closer than between A or B and C, even though B and C were consecutive measurements.

error term is also subtracted from each set. This procedure is described in Section 5.5.2.

Contamination issues. The fringes visible in the central part of the interferograms are an indication of contamination in the PDI pinhole membrane, as described in Section 3.5.2.4. The interference of the reference wave with the light diffracted from the contamination produces these fringes, which are most easily identifiable in the regions where the test wave intensity is small. However, this interference must also span the entire NA, adding uncertainty to the measurements.

One way to estimate the amplitude of the wave diffracted from the contamination is to compare the fringe modulation in the two regions. Since the reference wave amplitude is the nearly the same in both regions, the difference in the fringe modulations reveals the relative amplitudes of the test wave and the "contamination" wave. (See Section 3.8 for a description of this method.) Based on this simple approach, the contribution of the contamination has an amplitude of approximately 1/10-th of the primary interference pattern. Hence, the contamination contributes not more than ±0.1 radians, or ±0.016 waves (0.21 nm, or ~$\lambda/63$), to the phase measurements.

3.6.2 *Wavefront Analysis*

For each of the three data sets, the average wavefront is computed and displayed in Fig. 13. Here the wavefronts are represented in two ways, both as surface phase maps and as contour plots. Another representation of the wavefront data is shown in Figs. 14 and 15 in terms of the set of 37 Zernike annular polynomials. (This plotting format is discussed in Appendix 7.) Since the polynomial fit coefficients are calculated separately for each interferogram, a measure of the uncertainty in each term is available in the standard deviation. Each term in the plot a_n is the average of the measured coefficients; the standard deviation σ_{a_n} is indicated by the grey region. The global statistics for the three average wavefronts are shown in Table 2. Although there are qualitative differences in the measurements, these global statistics are in excellent quantitative agreement.

3.7 CONCLUSION

Several conclusions can be drawn from the interferometric zoneplate wavefront measurements described here. Foremost is the conclusion that from this high quality zoneplate, the wavefront aberrations are smaller than or on the same order as the resolution of the measurements. *Within* each series the uncertainties are low relative to the comparison of the three. This means only that the wavefront measurements were reproducible in a very limited way — a change of the experimental geometry affected the outcome of the test. The primary explanations for this are the poor spatial filtering capabilities of the over-sized reference pinholes, and the difficulties caused by the contamination of or damage to the reference pinhole membrane.

These tests represent some of the first at-wavelength wavefront measurements performed on high-

resolution EUV optics, and are the first using a point diffraction interferometer. At the time they were conducted, they demonstrated the ability to measure sub-wavelength aberration magnitudes. Further progress on the development of the EUV PDI was arrested by the invention and implementation of the PS/PDI, which is in many ways a superior tool.

3.8 NOTE: THE CONTRIBUTION OF CONTAMINATION TO WAVEFRONT MEASUREMENTS

To determine the effect of the waves diffracted by the mask contamination, consider a simplistic model of the interferogram intensity pattern that is composed of three waves: the test wave T, the reference wave R (of comparable magnitude to T), and a small contribution from the light diffracted from the contamination c. The intensity pattern may be written as follows using three arbitrary phase functions:

$$I = |T + R + c|^2 = |T|^2 + |R|^2 + |c|^2 + 2|TR|\cos\phi_1 + 2|Tc|\cos\phi_2 + 2|Rc|\cos\phi_3 . \quad (2)$$

This simplifies to a stationary intensity A, plus the modulation terms from the three cross-products.

$$I = A + 2|TR|\cos\phi_1 + 2|Tc|\cos\phi_2 + 2|Rc|\cos\phi_3 . \quad (3)$$

Outside of the main illuminated area, where the test wave amplitude is small ($T \approx 0$) and the reference wave overlaps the contamination wave, the total peak-to-valley fringe height is

$$I_{small} \approx 4|Rc| . \quad (4)$$

In the *main region* of the interferogram, the pattern is dominated by the interference of the test and reference waves.

$$I_{large} \approx 4|TR| . \quad (5)$$

The ratio of the fringe heights in the two areas allows us to estimate the relative amplitude of the contamination wave.

$$\frac{I_{small}}{I_{large}} \approx \frac{4|Rc|}{4|TR|} = \left|\frac{c}{R}\right| . \quad (6)$$

Based on the addition of the two complex waves c and R, within this simple model the wavefront phase uncertainty, in radians, is given by this ratio.

III. THE PHASE-SHIFTING POINT DIFFRACTION INTERFEROMETER

4

The Phase-Shifting Point Diffraction Interferometer

4.1 INTRODUCTION AND MOTIVATION

Experience with the EUV PDI yielded an understanding of the serious limitations of the conventional point-diffraction interferometer for high-accuracy measurements, and led ultimately to the development of a novel point diffraction interferometer design capable of greatly improved throughput and possessing the capacity for phase-shifting interferometry — the *Phase-Shifting Point Diffraction Interferometer* (PS/PDI) (Medecki et al. 1996, Goldberg et al. 1997, Tejnil et al. 1997) This chapter describes the design and basic operational principles of the PS/PDI. The advantages of the PS/PDI are described relative to other common-path EUV interferometer designs.

High-accuracy wavefront measurement with the Conventional PDI (hereafter referred to as simply PDI) is hindered by several factors. In the PDI design (Fig. 1(a)), the reference wavefront is generated by diffraction from a sub-resolution *reference pinhole* in a partially-transmitting membrane. The test beam is formed from the light that is transmitted through the membrane, containing the aberrations of the optic under test. Since the reference beam is sampled from the test beam, there is no available means to introduce a controllable relative phase-shift between the two; therefore static fringe pattern analysis methods must be used. The reliability of such analyses is limited in the presence of mid- and high-spatial frequency variations of the test beam intensity. Furthermore, significant lateral displacements of the reference pinhole from focus, typically 10-25 times λ/NA (1-2 μm in EUV interferometry), are required to generate enough fringes for static fringe pattern analysis. Such displacement greatly decreases the amount of pinhole-diffracted light available for the reference wavefront. Consequently, to match the intensities of the two waves, and to provide good fringe contrast, the membrane must *significantly* attenuate the test wavefront; this reduces the overall throughput, or efficiency, of the interferometer. Such necessary beam attenuation may make alignment and measurement difficult by pushing the required single-image exposure time into the range of several minutes.

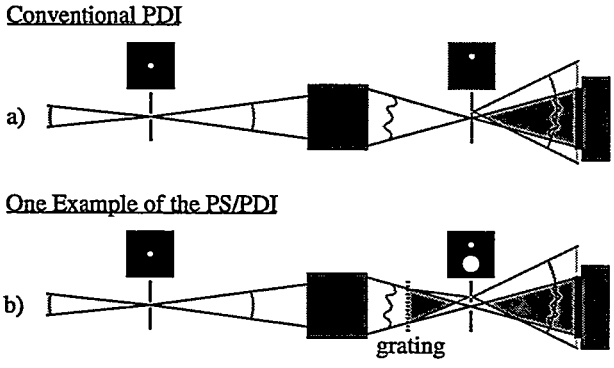

Figure 1. Schematic representations of (a) the Conventional Point Diffraction Interferometer (PDI), and (b) the closely related Phase-Shifting Point Diffraction Interferometer (PS/PDI). Both systems require coherent illumination of the optic under test. The PDI uses a partially-transmitting membrane and a sub-resolution pinhole to sample the aberrated test beam and produce a reference wavefront. The PS/PDI utilizes a low-angle beamsplitter to divide the test beam into multiple separate beams in the image plane. One beam passes through a large open window in an opaque image-plane membrane. A second beam is focused onto a sub-resolution pinhole and produces a reference wavefront.

4.2 PS/PDI DESCRIPTION

In the PS/PDI designs, of which one example is shown in Fig. 1(b), a small-angle beamsplitter (such as a coarse grating) is employed to separate the test and reference beams, forming multiple foci in the image-plane. Using a two-pinhole spatial filter in the image-plane, two beams are selected: one beam passes through a large *window* in an opaque membrane, while another beam is diffracted by a sub-resolution *reference pinhole* placed at the center of the focal spot.

This design overcomes several of the limitations of the conventional PDI. Translating the grating beamsplitter perpendicular to the grating ruling introduces a controllable relative phase-shift between the test and reference wavefronts, facilitating *phase-shifting interferometry* (PSI), a powerful category of data analysis techniques. Additionally, the centered reference pinhole and the large open window lead to an overall throughput increase of at least two orders of magnitude compared to the conventional PDI.

There are many ways in which the PS/PDI may be used, and several available variations on the basic design. Besides the ever-present concern about the size of the reference pinhole, the grating beamsplitter may be placed in several available locations. The position and pitch of the grating determine the separation of the test and reference beams in the image-plane. The appropriate separation depends on the quality of the optical system under test and on the desired mid-spatial frequency resolution of the interferometer. There are also advantages and disadvantages related to the selection of which of the diffracted orders becomes the test and reference beams. These issues and others are addressed in the following sections.

4.3 CONFIGURATIONS OF THE PS/PDI

One central advantage of the PS/PDI over the PDI is that the reference pinhole is centered on the brightest part of the focused illumination, greatly enhancing the amount of transmitted light in the reference beam. In any configuration of the PS/PDI, one primary motivation is to deliver the highest available flux to the reference pinhole. Since the pinhole acts as a spatial filter, removing any aberration in the reference beam, the primary quality of concern for the reference beam is simply its focused intensity. In principle, the beamsplitter may be placed in any available position ahead of the image-plane.

Figure 2(a) shows the conventional PDI alongside several configurations of the PS/PDI with a grating beamsplitter and one using a glancing-incidence mirror. Figures 2(b) and (c) show two similar configurations with the grating placed either before or after the test optic. When the wavefront division occurs ahead of the test optic, the multiple beams will travel along different paths through the system; in extreme cases, consideration must be given to the fact that apertures in the system may block all or part of the beams.

In any of the PS/PDI configurations, a choice must be made as to which beam is the test beam and which beam is filtered to become the reference beam. These are called the *first-order reference* and the *zeroth-order reference* configurations, denoting which beam becomes the reference. Since the beam separa-

tion is typically small in the image-plane, switching between the two configurations is usually a trivial matter. However, intensity and beam quality issues, discussed here and in Section 5.10, often motivate the use of one configuration over the other.

Figure 2(d) shows the *upstream grating configuration* applicable in circumstances where the illuminating beam is of high quality. In this design, two similar two-pinhole spatial filters are used: one in the object plane, and a second in the image-plane. A grating placed ahead of the object pinholes separates the converging test and reference beams. A small object pinhole filters the test beam, guaranteeing a spatially coherent, spherical illumination wavefront. The reference beam, however, passes through a large window in the object plane and is filtered by the reference pinhole in the image plane. In bypassing the spatial filter pinhole in the object plane, the reference beam reaches the image plane with much greater intensity than in the other PS/PDI configurations. Although advantageous in this regard, the upstream grating configuration requires that the illuminating beam incident on the object plane be of sufficiently high quality (i.e. nearly diffraction-limited) to be well separable. This requirement precludes its implementation in EUV applications where the illuminating optics typically are not of near-diffraction-limited quality.

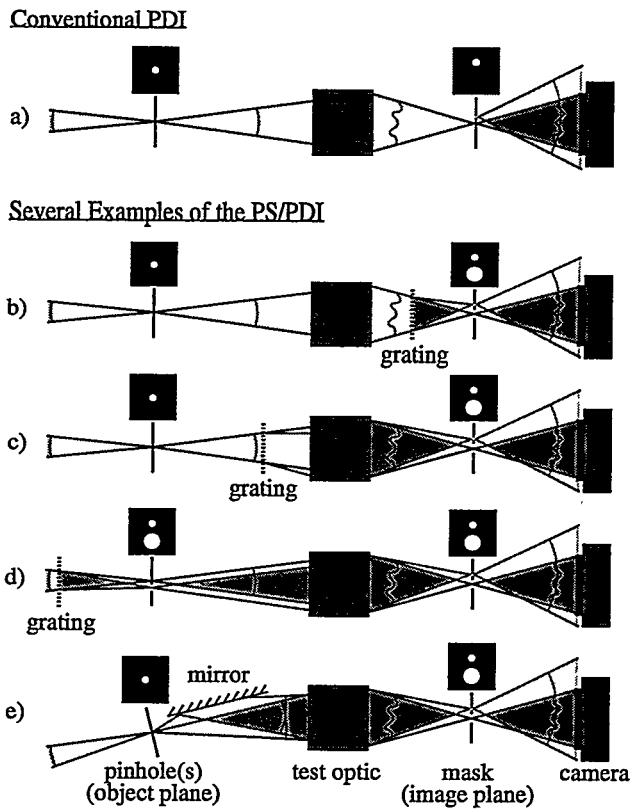

Figure 2. The PDI (a) is compared to four configurations of the PS/PDI (b-e). (b) and (c) are different only in the placement of the grating beamsplitter. In configuration (d) the beam is split upstream of the object pinhole, and similar window-plus-pinhole masks are placed in both the object- and image-planes. Configuration (e) shows a different mechanism of beam-splitting, using a Lloyd mirror.

Depending on the operational beam wavelength, there may be several available ways of achieving the required wavefront division. The grating systems are convenient because a relative phase-shift between any two diffracted orders is induced by a simple lateral translation of one component, and is therefore straightforward to implement and control. Another system, shown in Fig. 2(e), is reminiscent of Lloyd's mirror (Born and Wolf 1980:262-263), where a glancing-incidence mirror is used to *fold* the illuminating beam onto itself over the entrance pupil. Here, the NA of the illuminating wavefront must be of more than double the object-side NA of the system. The implementation of phase-shifting in this configuration is problematic, if it is possible.

4.4 COMPETING INTERFEROMETER DESIGNS

In addition to the two point-diffraction interferometer designs used in this research, two other common-path interferometer designs have been implemented for EUV optics testing: the *Knife-Edge* or *Foucault Test* (Foucault 1858, 1859), and the grating-based *Lateral Shearing Interferometer* (LSI), or *Ronchi Interferometer* (Ronchi 1923, 1964), shown in Fig. 3.

The simple-to-perform Knife-Edge test involves placing a high-quality opaque edge at the focus of the optical system under test. By blocking some of the aberrated rays, the resultant far-field intensity pattern reveals the slope of the wavefront. This test was successfully employed in the alignment of an EUV Schwarzschild objective (Ray-Chaudhuri 1994). For high-accuracy applications, the advantages of the Foucault test in simplicity, sensitivity, and high-efficiency are outweighed by the difficulty in performing accurate analysis of the data.

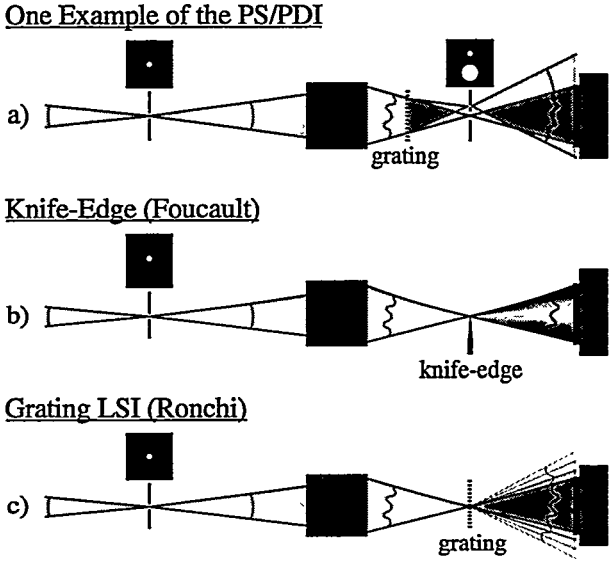

Figure 3. Schematic drawings of the PS/PDI and two common-path interferometers that have been used in EUV interferometry.

The grating-based LSI is another test convenient because of its relative simplicity. This interferometer design has also been used to test 10× Schwarzschild objectives identical in design to those under investigation with the PS/PDI (Ray-Chaudhuri 1997, Wood et al. 1997). A coarse grating is placed near the focus of the optic under test. The grating divides the beam into multiple, overlapping orders which are *sheared* angularly in the direction perpendicular to the grating rulings. In a typical *shearing interferometer*, the interference of *two* slightly-displaced overlapping beams reveals the wavefront slope along the direction of the shear. Here, analysis is complicated by the presence of multiple overlapping beams. The shear angle is determined by the grating pitch; the important parameter is the ratio of the shear angle to the NA. The amount of shear dictates the slope of the measured wavefront, and therefore largely determines the sensitivity of the technique. Using grating translation to induce phase-shifting into the measurements, wavefront slope data is gathered along two shear directions, and the two separate measurements must be reconciled to reconstruct the wavefront. Although the success of this technique has been demonstrated, its applicability to high accuracy wavefront measurement is still under investigation.

Both of these interferometer designs have advantages over the PS/PDI: higher efficiency, because a second spatial-filter pinhole is not used, and ease of alignment, because the placement of a tiny pinhole onto the beam focus is unnecessary. There are fewer critical components and stages, and those compo-

nents are easier to obtain. Acknowledging these advantages, however, the PS/PDI design has many positive attributes not possessed by the other two. In generating a single reference wavefront by pinhole diffraction, extremely high accuracies may be achieved. The interference data that is collected enables measurement of the wavefront itself, not the wavefront slope, so analysis is more straightforward and uncertainties are greatly reduced. Because of the high-brightness synchrotron source in use for the EUV PS/PDI experiments, the relatively lower efficiency of the PS/PDI has not presented any significant experimental disadvantage.

4.5 INTENSITY AND EFFICIENCY CONSIDERATIONS

The relative efficiencies of the PDI and PS/PDI configurations vary widely. This issue may be of foremost concern in circumstances where the available intensity of coherent illumination is limited. The efficiency dictates how much time is required to conduct interferometric measurements. Here, to illustrate this variation, a few simplified assumptions about the loss mechanisms are applied to a side-by-side comparison of the different point diffraction interferometer configurations. The relative efficiencies of the PS/PDI, the Knife-Edge Test, and the LSI are also compared.

The EUV PS/PDI, configured for the testing of a 10× Schwarzschild objective as described in this thesis, will serve as a model for this exercise. Experimental characteristics of the synchrotron beamline source and several of the interferometer's components are applied here. The inherent efficiency of the test optic will affect each of these common-path interferometers in the same way and is therefore neglected in this discussion.

The object pinhole is illuminated by a beam of marginal quality, forming a focal spot of approximately 50-μm^2 area (at 0.008 NA). A 0.5-μm-diameter object pinhole transmits approximately 1/200th of the incident illumination. Assume in this discussion that for high-quality optics, the image-plane reference pinholes transmit 1/10th of the incident illumination; also assume that the large *window* pinholes of the PS/PDI have 100% transmission. When aberrated optical systems are tested, the size of the focal spot increases and transmission through the reference pinhole is reduced. This does not affect the efficiencies of the Knife-Edge or LSI test, but it *significantly* affects the assumptions made here about transmission through the reference pinhole.

Assume for simplicity that the transmission gratings are binary: alternating opaque and transparent stripes of 1:1 line-to-space ratio. Phase-gratings and gratings with a line-to-space ratio other than 1:1 could be used to improve throughput or to match the relative intensities of the test and reference beams; but in this example, only the simple grating will be considered. For such an ideal grating, the intensity transmitted into the zeroth-order beam is 1/4, and the intensity in one of the the first-order beams is $1/\pi^2$.

(A good rule of thumb for such gratings is that the ratio of the intensities of the first order to the zeroth order is $4/\pi^2 \approx 40\%$.) The gratings used in EUV interferometry are typically supported by a 1000-Å silicon-nitride membrane, with a transmission of 1/4. Thus the total intensity transmitted into the zeroth- and first-orders is 1/16, and $1/4\pi^2 \approx 1/40$ respectively.

Regarding the conventional PDI, assume for example that 20 fringes are desired, necessitating a lateral displacement of the reference pinhole by approximately 10 λ/NA. If the area of this displaced pinhole is one-quarter of the central Airy disk area (a desirable size), then the amount of light transmitted through this pinhole in a high-quality optical system can be on the order of 10^{-5} to 10^{-6}. To balance the

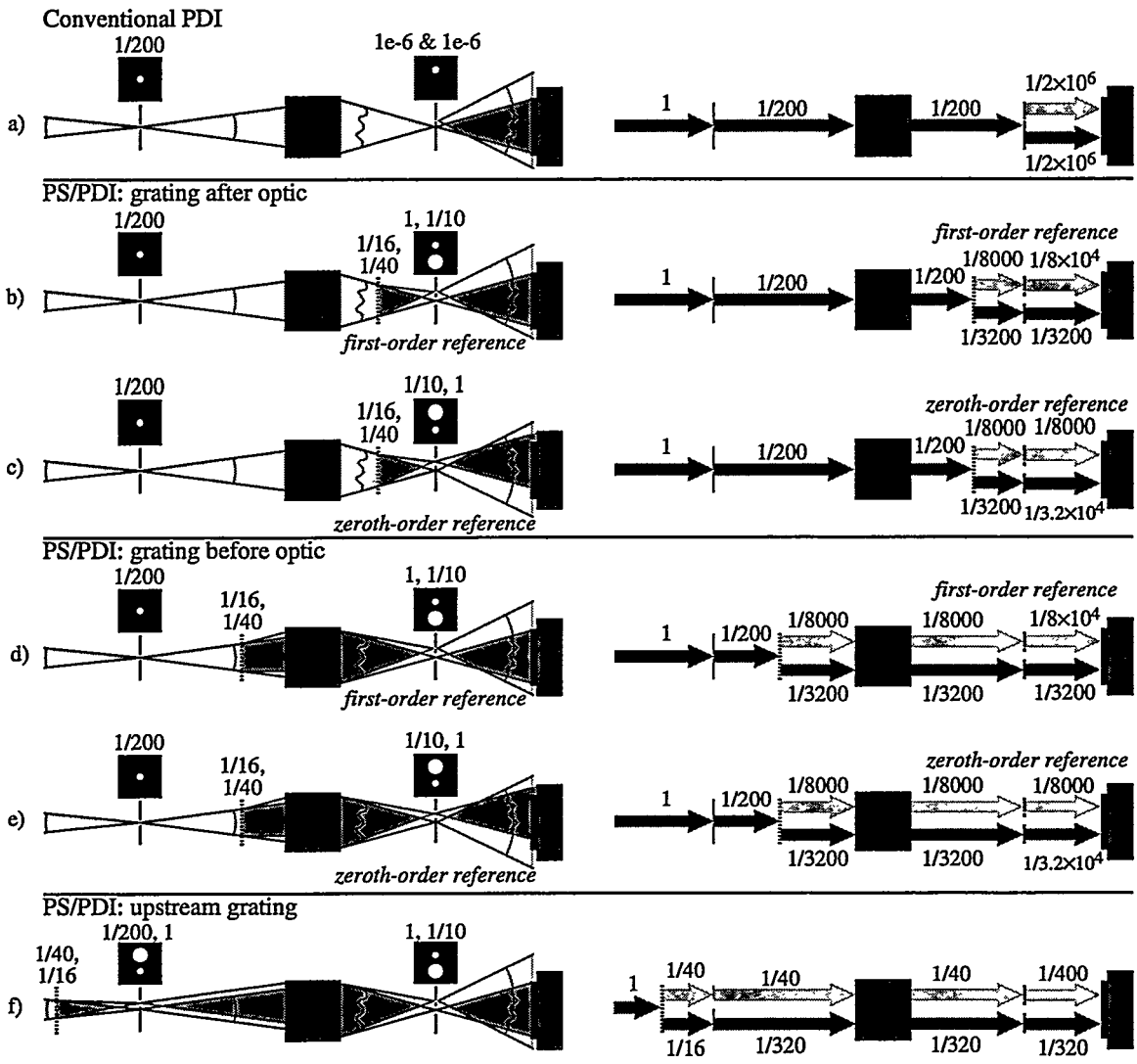

Figure 4. An efficiency comparison of the different point diffraction interferometer designs. On the left, the approximate efficiency of each element is shown. The efficiency of the optic itself, the same in all configurations, is omitted. On the right are shown the approximate integrated intensities of the test and reference beams as they propagate through the interferometers. The first-order reference and the zeroth-order reference configurations are also compared: in (b) and (c), and in (d) and (e). This side-by-side comparison reveals the efficiency advantages of some configurations over others. Numbers are given in Table 1.

two illuminating beams, the transmission of the semi-transparent membrane must be of this same order of magnitude. In practice, it is possible that an optic with large mid-spatial-frequency errors may scatter more radiation away from the center and into the vicinity of the displaced pinhole. Furthermore, if the reference pinhole is larger than it should be, the flux transmitted into the reference beam may be closer to 10^{-4} than to 10^{-6}.

Figure 4 compares of the efficiency of each PS/PDI design. On the left are schematic representations of interferometers. Above each of the essential components, the approximate efficiencies (photons *out* versus photons *in*) used in the calculations are shown. On the right are representations of the integrated test and reference beam intensities in each segment of the interferometers. There are several important values to consider. These require the following definition: the test and reference beams combine to form a *stationary intensity* and a *modulated intensity* that can be represented as

$$I = I_{stationary} + I_{modulated} \cos \Phi, \tag{1}$$

with Φ as the arbitrary optical path difference in radians. This and the definition of fringe contrast are

Table 1. Comparison of the relative intensities in six point diffraction interferometer configurations. The stationary intensity is the average intensity in the interference pattern, while the modulated intensity describes the half-height of the fringes. Contrast is the ratio of these two intensities. The efficiency comparison is based on the ratios of the modulated intensities among the different configurations shown. Intensity magnitudes are given relative to the illuminating beam upstream of the object pinhole, neglecting the efficiency of the test optic.

	Schematic	$I_{stationary}$ [$\times 10^{-6}$]	$I_{modulated}$ [$\times 10^{-6}$]	fringe contrast	relative efficiency
	Conventional PDI				
a)	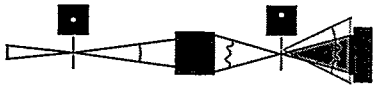	1	1	100%	8×10^{-3}
	PS/PDI: grating after optic				
b)	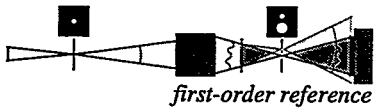 *first-order reference*	325	125	38%	1
c)	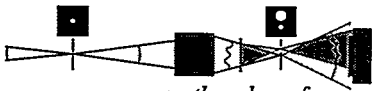 *zeroth-order reference*	156	125	80%	1
	PS/PDI: grating before optic				
d)	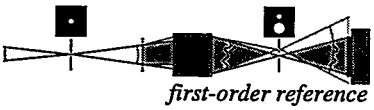 *first-order reference*	325	125	38%	1
e)	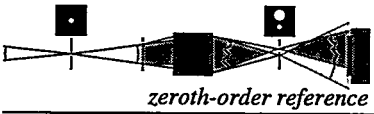 *zeroth-order reference*	156	125	80%	1
	PS/PDI: upstream grating				
f)		5625	5590	99%	45

given in Appendix 5. (Note: because the two interfering beams travel with the same divergence angles and fully overlap, the terms *intensity* and *flux* are used interchangeably in this discussion.) The stationary intensity represents the average amount of light recorded in the interference pattern, while the modulated intensity describes the intensity *height* of the interference fringes. 100% contrast is achieved when the two intensities have equal magnitude.

One significant advantage of the PS/PDI revealed in Table 1 is that the PS/PDI has over 100 times greater efficiency than the PDI. Comparison of the first-order and zeroth-order reference configurations produces two interesting results. First, the efficiency of the first-order reference configuration is twice as high because the brighter zeroth-order beam is unattenuated in the image-plane. Second, the modulated intensity is *the same* in the two configurations. This result is due to the fact that the modulated intensity comes from the cross-product of the two intensities, and is proportional to the geometric mean. No matter which of the two beams is attenuated by the spatial filtering, the geometric mean is the same. Having the same modulated intensity in the two configurations, the one with lower stationary intensity will produce higher fringe contrast — indeed, the contrast is twice as high in the zeroth-order reference configuration.

Another result of this comparison is the observation that the upstream grating configuration is 45 times more efficient than the configuration of the PS/PDI used for experiments. Because no object-plane spatial filtering is performed on the reference beam, to avoid beam overlap this configuration needs a very high-quality

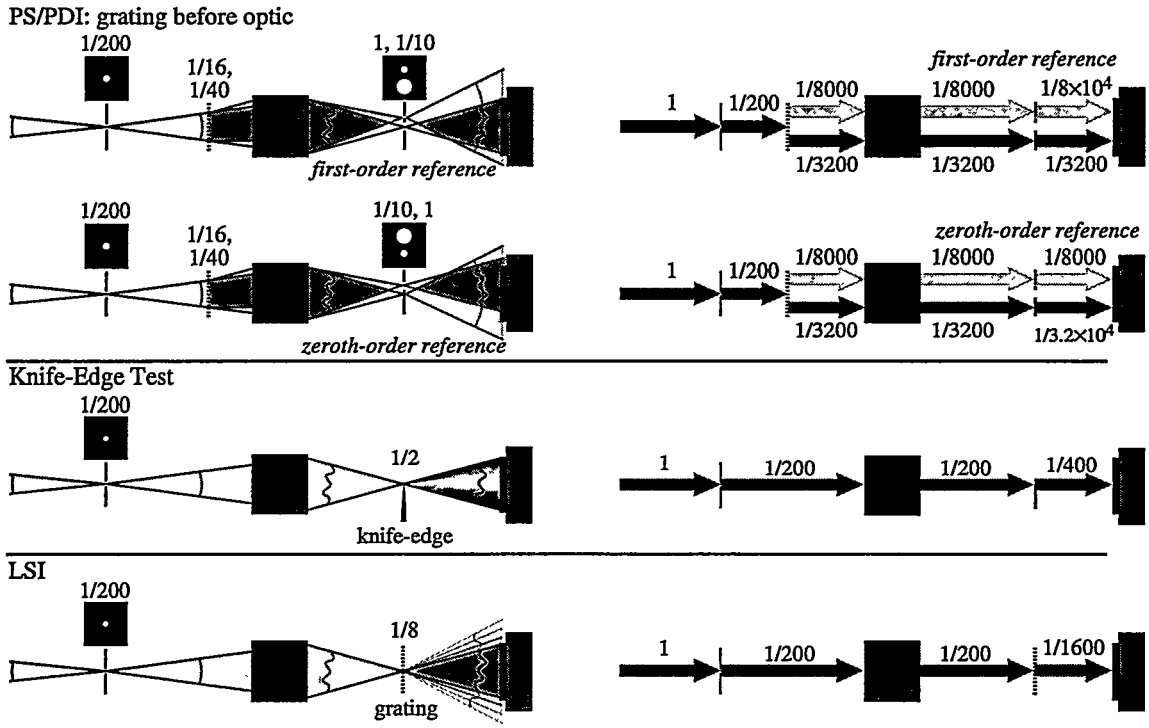

Figure 5. A comparison of the efficiencies of the PS/PDI and two non-point-diffraction interferometer designs. (a) through (c) show the approximate efficiency of each element, neglecting the optic itself. Schematics (d) through (f) separately model the approximate integrated intensities of the test and reference beams as they propagate.

Table 2. Comparison of the relative intensities of three interferometer designs. The intensity magnitudes are given relative to the unfiltered illuminating beam, neglecting the efficiency of the test optic.

	Schematic	$I_{stationary}$ [$\times 10^{-6}$]	$I_{modulated}$ [$\times 10^{-6}$]	fringe contrast	relative efficiency
	PS/PDI				
a)	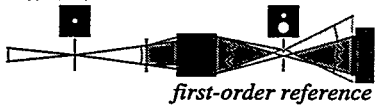 *first-order reference*	325	125	38%	1
b)	 *zeroth-order reference*	156	125	80%	1
	Knife-edge				
c)	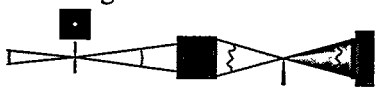	5000	5000	100%	40
	LSI				
d)	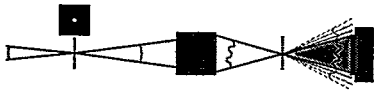	1250	1250	100%	10

illuminating beam. If the reference beam were not of high quality, then the attenuation of the image-plane pinhole would be much greater and this configuration will have comparable efficiency to the others.

4.4.1 *Comparison with Other Interferometer Designs*

In Fig. 5 and Table 2, an efficiency comparison is made between the PS/PDI, the Knife-Edge test, and the grating-based LSI. For a given application, it would appear that there is a necessary trade-off between efficiency and accuracy. When implemented experimentally, the efficiency advantages of the LSI design may be outweighed by the longer time required for analysis and larger uncertainties in the measurements. The time saved by the predicted factor-of-ten reduction in the single-image LSI exposure time may be undone by the increased analysis time and the need to record more exposures than in the PS/PDI scheme.

4.6 CHOOSING THE OPTIMAL PINHOLE SIZE

Selecting the optimal pinhole diameter for a given application of the PS/PDI requires the balancing of several opposing concerns. The desire for a high degree of spatial filtering and a reference wave of uniform intensity motivates the use of the smallest available pinhole. However, the intensity of the reference wave is critical to achieving fringes of good contrast, a vital aspect of measurement precision. Based on a simple scalar diffraction model, this section outlines two methods for determining the optimal pinhole size for a given application, as applied to the study of EUV systems with 0.08 or 0.1 NA. Until such time as the results from a more detailed analysis of EUV pinhole diffraction (such as that presented in Chapter 2) are readily available, these two methods provide approximate results and illustrate important physical effects that require future study.

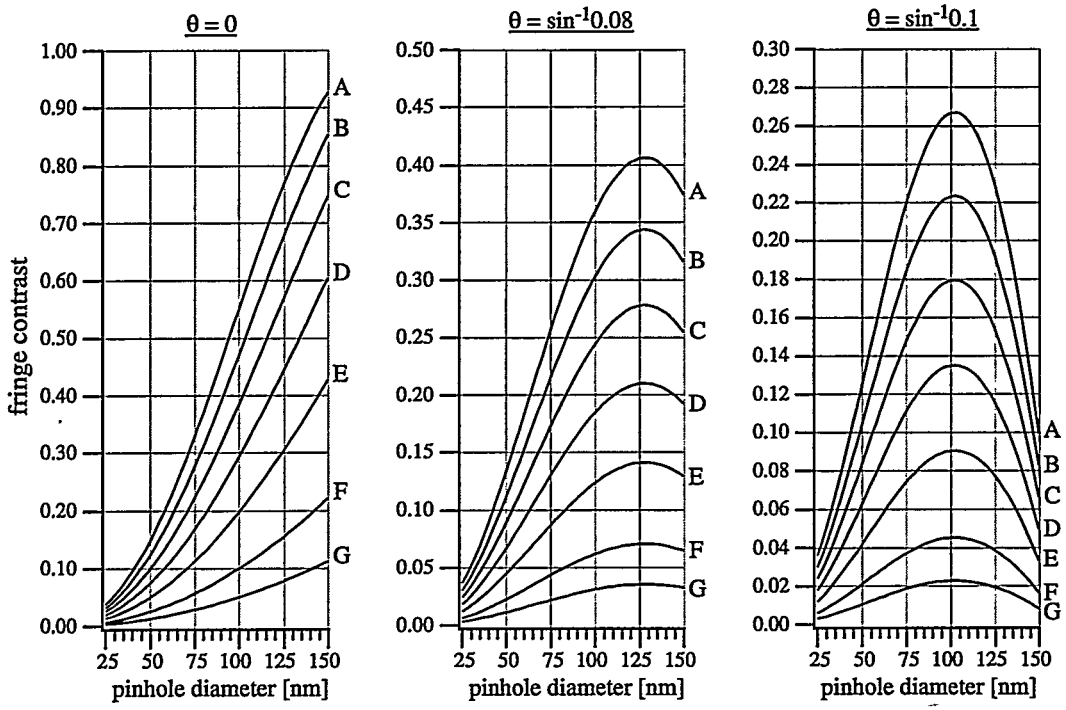

Figure 6. A simple model of the dependence of the fringe contrast on the pinhole diameter, based on "Airy pattern" diffraction from a circular reference pinhole at 13.4 nm wavelength. Given the relative strengths of the test and reference beams and the transmitting properties of the reference pinhole, the contrast dependence on pinhole diameter will follow one of the labeled contours from the graphs. For example, if a measured 100-nm reference pinhole produces 20% fringe contrast at the center of the interferogram, following contour "E" the fringe contrast will be 12% at the edge of the 0.08 NA and 9% at the edge of 0.1 NA. If a 50-nm pinhole were placed in this same system, then the expected fringe contrast would drop to 5.0% at the center, 4.4% at 0.08 NA and 4.2% at 0.1 NA.

4.6.1 *Reference Wave Uniformity*

When the pinholes are smaller than the central lobe of the focal pattern of an optical system under test, the amplitude of the field transmitted through a pinhole should be roughly proportional to the pinhole area. Although this simple model neglects the complicated attenuating effects of high-aspect-ratio, highly absorptive pinholes on the order of a few wavelengths in diameter, it will serve as a good starting point for these calculations. To keep the model simple and useful, assume circular pinholes in opaque membranes, and scalar diffraction of ideal, Airy-like reference waves. With d as the pinhole diameter, the diffracted field amplitude E is

$$E(d,\theta) = Ad^2\left[2\frac{J_1\left(\frac{1}{2}kd\sin^{-1}\theta\right)}{\left(\frac{1}{2}kd\sin^{-1}\theta\right)}\right]. \tag{3}$$

A is a constant multiplier dependent on the characteristics of the pinhole and on the relative strengths of the test and reference beams. If we define the amplitude of the test wave in the plane of the detector as 1, then A is on the order of $1/d^2$. Yet A is an experimental parameter and cannot be known ahead of time.

Using this simplified model, the intensity I of the interfering test and reference beams is

$$I = \left| e^{i\phi} + E \right|^2 = 1 + |E|^2 + 2|E|\cos\phi\,, \tag{4}$$

where ϕ represents the phase of the test wavefront plus a significant PS/PDI spatial carrier frequency. The spatial carrier frequency typically introduces a large number of fringes, and the resultant field varies from its maximum to its minimum value over a short distance. The fringe contrast C is defined (Appendix 5) as

$$C = \frac{2|E|}{1 + |E|^2}. \tag{5}$$

When the intensities of the test and reference beams are matched, the contrast is one.

One goal in selecting a pinhole is to have high contrast across the entire NA of measurement. For several values of the parameter A, Fig. 6 shows the fringe contrast at the center of the interferogram and at the maximum polar angles within numerical apertures of 0.08 and 0.1. The contrast is calculated from Eqns. (3) and (5). The non-uniformity in the diffracted reference wave causes a greater contrast variation from the large pinholes than from the small pinholes. The corresponding labeled contours in the three graphs represent the same values of the parameter A.

4.6.2 A Simple Approach to Pinhole Spatial Filtering Considerations

Determining the optimal reference pinhole size for a given PDI or PS/PDI application is a daunting task theoretically, and a laborious task experimentally. Abandoning the level of detail used in the TEMPEST simulations of Chapter 2, a simple approach to this problem proves useful for assessing the level of spatial filtering produced by different pinhole sizes in the presence of aberrated test beams. Based only on Kirchoff diffraction from an idealized opaque planar screen, this study gives insight into the troublesome problems associated with filtering astigmatic aberrations.

In order to study the isolated effects of individual low-ordered aberrations, an initial 0.08 NA (reference) wavefront is given varying aberration magnitudes composed of a single low-ordered aberration component at a time. For this mathematical study (similar to studies by SangHun Lee), ideal circular pinholes of varying diameter are placed precisely at the center of the focal pattern produced by an optical system operating at 13.4 nm wavelength. In approximation to the Kirchoff boundary conditions, the simple discrete Fourier-transform (DFT) is used to mathematically propagate the scalar electric field (Sections 2.3 and 11.3.1). On propagation to the detector at far-field, the pinhole field produces the reference wavefront. A wavefront-phase analysis of the reference wave is performed within 0.08 NA, and the contributions of defocus, astigmatism, coma, and spherical aberration are identified. As the pinhole size is varied, the diffracted reference wavefront is studied within 0.08 NA. Displacement of the pinhole from the position of best-focus is not considered here.

This study is limited to the case where the pinhole is centered in the focal pattern. Experimentally,

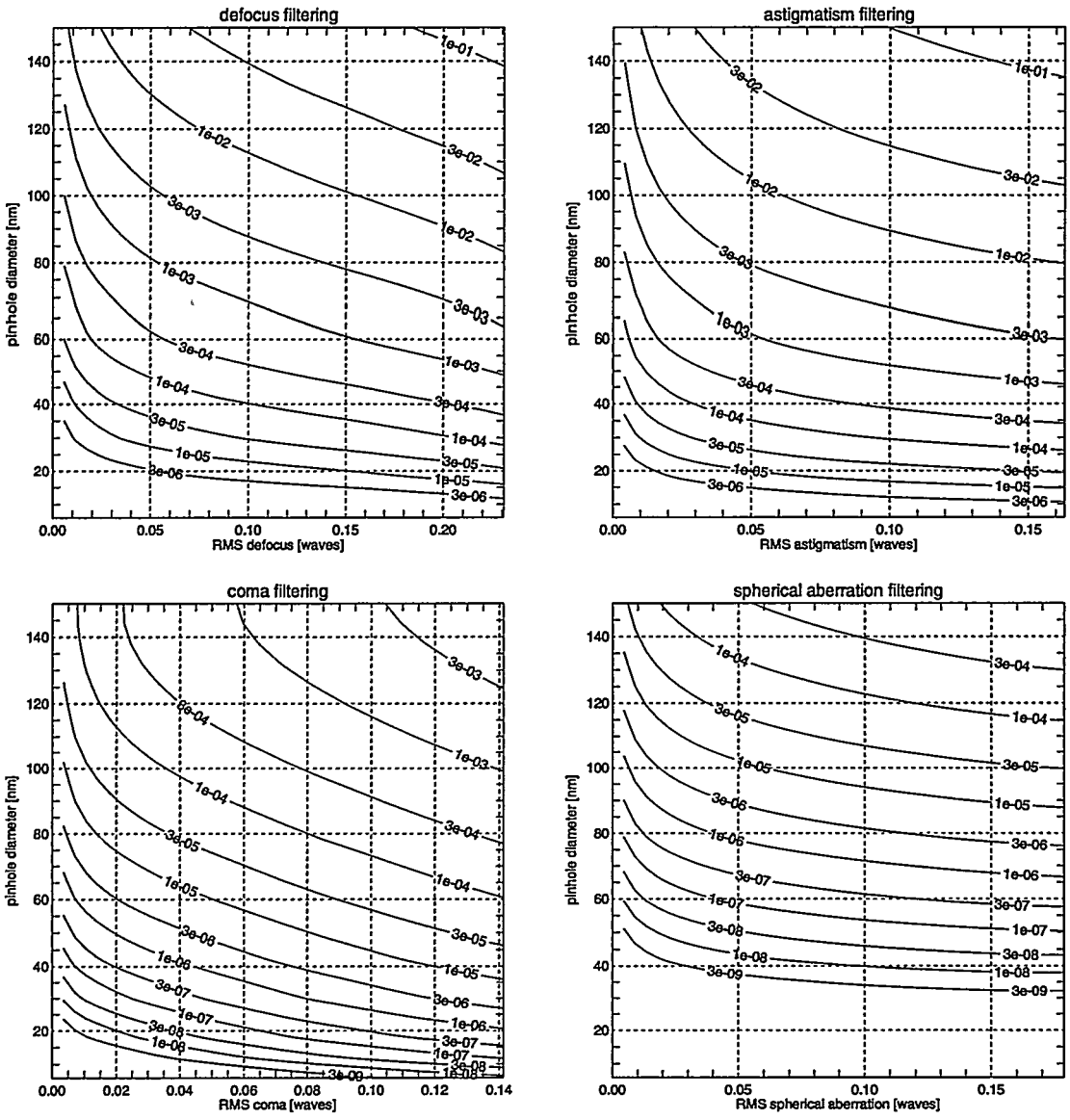

Figure 7. A simple study of pinhole spatial filtering designed to assess the degree of filtering produced by different circular pinholes sizes in the presence of varying degrees of primary wavefront aberrations. Calculations are performed for a 0.08 NA optical system operating at 13.4 nm wavelength. Defocus, astigmatism, coma, and spherical aberration are investigated. The abscissa in each plot is given in RMS wavefront displacement of the single aberration component being investigated. The RMS wavefront displacement of the diffracted wave is given.

in the PS/PDI, every effort is made to center the pinhole in order to maximize the intensity transmitted into the reference wave. This situation is very different from the PDI, in which the pinhole is significantly displaced from the center of the pattern in order to produce an analyzable interference pattern.

Figure 7 contains the results of this study. Here, as the RMS aberration magnitudes are *increased,* the pinhole diameters required to produce a reference wavefront with an arbitrarily small RMS displacement (such as $\lambda/100$) *decrease.* Of the four primary aberrations studied, astigmatism is by far the most troublesome, as it is the most difficult aberration to spatially filter. This property is born-out by the experimen-

tal observations that astigmatism creates the greatest uncertainty in the measurements (Chapters 3, 7, and 8). According to this simple model, in the presence of 0.1 waves RMS of astigmatism, the pinhole size required to filter the aberrations down to 0.03 waves ($\lambda/33$) is 114 nm, to filter down to 0.01 waves ($\lambda/100$) is 89 nm; and to filter down to 0.003 waves ($\lambda/333$) is 67 nm.

This simple study leads to two important conclusions. First, the optimal pinhole size to achieve a desired reference wavefront quality depends strongly on the aberrations present in the system. Second, astigmatism is *the* most difficult aberration to filter. The measured astigmatism in sub-aperture A of the Schwarzschild objective examined in this thesis is 0.42 waves P-V or 0.0856 waves RMS (see Chapter 7). According to the simple calculation shown in Fig. 7, a sub-90-nm pinhole is required to filter this astigmatism magnitude to below 0.01 waves RMS in the reference beam. By comparison, coma and spherical aberration magnitudes much larger than this are easily filtered by considerably larger pinholes.

Because of its critical importance, more research in the area of EUV pinhole diffraction and spatial filtering is certainly required. Both detailed and simple calculations should support the experimental research so that a greater understanding of the pinhole size requirements of high-accuracy applications will be known. With the recent availability of pinholes from well-controlled pinhole fabrication processes at this small scale (fabricated by Erik Anderson) and the continued measurement of optical systems of various wavefront quality, important empirical data will be gathered.

5

Systematic Errors and Measurement Issues

5.1 OVERVIEW

In the pursuit of the highest achievable accuracy, it is important to consider all elements of the system, including the system geometry, as potential sources of systematic errors. This chapter is devoted to mathematical investigations of each of the PS/PDI components with the goal of identifying the most significant sources of systematic error. A very general approach is adopted so that this discussion may be applied to the design of interferometers for the measurement of arbitrary optical systems. Where appropriate, the results of these sections are applied to the specific configurations used in EUV interferometry of lithographic optics. These EUV calculations are highlighted at the end of each section and summarized at the end of this chapter. Random error sources and issues relating to inadequate pinhole spatial filtering are *not* covered in this chapter.

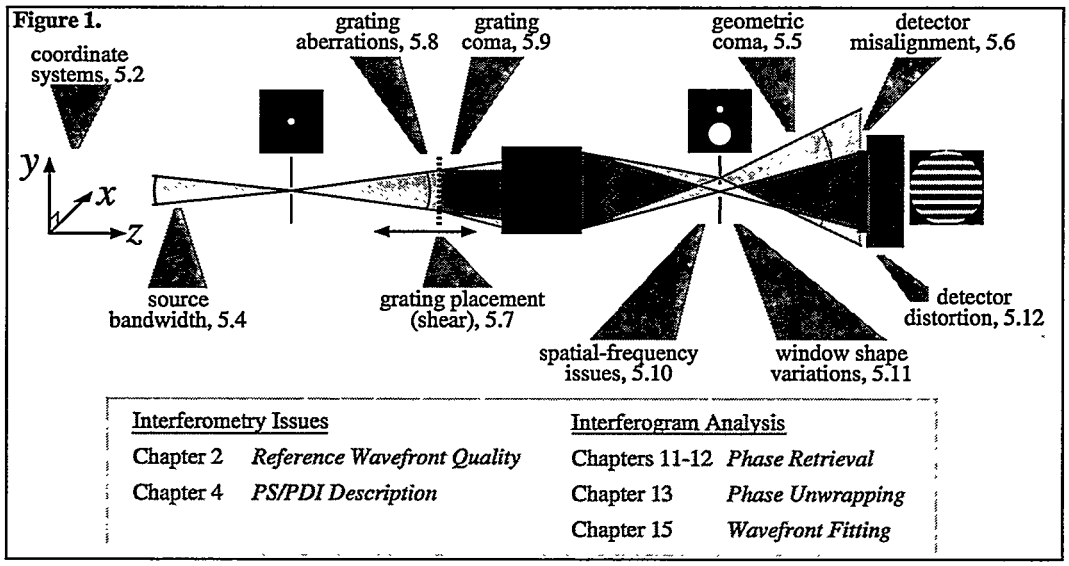

5.1.1 *Outline*

In low-NA configurations, a few definitions and formulae lead to simple mathematical descriptions of the various components. The predicted performance of an interferometer configuration can be judged based on the magnitude of the effects identified in this chapter. Figure 1 enumerates the most significant effects and indexes the sections of this thesis in which they are addressed.

5.1.2 System Parameters

There are at least three interferometer configurations of special interest here: both EUV and visible-

Table 1: Lithographic system parameters of interest. These numbers will be used for comparison throughout this chapter's investigation of systematic effects. Particular attention is paid to the EUV parameters as they pertain directly to experiments described in this thesis.

Parameter	EUV	Visible	Deep UV
wavelength, λ	13.4 nm	632.8 nm	193 nm
NA_i	~0.08	~0.08	~0.6-0.7
magnification	4-10	4-10	4-10
$\lambda/2NA$	.084 μm	3.96 μm	0.16 μm

light measurements of an EUV lithographic optic and, for comparison, a 193-nm-wavelength lithographic system with NA > 0.6. Approximate system parameters for each are given in Table 1.

5.2 DEFINITION OF COORDINATE SYSTEMS

Mathematical descriptions of the interferometer are simplified by the introduction of several interrelated coordinate systems, individually appropriate to different regions or components. This section introduces three coordinate systems and the expressions that relate them: the *Laboratory System,* the *Beam System,* and the *Detector System.*

Common to all of the coordinate systems is the NA of the beam in the region of interest, called the *local NA.* The local NA is determined by the sizes of various apertures and pupils in the system and describes the cone of rays that eventually reaches, or emanates from, an image or object point. These are the rays relevant to interferometric measurement of low spatial-frequency aberrations. In a reflective, cylindrically symmetric optical system, α is defined as the maximum half-angle within the system NA. By definition,

$$\mathrm{NA} \equiv \sin\alpha . \tag{1}$$

Where the spherical beams are incident on planar surfaces normal to the central ray, the tangent of α is a useful quantity. Define t as

$$t \equiv \tan\alpha = \frac{NA}{\sqrt{1-NA^2}} . \tag{2}$$

5.2.1 *The Laboratory System*

The Cartesian system, or *Laboratory Coordinates*, shown in Fig. 2, defines points in 3-D space as $P(x, y, z)$. The z-axis coincides with the central ray of the interferometer's *test* beam; the origin of the coordinates is defined as the center of curvature of the diverging (or converging) spherical beam. This point is typically determined by the position of a pinhole spatial filter in either the object- or the image-plane, or by the focal point of the interferometer's test beam.

The *Laboratory Coordinates*

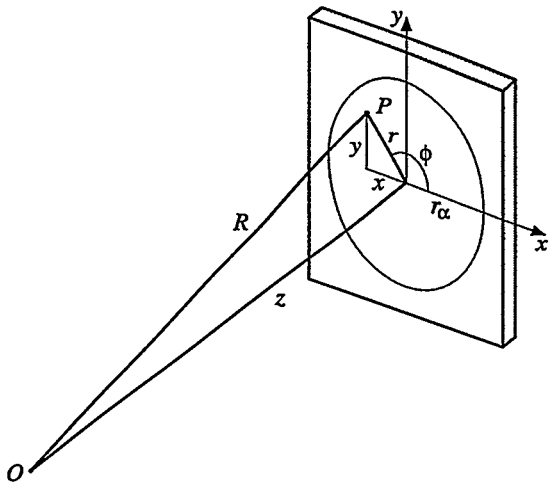

Figure 2. The *Laboratory Coordinate System* is based on Cartesian or cylindrical coordinates using the measurement units of the experimental system. The z-axis is defined to be collinear with the central ray of the *test* beam, with the center-of-curvature as the origin.

$$R = \sqrt{x^2 + y^2 + z^2} . \tag{3}$$

$$r = \sqrt{x^2 + y^2} . \tag{4}$$

Where spherical beams are incident on a planar surface, cylindrical coordinate systems have a maxi-

Two equivalent representations of the spherical *Beam Coordinates*

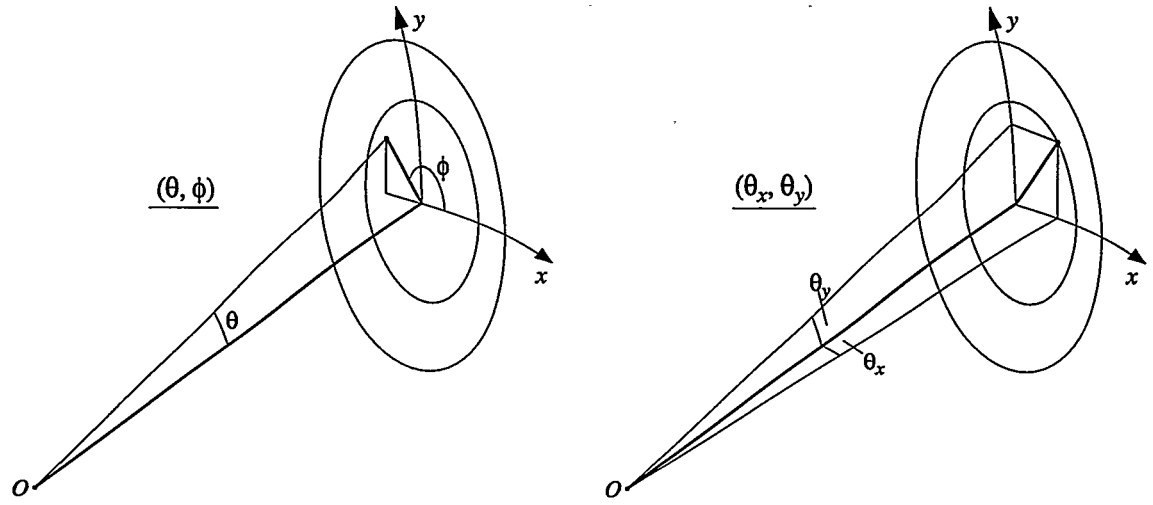

Figure 3. The spherical *Beam Coordinate System* uses polar and azimuthal angles to represent an *angular position* within the diverging or converging spherical beam. An alternate representation of the same coordinate system defines an angular position using an x and y pair of polar angles. Again, the z-axis is defined to be collinear with the central ray of the *test* beam, with the center of beam curvature as the origin.

mum radius, r_α corresponding to rays at the angle α from the axis.

$$r_\alpha \equiv z\tan\alpha = zt\,. \tag{5}$$

5.2.2 *The Beam System*

A spherical coordinate system, shown in Fig. 3, provides a more natural description of the diverging or converging beams: for the optical systems of interest here, aberrations are described as departures from an ideal, spherical wavefront. Based on the central ray of the test beam, we define a *position* within the beam using the polar and azimuthal angles (θ, ϕ). It will also be convenient to define a polar angle *vector*, separated into x and y angular components:

$$\boldsymbol{\theta} \equiv (\theta_x, \theta_y) \equiv (\theta\cos\phi, \theta\sin\phi). \tag{6}$$

In some cases, this angular vector simplifies translation to the Cartesian Laboratory System. Other expressions in this coordinate system relate $\boldsymbol{\theta}$ to $\mathbf{k}$, which is also used to represent the beam propagation direction:,

$$\mathbf{k} = \left(k_x, k_y, k_z\right) = \left(\sin\theta\cos\phi, \sin\theta\sin\phi, \cos\theta\right), \quad |\mathbf{k}| = 1\,. \tag{7}$$

$$\theta_{x,y} = \tan^{-1}\left(\frac{k_{x,y}}{k_z}\right)\,. \tag{8}$$

Normalization of the polar angle relative to the local NA will simplify calculations in some cases. This system is called the *Normalized Beam Coordinates*. For this purpose, define a normalized *angle* γ as

$$\gamma \equiv \frac{\theta}{\alpha}\,. \tag{9}$$

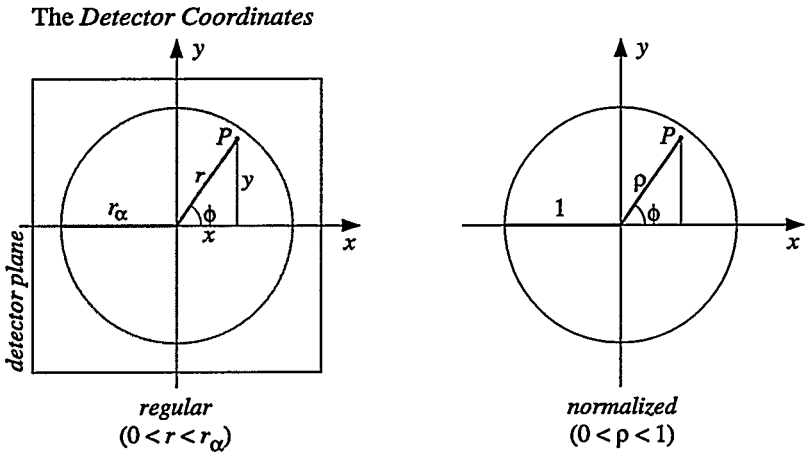

Figure 4.. The *Detector Coordinate System* is used to represent measurements recorded on a planar detector. Both Cartesian and polar representations are used. The origin is taken to be the point of intersection of the central ray of the test beam and the detector plane.

5.2.3 *The Detector System*

The final coordinate system introduced here is the 2-D polar *Detector Coordinates*, defined in the plane of the detector and centered on the point of intersection of the central ray of the test beam with the detector plane. The Detector Coordinate System is shown in Fig. 4. A point in the detector plane may be represented in the units of the Laboratory frame, or by a corresponding set of *Normalized Detector Coordinates* utilizing a dimensionless radius ρ based on r_α.

$$\rho \equiv \frac{r}{r_\alpha}. \tag{10}$$

From Eqns. (2) and (10) we also have the relationships,

$$r = r_\alpha \rho = tz\rho. \tag{11}$$

The normalized coordinates (ρ, ϕ) eventually become the coordinate system of the data analysis, which is based on a unit circle representation of the system's exit pupil.

5.3 NUMBER OF FRINGES

From the mathematical description of the PS/PDI arises a convenient rule of thumb useful for determining the required position and pitch of a grating beamsplitter.

> **Rule of Thumb:** The number of fringes in the interferogram equals the number of grating lines illuminated within the NA of the optical system.

Subject to the fact that wavefront aberrations in the test optic cause curvature in the observed fringe patterns, this rule is approximate. An investigation of the origin of this rule leads to a description of how the PS/PDI can be used with broadband illumination (Section 5.4).

Let α_i and α_o be the maximum half-angles within the image-side and object-side numerical apertures NA_i and NA_o respectively. Constraining our discussion to one side of the optical system, in general

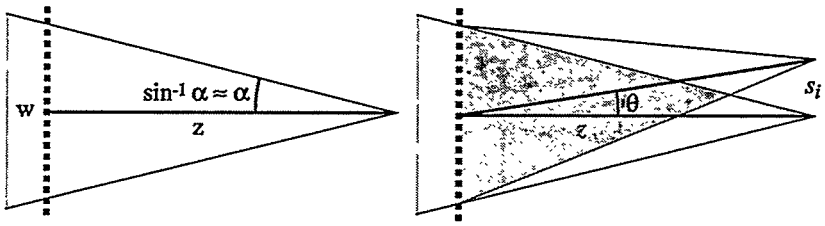

Figure 5. A grating beam-splitter is used to produce the test and reference beams of the PS/PDI. The first-order diffraction angle θ is determined only by the grating pitch *d*. The beam separation in the image-plane s_i depends on θ and on the position *z* of the grating with respect to focus.

we have,

$$\mathrm{NA} = \sin\alpha, \quad \text{and} \quad t \equiv \tan\alpha = \frac{NA}{\sqrt{1-NA^2}}. \qquad (12) \text{ and } (13)$$

Depending on the configuration, *z* is defined as the distance from the grating to the object-plane or as the distance from the grating to the image-plane.

For either an object-side or image-side grating (Chapter 4), the lateral width of the grating illuminated within the local NA is *w*, as shown in Fig 5.

$$w = 2zt. \qquad (14)$$

Therefore for a given grating pitch *d* the number of grating lines illuminated is

$$N_{lines} = \frac{w}{d} = \frac{2zt}{d}. \qquad (15)$$

When the grating is placed on the image-side, the converging beam from the optical system forms a series of real images corresponding to the diffraction orders of the grating. The lateral separation of two adjacent image-side foci s_i follows from the grating equation for the first diffracted order $\lambda = d\theta$ where θ is typically much smaller than α.

$$s_i \approx z\theta \approx \frac{z\lambda}{d}. \qquad (16)$$

Given s_i, the number of fringes within the NA is readily calculated from the maximum path length difference between the zeroth and the first diffracted orders. By symmetry, this maximum difference Δ is twice the difference between the central ray, and the rays at the angle α_i.

$$\Delta_{1/2} \approx s_i \sin\alpha_i = s_i NA_i, \quad \text{and} \quad \Delta = 2\Delta_{1/2} \approx \frac{2z\lambda}{d} NA_i. \qquad (17) \text{ and } (18)$$

The number of fringes $N_{fringes}$ is equal to the path length difference in waves (units of λ).

$$N_{fringes} = \frac{\Delta}{\lambda} \approx \frac{2z}{d} NA_i \approx \frac{2zt_i}{d} = N_{lines}, \qquad (19)$$

thereby justifying the rule of thumb. This number may also be written using s_i explicitly

$$N_{fringes} \approx N_{lines} \approx \frac{2s_i t_i}{\lambda}. \qquad (20)$$

When the grating is placed on the object-side, the rule of thumb still applies. In this case, however,

the grating divides the *diverging* beam, and each grating order besides the zeroth appears to originate from a separate virtual object source. By analogy with Eq. (16), the separation of these virtual objects is

$$s_o \approx z\theta \approx \frac{z\lambda}{d}. \tag{21}$$

In principle, the separation of the real foci in the image-plane is equal to the separation of the virtual objects, scaled by the magnification of the system.

$$s_i \approx m s_o. \tag{22}$$

The relationship of the object-side and image-side NA angles,

$$\alpha_i = \alpha_o / m, \tag{23}$$

allows Eq. (20) to be written independent of the system magnification.

$$N_{fringes} \approx N_{lines} \approx \frac{2 s_i t_i}{\lambda} \approx \frac{2 s_o t_o}{\lambda}. \tag{24}$$

In the small-NA range where $\sin\alpha \approx \tan\alpha$ a useful approximation for the number of fringes is

$$N_{fringes} \approx N_{lines} \approx \frac{2 s_i}{\lambda} NA_i \approx \frac{2 s_o}{\lambda} NA_o. \tag{25}$$

In the *upstream grating configuration* (Section 4.3) the multiple object sources are real, and the same rules apply.

5.3.1 *Numbers*

For a specified number of fringes, we can investigate the corresponding image-plane beam separation by solving for s_i in Equation (25):

$$s_i = \frac{N\lambda}{2NA_i}. \tag{26}$$

Figure 6 shows Eq. (26) plotted versus NA for three wavelengths of interest. To achieve 40 fringes at 0.08 NA in the EUV, 193-nm, and HeNe configurations requires beam separations of 4.2 µm, 60 µm, and 198 µm respectively. Forty fringes at 193 nm with 0.6 NA requires a beam separation of 6.4 µm.

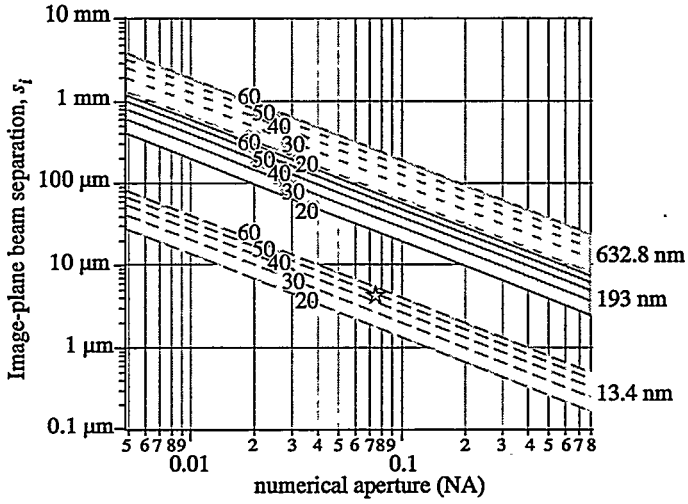

Figure 6. The number of interferogram fringes depends on the wavelength, the image-plane beam separation, and the measurement NA. For a wide range of numerical apertures, this figure shows the beam separation required to produce a given number of fringes. Three experimentally relevant wavelengths are considered: EUV(13.4 nm), deep UV (193 nm) and visible (632.8, HeNe). The star indicates EUV numbers relevant to experiments conducted in this thesis.

5.3 Summary

Beam Separation. $s/N_{fringe} = \lambda/2t = 0.084$ μm/fringe $\Rightarrow$ $N_{fringe}/s = 2t/\lambda = 12$ fringes/μm.

5.4 WHITE-LIGHT CONFIGURATION AND BANDWIDTH

For the grating-based configurations of the PS/PDI, the rule of thumb presented in the previous chapter equates the number of grating lines illuminated to the number of fringes observed. The fact that this rule is independent of the illumination wavelength leads to the conclusion that, aside from chromatic aberrations (wavelength-dependent effects) in the test optical system, the PS/PDI may be regarded as a *broad-band* interferometer. This section describes the most important wavelength-dependent effects of the interferometer. Note that this discussion addresses only an ideal, diffraction-limited, achromatic optical system under test.

Since the NA is a property of an optical system independent of wavelength, the number of grating lines that fall within the NA is determined only by the geometry. For a given wavelength, the number of observed fringes is related to the image-plane beam separation s_i, according to Eq. (24):.

$$N_{fringes} \approx N_{lines} \approx \frac{2s_i t_i}{\lambda}. \tag{27}$$

Using N as a convenient system invariant, s_i may be written as

$$s_i \approx \frac{N\lambda}{2t_i}, \tag{28}$$

showing that the image-plane beam separation is proportional to the wavelength. When the illumination is not monochromatic, grating-diffracted beams are focused to different lateral positions in the image-plane. The position of the zeroth-order focus does not depend on the grating pitch, and is thus not wavelength-dependent.

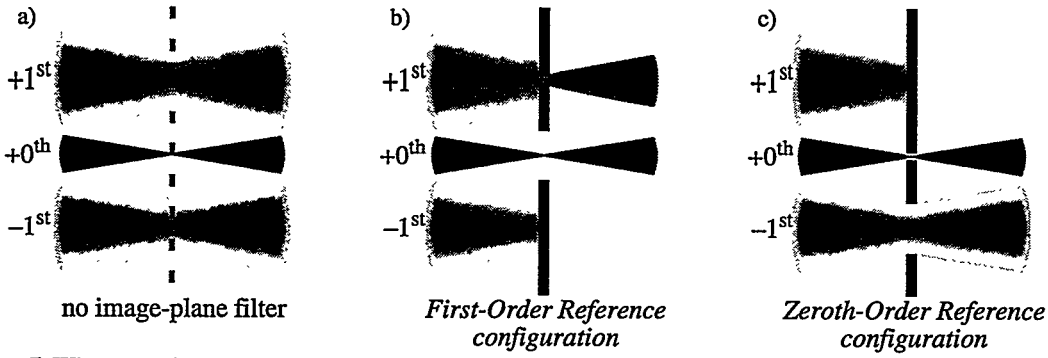

Figure 7. When a grating is used to separate the test beam, the diffractive orders are affected by the bandwidth of the illumination. (a) Different wavelength components of the first-order beams are separated by a lateral displacement in the image plane. (b) In the first-order reference configuration, the reference pinhole behaves as a monochromator, selectively transmitting a portion of the bandwidth more effectively than the rest. (b) A small translation of the image-plane spatial filter puts the system into the zeroth-order reference configuration, in which a much broader range of wavelengths is transmitted.

In the image-plane, the positive and negative first-order beams form foci on opposite sides of the zeroth-order beam. As shown in Fig. 7, a simple lateral translation of the two-pinhole spatial filter allows selection of either of the two first-order beams or of the zeroth-order as the reference or test beam. These two configurations are referred to as the *first-order reference* and the *zeroth-order reference* configurations, respectively. These names indicate which beam is filtered by the reference pinhole. In the presence of finite-bandwidth illumination, these two configurations do behave somewhat differently. Some advantages and disadvantages of these two similar arrangements are discussed in Section 5.8.

In the first-order reference configuration, the tiny reference pinhole serves as a monochromator by geometrically selecting some wavelengths to pass through the pinhole more efficiently than others. For this to be true, however, the test optic must be of nearly diffraction-limited quality. In the complementary zeroth-order reference configuration, the large window transmits a range of wavelengths determined by the window size and position. Hence, the range of recorded wavelength components may be different in the two configurations.

Due to the typically long time scale of measurement, relative to the frequency of the radiation, light of different wavelengths adds *incoherently*. Therefore, if there are wavelength components present in either the test or the reference beam but not in both, those components will contribute only to the unmodulated background intensity in the recorded data. *Unmodulated* refers to the recorded light that does not contribute to the interference fringes.

5.4.1 *Effect of Bandwidth on the Measured Fringe Pattern*

When using the PS/PDI with broad-band illumination, interpretation of the measured interference fringe patterns may require careful consideration. Chromatic aberrations and geometrical considerations must both be considered. The relevant bandwidth here is *not* the source bandwidth; strictly speaking, it is only those wavelength components that reach the detector and are present in both the test and reference beams. These are the only wavelength components capable of producing interference fringes. For reasons stated above, this restriction may exclude some components of the original source bandwidth.

One design consideration of the interferometer is that different wavelength components separated

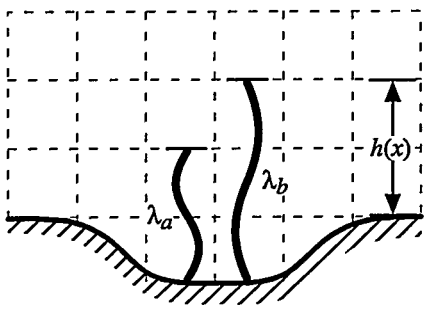

Figure 8. The origin of interferogram chromatic-dependence in a reflective achromatic system. For a particular wavelength component, the interferogram fringes reveal the optical path difference between two waves, measured in wavelengths. With a mirror surface height profile $h(x)$ different fringe patterns will be observed for each wavelength of measurement. The surface depression shown in the figure is one-half of λ_a yet is one-third of λ_b. Upon reflection the aberration path length is doubled. Thus, these two wavelengths generate different fringe patterns for the same aberration.

by a grating placed before (on the object-side of) the optical system will travel along different paths through the optical system. The significance of this effect must be evaluated based on the illumination bandwidth and the design on the test optical system.

If a range of wavelengths is present, then the measured interferogram will be an additive combination of the wavelength intensity components allowed to reach the detector. In a perfect optical system, the pattern of equally-spaced, parallel interference fringes is the same for *all wavelengths*. However, in the presence of aberrations, each wavelength component may contribute a different, overlapping interference pattern, thereby confusing measurement.

Even in the absence of true chromatic aberrations, geometrical effects can contribute wavelength-dependence to measurements. For example, consider a reflective optical system with a surface figure error of arbitrary depth (or height). Light reflected from the region of a depression travels a relatively longer distance than the light in adjacent areas. This situation is depicted in Fig. 8.

The significance of a given path-length difference on the interference pattern is inherently wavelength-dependent. For each spectral component, the interference fringes represent contours of constant path-length difference, separated by one wavelength. Thus, for a given path-length difference, different wavelengths will generate different fringe patterns. In the presence of finite bandwidth illumination, this effect can *blur* a fringe pattern. However, a special situation arises if the spectral intensity distribution is symmetric about a central wavelength: the contrast is reduced, but the fringe positions are unaffected. Such a situation only affects the signal-to-noise ratio of the wavefront measurements. This can be demonstrated mathematically as follows.

The measured intensity is the sum of the intensity contributions from all of the available wavelengths. Eq. (3) defines an intensity-weighting function $w(\lambda)$ with units of λ^{-1}, and an intensity function $J(\mathbf{r};\lambda)$.

$$I(\mathbf{r}) = \int_{\lambda} dI(\mathbf{r};\lambda) = \int_{\lambda} w(\lambda) J(\mathbf{r};\lambda) d\lambda \,, \tag{29}$$

where

$$\int_{\lambda} w(\lambda) d\lambda = 1 \,. \tag{30}$$

A general expression for a single wavelength component $J(\mathbf{r};\lambda)$ is

$$J(\mathbf{r};\lambda) = A + B\cos\left[\boldsymbol{\kappa}\cdot\mathbf{r} + \frac{4\pi h(\mathbf{r})}{\lambda}\right], \tag{31}$$

where the vector $\boldsymbol{\kappa}$ represents the spatial carrier frequency of the fringe pattern, and is invariant of wavelength. $h(\mathbf{r})$ is the combined mirror figure *error* as seen by a given ray in an arbitrary reflective optical system. The path length of a particular ray is doubled upon reflection from a surface, as the light must twice travel the distance h.

Consider the addition of two different closely-spaced wavelength components $\lambda_o-\Delta\lambda$ and $\lambda_o+\Delta\lambda$ with $\Delta\lambda \ll \lambda_o$.

$$\tfrac{1}{2}J(\mathbf{r};\lambda_o-\Delta\lambda)+\tfrac{1}{2}J(\mathbf{r};\lambda_o+\Delta\lambda) = A(\mathbf{r})+\tfrac{1}{2}B(\mathbf{r})\cos\left[\kappa\cdot\mathbf{r}+\frac{4\pi h(\mathbf{r})}{\lambda_o-\Delta\lambda}\right]+\tfrac{1}{2}B(\mathbf{r})\cos\left[\kappa\cdot\mathbf{r}+\frac{4\pi h(\mathbf{r})}{\lambda_o+\Delta\lambda}\right] \quad (32a)$$

$$\approx A(\mathbf{r})+B(\mathbf{r})\cos\left[\kappa\cdot\mathbf{r}+\frac{4\pi h(\mathbf{r})}{\lambda_o}\right]\cos\left[\frac{4\pi h(\mathbf{r})}{\lambda_o}\frac{\Delta\lambda}{\lambda_o}\right] \quad (32b)$$

$$\approx A(\mathbf{r})+B(\mathbf{r})\cos\left[\kappa\cdot\mathbf{r}+\frac{4\pi h(\mathbf{r})}{\lambda_o}\right]\left\{1-\frac{\pi^2}{8}\left[\frac{h(\mathbf{r})}{\lambda_o}\right]^2\left(\frac{\Delta\lambda}{\lambda_o}\right)^2\right\}. \quad (32c)$$

In Eq. (32b), the wavelength-dependence is expanded to first-order in the $\Delta\lambda$. In the limit of narrow bandwidth $\Delta\lambda$ or small aberrations $h(\mathbf{r})$ Eqns. (32a) to (32c) *reduce* to the intensity pattern of the central wavelength, as expected. This fact leads to the illustration of an important result, worth elaboration.

> The addition of two closely spaced and equally-weighted wavelength components yields the same fringe pattern as the central wavelength, with a reduction of fringe modulation determined by the magnitude of $h(\mathbf{r})$ and $\Delta\lambda$.

5.4.2 *Fringe Blurring in Symmetric Intensity Distributions*

In the special case of symmetric intensity distributions we can derive a general form of the resultant fringe pattern. The predicted reduction of the fringe modulation can be used as a criterion to set an upper limit on the allowable bandwidth. Non-symmetric distributions may be represented by the addition of a symmetric distribution with an asymmetric distribution. In this case, the following treatment would apply to the symmetric part, and the asymmetric part would have to be addressed separately.

When the wavelength distribution $w(\lambda)$ is symmetric about λ_o, pairs of intensity components within the distribution add to re-create the pattern of the central wavelength. For a symmetric distribution,

$$w(\lambda_o-\Delta\lambda)\equiv w(\lambda_o+\Delta\lambda). \quad (33)$$

The sum of a pair of intensities within the distribution integral of Eq. (29) will be

$$w(\lambda_o-\Delta\lambda)J(\mathbf{r};\lambda_o-\Delta\lambda)+w(\lambda_o+\Delta\lambda)J(\mathbf{r};\lambda_o+\Delta\lambda)$$

$$\approx 2w(\lambda_o+\Delta\lambda)\left(A(\mathbf{r})+B(\mathbf{r})\cos\left[\kappa\cdot\mathbf{r}+\frac{4\pi h(\mathbf{r})}{\lambda_o}\right]\left\{1-\frac{\pi^2}{8}\left[\frac{h(\mathbf{r})}{\lambda_o}\right]^2\left(\frac{\Delta\lambda}{\lambda_o}\right)^2\right\}\right). \quad (34)$$

By symmetry, and Eq. (34), we have

$$I(\mathbf{r})=\int_{\lambda} w(\lambda)J(\mathbf{r};\lambda)d\lambda=\int_{\Delta\lambda} w(\lambda_o+\Delta\lambda)J(\mathbf{r};\lambda_o+\Delta\lambda)d(\Delta\lambda) \quad (35a)$$

$$\approx 2\int_{\Delta\lambda>0} w(\lambda_o+\Delta\lambda)\left(A(\mathbf{r})+B(\mathbf{r})\cos\left[\kappa\cdot\mathbf{r}+\frac{4\pi h(\mathbf{r})}{\lambda_o}\right]\left\{1-\frac{\pi^2}{8}\left[\frac{h(\mathbf{r})}{\lambda_o}\right]^2\left(\frac{\Delta\lambda}{\lambda_o}\right)^2\right\}\right)d(\Delta\lambda) \quad (35b)$$

$$\approx A(\mathbf{r})+B(\mathbf{r})\cos\left[\boldsymbol{\kappa}\cdot\mathbf{r}+\frac{4\pi h(\mathbf{r})}{\lambda_o}\right]\left\{1-\frac{\pi^2}{8}\left[\frac{h(\mathbf{r})}{\lambda_o}\right]^2\int_{\Delta\lambda} w(\lambda_o+\Delta\lambda)\left(\frac{\Delta\lambda}{\lambda_o}\right)^2 d(\Delta\lambda)\right\} \tag{35c}$$

This representation allows us to define a bandwidth-dependent *fringe blurring function* $W(\delta)$ to simplify this discussion,

$$W(\delta)\equiv\frac{\pi^2}{8}\int_{\Delta\lambda} w(\lambda_o+\Delta\lambda)\left(\frac{\Delta\lambda}{\lambda_o}\right)^2 d(\Delta\lambda). \tag{36}$$

The dimensionless parameter δ that describes the *width* of the spectral intensity distribution will be defined differently for different distribution models (Gaussian, top-hat, etc.). Continuing to simplify Eq. (35c),

$$I(\mathbf{r})\approx A(\mathbf{r})+B(\mathbf{r})\cos\left[\boldsymbol{\kappa}\cdot\mathbf{r}+\frac{4\pi h(\mathbf{r})}{\lambda_o}\right]\left\{1-\left[\frac{h(\mathbf{r})}{\lambda_o}\right]^2 W(\delta)\right\}, \tag{37a}$$

$$I(\mathbf{r})\approx J(\mathbf{r};\lambda_o)-B(\mathbf{r})\cos\left[\boldsymbol{\kappa}\cdot\mathbf{r}+\frac{4\pi h(\mathbf{r})}{\lambda_o}\right]\left[\frac{h(\mathbf{r})}{\lambda_o}\right]^2 W(\delta). \tag{37b}$$

In Eqns. (37a) and (37b), the bandwidth-dependent term acts to reduce the magnitude of the fringe modulation B *without changing the positions of the inflection points.* Furthermore, when $A(\mathbf{r})$ and $B(\mathbf{r})$ are slowly varying functions relative to the spatial period of the fringes, then the positions of the fringe maxima and minima will match the monochromatic case. Thus in the presence of a symmetric spectral distribution, the fringe contrast is merely reduced, and $W(\delta)$ represents the fractional loss in fringe modulation.

5.4.3 *Determining $W(\delta)$ for the Gaussian and Top-Hat Distributions*

For quantitative results we investigate two spectral intensity distribution models: *Gaussian*, and *top-hat.* The Gaussian distribution is defined by its full-width at half-maximum (FWHM), defined as δ_g; the top-hat is defined simply by its full-width δ_t.

5.4.3.1 Gaussian Distribution. Consider a Gaussian distribution centered about λ_o, with an RMS width of $\lambda_o\sigma$. In this definition, σ is the dimensionless parameter describing the distribution width relative to the central wavelength. Normalization requires that Eq. (30) must be satisfied.

$$w_g(\lambda_o+\Delta\lambda)=\frac{1}{\sqrt{2\pi}\sigma}\exp\left[-\frac{(\Delta\lambda)^2}{2\sigma^2}\right]. \tag{38}$$

Solution of the integral in Eq. (36) yields $W_g(\sigma)$.

$$W_g(\sigma)=\frac{\pi^2\sigma^2}{8}. \tag{39}$$

As stated previously, W_g is defined differently for each distribution shape; the definition may use any convenient parameter that describes the distribution width. Often, a more convenient representation of the

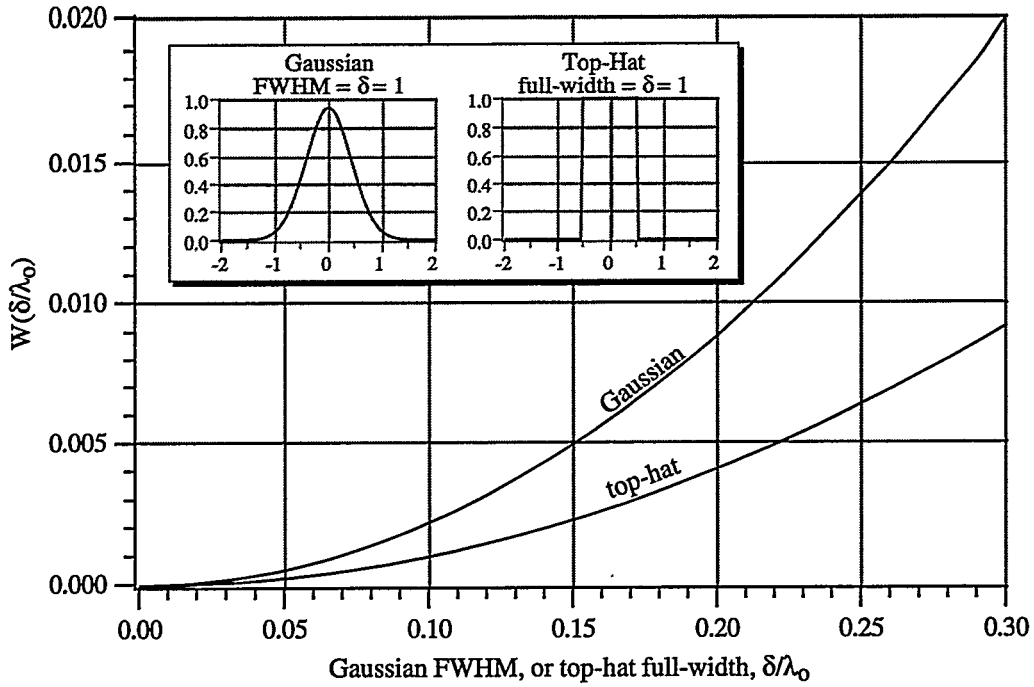

Figure 9. A plot of the fringe-blurring function $W(\delta)$ for the Gaussian and top-hat spectral distributions as a function of the distribution widths. $W(\delta)$ is a parameter that describes the reduction in fringe height that can be expected in PS/PDI interferometry in the presence of a symmetric spectral distribution. Note that the two distribution widths are defined differently: this primarily accounts for the difference in $W(\delta)$. The two width definitions are illustrated in the inset graphs.

Table 2. Values of the fringe blurring function $W(\delta)$ for the Gaussian and the top-hat spectral intensity distributions, and a selected distribution widths, δ. W describes the expected reduction in fringe contrast related to non-monochromatic illumination of a reflective optical system. * is the measured bandwidth used in EUV interferometry.

δ	W_g(Gaussian)	W_t(top-hat)
0.000	0.00	0.00
0.001*	2.22×10^{-7}	1.03×10^{-7}
0.002	8.90×10^{-7}	4.11×10^{-7}
0.005	5.56×10^{-6}	2.57×10^{-6}
0.010	2.22×10^{-5}	1.03×10^{-5}
0.020	8.90×10^{-5}	4.11×10^{-5}
0.050	5.56×10^{-4}	2.57×10^{-4}
0.100	2.22×10^{-3}	1.03×10^{-3}
0.200	8.90×10^{-3}	4.11×10^{-3}

Gaussian distribution will be in terms of the full-width at half-maximum (FWHM) δ_g rather than σ.

δ_g and σ are related by a constant coefficient. It is easily shown that

$$(FWHM)^2 \equiv \delta_g^2 = (8\ln 2)\sigma^2 . \tag{40}$$

Defining W_g using the FWHM δ_g instead of the RMS width σ,

$$W_g(\delta_g) = \frac{\pi^2\sigma^2}{8} = \frac{\pi^2\delta_g^2}{64\ln 2} = 0.222\delta_g^2 . \tag{41}$$

5.4.3.2 Top-Hat Distribution. In a similar manner as above, choose a normalized top-hat distribu-

tion centered about λ_o with a full-width $\lambda_o\delta$.

$$w_t(\lambda_o+\Delta\lambda)=\begin{cases}\dfrac{1}{\lambda_o\delta_t}, & |\Delta\lambda|<\frac{1}{2}\lambda_o\delta_t \\ 0, & |\Delta\lambda|>\frac{1}{2}\lambda_o\delta_t\end{cases}. \tag{42}$$

From Eq. (36) the fringe-blurring function is

$$W_t(\delta_t)=\frac{\pi^2\delta_t^2}{96}=0.103\delta_t^2. \tag{43}$$

Selected values of the blurring-function $W(\delta)$ from Fig. 9 are listed in Table 2. Even for significant bandwidths, the magnitude of the blurring-function, shows that in the presence of mirror surface aberrations, small on the scale of the central wavelength, the fringe modulation is not substantially reduced.

5.4 Summary

Bandwidth. $W_g = 2.22\times10^{-7}$ @ 0.1% BW (Gaussian distribution). Fringe amplitude is reduced by 2.22×10^{-7} per wave^2 of aberration at this bandwidth.

5.5 GEOMETRICAL COMA SYSTEMATIC ERROR

This section describes a systematic, geometric coma error introduced by the image-plane separation of the test and reference beams. Three methods for the removal of this error are proposed.

For several reasons, high-accuracy implementations of the EUV PDI and PS/PDI do not utilize *re-imaging optics* to image light from the exit pupil onto the detector plane. Such optics are common in most conventional interferometer designs. The primary reasons for their absence is the unavailability of optical elements of suitable quality and the fact that low-NA EUV measurements suffer only localized effects from diffraction. An important geometrical effect related to the absence of re-imaging optics causes a third-order systematic error to be introduced. Experimental observation of this effect has been used as a verification of system sensitivity (Section 8.9). The magnitude of this effect depends linearly on the image-plane separation of the test and reference beams, and thus affects both the PDI and the PS/PDI configurations.

Essentially, the test and reference beams are two diverging spherical beams with a lateral displacement of their centers-of-curvature. As they propagate toward the detector plane, the relative path-length difference generates the interference pattern. Neglecting aberrations in the optical system, the pattern consists primarily of parallel, uniformly-spaced, straight fringes; but consideration of the path-length difference including terms out to third order, reveals a systematic *coma* of magnitude comparable with the sensitivity of the EUV PS/PDI interferometer.

In Fig. 10, light from the two beams reaches a common point at the detector. Without loss of gener-

ality, we take the displacement vector s to lie along the x-axis. Setting the origin on one of the rays, the path lengths are

$$R_1 = \sqrt{x^2 + y^2 + z^2}\,, \tag{44}$$

$$R_2 = \sqrt{(x-s)^2 + y^2 + z^2}\,, \tag{45}$$

$$\Delta R = z\sqrt{1+\left(\frac{x}{z}\right)^2+\left(\frac{y}{z}\right)^2} - z\sqrt{1+\left(\frac{x-s}{z}\right)^2+\left(\frac{y}{z}\right)^2}\,. \tag{46}$$

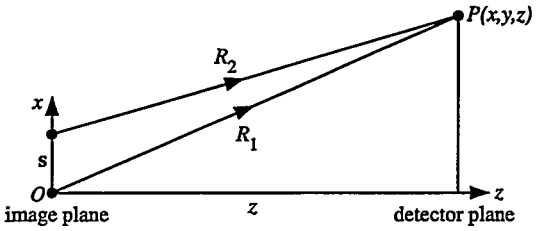

Figure 10. The description of systematic errors begins with the path length difference of the test and reference beam centers to a point on the detector. The figure shows the beam separation s and the image-to-detector-plane distance z.

At this point it is convenient to define the following dimensionless quantities

$$\begin{cases} u \equiv x/z \\ v \equiv y/z \\ \delta \equiv s/z << \max\{u\}, \max\{v\} \end{cases}. \tag{47}$$

Now re-write ΔR in term of the dimensionless variables.

$$\Delta R = z\sqrt{1+u^2+v^2} - z\sqrt{1+(u-\delta)^2+v^2}\,. \tag{48}$$

Using the binomial expansion, expand the square-roots keeping terms up to first-order in δ only. Many terms in the expansion cancel leaving

$$\Delta R = z\delta u\left[1-\tfrac{1}{2}\left(u^2+v^2\right)+\tfrac{3}{8}\left(u^2+v^2\right)^2-\cdots\right] = \frac{z\delta u}{\sqrt{1-\left(u^2+v^2\right)}}\,. \tag{49}$$

To express this as a wavefront aberration observable in the data, it is convenient to use the normalized cylindrical *Detector Coordinate System* (see Section 5.2), normal to the z-axis.

$$\begin{cases} t \equiv \tan\alpha, \text{ where NA} \equiv \sin\alpha \\ \rho \equiv \dfrac{1}{t}\sqrt{u^2+v^2} \in [0,1], \text{ within the system NA} \\ \phi \equiv \tan^{-1}(v/u), \text{ the azimuthal angle} \end{cases}. \tag{50}$$

The path-length difference of interest may now be written as the product of radial and angular terms,

$$\Delta R = z\delta t\left[1-\tfrac{1}{2}t^2\rho^2+\tfrac{3}{8}t^4\rho^4-\cdots\right]\rho\cos\phi = \frac{z\delta t}{\sqrt{1-t^2\rho^2}}\rho\cos\phi\,. \tag{51}$$

Generalizing the direction s as ϕ_s, and replacing δ with s/z, ΔR becomes

$$\Delta R = z\delta t\left(1-\tfrac{1}{2}t^2\rho^2+\tfrac{3}{8}t^4\rho^4-\cdots\right)\rho\cos(\phi-\phi_s) = \frac{z\delta t}{\sqrt{1-t^2\rho^2}}\rho\cos(\phi-\phi_s), \tag{52}$$

$$\Delta R = st\left(1-\tfrac{1}{2}t^2\rho^2+\tfrac{3}{8}t^4\rho^4-\cdots\right)\rho\cos(\phi-\phi_s) = \frac{st}{\sqrt{1-t^2\rho^2}}\rho\cos(\phi-\phi_s)\,. \tag{53}$$

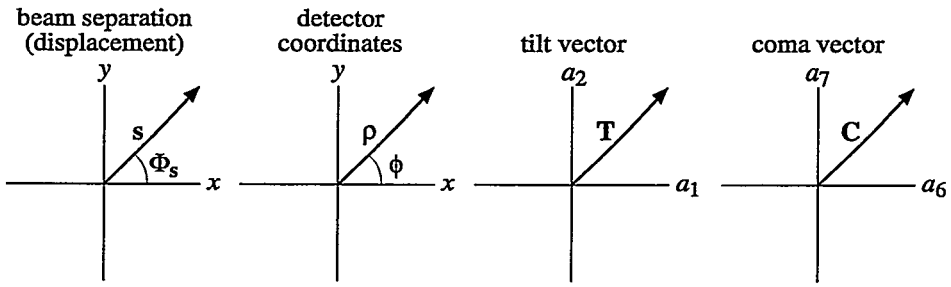

Figure 11. The description of several experimental quantities is facilitated by representation in pairs of coordinates. The test and reference beam separation in the image plane may be represented by a single vector **s**. The tilt and coma components of the path length difference have a convenient representation in a single **T** or **C** vector defined from the Zernike polynomial coefficients (a_1, a_2) and (a_6, a_7) respectively. Since they share the same radial dependence, and differ only in the cosθ or sinθ angular dependence, these vector representations simplify many aspects of the analysis.

It will be useful to separate the angular dependence of Eq. (53) into cosine and sine components as follows.

$$\Delta R = st\left(1-\tfrac{1}{2}t^2\rho^2+\tfrac{3}{8}t^4\rho^4-\cdots\right)\rho\left(\cos\phi_s\cos\phi+\sin\phi_s\sin\phi\right). \tag{54}$$

The first term in the expansion is the tilt that defines the fundamental fringe pattern. The negative sign of the third-order term in Eq. (54) shows that the effect of the geometric coma is a *reduction* of the fringe period at the edges of the measurement. (This also may be understood that from the perspective that at the edge of the field, a small change in angle results in a larger change in position on the detector than at the center.) The higher-order effects are always aligned parallel with the *tilt* term (also the beam separation), so there is no induced curvature of the fringes.

For a given optical system, the magnitude of this effect depends primarily on the image-plane separation of the test and reference beams. The bandwidth discussion of Section 5.4 showed that in the configuration where the beam from the first-diffracted order is used as the test beam, different wavelength components are brought to different image-plane separations. From the combination of these two effects, it is clear that attention to the chromatic dependence of the systematic coma may be necessary in some cases.

5.5.1 *Representation of Zernike Pairs in Vector Notation*

Further simplification of the path-length difference expansion can be made by introducing a vector notation for the pairs of Zernike terms that naturally separate into x- and y-oriented components. The definitions of the Zernike polynomials may be found in Chapter 14, and the Zernike coefficient-pair vector notation is discussed in Section 14.3.1. Here, the relevant terms are only the *tilt* and *coma* components.

Any wavefront aberration on an unobstructed circular aperture may be described by a series of Zernike polynomials, with coefficients $\{a_i\}$.

$$W(\rho,\phi)=\sum a_i Z_i(\rho,\phi). \tag{55}$$

The tilt and coma components are defined specifically as

$$\text{Tilt:} \quad Z_1 \equiv \rho\cos\phi\,, \quad Z_2 \equiv \rho\sin\phi\,, \tag{56a}$$

$$\text{Coma:} \quad Z_6 \equiv \left(3\rho^3 - 2\rho\right)\cos\phi\,, \quad Z_7 \equiv \left(3\rho^3 - 2\rho\right)\sin\phi\,, \tag{56b}$$

$\rho^3\cos\phi$ and $\rho^3\sin\phi$ do not appear independently within the Zernike polynomials. A linear combination of tilt and coma is required to represent these terms.

$$\rho^3\cos\phi = \tfrac{1}{3}Z_6 + \tfrac{2}{3}Z_1\,, \text{ and } \rho^3\sin\phi = \tfrac{1}{3}Z_7 + \tfrac{2}{3}Z_2\,. \tag{57}$$

For a simplified vector notation, define a position vector $\boldsymbol{\rho}$

$$\boldsymbol{\rho} \equiv (\rho\cos\phi, \rho\sin\phi), \tag{58}$$

and two more vectors representing the tilt and coma coefficients of a Zernike Polynomials series.

$$\begin{cases} \mathbf{T} \equiv (a_1, a_2), & \text{"tilt vector"} \\ \mathbf{C} \equiv (a_6, a_7), & \text{"coma vector"} \end{cases} \tag{59}$$

These vectors are shown in Fig. 11.

Now, keeping only terms up to third-order, the path-length difference in Eq. (54) may be re-written. (The inclusion of higher-order terms, necessary only when NA or s is large, is straightforward.)

$$\Delta R = t\left(1 - \tfrac{1}{2}t^2\rho^2\right)\boldsymbol{\rho}\cdot\mathbf{s} = t(\boldsymbol{\rho}\cdot\mathbf{s}) - \tfrac{1}{2}t^3\left(\rho^2\boldsymbol{\rho}\cdot\mathbf{s}\right) = t\left(1 - \tfrac{1}{3}t^2\right)\mathbf{s}\cdot(Z_1, Z_2) - \tfrac{1}{6}t^3\mathbf{s}\cdot(Z_6, Z_7)\,. \tag{60}$$

Hence, $$\mathbf{T} = t\left(1 - \tfrac{1}{3}t^2\right)\mathbf{s}\,, \text{ and } \mathbf{C} = -\tfrac{1}{6}t^3\mathbf{s}\,. \tag{61a) and (61b}$$

Notice that $\mathbf{s} \parallel \mathbf{T} \parallel \mathbf{C}$. Finally, the path-length difference may be written as the sum of tilt and coma components.

$$\Delta R = \mathbf{T}\cdot(Z_1, Z_2) + \mathbf{C}\cdot(Z_6, Z_7) = t\left(1 - \tfrac{1}{3}t^2\right)\mathbf{s}\cdot(Z_1, Z_2) - \tfrac{1}{6}t^3\mathbf{s}\cdot(Z_6, Z_7)\,. \tag{62}$$

5.5.2 Isolating and Removing the Geometric Coma Effect

Accurate PDI or PS/PDI wavefront measurement in the absence of re-imaging optics requires that the systematic error from the geometrical coma be identified and subtracted from the data. There are several means available for determining the magnitude of this effect. Two methods are described here.

The magnitude of the geometric coma depends very sensitively on the NA of measurement (NA^3 dependence). When the data is analyzed, this NA is not strictly the NA on the measurement-side of the optical system. Typically a sub-region of the available data is selected: the relevant NA of interest here is the NA *defined* by the selected sub-region and the cone of rays that created it. In practice it may therefore be difficult to precisely know the *measurement NA*.

Method 1 outlines a procedure to follow when the measurement NA is well known. In Method 2, two separate measurements with different fringe rotations and/or densities are combined, and *a priori* knowledge of the measurement NA is *not* required. In both cases, the goal is to determine the change

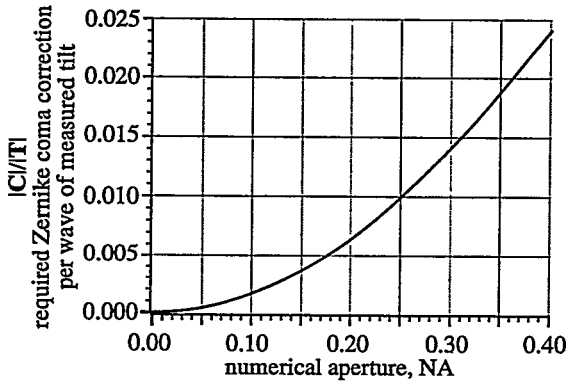

Figure 12. The image plane separation of the test and reference beams introduces a systematic geometric coma error. This graph shows the magnitude of the required Zernike coefficient coma correction per wave of measured tilt as a function of NA. At 0.08 NA, the correction is 0.0011 waves of coma is required for each wave of measured tilt. At 0.1 NA, the correction is 0.0017 waves per wave of tilt.

required to remove the geometric coma from the Zernike polynomial series, or, equivalently, from the measured wavefront itself.

5.5.2.1 ***Method 1: Removing the Geometric Coma with Known Measurement NA.*** If the measurement NA is precisely known, then the removal of the geometric coma systematic error is straightforward. Analysis proceeds from the path-length difference of Eq. (62). The tilt and coma vectors are parallel and have a fixed relationship based on t, the tangent of the NA angle.

$$\mathbf{C} = -\frac{t^2\mathbf{T}}{6\left(1-\frac{1}{3}t^2\right)} = -\frac{t^2\mathbf{T}}{6-2t^2} \approx -\tfrac{1}{6}t^2\mathbf{T}. \tag{63a}$$

In terms of the NA,

$$\mathbf{C} = -\frac{NA^2\mathbf{T}}{6-8NA^2} \approx -\tfrac{1}{6}NA^2\mathbf{T}, \tag{63b}$$

The approximation holds for small NA.

In the presence of wavefront aberrations, the measured coma $\mathbf{C}_o$ may take any arbitrary value. From this coma, the geometric coma error **C** must be subtracted to yield **C'** the *actual* coma. Using the measured tilt and the known NA, the geometric coma subtraction is as follows:

$$\mathbf{C}' = \mathbf{C}_o - \mathbf{C} = \mathbf{C}_o - \frac{t^2\mathbf{T}}{6-2t^2}. \tag{64}$$

Figure 12 shows the significance of this correction by plotting the amount of coma correction required (in waves) per wave of measured tilt. If the system has 40 fringes, multiply the ordinate by 40 to find the magnitude of required coma correction in waves.

Section 5.9 describes a coma that comes from the planar grating diffracting spherical beam. If this effect is present in the test wavefront, then Eqns. (63) and (64) may need modification to account for this effect. Like the geometric coma, the grating coma is also proportional to the tilt, so the modification is not complicated.

5.5.2.2 ***Method 2: Removing Geometric Coma Using the Difference Wavefront.*** Performing two separate experiments using gratings aligned at different angles or with different pitch, enables a combina-

tion of measurements that can be used to identify and remove the geometric coma. (The image-plane reference pinhole(s) and window must be designed to accommodate this.) This analysis method utilizes a Zernike polynomial fit to the *difference wavefront*, representing the difference between two separate measurements. Equivalently, since the fitting polynomials are orthogonal, the first set of coefficients may be simply subtracted from the second set to provide the fitting coefficients of the difference wavefront.

Consider separate measurements using to two gratings inserted into the same beam position, normal to the central ray, but with the rulings oriented along different directions. The image-plane beam separations will be $\mathbf{s}_1$ and $\mathbf{s}_2$, not necessarily equal in magnitude. Assume that the optical system under test has an arbitrary wavefront aberration $W(\rho, \phi)$. To reduce measurement uncertainties, the two wavefronts used here may themselves be composite wavefronts formed from multiple series of similar measurements.

If for both measurements the test beam passes through the same image-plane point, then the contribution of tilt and geometric coma to the two observed path length differences may be written according to Eq. (59). Including arbitrary wavefront aberrations W,

$$\Delta R_1 = W + t\left(1-\tfrac{1}{3}t^2\right)\mathbf{s}_1\cdot(Z_1,Z_2) - \tfrac{1}{6}t^3\mathbf{s}_1\cdot(Z_6,Z_7) = \mathbf{T}_1\cdot(Z_1,Z_2) + \mathbf{C}_1\cdot(Z_6,Z_7), \tag{65a}$$

$$\Delta R_2 = W + t\left(1-\tfrac{1}{3}t^2\right)\mathbf{s}_2\cdot(Z_1,Z_2) - \tfrac{1}{6}t^3\mathbf{s}_2\cdot(Z_6,Z_7) = \mathbf{T}_2\cdot(Z_1,Z_2) + \mathbf{C}_2\cdot(Z_6,Z_7). \tag{65b}$$

Taking the difference,

$$\Delta R_1 - \Delta R_2 = (\mathbf{T}_1-\mathbf{T}_2)\cdot(Z_1,Z_2) + (\mathbf{C}_1-\mathbf{C}_2)\cdot(Z_6,Z_7) = \mathbf{T}_\Delta\cdot(Z_1,Z_2) + \mathbf{C}_\Delta\cdot(Z_6,Z_7), \tag{66}$$

where $(\Delta R_1 - \Delta R_2)$ is the measured difference wavefront, and $\mathbf{T}_\Delta$ and $\mathbf{C}_\Delta$ are the *measured* Zernike coefficients that describe it.

$$\begin{cases} \mathbf{T}_\Delta \equiv (\mathbf{T}_1-\mathbf{T}_2) = (a_1,a_2) \\ \mathbf{C}_\Delta \equiv (\mathbf{C}_1-\mathbf{C}_2) = (a_6,a_7) \end{cases}. \tag{67}$$

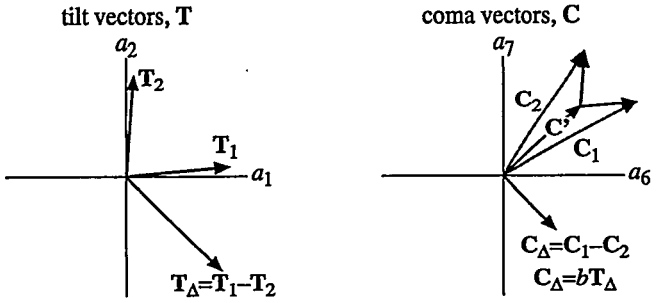

Figure 13. When two or more measurements are made at different orientations of the spatial carrier frequency of the fringe pattern, the systematic coma may be isolated and removed. This is facilitated by the definition of two *difference vectors* $\mathbf{T}_\Delta$ and $\mathbf{C}_\Delta$, as shown. The systematic coma components must be parallel to the tilt in the individual measurements. Experimentally the measured comas $\mathbf{C}_1$ and $\mathbf{C}_2$ come from the inherent coma $\mathbf{C}'$ plus the systematic coma, oriented parallel to the tilt in each measurement. By using the difference coma $\mathbf{C}_\Delta$, the inherent coma is separated from the systematic coma components. The proportionality constant b between $\mathbf{C}_\Delta$ and $\mathbf{T}_\Delta$ is easily found using a least-squares technique.

The contributions of the wavefront we are trying to measure W are removed by the subtraction. Figure 13 shows the tilt and coma vectors of two separate measurements, and the difference vectors described by Eq (67). The measured coma vectors $\mathbf{C}_1$ and $\mathbf{C}_2$ both contain the inherent coma **C'**, which is removed by subtraction.

Even though the NA (and thus t) is not known, we may utilize the fact that the *ratio* of $\mathbf{T}_1$ to $\mathbf{C}_1$ and of $\mathbf{T}_2$ to $\mathbf{C}_2$ is fixed, and solve for the proportionality constant b that provides the best fit. Using the method of least-squares, the criterion for the best fit to the data is to find the minimum of the error function $E^2(b)$.

$$E^2(b) = \|\mathbf{C}_\Delta - b\mathbf{T}_\Delta\|^2 = \|\mathbf{C}_\Delta\|^2 + b^2\|\mathbf{T}_\Delta\|^2 - 2b(\mathbf{T}_\Delta \cdot \mathbf{C}_\Delta). \tag{68}$$

The minimum occurs where the derivative with respect to b is zero.

$$\frac{dE^2(b)}{db} = 0 = 2b\|\mathbf{T}_\Delta\|^2 - 2(\mathbf{T}_\Delta \cdot \mathbf{C}_\Delta). \tag{69}$$

Solving for b,

$$b = \frac{\mathbf{T}_\Delta \cdot \mathbf{C}_\Delta}{\|\mathbf{T}_\Delta\|^2} = \frac{a_1a_6 + a_2a_7}{a_1^2 + a_2^2}. \tag{70}$$

By the known relationship of tilt and coma in Eq. (63), we can solve for t, and thus NA.

$$b = -\frac{t^2}{6 - 2t^2}, \text{ and } t = \sqrt{\frac{6b}{2b-1}}. \tag{71) and (72}$$

$$\mathrm{NA} = \sin\left(\tan^{-1} t\right) = \frac{t}{\sqrt{1+t^2}}. \tag{73}$$

From here, the procedure for removing the coma follows Method 1. From the two measured comas $\mathbf{C}_{1,2}$ and the measured tilts $\mathbf{T}_{1,2}$ the geometric coma is subtracted. Separately, for each measurement (1 and 2), we find the underlying coma **C'**.

$$\mathbf{C}' = \mathbf{C}_{1,2} - \mathbf{C} = \mathbf{C}_{1,2} - b\mathbf{T}_{1,2} = \mathbf{C}_{1,2} - \left(\frac{a_1a_6 + a_2a_7}{a_1^2 + a_2^2}\right)\mathbf{T}_{1,2}. \tag{74}$$

The measured wavefront, after the removal of the systematic coma, is found from the *average* or another suitable combination.of the two sets of measurements.

As stated earlier, if the so-called *grating coma* systematic error is present in the test wavefront, then the above discussion requires some simple modifications. The addition of the grating coma only affects the proportionality constant between the tilt and coma terms. Since for Method 2, the measurement NA is a parameter of the fit, and the proportionality constant is unknown, no modification is required to determine the inherent coma. However, Equations (71) through (73) which relate the fitting parameter b to the measurement NA, do require modification.

5.5.2.3 *Alternate description of Method 2: Removing Geometric Coma*

There is an alternate geometric description of the coma subtraction in Method 2 that does not use the difference wavefront, but yields the same solution. We utilize the two separate measurements, and the fact that the tilt vectors in each must be proportional to the geometric coma, *with the same proportionality constant.*

Figure 14 shows a graphical representation of this method. Using the coma terms from two measurements performed at different beam displacements $\mathbf{C}_1$ and $\mathbf{C}_2$, *vectors* proportional to the tilts $\mathbf{T}_1$ and $\mathbf{T}_2$ are subtracted to reach the best agreement. The distance between the two points is minimized (they may not match exactly) at the location of the inherent coma **C'** we are trying to find. Following the least-squares method we define an error function $E^2(b)$ that here represents a distance in the coefficient *vector* space shown in Fig. 14.

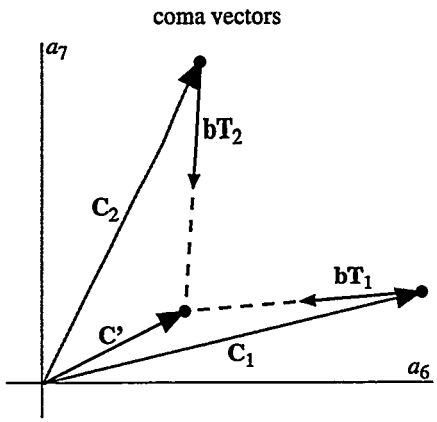

Figure 14. A geometrically alternate, yet mathematically identical description of the systematic coma removal. Here the measured coma, $\mathbf{C}_1$ and $\mathbf{C}_2$, contain both the inherent coma **C'** and the systematic coma components that are parallel to the measured tilts $\mathbf{T}_1$ and $\mathbf{T}_2$. The constant of proportionality b depends only on the NA and is the same for both. Finding the b that provides the best agreement between the inherent coma of the two separate measurements yields **C'**.

$$E^2(b) = \left\|(\mathbf{C}_1 - b\mathbf{T}_1) - (\mathbf{C}_2 - b\mathbf{T}_2)\right\|^2 = \left\|\mathbf{C}_\Delta\right\|^2 + b^2\left\|\mathbf{T}_\Delta\right\|^2 - 2b(\mathbf{T}_\Delta \cdot \mathbf{C}_\Delta). \tag{75}$$

This expression is identical to Equation (68), and thus its solution will be the same.

5.5 Summary

Measured Geometric Coma. $|\mathbf{C}| \approx 1/6\ \mathrm{NA}^2\ |\mathbf{T}| \Rightarrow$ At 0.08 NA, $|\mathbf{C}|/|\mathbf{T}| = 1/6\ 0.08^2 =$ 0.0011 waves per wave of tilt = 5.5×10^{-4} waves per fringe. $|\mathbf{C}| = 0.37$ nm @ 50 fringes. At 0.1 NA, $|\mathbf{C}|/|\mathbf{T}| = 1/6\ 0.1^2 = 0.0017$ waves per wave of tilt = 8.3×10^{-4} waves per fringe. $|\mathbf{C}| = 0.56$ nm @ 50 fringes.

5.6 SYSTEMATIC ERROR FROM DETECTOR MISALIGNMENT

It is reasonable to assume that the planar detector used in PS/PDI interferometry is not perfectly aligned, with its surface-normal parallel to the central ray of the optical system. Such misalignment, represented as a small inclination of the detector plane, introduces a systematic astigmatic error. The magnitude of this error depends on the beam separation and may be comparable to the target accuracy. The sensitivity of a given configuration to detector misalignment is presented at the conclusion of this section.

Following Section 6.5 on the geometrical coma systematic error, the effect of the detector misalignment on the observed interference pattern may be derived in terms of its effect on the path-length difference between the test and reference beams, observed in a coordinate system appropriate for the detector.

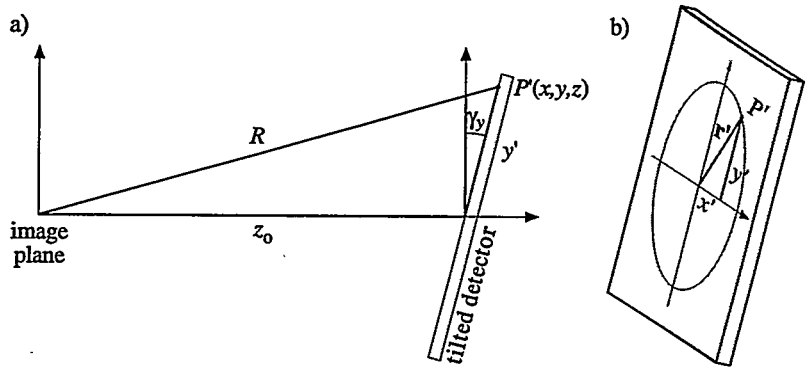

Figure 15. Definition of the coordinate systems used in the description of the detector misalignment systematic error.

Begin with Equation (51) for the path length difference, using z_o as the distance from the image-plane to the detector along the z-axis, as shown in Fig. 15. In terms of the dimensionless coordinates, the path length difference ΔR_o is written in the case of perfect alignment

$$\Delta R_o = z_o \delta t\left(1-\tfrac{1}{2}t^2\rho^2\right)\rho\cos\phi\,, \tag{76}$$

where, without loss of generality, the x-axis is defined along the displacement s of the test and reference beams. As before, t is the tangent of the NA angle, δ is the dimensionless angle related to the beam separation, and ρ is a dimensionless radial coordinate in the detector system. Maintaining the cylindrical coordinate system, and reintroducing $r = \rho t z_o$ as the *regular, Laboratory* radial coordinate,

$$\Delta R_o = \frac{s}{z_o}\left(1-\frac{r^2}{2z_o^2}\right)r\cos\phi\,. \tag{77}$$

Figure 15 shows how the coordinate systems are defined. r' represents the radial coordinate in the detector plane, while r is the real-space radial coordinate. With a non-zero detector tilt angle γ, there are small changes in z, x, and y across the detector. Define the vectors $\mathbf{r'} \equiv (x', y')$ in the detector plane, and $\mathbf{r} \equiv (x, y)$ in the Laboratory System, and, as before, the polar *angular vector* $\boldsymbol{\gamma} \equiv (\gamma_x, \gamma_y)$. Based on the tilt angle $\boldsymbol{\gamma}$, misalignment of the detector introduces a first-order change in z and a second-order change in the lateral coordinates. Assuming small misalignments, only terms up to first order in $\boldsymbol{\gamma}$ will be kept in the following discussion.

$$z \approx z_o + \gamma_x x' + \gamma_y y' = z_o + \boldsymbol{\gamma}\cdot\mathbf{r'} = z_o\left(1+\frac{\boldsymbol{\gamma}\cdot\mathbf{r'}}{z_o}\right). \tag{78}$$

The new path length difference becomes

$$\Delta R = \frac{s}{z}\left(1-\frac{r^2}{2z^2}\right)r\cos\phi\,. \tag{79}$$

Using the first-order expansion of z in $\boldsymbol{\gamma}$ from Eq. (78), Eq. (79) gives

$$\Delta R \approx \frac{1}{z_o}\left(1-\frac{\boldsymbol{\gamma}\cdot\mathbf{r'}}{z_o}\right)\left[1-\frac{r^2}{2z_o^2}\left(1-\frac{2\boldsymbol{\gamma}\cdot\mathbf{r'}}{z_o}\right)\right]sr\cos\phi\,. \tag{80}$$

Keeping only the most significant terms, Eq. (80) becomes

$$\Delta R \approx \Delta R_o - \frac{\boldsymbol{\gamma}\cdot\mathbf{r}'}{z_o^2} sr\cos\phi\,. \tag{81}$$

Putting this back in terms of the dimensionless coordinates (ρ, ϕ, *z*),

$$\Delta R \approx \Delta R_o - t^2 s(\boldsymbol{\gamma}\cdot\boldsymbol{\rho})\rho\cos\phi\,. \tag{82}$$

To simplify this expression, redefine how the detector tilt is described: the detector is inclined by an angle γ, in the azimuthal direction ϕ_γ. Then

$$\boldsymbol{\gamma}\cdot\boldsymbol{\rho} = \gamma\rho\cos\left(\phi-\phi_\gamma\right), \tag{83}$$

and Eq. (82) becomes

$$\Delta R \approx \Delta R_o - s\gamma t^2\rho^2\cos\left(\phi-\phi_\gamma\right)\cos\phi = \Delta R_o - \tfrac{1}{2}s\gamma t^2\rho^2\left[\cos\left(2\phi-\phi_\gamma\right)+\cos\phi_\gamma\right]. \tag{84}$$

This has the effect of adding a small astigmatism to the measurements. Isolating the difference from ΔR_o leaves

$$\Delta R' \approx -\tfrac{1}{2}s\gamma t^2\rho^2\left[\cos\left(2\phi-\phi_\gamma\right)+\cos\phi_\gamma\right]. \tag{85}$$

The presence of the constant cos ϕ_γ term adds defocus and makes the magnitude of this effect different when the tilt direction is parallel or perpendicular to the beam separation direction. A detector tilt in the s-direction ($x \parallel s$) produces a "cylindrical" path length difference of

$$x\text{-tilt:}\quad \Delta R'_x \approx -\tfrac{1}{2}s\gamma t^2\rho^2(\cos 2\phi+1)\quad . \tag{86}$$

For a tilt in the *y*-direction ($y \perp s$). the path-length change is astigmatic.

$$y\text{-tilt:}\quad \Delta R'_y \approx -\tfrac{1}{2}s\gamma t^2\rho^2\sin 2\phi\quad . \tag{87}$$

The term in Eq. (86) behaves as a small defocus, arising from the fact that one of the beams is off-axis.

5.6.1 *Numbers*

The peak-to-valley magnitude of the astigmatism described by Eq. (87) is

$$\text{peak-to-valley:}\quad \left|\Delta R'_y\right| \approx s\gamma t^2 \approx s\gamma NA^2\,. \tag{88}$$

The approximation holds for small NA. Equation (88) is plotted in Fig. 16 as a function of NA for beam separations in the range relevant to EUV, visible, and 193 nm system measurements. For convenience, we can re-write Eq. (88) putting γ in degrees rather than radians. The peak-to-valley astigmatism magnitude per degree of detector tilt is

$$\text{peak-to-valley:}\quad \left|\Delta R'_y\right| \approx 0.0175\, s\, NA^2 \approx 1.1\times10^{-4} s \;@\; NA = 0.08\,. \tag{89}$$

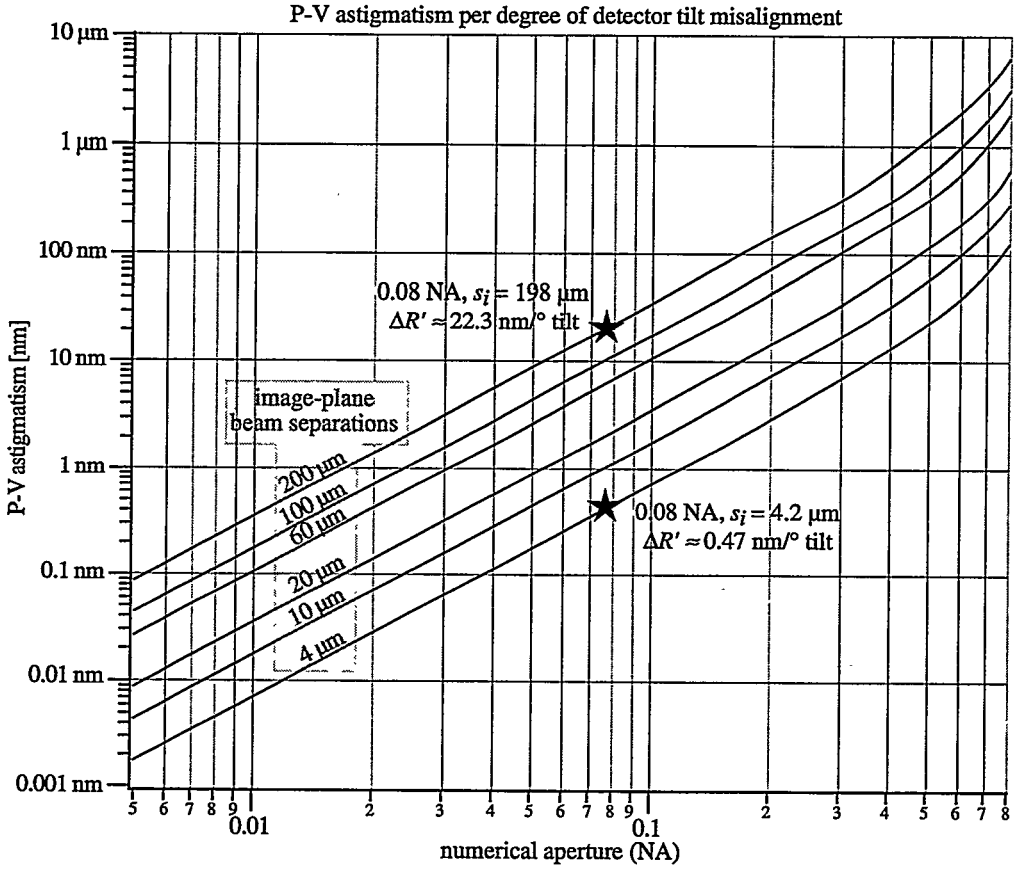

Figure 16. Detector misalignment (tilt) introduces a path-length difference between the test and reference beams causing a systematic astigmatic error dependent on the beam separation and the measurement NA. The gray stars indicate relevant values for EUV and visible-light PS/PDI interferometry at 0.08 NA.

5.6 Summary

Detector Misalignment. P-V astigmatism $A = s\gamma NA^2 \Rightarrow$ ~0.47 nm/° tilt. Also, $A/\gamma N_{fringe} = \lambda$ NA/2 = 0.54 nm/° tilt/fringe. The measured Zernike coefficient of astigmatism is half of this, or 0.27 nm/° tilt/fringe.

5.7 GRATING PLACEMENT CONSIDERATION: SHEAR

As discussed in Section 4.4, the PS/PDI shares many similarities to a conventional lateral shearing interferometer (LSI) in that both systems introduce a relative beam *shear*, or displacement, to generate the interference pattern. In principle, the various configurations of the LSI interfere the test beam with a sheared copy (or copies) of itself. The PS/PDI, on the other hand, produces a spherical reference wavefront by spatially filtering one copy of the test beam in the image-plane where the beams are separated. When the measurement involves spherically diverging beams and no re-imaging optics, in both configurations the central rays of the two beams are directed at slightly different angles. The beam shear in the PS/PDI is determined by the grating pitch and the illumination wavelength. A comparison of the importance of shear

in the two interferometers is shown in Fig. 17.

By rule, the PS/PDI reference pinhole should be chosen small enough that the reference wavefront *significantly overfills* the measurement NA. However, since pinhole-diffracted reference wavefronts are typically of suitably high quality only within a cone of finite angle, selection of the grating position and pitch should be made with attention to the beam shear angle. For a given optical system and wavelength, the number of fringes in the interferogram depends only on the image-plane separation of the test and reference beams (Section 5.3). There are, however, infinite combinations of grating pitch and position that yield the same separation.

Here, the discussion is limited to the PS/PDI configuration with the grating placed between the test optic and the image-plane. Similar analysis for other PS/PDI configurations follow a nearly identical form: where the grating is placed before the test optic, the shear angle is scaled by the system magnification.

From the grating equation, the shear angle θ is equal to λ/d. For a grating of pitch d and distance from the image-plane z the image- or object-plane separation of beam is

$$\theta z \approx \frac{\lambda z}{d} \approx s\,. \tag{90}$$

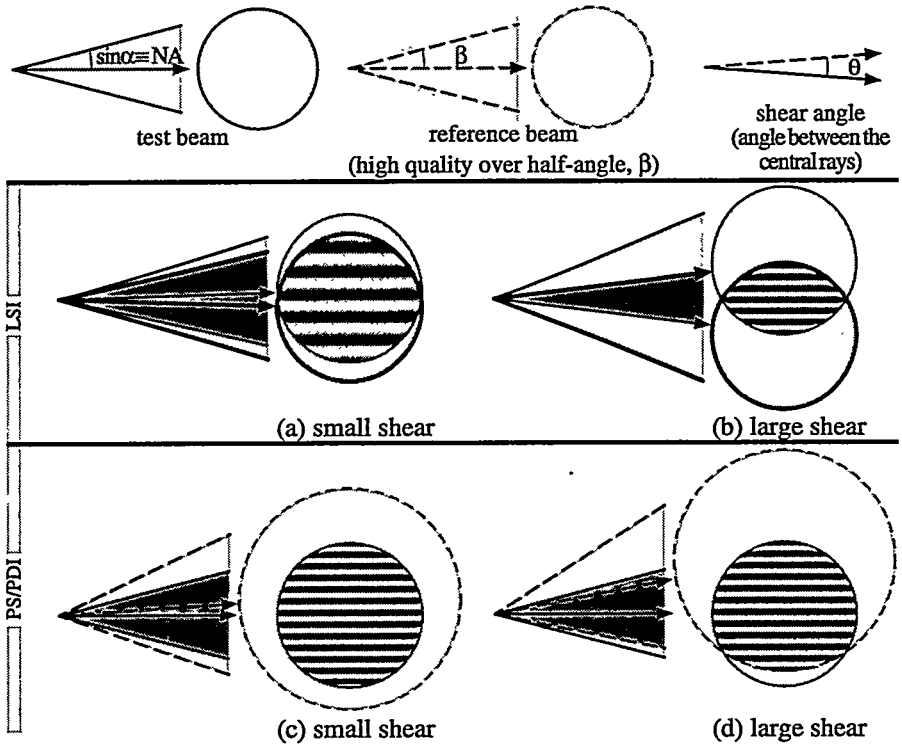

Figure 17. The importance of beam shear considerations is shown in this figure. Shear is here defined as the angle between the central rays of the test and reference beams. The test beam is represented with solid lines, and the reference beam with dashed lines, as shown in the top row. In the LSI (a) and (b), the test beam interferes with a sheared copy of itself, and fringes are produced in the overlap region. When the shear is large (b), only a fraction of the available area is investigated. In the PS/PDI the spatially-filtered reference beam should have an NA larger than the test optic (c). However, if the shear angle is large (d), then to guarantee that the reference beam will overlap the test beam over the measurement NA, the requirement on the diffraction angle of the reference beam becomes more severe.

Assume for a given application that the reference wavefront is of arbitrarily high quality only over a cone defined from the central ray, out to a half-angle β. Clearly, a minimum requirement for measurement is that $\beta > \alpha$, the maximum half-angle within the NA of measurement. When the shear angle θ is significant relative to α, and the test and reference beams are displaced, the new requirement on β becomes

$$\beta > \alpha + \theta . \tag{91}$$

Producing a high-quality reference wavefront is a matter of foremost importance and a significant challenge to point-diffraction interferometry. Any method of relaxing the requirements on the magnitude of β gives more freedom to other experimental parameters. One direct means of reducing β is to keep the shear angle θ as small as possible. For a given image- or object-plane beam separation s, θ may be reduced by moving the grating away from the image-plane (or away from the object plane in other PS/PDI configurations). Choosing the optimum grating position requires balances the often opposing concerns of the grating's pitch and the illuminated area. Fabrication issues may constrain the maximum size of the grating, but gratings of larger pitch (coarser) may often be made to higher quality.

5.7 Summary

Shear Angle. $\theta = \lambda/d$ = shear angle. d = grating pitch. β = half-angle over which reference wavefront is of arbitrarily high quality. α = NA. Minimum requirement: $\beta > \theta + \alpha$.

5.8 GRATING FABRICATION ERRORS

Aberrations and local imperfections in the grating-beamsplitter can contribute directly measurement errors. This section describes the most significant grating error contributions, and recommends various methods of overcoming them. The most important recommendation is that when the quality of the grating cannot be guaranteed to beyond the level of measurement accuracy desired, then one of the first-diffracted order beams should be filtered to become the reference beam.

It is helpful to view the grating, which serves a dual role as beamsplitter and phase-shifting element, as a binary transmission hologram approximating the coherent interference of multiple plane waves separated by small angles. Imperfections in the grating pattern can be described by aberrations in the interfering beams. The *inversion* of this description (by Babinet's Principle) is a single illuminating beam diffracted by the imperfect grating into multiple, coherent, aberrated beams.

For the following discussion it is useful to treat different types of grating imperfections separately. Figure 18(b) shows several types of grating defects. Pattern placement errors, in which the unbroken opaque lines are not accurately drawn, are referred to as *grating aberrations*. The other kinds of defects in which the opaque lines are missing, transparent regions are obstructed, or the thickness of the supporting substrate

is non-uniform are addressed separately from the grating aberrations.

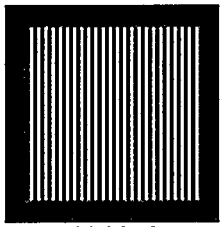

(a) ideal binary grating

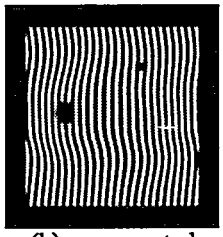

(b) exaggerated *non*-ideal grating

Figure 18. Imperfections in the PS/PDI grating beamsplitter can introduce aberrations into the test and reference beams. (a) shows an ideal binary transmission grating of equal line and space ratio. The grating in (b) contains several aberrations types discussed in this section: low-spatial frequency pattern errors, dust or substrate errors, and pattern defects. These types of aberrations can affect the test and reference beam in different ways.

5.8.1 *Grating Aberrations*

It is important to note that the phase of the zeroth-order diffracted beam is *not affected* by the grating pattern itself. Light propagating into the zeroth-order adds *in-phase*, independent of the positions of the rulings. This is because the grating pattern introduces no path-length change into the various parts of the zeroth-order beam. On the other hand, the diffracted beams are *defined by* the grating positions: the wavefront phase of these diffracted beams is subject directly to the grating aberrations. The following discussion presents a simple analogy that is used to demonstrate this point.

In the absence of a grating, the superposition of multiple coherent beams would form a stationary intensity pattern in the grating plane. By Babinet's Principle (Babinet 1837), the single-beam illumination of a grating that approximates this same intensity pattern generates the diffraction of multiple beams similar to the former configuration.

To illustrate this point, consider a grating of pitch d with rulings aligned perpendicular to the x-axis. Define the spatial carrier frequency of the grating $\boldsymbol{\kappa}$

$$\boldsymbol{\kappa} = \frac{2\pi}{d}\hat{\mathbf{x}}. \tag{92}$$

We may represent the grating transmission function $T(\mathbf{r})$ as a *square wave* defined by an arbitrary, spatially varying grating phase $\Phi(\mathbf{r})$. Separating the grating phase into an aberration function $\phi(\mathbf{r})$ and a carrier frequency, we have

$$\Phi(\mathbf{r}) = \phi(\mathbf{r}) + \boldsymbol{\kappa}\cdot\mathbf{r} = \phi(\mathbf{r}) + \kappa x, \tag{93}$$

and

$$T(\mathbf{r}) = \begin{cases} 1, & \cos[\Phi(\mathbf{r})] \geq 0 \\ 0, & \cos[\Phi(\mathbf{r})] < 0 \end{cases}. \tag{94}$$

This description leads naturally to a representation of the grating as the interference of two beams. At this point, we neglect the spherically diverging or converging angle of incidence, and consider the beams as plane waves. (Section 5.9 addresses the systematic error issues related to the planar grating in a

spherical beam.) In this description, assume unit intensity of the beams, neglect variation of the beam intensities, and assume that the test beam is unaberrated. The normalized intensity of the two interfering beams is given by

$$I(\mathbf{r}) = \tfrac{1}{4}\left|1 + e^{i\Phi(\mathbf{r})}\right|^2 = \tfrac{1}{2} + \tfrac{1}{2}\cos\left[\Phi(\mathbf{r})\right]. \tag{95}$$

The square-wave grating transmission function of Eq. (94) is an approximation to this sinusoidal variation. Placing a simple threshold on Eq. (95) completes the analogy to Eq. (94), and justifies the approximation. Since Φ was chosen arbitrarily, then for any grating phase function $\Phi(\mathbf{r})$ the diffracted beams acquire a wavefront aberration $\phi(\mathbf{r})$ and a direction determined by $\boldsymbol{\kappa}$.

Regarding the description of spherical beams, Eq. (95) may be generalized to allow both of the interfering beams to contain an additional phase term representing the path length difference between a spherical surface and the grating plane. This additional phase, defined as $\Gamma(\mathbf{r})$, appears in both beams, and thus the resultant intensity pattern is unaffected. Mathematically,

$$I'(\mathbf{r}) = \tfrac{1}{4}\left|e^{i\Gamma(\mathbf{r})} + e^{i\Phi(\mathbf{r})+i\Gamma(\mathbf{r})}\right| = \tfrac{1}{2} + \tfrac{1}{2}\cos\left[\Phi(\mathbf{r})\right] = I(r). \tag{96}$$

The analogy may be extended to include the higher diffracted orders. Re-creation of a square-wave intensity profile in the grating plane requires an infinite series of interfering beams, each with the same phase aberration, but with a different propagation direction and intensity. These beam directions are given by positive and negative integer multiples of $\boldsymbol{\kappa}$ (. . . -2$\boldsymbol{\kappa}$, -$\boldsymbol{\kappa}$, 0, $\boldsymbol{\kappa}$, 2$\boldsymbol{\kappa}$, . . . $n\boldsymbol{\kappa}$, . . .). The illumination of the square-wave grating with the single test beam generates this same series of diffracted orders. This series may be generalized as a Fourier cosine series.

$$T(\mathbf{r}) = \sum_n a_n \cos\left[\phi(\mathbf{r}) + n\boldsymbol{\kappa}x\right]. \tag{97}$$

5.8.2 *Phase-Shifting*

The origin of the phase-shifting properties of the grating is easily shown from the discussion of the previous section. Here, neglect aberrations and imperfections in the grating, and assume that the grating is defined by a carrier-frequency $\boldsymbol{\kappa}$ and a square-wave transmission function. Once again we equating the coherently-combined intensity of a series of interfering beams with the grating transmission function. As above, taking $\boldsymbol{\kappa}$ to be aligned with the x-axis, the translational invariance of the grating along the y-direction allows the substitution of x for $\mathbf{r}$.

$$I(x) = T(x) = \sum_n a_n \cos(n\boldsymbol{\kappa}x). \tag{98}$$

Physical translation of the grating in the x-direction, perpendicular to the grating rulings, may be expressed as

$$I(x-x_o)=T(x-x_o)=\sum_n a_n\cos\left[n\kappa(x-x_o)\right]=\sum_n a_n\cos(n\kappa x-\Delta_n)\ , \tag{99}$$

where we defined the phase step as $\Delta n \equiv n\kappa x_o$. This very important result shows that a physical translation of the grating produces the same effect on the diffracted waves as a constant phase offset between the interfering beams in our model. Furthermore, between any two *adjacent* grating orders ($\Delta n = \pm 1$), for a given grating translation the relative phase shift will be the same. That is, the expression

$$\Delta\phi(n,n-1;x_o)=n\kappa x_o-(n-1)\kappa x_o=\kappa x_o \tag{100}$$

is invariant in n.

Another important, albeit obvious, by-product of this discussion is that the grating translation required to produce a 2π, single-cycle, phase shift between adjacent diffracted beams is simply d. (Recalling the definition of $\kappa \equiv 2\pi/d$, we can see from Eq. (100) that the translation x_o required to produce a 2π phase change is in fact d.) Since the ideal grating in this treatment is periodic in x with period d, we should expect that translation by d returns the system to its original state.

5.8.3 *Local Imperfections and Substrate Errors*

Besides the low-spatial frequency pattern errors which introduce phase aberrations into the diffracted beams, there are other, higher-spatial frequency errors of concern. An opaque dust particle or a defect within the illuminated area of the grating may appear as a dim region, or a region of low (or zero) fringe contrast in the data. Since the plane of the grating is not typically imaged onto the detector plane, diffraction broadens the features of these high-spatial frequency aberrations. As the grating is translated over several fringe cycles, the motion of these aberrations will distinguish them from the stationary defects in the optics or elsewhere. By performing careful measurement, it may be possible to overcome localized grating defects by using other *clean* regions of the grating.

One form of grating fabrication error is perhaps the most troublesome. If the grating is patterned on a membrane or substrate, then substrate thickness variations can introduce phase errors that could be very difficult errors to overcome. In that case, the quality of the test beam is directly compromised. Once again, careful measurements performed using different regions of a large grating may reveal the presence of such systematic errors.

5.8.4 *Recommendations*

The above discussion leads to a recommendation that may appear counter-intuitive. It has been shown that aside-from local imperfections and substrate errors, grating pattern aberrations create phase errors only in the diffracted beams. By allowing the zeroth-order to become the test beam, and by spatially filtering one of the diffracted orders to become the reference beam, these grating aberrations may be over-

come. That is, where concerns about the grating quality exist, the first-order reference configuration is recommended over the zeroth-order reference configuration. This recommendation, however, runs contrary to the assertion that the zeroth-order reference configuration should be used to achieve high fringe-contrast.

5.8 Summary

Grating Fabrication Errors. Recommendation: use the *first-order reference* configuration whenever grating fabrication error magnitudes are unknown, or are known to be comparable with the desired accuracy.

5.9 GRATING COMA

Another potentially significant systematic error comes from the use of a planar grating beamsplitter in a spherically diverging or converging beam. Since the angles of incidence vary across the illuminated region of the grating, a small phase error is introduced into the diffracted beams. In a geometrical description, the grating pitch appears reduced to the off-axis rays perpendicular to the grating rulings. This leads to a variation in the diffraction angle within the cone of the beam.

The *grating coma* introduced here may be filtered, and therefore eliminated, when the interferometer is used in the first-order reference configuration — the grating aberrations are manifest only in the non-zero diffracted orders (Section 5.8). Therefore with appropriate filtering, the relevance of the grating coma may be limited to the zeroth-order reference configuration only.

The mathematical formulation presented here follows from the discussion of grating aberrations in Section 5.8. It is important here to consider the spherical divergence of the illuminating beam. As before, we create an analogy between the grating transmission, and the intensity pattern produced by a pair of coherently interfering beams in the grating plane. Starting with a single, illuminating beam, we solve for the phase aberrations of a *diffracted beam* required to produce the desired pattern. Limiting our discussion to the interference of only two beams simplifies the problem considerably. To that end, consider only the fundamental sinusoidal-transmission of an ideal grating of pitch d. The descriptions for *converging* and *diverging* beams, with a radius of curvature R are identical in form.

Consider the illuminating beam to be an ideal spherical wave diverging from a point source located a distance z from the grating plane. The path length of a ray traveling from the source to a point x is R, as shown in Fig. 3. θ and ϕ are defined as the spherical polar and azimuthal angles, and the x-axis is defined perpendicular to the direction of the grating lines.

In the plane of the grating, the radial coordinate,

$$r = z\tan\theta\,, \tag{101}$$

and x in the new coordinate system is

$$x = r\cos\phi = z\tan\theta\cos\phi\,. \tag{102}$$

The path length R from the source point to the grating is

$$R = z + r\sin\theta = z + z\tan\phi\sin\theta = z(1+\tan\theta\sin\theta)\,. \tag{103}$$

Our immediate goal is to discover the phase of a beam that interferes with the illuminating beam to produce the grating pattern in intensity. As before, we assume the two interfering beams are of uniform intensity across the illuminated area. We may express the grating transmission function in the new coordinate system, using κ defined as before: $\kappa \equiv 2\pi/d$.

$$T(x) = \tfrac{1}{2} + \tfrac{1}{2}\cos(\kappa x) = \tfrac{1}{2} + \tfrac{1}{2}\cos(\kappa z\tan\theta\cos\phi)\,. \tag{104}$$

The normalized intensity pattern produced by the interference of two beams is

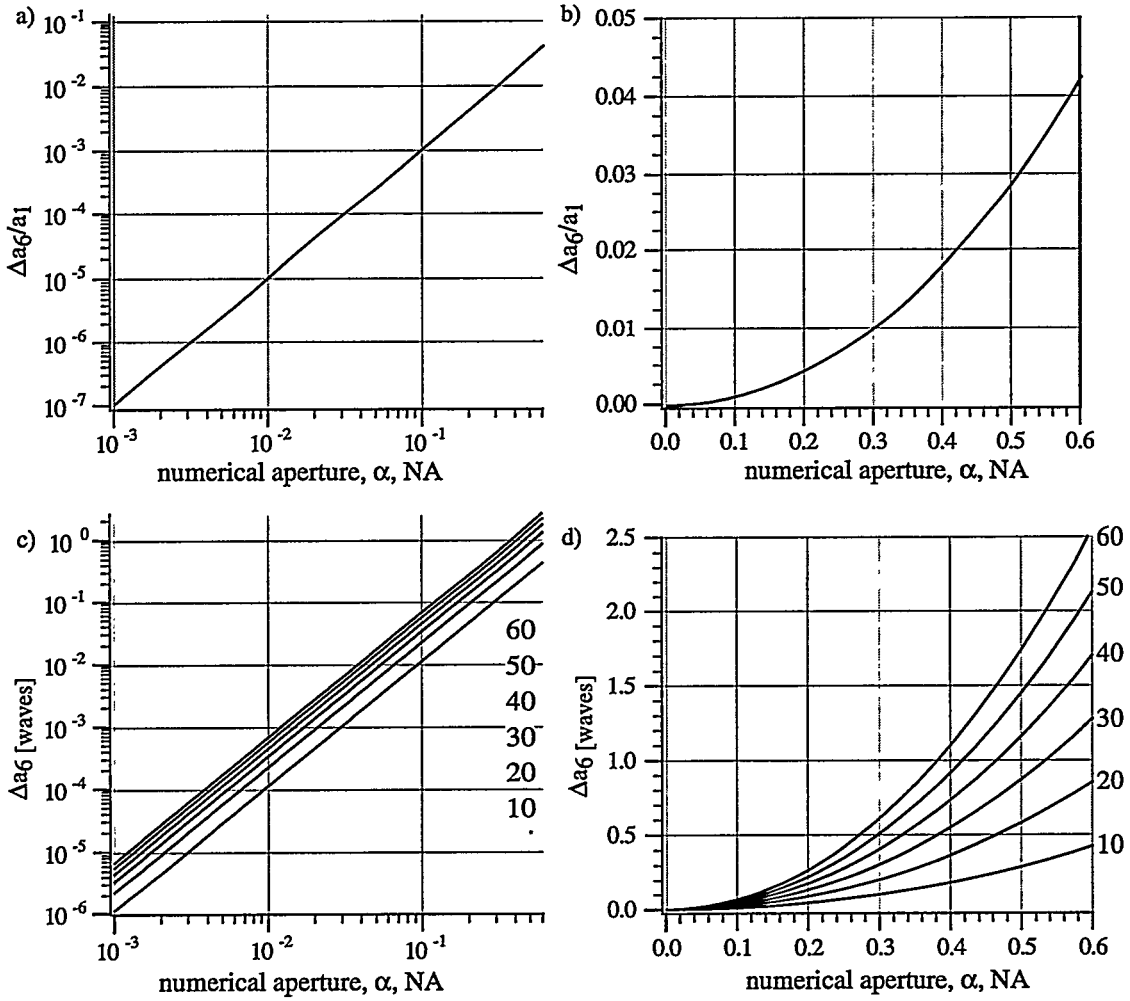

Figure 19. The amount of systematic coma error introduced by the planar grating in a spherical beam depends on the system NA in the vicinity of the grating, and on the amount of tilt or equivalently the number of fringes in the measurement. The top row shows the ratio of the Zernike coma coefficient to the tilt coefficient plotted in log-log and linear scales. The lower row calculates the amount of coma for a certain number of interferogram fringes within the measurement NA. The same information is plotted in log-log and linear scale. The grating angle is arbitrary and therefore this discussion is easily extended to the a_7 coma and the a_2 tilt components.

$$I(\mathbf{r}) = \tfrac{1}{4}\left|e^{ikR} + e^{i\Phi}\right|^2 = \tfrac{1}{2} + \tfrac{1}{2}\cos(\Phi - kR). \tag{105}$$

Comparing Eqns. (104) and (105) allows us to solve for the phase function Φ.

$$\Phi = kR + \kappa x = kR + \kappa z \tan\theta\cos\phi. \tag{106}$$

Here the kR term is not expanded in order to keep the form of the diverging (or converging) beam in the expression of interfering beam. The remaining term has only x dependence because of the cosϕ component. A series expansion in θ reveals separate terms that represent the spherical component, the diffraction angle of the second beam, and higher-order phase aberrations.

$$\Phi = kR + \kappa z\cos\phi\left[\theta + \tfrac{1}{3}\theta^3 + \tfrac{2}{15}\theta^5 + \cdots\right] = kR + (\kappa z\cos\phi)\theta + \tfrac{1}{3}(\kappa z\cos\phi)\theta^3 + \tfrac{2}{15}(\kappa z\cos\phi)\theta^5 + \cdots \tag{107}$$

$$\Phi = (\text{spherical part}) + (\text{tilt}) + (\text{higher-order aberrations}). \tag{108}$$

As a final step, it is convenient to represent the phase terms in the *Normalized Beam Coordinate System* where the polar angle θ is normalized to the NA angle α: $\rho \equiv \theta/\alpha$. Here, ρ is a dimensionless *angular radius* variable, that allows us to make the transition from a *Beam Coordinate System*, to a representation on a unit circle, over which the Zernike Polynomials are orthogonal. Here it is important to remember that α is the *local NA* angle describing the optical system in the vicinity of the grating. Clearly, if the beam is planar (collimated) as it reaches the grating, then $\alpha = 0$, and there is no systematic effect introduced by the grating, regardless of the image-side NA.

$$\Phi = kR + (\alpha\kappa z)\rho\cos\phi + \left(\tfrac{1}{3}\alpha^3\kappa z\right)\rho^3\cos\phi + \left(\tfrac{2}{15}\alpha^5\kappa z\right)\rho^5\cos\phi + \cdots \tag{109}$$

We can write this explicitly in terms of the Zernike polynomials, as described in Chapter 14, using the shorthand notation for the Zernike polynomials $Z_i \equiv Z_i(\rho,\phi)$. After tilt, the third and fifth-order x-direction coma terms are

$$Z_1 = \rho\cos\phi, \tag{110a}$$

$$Z_6 = \left(3\rho^3 - 2\rho\right)\cos\phi, \tag{110b}$$

$$Z_{13} = \left(10\rho^5 - 12\rho^3 + 3\rho\right)\cos\phi. \tag{110c}$$

The isolated cubic, and fifth-order terms that appear in Eq. (109) can be re-written using

$$\rho^3\cos\phi = \tfrac{1}{3}Z_6 + \tfrac{2}{3}Z_1, \tag{111a}$$

and

$$\rho^5\cos\phi = \tfrac{1}{10}Z_{13} + \tfrac{2}{5}Z_6 + \tfrac{1}{2}Z_1. \tag{111b}$$

Keeping only terms up to fifth-order, we can now rearrange terms to write Eq (109) as

$$\Phi = kR + kz\alpha\left(1 + \tfrac{2}{9}\alpha^2 + \tfrac{1}{15}\alpha^4\right)Z_1 + kz\alpha^3\left(\tfrac{1}{9} + \tfrac{4}{75}\alpha^2\right)Z_6 + \tfrac{2}{75}kz\alpha^5 Z_{13} \tag{112}$$

Aside from the aberrations in the test optics, and other unrelated systematic error sources, this is the measured phase.

The methods for removing the grating coma follow directly from the removal of the systematic coma, described in Section 5.5. If α, the *local NA* in the vicinity of the grating, is well-known then the removal may be straightforward. Note that it may be the case that the *measurement NA*, which includes only the sub-region of the beam involved in the analysis, is smaller than the available NA at the detector. In such cases, the α used in the calculations should be the *measurement* α, representing only the subset of rays that eventually reach the detector and are used in the analysis.

At this point, the direction of the grating rulings can be generalized. The description is simplified by using the representation of Zernike pairs in vector notation, as described in Section 5.5.1. Here, we utilize a tilt vector $\mathbf{T} \equiv (a_1, a_2)$, a coma vector $\mathbf{C} \equiv (a_6, a_7)$, and we introduce a fifth-order coma vector $\mathbf{C}_5 \equiv (a_{13}, a_{14})$. By matching the coefficients in Eq. (112) the magnitude of the grating coma is proportional to the tilt

$$\Delta\mathbf{C} = \frac{\left(1+\frac{12}{25}\alpha^2\right)\alpha^2}{9+2\alpha^2+\frac{3}{5}\alpha^4}\mathbf{T} \approx \frac{1}{9}\alpha^2\mathbf{T} \ . \tag{113}$$

Hence the adjustment to $\mathbf{C}$ required to remove the grating coma is

$$\mathbf{C} = \mathbf{C} - \Delta\mathbf{C} \ . \tag{114}$$

The fifth-order correction $\mathbf{C}_5$ is always more than one order of magnitude smaller than the third-order correction.

$$\Delta\mathbf{C}_5 = \frac{\frac{2}{75}\alpha^4}{1+\frac{2}{9}\alpha^2+\frac{1}{15}\alpha^4}\mathbf{T} \approx \frac{2}{75}\alpha^4\mathbf{T} \ , \tag{115}$$

and the required adjustment is $$\mathbf{C}_5 = \mathbf{C}_5 - \Delta\mathbf{C}_5 \ . \tag{116}$$

Figures 19(a) and (b) shows the magnitude of Δa_6 relative to a_1, calculated for between 10 and 60 fringes. The magnitude in waves is plotted in Figs. 19(c) and (d).

If the measurement NA is not well known, then a method of combining orthogonal measurements, as described in Section 5.5.2, should be employed.

5.9 Summary

Grating Coma. $|\mathbf{C}| \approx 1/9\ \mathrm{NA}^2\ |\mathbf{T}| = 3.6 \times 10^{-4}$ waves per fringe. $|\mathbf{C}| = 0.19$ nm @ 40 fringes.

5.10 SPATIAL FILTERING BY THE IMAGE-PLANE WINDOW

Iy passing the test beam through a finite window in the image plane, the PS/PDI performs an inher-

ent spatial filtering of the light in a way that the PDI does not. The significance of this low-pass filtering depends on the size and shape of the window relative to the size of the focused beam. The relevant length scale, it will be shown, is λ/NA.

A certain amount of filtering is required to ensure that the overlap of the adjacent orders is minimized as the test beam passes through the window. If the system is designed carefully, then with the reference beam centered on the reference pinhole, the test beam passes through the center of the window.

Since the filter sits in the image plane of the test optic, and measurements are performed in the far-field, the window may be regarded simply as a spatial filter in the *Fourier domain* of the beam. This description is represented in Fig. 20. For the test beam, the window acts as a broad, low-pass filter. The pinhole acts as a *very narrow* low-pass filter for the reference beam (ideally, a delta-function). The window, displaced significantly from the central ray of the reference beam, functions as a band-pass filter, transmitting, or *leaking*, higher spatial-frequency components. The fact that these effects are readily observed in the data has led to the development of an alignment system based on a rapid 2-D Fourier-transform of the measured data. These observations are discussed in Section 6.5.)

5.10.1 *A Simple Model for Spatial Filtering*

This section presents a simple mathematical treatment of the window's spatial filtering effect. Based on the fact that the light propagates from the exit pupil of the test system to a focus in the image-plane, and then to the detector in the far-field, we may regard the pinhole and window as spatial filters in the Fourier domain of the beam, as stated above. For spatial filters of moderate dimension, and sufficient distance to the detector, the far-field (Fraunhofer) approximation for the diffraction calculations is suitable (Goodman 1988:61). The near-field term becomes significant only when for the lateral distance r,

$$r \geq \sqrt{\frac{\lambda z}{\pi}}. \tag{117}$$

This is approximately 20 μm at 13.4-nm wavelength and 10-cm distance.

Define G_i as the electric field of the test beam in the exit pupil of the test optic. G_d is the test beam field as it reaches the detector, after having passed through the image plane. Let g be the field in the image-plane, and t be the transmission function of the window; either or both may be complex. Here we

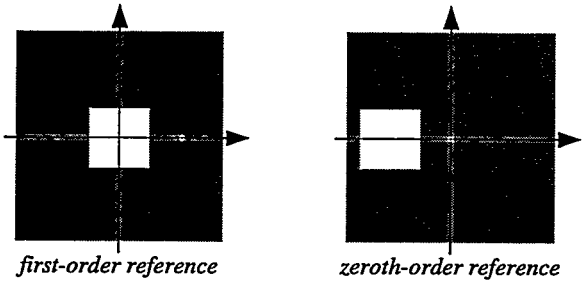

Figure 20. A simple lateral translation of the image-plane spatial filter in the PS/PDI switches between the first-order reference and the zeroth-order reference configurations. The axes here are centered on the test beam focus. The positive and negative first-diffracted-orders fall on opposite sides of the focus. Translating the spatial-filter makes either the zeroth-order beam or one of the first-order beams the reference beam.

will use the symbol $\mathcal{F}\{\ \}$ to denote the Fourier-transform in the following manner:

$$\mathcal{F}\{b(\mathbf{k})\} \equiv \int_A b(\mathbf{k}) e^{i\mathbf{k}\cdot\mathbf{r}} d\mathbf{k} \equiv B(\mathbf{r}) \ . \tag{118}$$

Based on our assumptions for G_i and g,

$$\mathcal{F}\{G_i\} = g, \quad \mathcal{F}\{T\} = t \ . \tag{119}$$

The Convolution Theorem allows us to determine G_d

$$\mathcal{F}^{-1}\{g \cdot t\} = G_i \circ T \equiv G_d \quad . \tag{120}$$

The features of G_i are essentially mapped onto G_d. The effect of the filtering appears in the detected field as a convolution of the propagated test beam and the Fourier-transform of the window transmission function.

The effect of an arbitrary filter may be studied in terms of its transform T. When the window is small, then the central peak of T is angularly broad, and the convolution of G_i with T blurs any sharp features in G_i, decreasing the spatial frequency content of the measurement. Otherwise, when the window is large, the peak of T will be very narrow, and the convolution of G_i with T will leave G_i largely unaffected. T helps us to define the *angular resolution* of a given filter.

Let us consider a square window of width w, and explicitly write the diffraction equation. Some leading constant coefficients are ignored for simplicity.

$$T(\mathbf{k}) = \int_{w/2}^{w/2} t(\mathbf{r})\, e^{i\mathbf{k}\cdot\mathbf{r}} d\mathbf{r} = \int_{w/2}^{w/2} e^{ik_x x} dx \int_{w/2}^{w/2} e^{ik_y y} dy \, . \tag{121}$$

$$T(\mathbf{k}) = w^2 \ \mathrm{sinc}\left(\tfrac{1}{2} w k_x\right) \mathrm{sinc}\left(\tfrac{1}{2} w k_y\right) . \tag{122}$$

T may be expressed in terms of the polar angles in the x- and y-directions $\boldsymbol{\theta} \equiv (\theta_x, \theta_y)$.

$$T(\boldsymbol{\theta}) = w^2 \ \mathrm{sinc}\left(\tfrac{1}{2} w k \theta_x\right) \mathrm{sinc}\left(\tfrac{1}{2} w k \theta_y\right) . \tag{123}$$

The full-width of the central peak of $\mathrm{sinc}(x)$ is approximately π. Thus, the angular width of T is given approximately by

$$\frac{wk\,\Delta\theta}{2} = \pi \ \Rightarrow \ \Delta\theta = \frac{2\pi}{wk} = \frac{\lambda}{w} \, . \tag{124}$$

This width itself has no dependence on NA. However, its significance on the highest measurable spatial frequencies, is given by the ratio of the full angle of the optical system 2α to $\Delta\theta$.

$$\text{highest frequency} \ = \ \frac{2\alpha}{\Delta\theta} = \frac{2\alpha w}{\lambda} = \frac{2w}{\lambda / NA} \ \text{cycles} \, . \tag{125}$$

Features of higher spatial frequency than this will subtend an angle smaller than $\Delta\theta$; the convolution will strongly blur these features. $\Delta\theta$ may be regarded as the *angular resolution* of the PS/PDI in any direction. For the EUV configuration of 13.4-nm wavelength, with 0.08 or 0.1 NA, Fig. 21 shows the highest trans-

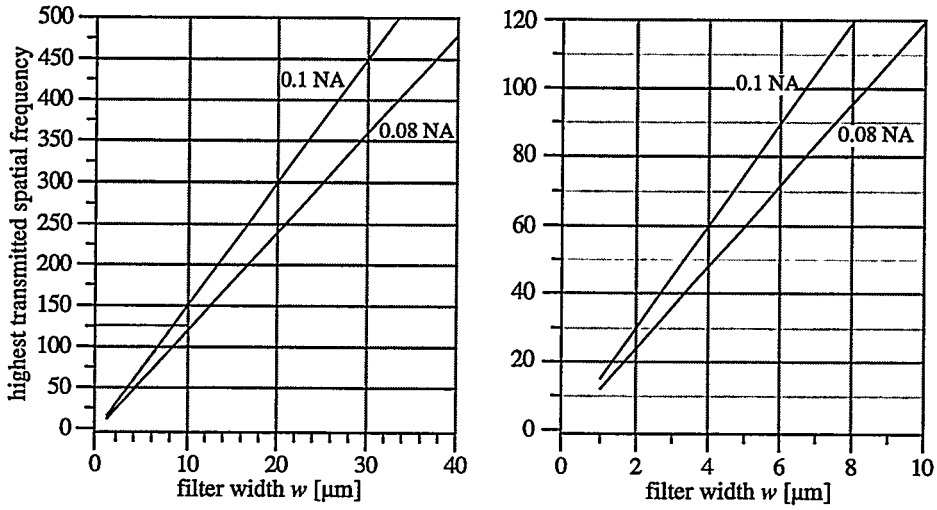

Figure 21. For the EUV configuration of 13.4-nm wavelength, and 0.08 or 0.1 NA, the figure shows the highest transmitted spatial frequency for a given filter width *w*. The graph on the right is a detail of the shaded area on the left. The filter width used in EUV interferometry experiments has been 4.5 μm.

mitted spatial frequency for a range of reasonable window sizes.

5.10.2 *Effect of Spatial Filtering on the Intensity and Phase Measurement*

The above description showed that the image-plane spatial filtering of the window may *blur* sharp (angularly narrow) features in the test wavefront when the window is relatively small. It is important to understand how this blurring may affect the measured intensity *and phase* of the test wavefront. For every specific design of the window's size, shape, and position, this effect will be somewhat different. In this section, an informal, heuristic argument provides a useful tool for demonstrating that when the test optics are of high quality, intensity ripples adjacent to sharp features may not be accompanied by ripples in the phase.

If the centered window transmission function $t(\mathbf{r})$ is strictly real and has polar symmetry, then its Fourier-transform $T(\mathbf{k})$ is also strictly real. The following equation demonstrates this point for an arbitrary real function $t(\mathbf{r})$.

$$T(\mathbf{k}) = \int_A t(\mathbf{r}) e^{i\mathbf{k}\cdot\mathbf{r}} d\mathbf{r} = \int_{\frac{A}{2}} t(\mathbf{r}) \left(e^{i\mathbf{k}\cdot\mathbf{r}} + e^{-i\mathbf{k}\cdot\mathbf{r}} \right) d\mathbf{r} = 2\int_{\frac{A}{2}} t(\mathbf{r}) \cos(\mathbf{k}\cdot\mathbf{r})\, d\mathbf{r} \in \boldsymbol{R}\,. \tag{126}$$

Depending on the shape of the window, T may have a series of positive and negative lobes. (This is the case for the rectangular window and its accompanying sinc function transform. Furthermore, in an aberration-free optical system, apart from any constant coefficient the test beam G_i is also real. Thus the convolution of the test beam G_i with T (that is, G_d) is real.

Sharp changes in the test beam intensity may occur where there are physical apertures or pupils within the system, or where defects in the optical surfaces create localized dark regions. At the detector, these sharp changes in the intensity may be accompanied by intensity oscillations, due (mathematically) to the convolution of the test beam with the lobes of T. As T is a strictly real function, however, there is be *no variation* in the phase of G_d. Clearly, if the test optic contains features that create rapid *phase* variations across the aperture then there will be accompanying ripples in phase as well.

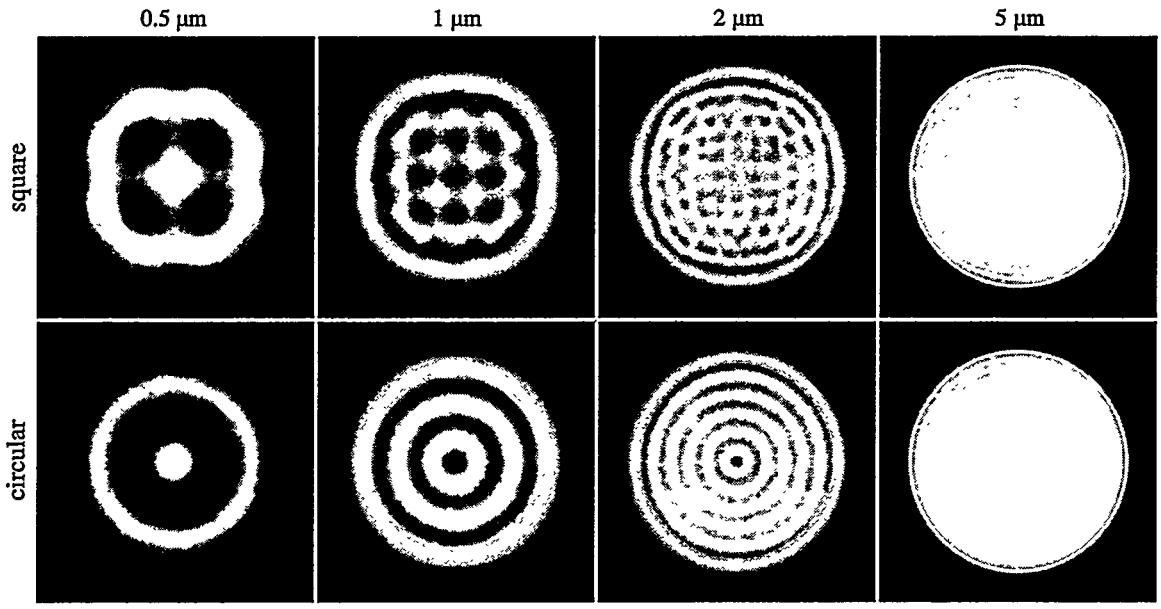

Figure 22. Simulated image-plane spatial filtering of a uniformly illuminated optical system with a circular aperture. The window in the PS/PDI spatial filter transmits the test beam with some spatial filtering. For 13.4 nm wavelength and 0.08 NA, the effect of variously sized square and circular filters is shown. The intensity recorded in the detector plane clearly shows the effects of filtering at 5-μm-width and below..

5.10.3 *Examples*

A straightforward diffraction simulation is performed to illustrate the effect of various amounts of spatial filtering on a PS/PDI interferometer for EUV optical system measurement. Considering an aberration-free optical system operating at 13.4 nm wavelength with 0.08 NA, both circular and square windows of different widths are studied.

Figure 22 shows the (simulated) detected intensities for square (top row) and circular (bottom row) windows 0.5- to 5.0-μm-wide. As described above, the ripples are caused by the convolution of the circular pupil with the Fourier-transform of the window transmission function.

Another subject of interest is the way in which spatial filtering affects small, localized defects in the optic. Figure 23 shows the results of a simulation in which these defects are modeled as dark circles in an otherwise bright region far from the edge of the aperture. The top row shows how these sharply-defined dark regions appear in the exit pupil. At 0.08 NA, the fraction of the whole aperture subtended by these features is shown above each. For reference, these relative sizes are also provided for the two cases of the zoneplate and the Schwarzschild objective experiments. The pupil sizes in these cases are 200 μm and 4 mm respectively. The relevant dimension of the dark features is their angular size with respect to the full aperture of the test optic. The bottom row shows the (simulated) intensity patterns at the detector, scaled for display. The *angular width* of these simulation images is 1/10-th of the aperture.

Notice that below 1/40-th of the aperture width, the features are below the angular resolution of the

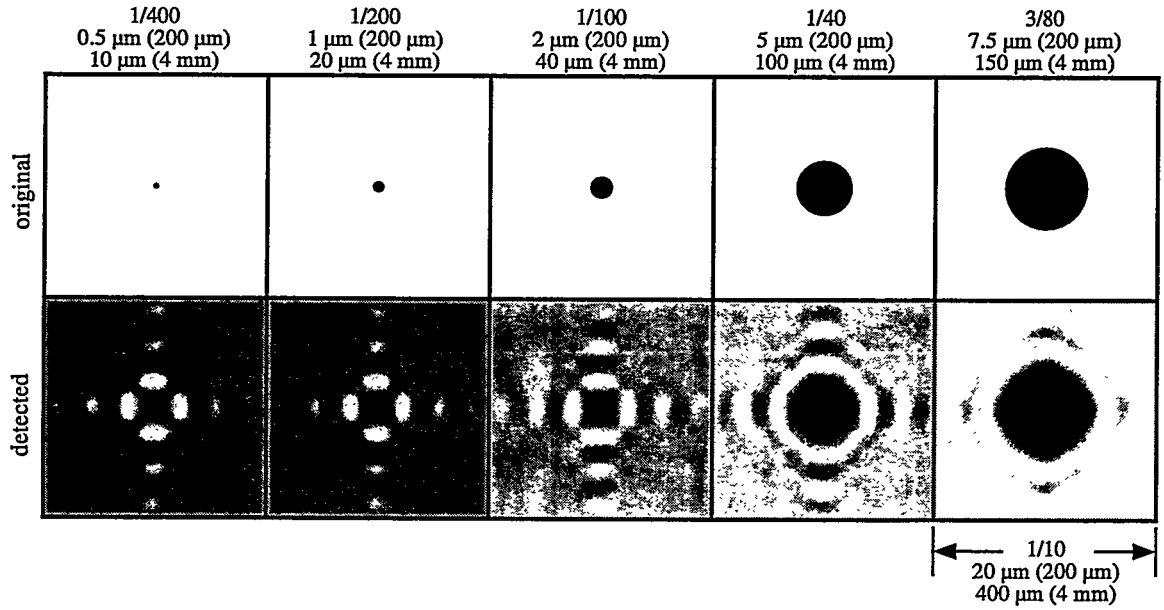

Figure 23.. Spatial filtering of defects in the test optic is simulated in this figure. Here, defects are modeled as dark solid circles in an otherwise bright pupil illumination pattern. Above each simulation, the defect sizes are given as a fraction of the full angular width of the optic, with relevant numbers quoted for the zoneplate experiment and the 10× Schwarzschild objective. Here the defect size is given with the full aperture size shown in parentheses. The filter width is 5 μm. Details of the same angular area of the pupil as recorded in the detector plane are shown in the lower row; the images are scaled for display. Below 1/40-th of the full-angle, the defects behave essentially as delta-function aberrations, unresolved by the spatial filter. Above 1/40-th of the full-angle, the recorded test beam patterns follow the increasing angular size of the defects. The horizontal and vertical pattern in the test beam images is the sinc function generated by the square window shape.

window, and all appear very similar. Because of their relatively small size, the resultant intensity patterns reveal the behavior of T. Mathematically this situation is analogous to the convolution of a delta-function with T. In qualitative agreement with Eq. (125) plotted in Fig. 21, the highest transmitted frequency lies between 1/40 and 1/100 of the aperture width. Features smaller than this size are not *resolved* by the filter.

5.10 Summary

Spatial Filtering. Highest spatial frequency $f = 2w/(\lambda/\mathrm{NA})$ cycles $\Rightarrow$ 12 cycles/μm filter width.

5.11 VARIATIONS OF THE PS/PDI SPATIAL FILTER

The previous section described the way in which the size of the image-plane window affects the highest spatial frequencies resolvable with a given configuration of the PS/PDI. Along the window-pinhole displacement direction, the maximum allowable width of the window is constrained by the image-plane separation of the test and reference beams. However, in the perpendicular direction, there is no constraint on the size of the window: the window may be defined as a long slit, narrow in the displacement direction.

The square window design is easily generalized to the case of a rectangular window of dimensions w_x and w_y. The Fourier-transform of the rectangular window transmission function is

$$T(\boldsymbol{\theta}) = w_x w_y \operatorname{sinc}\left(\tfrac{1}{2} w_x k\theta_x\right) \operatorname{sinc}\left(\tfrac{1}{2} w_y k\theta_y\right). \tag{127}$$

Separating the x- and y- directions allows the definition of two angular convolution half-widths.

$$\Delta\theta_x = \frac{\lambda}{w_x}, \text{ and } \Delta\theta_x = \frac{\lambda}{w_y}. \tag{128}$$

These serve as the x- and y-direction angular resolution of the system. As described in Section 5.10, to maintain a high spatial frequency response, it is desirable to keep $\Delta\theta$ as small as possible. It is not necessary, however, to reduce $\Delta\theta$ significantly beyond the angular resolution of the detector, usually determined by the pixel size and the detector placement.

To minimize overlap of adjacent orders on either side of the test beam, the size of the window is constrained in the displacement direction. The width should not exceed the beam separation distance s. With x aligned parallel to the displacement, this constraint on the maximum size of w_x ($w_x < s$) limits the minimum achievable $\Delta\theta_x$. In the y-direction, since there is no such constraint, $\Delta\theta_y$ may be made as small as desired.

5.11.1 ***Image-Plane Window/Pinhole Filter Designs***

There are a number of available designs for the window and pinhole spatial filters some of which are shown in Fig. 24. These designs, each allows only two beams to pass through at a time, are divided into two sets to distinguish between the *first-order reference* and the *zeroth-order reference* configurations. By definition, the reference beam is whichever beam is filtered by passing through the small reference pinhole.

Several designs enable measurement in two directions without requiring window translation. In two measurements, one grating may be replaced by another, oriented with its rulings rotated by 90 degrees from the first. Sections 5.5 describes the importance of having separate measurements performed with different test and reference beam displacements.

One advantage of the first-order reference configuration not previously addressed is the fixed position of the test beam when separate measurements are preformed. This guarantees that the same field point is being measured. Plus, as described in Sections 5.8 and 5.9, the first-order reference configuration can be used to filter aberrations introduced by a grating beamsplitter. The first-order reference *two-directions* design shown in Fig. 24 was chosen for the experiments in EUV interferometry described in this thesis. The ability to perform a pair of measurements without translating the beam is very important if the beam separation distance is significant with respect to the field-of-view of the test optic.

In the presence of large mid- or high-spatial frequency aberrations, which scatter light away from the central peak in the image-plane, it may be desirable to reduce the amount of beam overlap, by

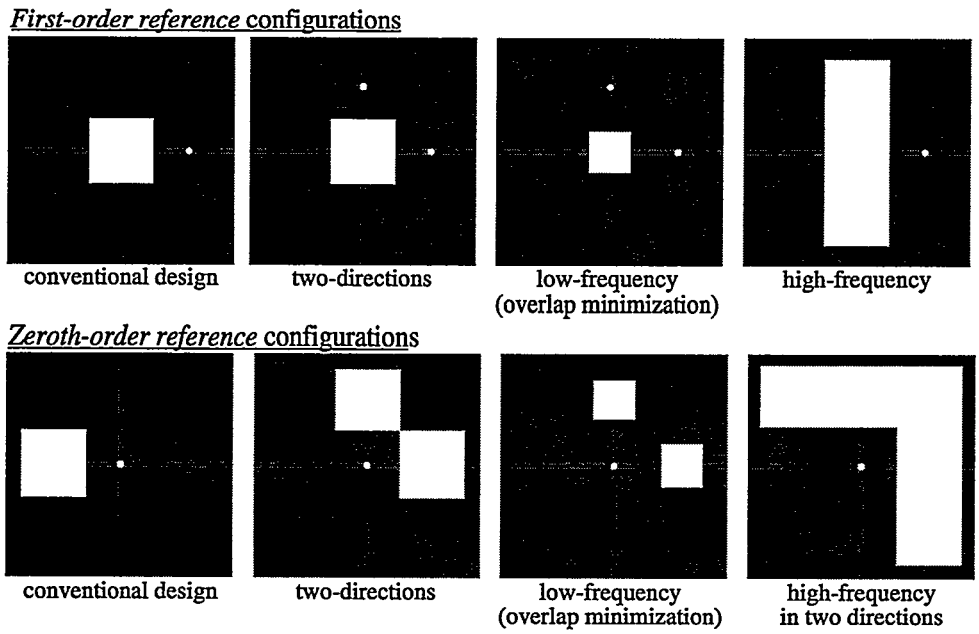

Figure 24. Several designs for the PS/PDI image-plane spatial-filter in both the first-order reference and the zeroth-order reference configurations. Patterns that are symmetric about $\theta = 45°$ are designed to be used with two separate 90° orientations of the beamsplitter. Larger windows transmit a greater range of test beam spatial frequencies, however *leakage* of the reference beam through the windows may introduce measurement uncertainties.

decreasing the size of the window. The so-called *low-frequency* designs shown in Fig. 24 sacrifice spatial resolution to improve data quality.

As described above, there is no constraint on the size of the window perpendicular to the beam separation direction. The *high-frequency* designs shown in Fig. 24 exploit this fact by using a rectangular window, long in one direction, to transmit high-spatial-frequencies. In the first-order reference configuration, however, it may not be possible to have two orientations of measurement with a single high-frequency design. The filter design shown in Fig. 25 achieves the objectives of having two different beam separations *and* high-spatial-frequency response (in one direction) with either the zeroth-order reference or the first-order reference configurations. Two gratings of different pitch but oriented in the same direction may be placed on the same translation stage to simplify the experimental apparatus.

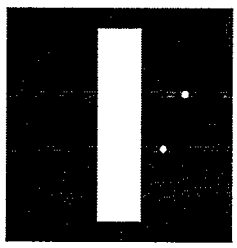

Figure 25. An image-plane spatial filter design that allows measurement with two different beam separations, and provides high-spatial-frequency response in both the zeroth-order and the first-order reference configurations. Two gratings of different pitch, but same orientation are used. The reference pinholes are intentionally displaced to avoid overlap from adjacent diffracted orders.

5.11 Summary

- **Filter Design.** Place pinholes at 90° adjacent to a square window to enable direct measurements of systematic effects. Separately, adjust width perpendicular to beam separation to improve spatial frequency response.

5.12 DISTORTIONS DUE TO THE PLANAR DETECTOR

In the absence of re-imaging optics, the test and reference beams propagate as spherically diverging beams incident on a planar detector. Previous sections (5.5 and 5.6) have described the systematic error contributions of the beam separation at focus, and detector misalignment, based on the geometry of the system. Another source of systematic error is the small geometric distortion arising from the planar geometry of the detector itself, intercepting the spherical beams.

Unlike the previous systematic error components which arise from a path-length difference between the test and reference beams, this effect may be described as a systematic, radial distortion across the measured area. In the angular representation of the *Beam Coordinates*, the planar *Detector Coordinate System* becomes non-linear with a purely radial dependence.

In the *Beam Coordinate System*, the polar angle at a given detector position is θ. r is the radial detector position.

$$r(\theta) = z\tan\theta \;\Leftrightarrow\; \theta(r) = \tan^{-1}\left(\frac{r}{z}\right). \tag{129}$$

The radius r_α in the detector plane corresponds to rays at the maximum angle within the NA of measurement α,

$$r_\alpha = z\tan\alpha. \tag{130}$$

As before, t is the tangent of the NA angle α.

$$\frac{r_\alpha}{z} = \tan\alpha \equiv t. \tag{131}$$

In the *Normalized Detector Coordinates*, the dimensionless radius ρ is defined as

$$\rho \equiv \frac{r}{r_\eta}. \tag{132}$$

Now, θ may be rewritten in terms of these new parameters

$$\theta(r) = \tan^{-1}\left(\frac{r}{z}\right) = \tan^{-1}\left(\frac{r_\alpha}{z}\frac{r}{r_\alpha}\right) = \tan^{-1}(t\rho) = \theta(\rho). \tag{133}$$

When a measurement is made, the wavefront is typically sampled on an array linear in r (or ρ). Equation (133) represents a *correction* which must be performed after measurement, to put the wavefront back into its natural, spherical coordinate system. To make the transition from the normalized *Detector* coordinate system to a normalized *Beam* coordinate system, we divide θ by α as described in Section 5.2. Define γ as the normalized polar angle.

$$\gamma(\rho) = \frac{\theta(\rho)}{\alpha} = \frac{1}{\alpha}\tan^{-1}(t\rho). \tag{135}$$

By their definitions, γ and ρ will be equal only at the central point ($\gamma = \rho = 0$) and at the edge of the mea-

surement NA ($\gamma = \rho = 1$). For the domain of ρ on (0,1), there is some distortion, dependent on the NA. For small measurement NA, γ approximates ρ over the entire range. For large measurement NA, however, the non-linearity causes the two to diverge. This dimensionless distortion may be characterized by introducing a parameter Δ defined as

$$\Delta(\rho) = \gamma(\rho) - \rho = \frac{1}{\alpha}\tan^{-1}(t\rho) - \rho = \frac{1}{\alpha}\tan^{-1}(\tan\alpha\,\rho) - \rho\,. \tag{136}$$

Δ, which is defined in the normalized coordinate system, indicates the difference between the actual polar angle (normalized) and the radial position on the detector. In one interpretation, for a given ρ, Δ represents the amount of *radial shift* that is required to remove the distortion. Since by definition γ and ρ agree at 0 and 1, Δ must be zero at these points. Figure 26 shows $\Delta(\rho)$ plotted for nine different values of NA (recall, $\alpha \equiv$ NA). Table 3 first lists the peak value of the distortion for each NA shown in Fig. 26, and then translates that number into pixels in several experimental measurement domains. With N as the pixel-width of a measured interferogram, the normalized peak distortion Δ_{peak} is multiplied by the radius $N/2$ to calculate the amount of distortion in pixels. Note that at 0.08 NA, the approximate image-side NA of present EUV lithographic optical systems, the peak distortion is 8.22×10^{-4}, less than 0.1%. This indicates the presence of a tiny, 0.33-pixel peak distortion in a typical, 800-pixel-diameter measurement.

5.12 Summary

Planar Detector Distortion. For 800-pixel measurement diameter, and 0.08 NA, peak distortion$\Delta = 8.22 \times 10^{-4} \Rightarrow$ 0.33 pixels.

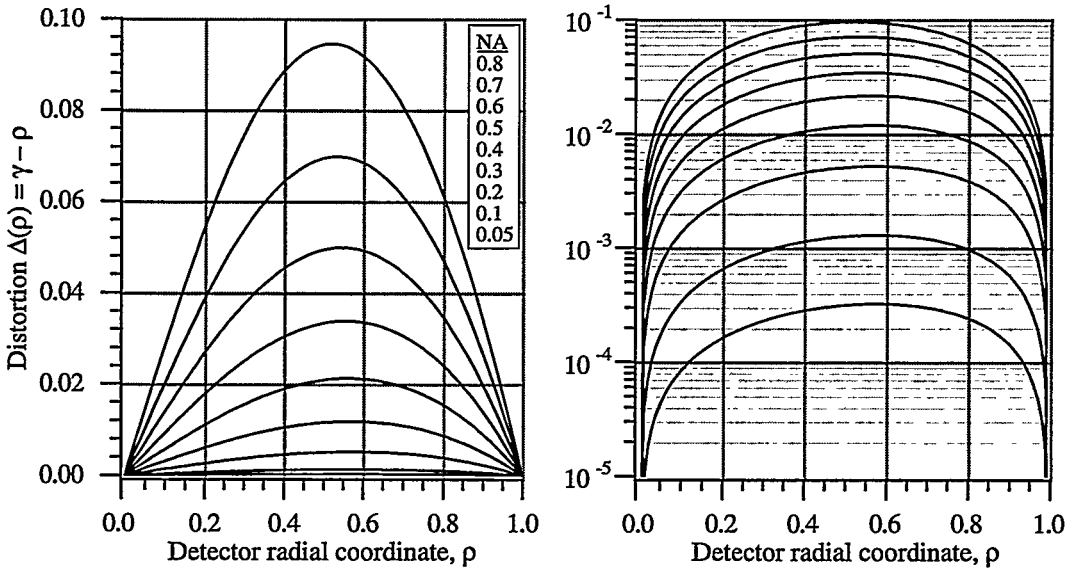

Figure 26. The use of a planar detector to record the spherically diverging interference pattern introduces a radial distortion into the coordinate system of measurement. As the radial position of a point on the detector is translated into an angular position in the beam, the two coordinate systems match only at the center and the domain edge. Within the array, the radial distortion $\Delta(\rho)$ is defined in Eq. (136).

Table 3. Peak measurement distortion (in *pixels*) for a various array sizes, at different NA. $\Delta_{peak}[\text{pixels}] = \Delta_{peak} * (N_{pixels}/2)$.

		Measurement Array Size (pixels)			
NA	Distortion	250	500	750	1000
0.05	3.20×10^{-4}	0.04	0.08	0.12	0.16
0.1	1.29×10^{-3}	0.16	0.32	0.48	0.65
0.2	5.17×10^{-3}	0.65	1.29	1.94	2.59
0.3	1.18×10^{-2}	1.48	2.95	4.43	5.9
0.4	2.12×10^{-2}	2.65	5.3	7.95	10.6
0.5	3.38×10^{-2}	4.23	8.45	12.68	16.9
0.6	4.98×10^{-2}	6.23	12.45	18.68	24.9
0.7	6.98×10^{-2}	8.73	17.45	26.18	34.9
0.8	9.45×10^{-2}	11.81	23.63	35.44	47.25

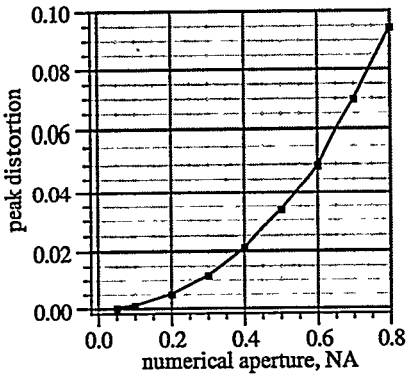

Figure 27. Peak distortion as a function of NA. The distortion is based on a unit-circle coordinate system.

5.13 SUMMARY OF SYSTEMATIC ERRORS AND RECOMMENDATIONS

The following list enumerates the most important results and systematic error effects described in this chapter. The numbers pertain to the at-wavelength measurement of an EUV lithographic optic operating at 13.4-nm wavelength with 0.08 NA.

- **5.3 Beam Separation.** $s/N_{fringe} = \lambda/2t = 0.084$ μm/fringe $\Rightarrow$ $N_{fringe}/s = 2t/\lambda = 12$ fringes/μm.
- **5.4 Bandwidth.** $W_g = 2.22 \times 10^{-7}$ @ 0.1% BW (Gaussian distribution). Fringe amplitude is reduced by 2.22×10^{-7} per wave^2 of aberration at this bandwidth.
- **5.5 Measured Geometric Coma.** $|C| \approx 1/6\ NA^2\ |T|$ $\Rightarrow$ At 0.08 NA, $|C|/|T| = 1/6\ 0.08^2 = 0.0011$ waves per wave of tilt = 5.5×10^{-4} waves per fringe. $|C| = 0.37$ nm @ 50 fringes. At 0.1 NA, $|C|/|T| = 1/6\ 0.1^2 = 0.0017$ waves per wave of tilt = 8.3×10^{-4} waves per fringe. $|C| = 0.56$ nm @ 50 fringes.
- **5.6 Detector Misalignment.** P-V astigmatism $A = s\gamma NA^2$ $\Rightarrow$ ~0.47 nm/° tilt. Also, $A/\gamma N_{fringe} = \lambda\ NA/2 = 0.54$ nm/° tilt/fringe. The measured Zernike coefficient of astigmatism is half of this, or 0.27 nm/° tilt/fringe.
- **5.7 Shear Angle.** $\theta = \lambda/d$ = shear angle. d = grating pitch. β = half-angle over which reference wavefront is of arbitrarily high quality. α = NA. Minimum requirement: $\beta > \theta + \alpha$.
- **5.8 Grating Fabrication Errors.** Recommendation: use the *first-order reference* configuration whenever grating fabrication error magnitudes are unknown, or are known to be comparable with the desired accuracy.
- **5.9 Grating Coma.** $|C| \approx 1/9\ NA^2\ |T| = 3.6 \times 10^{-4}$ waves per fringe. $|C| = 0.19$ nm @ 40 fringes.
- **5.10 Spatial Filtering.** Highest spatial frequency $f = 2w/(\lambda/NA)$ cycles $\Rightarrow$ 12 cycles/μm filter width.
- **5.11 Filter Design.** Place pinholes at 90° adjacent to a square window to enable direct measurements of systematic effects. Separately, adjust width perpendicular to beam separation to improve spatial frequency response.
- **5.12 Planar Detector Distortion.** For 800-pixel measurement diameter, and 0.08 NA, peak distortion $\Delta = 8.22 \times 10^{-4}$ $\Rightarrow$ 0.33 pixels.

6

The EUV PS/PDI — Schwarzschild Objective Testing

6.1 INTRODUCTION

The EUV PS/PDI was developed for at-wavelength measurement of lithographic-quality reflective optical systems operating near 13-nm wavelength and 0.1 NA. This chapter describes procedures and results of a wide range of experiments intended to study the properties of the Schwarzschild objective, the interferometer, and the testing methods themselves.

Using a specially-designed undulator beamline at the Advanced Light Source at Ernest Orlando Lawrence Berkeley National Laboratory, successful characterization of a multilayer-coated 10×-demagnification Schwarzschild objective was conducted between November 1996 and May 1997. These experiments include intensity and wavefront measurements of the three off-axis sub-apertures, investigation of the spatial filtering properties of the pinholes and windows used in the interferometer, studies of the mechanical properties of the interferometer system, and analysis of wavelength-dependent *chromatic aberrations* arising from the resonant-reflective multilayer coatings. Extensive tests were also performed to evaluate the measurement methods and their precision.

EUV PS/PDI interferometry demonstrated angstrom-range wavefront-measuring precision and sub-nanometer measurement accuracy. Repeated measurements conducted over a span of several weeks show a high degree of system stability and repeatability, yet careful investigations of the experimental data have enabled the identification of areas in which further improvements can be made. As of Fall 1997, the EUV PS/PDI experiments are still in progress. These ongoing experiments seek to push the measurement accuracy to new limits.

It was known in advance that the EUV PS/PDI system is best designed for the measurement of nearly diffraction-limited optical systems. When systems contain large wavefront aberrations or mid-spatial-frequency defects, accurate measurement becomes very challenging. From the three off-axis sub-apertures that were measured, a wide range of experimental conditions were encountered. Experiences and insights are discussed in this chapter.

6.2 EXPERIMENTAL COMPONENTS

Many of the components used in the PS/PDI experiments are the same as or are similar to those used in the earlier PDI experiments. A newer, dedicated beamline source is optimized for high flux and moderate bandwidth. Yet the same 8-cm-period undulator and optical table used in the EUV Fresnel zone-plate measurements are still in use. The CCD detector used to record the interference patterns is also of the same specifications as before. In this section, several of the most important components of the experiment are described in detail.

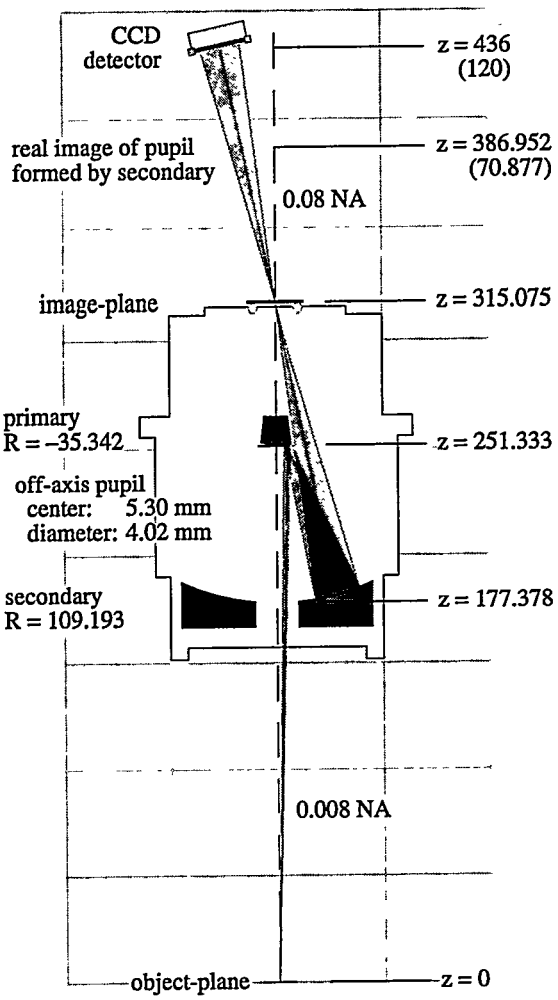

Figure 1. Optical design of the 10× Schwarzschild objective, shown to scale and in the proper orientation: light is incident vertically from the bottom. The primary and secondary mirror substrates are shown in gray. All units are in mm.

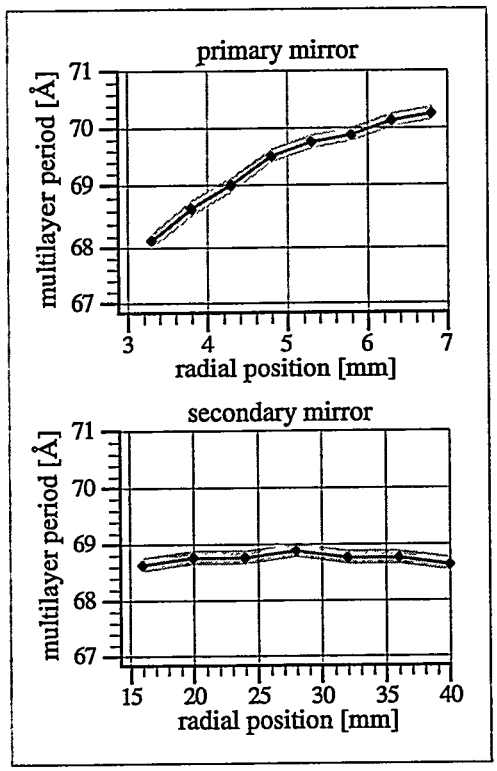

Figure 2. The measured period of the Mo/Si multilayer coatings of the 10× Schwarzschild objective. The primary mirror is designed with a graded coating to compensate for the large range of incident angles. The measurement uncertainty of 0.125 Å is indicated as a gray band about the measured points.

6.2.1 *The 10× Schwarzschild Objective*

The 10× Schwarzschild objective studied in these experiments is one of four Schwarzschild optics created to the same optical design specifications (Tichenor et al. 1993, 1994a; Kubiak et al. 1994, Bjorkholm et al. 1995, Wood et al. 1997). This particular optic is referred to as "10×B" (Berkeley) to distinguish it from two similar optics, 10×I and 10×II, which are used in prototype micro-stepper EUV imaging applications at Sandia National Laboratory, in Livermore, California. The fourth optic is used at Brookhaven National Laboratory by researchers from AT&T Bell Laboratories, also for interferometric applications.

The optical design calls for two nested spherical mirror substrates, Mo/Si multilayer-coated and designed for peak reflectivity and optimized performance at 13.4-nm wavelength. The specifics of the optical design are shown in Fig. 1. The full optic has an annular pupil, yet only one off-axis sub-aperture

is illuminated at a time. The unobstructed object-side and image-side numerical apertures of 0.008 and 0.08, respectively, are defined by a removable aperture stop that rests against the primary mirror. The optic is designed to have a circular, 400-μm-diameter field of view in the image-plane, with a 1-μm depth-of-focus.

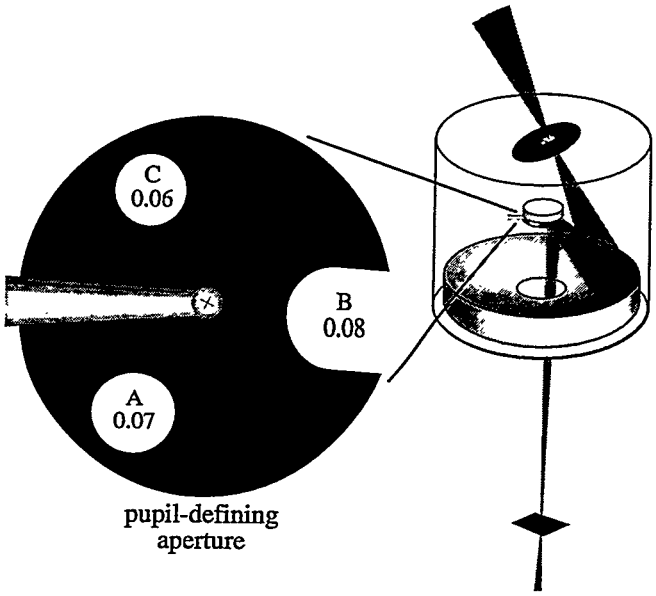

Figure 3. A removable aperture stop, placed against the primary mirror of the 10× Schwarzschild objective, defines three sub-apertures with 0.08, 0.07, and 0.06 NA. The 0.08 NA aperture (broken during fabrication) is positioned above the region predicted to have the highest wavefront quality, based on visible-light interferometry. All three sub-apertures are investigated at EUV wavelengths.

The multilayer-coating deposition and measurement were performed by David Windt. The large range of angles-of-incidence (13.1 to 29.1 mrad, or 0.75° to 1.67°) across the convex primary mirror necessitated the deposition of a graded multilayer substrate to maintain high reflectivity and uniform phase across the radius of the aperture. The experimentally-measured graded thickness variation is shown in Fig. 2.

Visible-light interferometry was used to measure the individual mirror substrates, and a process of *clocking* (aligning the relative azimuthal rotational orientation of the two mirrors) was performed to achieve the minimum predicted wavefront error in one of the off-axis sub-apertures.

Not knowing in advance what the magnitude or type of the EUV wavefront aberrations would be, a strategy was adopted wherein the optic was given an entrance pupil with three apertures of different sizes as shown in Fig. 3. The removable aperture stop rests against the central point of the primary mirror and separately defines 0.06, 0.07 and 0.08 NA apertures. The 0.08 NA sub-aperture was accidentally broken during fabrication, creating the "D" shape. The circular apertures occupy a plane normal to the mechanical axis of the optic. The off-axis illumination encounters the circular pupil at an angle of 1.2° from the central ray to the vertical, making the pupil appear slightly foreshortened in the radial direction and therefore elliptical. Because of the reflection, the beam passes through the aperture twice.

The optic and its mechanical housing were designed to be used in the vertical orientation with the image-plane at the top of the mechanical housing. The image-plane is defined by three small, carefully chosen steel balls. In imaging applications, the wafer rests on these three balls with the photoresist facing downward. Because the optic is designed to be used in this vertical orientation, and any change of orientation could possibly introduce mechanical or gravitational changes to the mirror substrates, all EUV inter-

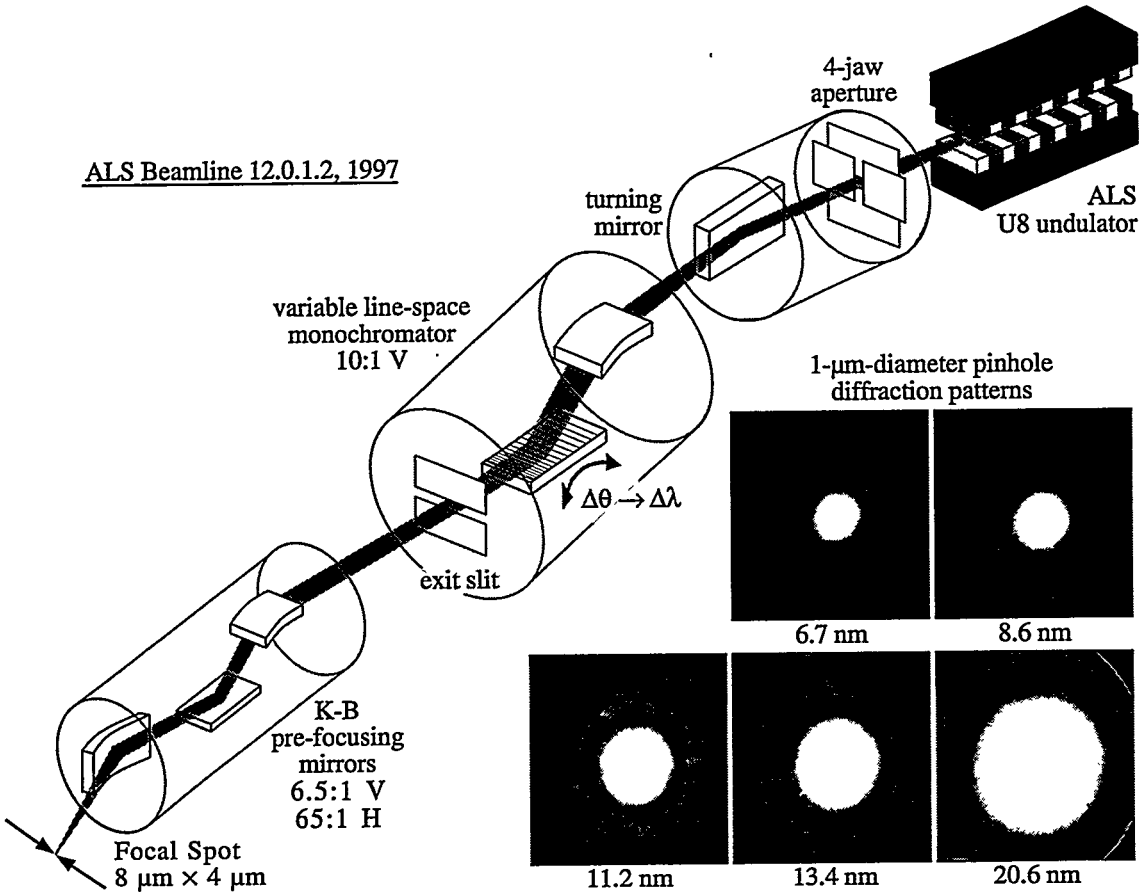

Figure 4. The key optical elements of ALS Undulator Beamline 12.0.1.2, a tunable, coherent EUV source, 1997. A four-jaw aperture and turning mirror select the EUV components of the narrow central cone of the undulator radiation. A variable-line-space planar-grating monochromator incorporating a vertical focusing mirror produces a resolution of $\lambda/\Delta\lambda$ = 200-1000. The Kirkpatrick-Baez (K-B) mirror pair vertically images the monochromator exit slit and horizontally images the source onto the object-plane of the interferometer. The entire beamline produces a demagnification of 65 in both the horizontal and vertical directions. Measured pinhole diffraction patterns are shown for five EUV wavelengths, using a logarithmic grayscale. Only the central portion of the diffraction pattern is used as the illumination reference wavefront.

ferometric tests were performed vertically with the optic illuminated from below.

6.2.2 *ALS Undulator Beamline 12.0*

An undulator beamline, containing a grating monochromator followed by a Kirkpatrick-Baez (K-B) mirror pair, delivers radiation from the undulator to the interferometer (Attwood et al. 1993, Beguiristain et al. 1996). The beamline is shown schematically in Fig. 4. The angular demagnification of the beamline is designed to maximize the coherent flux available for illumination of the Schwarzschild objective near 13-nm wavelength. The entire system operates under vacuum, in pressures ranging from 5×10^{-11} torr in the beamline to 5×10^{-7} torr in the interferometer chamber.

In conjunction with the undulator, the monochromator allows the wavelength to be tuned continuously from 5 to 25 nm, with a spectral resolution in the range of $\lambda/\Delta\lambda$ ~ 200-1000. The monochromator contains a planar blazed grating with variable line spacing, illuminated at glancing incidence. The exit slit

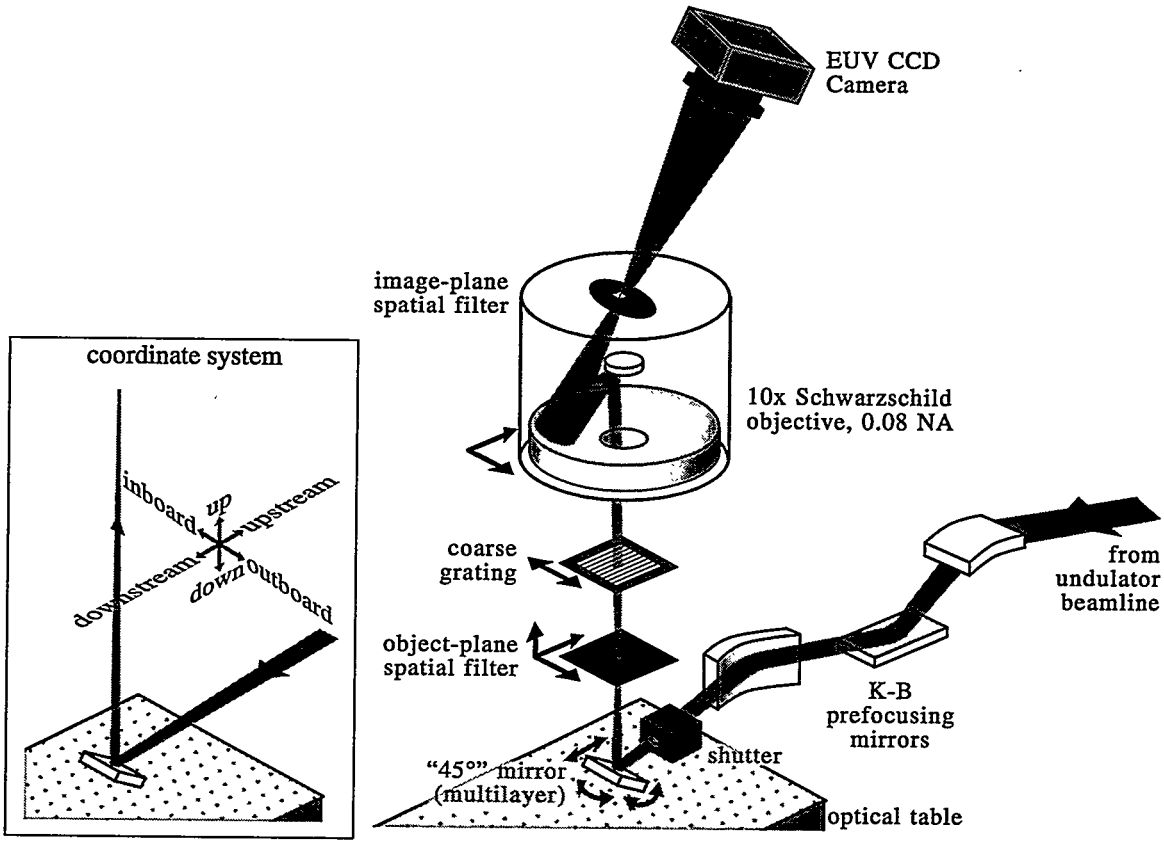

Figure 5. The key optical elements of the PS/PDI endstation configured for measurement of the 10× Schwarzschild objective. Light from the beamline is directed upward by a turning mirror at near 45° incidence. The image-plane pinholes and CCD camera are inclined at 12.1°, normal to the off-axis central ray. A high-speed shutter placed after the K-B mirrors protects the critical optical components from continuous EUV exposure. Black arrows indicate the degrees of freedom of the components. The experimental coordinate system is shown on the left. *Downstream* and *upstream* refer to the directions of photon flux in the beamline, with and against the flux, respectively. *Inboard* and *outboard* are respectively toward and away-from the storage ring.

remains stationary and in focus as the grating angle is adjusted for wavelength selection. To achieve good fringe contrast, the interferometer requires a source coherence-length greater than the largest path-length difference encountered in the interferometer. In a system designed for approximately 50 fringes across the aperture, this requirement translates into a spectral resolution of $\lambda/\Delta\lambda$ greater than 50. The resolution of the monochromator is therefore sufficient for this experiment, as demonstrated experimentally.

The K-B mirrors are thin carbon-coated silicon substrates that are polished flat and then bent into an approximately elliptical shape. Transverse widths of the mirrors are varied in such a way as to enable them to be bent into the proper final shape when bending forces are applied near the ends (James Underwood, personal communication).

The configuration of the interferometer endstation is shown in Fig. 5. To illuminate the Schwarzschild objective vertically, a flat, multilayer-coated turning mirror, mounted at an angle-of-incidence near 45°, is placed between the K-B and its focus, directing the beam upward. The turning mirror is

held on a kinematic Gimbals mount which pivots about the designed point-of-incidence of the beam with the mirror. The angle and longitudinal position of the mirror mount is manually adjustable using three micrometers that are attached to a self-contained, detachable stage unit. The adjustable beam angle and position facilitate beam alignment and enable the investigation of wavefront aberrations across the field-of-view of the optic. Within the field-of-view, wherever the object pinhole is placed the beam may be brought to the proper angle and position through the object-plane.

With a minor focusing error (since remedied) in one of the components of the monochromator, the bandwidth was approximately $\lambda/\Delta\lambda \sim 200$, or 0.067 nm full-width at half-maximum (FWHM) at 13.4-nm wavelength. The near-45° multilayer-coated turning mirror, designed for peak reflection at 13.4 nm, has a measured full-width at half-maximum bandpass of 0.9 nm, considerably wider than that of the monochromator. In principle, the exit slit of the monochromator controls its transmitted bandwidth. Since the vertical mirror in the K-B pair forms an image of the exit slit in the object-plane, if the K-B system were diffraction-limited, then the exit slit would be redundant with the object pinhole — the size of the pinhole would determine the transmitted bandwidth. Before a major overhaul in the summer of 1997, the performance of the K-B system was *aberration-limited,* meaning that the image of the exit slit in the object-plane was substantially blurred. Therefore the object pinhole was not performing as a wavelength filter.

EUV light from the beamline is strongly polarized in the inboard/outboard direction, parallel to the floor. On axis, the first-harmonic light from the undulator is polarized, and the glancing-incidence beamline optics do not significantly affect the direction of the polarization. The near-45° multilayer mirror is also a polarizing element (see Appendix 3). By directing the beam vertically, this mirror selects the inboard/outboard polarization approximately 12 times more efficiently than the vertically polarized components.

6.2.3 Hector's Magic Flange

In the focal plane of the K-B, coincident with the object-plane of the test optic, the sub-micron object pinhole is held in a kinematic mount attached to a three-axis stage, shown in Fig. 6. The stage enables horizontal translation of the object pinhole to position it within the narrow beam, and vertical translation to bring the pinhole into the desired object-plane. This versatile stage and housing arrangement has come to be called "Hector's Magic Flange" (HMF) after its designer, Hector Medecki. The flange is held between a pair of bellows that enable motion over a range of approximately 1 cm (vertical) × 5 mm × 5 mm.

A removable pinhole holder, shown in Fig. 6, consists of a metal cylinder with a tapered conical tip. This tip fits kinematically into a conical well of a slightly larger angle, mounted inside the HMF. Part of the cylinder is machined away and a flat area is created that allows the pinhole to sit on the axis of the cylinder. A hole is bored below the pinhole position to allow the light to reach the pinhole. The rotation angle of the cylindrical pinhole holder is set by a flexible arm attached at 90° to the cylinder axis. This

arm snaps into a grooved holder mounted to the HMF outside of the vacuum chamber. An o-ring seal is formed where the holder enters the HMF — the holder passes through an open cylindrical screw that, when tightened, compresses the o-ring against the holder. Figure 6 also shows a configuration for visible-light interferometry in which the pinhole holder is modified to introduce a polished, tapered-capillary fiber-optic source and a 45° turning mirror to bring a laser source into the object plane.

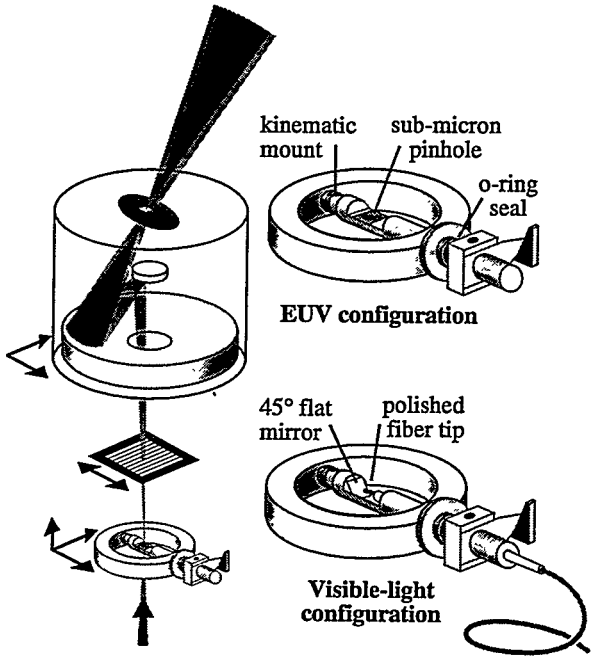

Figure 6. Illustration of *Hector's Magic Flange* (HMF), which performs as a object pinhole kinematic mount on a three-axis stage. Visible light may be introduced into the chamber via an optical fiber with a polished tip in conjunction with a small 45° mirror. A 1.5-mm orifice at the bottom of the flange (not shown) acts as a differential aperture for the vacuum system. A three-position stage can bring a detector or a small glass window valve onto the top of the orifice.

A small 1.5-mm-diameter circular *orifice* at the bottom of the HMF acts as a differential aperture separating the vacuum of the chamber from the rest of the beamline. Here, a three-position stage gives the HMF additional functionality. In one position, the orifice is open to allow the EUV beam to pass. Second, the orifice may be sealed with a small glass window-valve allowing the co-propagating visible-light beam from the ALS to be used for visible-light system alignment while the interferometer chamber is vented. This feature has proven to be an *invaluable* aid. In its third position, the stage contains a photodiode that can be positioned immediately above the orifice to aid in EUV alignment and diagnostics.

Also connected to the HMF is a thin capillary oxygen inlet line. It is widely known that the presence of a small pressure of oxygen is useful in the abatement of hydrocarbon contamination in EUV optical systems. Here the capillary directs a jet of oxygen gas into the HMF, directed toward the entrance-side of the object pinhole. The capillary conducts oxygen through a needle-valve so that a predictable and constant pressure of oxygen may be used. On a base pressure of 5×10^{-7} torr, the oxygen pressure is typically 2×10^{-4} torr in the interferometer chamber. Some oxygen flows through the orifice into the 45°-mirror chamber and the K-B mirror chamber. Although it has not been carefully characterized *in situ*, the presence of this low oxygen pressure may in fact be beneficial in removing contamination from those optical surfaces.

Aligning the narrow, focused EUV beam through the sub-micron object pinhole is not trivial. When the system is far from alignment and there is no detectable beam flux through the object pinhole, creative

measures are required. First, to ensure that the beam enters the 1.5-mm-diameter orifice at the entrance to the HMF, the area surrounding the hole is painted with phosphor. Using a viewport located above the 45° turning mirror and a small, adjustable, strategically-positioned mirror, the orifice may be observed when the system is at vacuum. The beam spot is clearly visible on the phosphor paint when it fails to enter the orifice. The detector on the three-position stage immediately above the orifice can be used to center the narrow beam through the orifice.

Once it is known that the beam clears the edges of the orifice, the object pinhole must be positioned in the beam. Here, to establish the location of the beam within the object-plane a thin mylar membrane is placed in the object-plane using a separate but identical pinhole holder. In a matter of seconds, the focused EUV beam burns through the mylar, leaving a visible burn-spot on the otherwise transparent membrane. In a microscope fitted with a copy of the HMF kinematic mount, the object pinhole can be hand-positioned in a matter of minutes into the proper location based on the mylar burn spot. Achieving the proper position within 10 or 20 μm is usually satisfactory for locating the pinhole *in situ*. A separate strategy involving an accurate stage that duplicates the orientation of the HMF translation axes and kinematic mount could simplify the alignment process by eliminating the need for fine hand-positioning. However, the recent installation of highly sensitive detector electronics has made locating pinholes from scratch easier and much less time-consuming.

6.2.4 *Other Stages and Components*

The elements of the beamline that are most difficult to adjust are the bendable and tiltable K-B mirrors. Once a satisfactory configuration of the K-B mirrors was found, and the nominal focal position was acceptable for the illumination of the Schwarzschild objective, no further adjustments of the K-B mirrors were made.

The particular K-B mirror substrates used during the time of these interferometry experiments were known to be of poor quality, yet these were the only mirrors available at the time. The longitudinal distribution of light near the imperfect K-B focus allows the object pinhole to be placed within a range of several hundred microns without suffering a dramatic loss in flux. Near the focal plane, the distribution of light is measurable by scanning the three-dimensional position of the object pinhole while using a retractable photodiode-detector placed several centimeters above the object plane to measure transmission. While the poor performance of the K-B system created a larger than expected focal spot and caused a lower than expected photon flux through the object pinhole, this unintended property of the beamline actually facilitated the positioning of the object pinhole over a broad range (1 cm) of longitudinal positions. K-B mirrors of much higher quality have since been fabricated, installed, and tested.

With the beam and object pinhole held stationary, lateral alignment of the image point is performed

by two-axis horizontal translation of the test optic. This translation with respect to a stationary object point takes advantage of the 10× demagnification to enable positioning of the image point with better than 0.1-μm resolution. The optic itself sits on a bearing-stage, and a pair of Picomotors are used to move the optic through several millimeters of travel. The Picomotor translations are demagnified 2:1 using flexural pivots and are coupled to the motion of the bearing through a pair of wobble-pins. Linear Variable Differential Transformers (LVDTs) are used to monitor the positions of the Picomotors (and hence the bearing on which the optic rests) through the vacuum chamber walls.

A coarse grating beamsplitter is placed between the object pinhole and the entrance aperture of the test optic. The grating, typically 18-μm-pitch, is made of a gold absorber pattern on a 100-nm-thick silicon-nitride membrane, with 5×5-mm^2 area (fabricated by Dino Chiarlo). In order to conduct measurements with the fringe patterns in two orientations, 90° apart, two separate gratings and grating-stages are used. To enable phase-shifting, the two gratings are held on separate one-dimensional horizontal translation stages, each with motion in the direction perpendicular to the rulings. The grating stages are attached to coarse translation mechanisms that allow the gratings to be completely retracted from the beam.

Custom-designed hardware (by Paul Denham) and software (by Joshua Cantrell and the author) are used to control the three axes of the HMF stage (object pinhole positioning), the grating stages, and the two axes of the Schwarzschild objective. The motor-control software programs were created to be very responsive with a high degree of interactivity and the inclusion of many features that facilitate the requirements of the interferometry experiments. Motor positions are adjustable using on-screen control panels containing scalable grid-displays of present and previous positions in three-dimensions, where appropriate. The programs include a position memory feature that allows tens of previous locations to be stored and recalled, rapidly returning the system to a previous state. Automatic *raster* and *spiral* scanning features are included to aid in the location of pinholes and other points of interest. The grating-control program stores calibrated step values to facilitate phase-shifting, and it keeps track of step numbers to aid in data collection.

6.2.5 *Pinhole Spatial Filters*

The quality of the pinhole-diffracted waves is the single element that has the most substantial impact on the accuracy and precision of the interferometer. The pinholes are the most critical elements of the interferometer; therefore the use of high quality pinholes in the object- and image-planes is imperative. Because of their small size, and because of their use as diffractive elements, *high quality* for pinholes has a functional definition based on their performance as spatial filters, *in situ*.

The commercially-available laser-drilled object pinholes used are on the order of 0.5-μm diameter, approximately one-fourth of the diameter required to produce a diffraction-limited beam at 0.008 NA. Evaluation of the quality of the diffracted waves is presented in Sections 6.3 and 8.3.

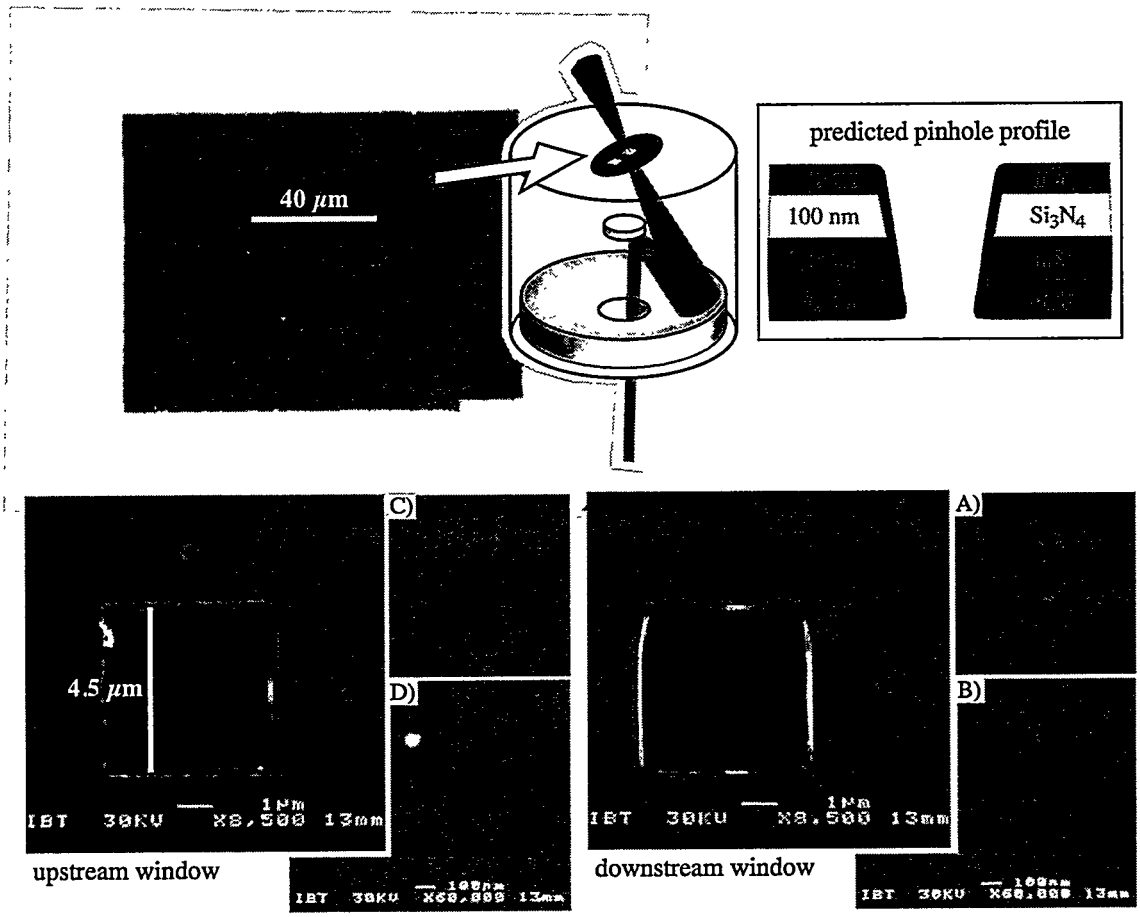

Figure 7. The image-plane reference pinholes used in the PS/PDI experiments were fabricated by focused ion-beam lithography in a 100-nm-thick Si_3N_4 membrane with a 70 nm InSb absorber layer. After the *open-stencil* pinholes and window were etched completely through the membranes, additional InSb absorber layers were deposited on the two sides of the membrane. The membrane contains two window and pinhole patterns separated by 40 μm, defining two closely-spaced field points displaced in the upstream-downstream direction. The pinholes were fabricated at Intel. Pinhole size is discussed in Section 6.4.

Two sets of image-plane pinhole membranes were used in the PS/PDI experiments described here. The first set of pinholes was made of a patterned gold absorber layer on a solid silicon-nitride membrane, fabricated by electron beam lithography. The pinhole pairs consisted of two sub-100-nm reference pinholes adjacent to a square window, 5.0 μm on edge, with center-to-center separations of 4.5 μm. This first pinhole membrane was abandoned because of problems created by contamination on the solid membrane. Without the benefits of oxygen gas, the membranes became unusable in a matter of minutes, as damage to the window membrane obstructed the transmission of the test beam.

A second set of image-plane pinholes, shown in Fig. 7, was fabricated on a membrane consisting of a 100-nm-thick silicon-nitride (Si_3N_4) support membrane, with a 70-nm-thick indium-antimonide (InSb) absorber layer. An open-stencil pattern of pinholes and windows was created using focused-ion-beam lithography to *drill* open holes in the membrane. Following the pattern definition, additional 70-nm-thick lay-

ers of InSb were deposited on both sides of the membrane to increase absorption and reduce the pinhole size. The $1/e$ intensity transmission depths of InSb and Si_3N_4 for 13.4 nm wavelength light are 15.2 nm and 117 nm respectively; therefore, based on thicknesses of 100 nm Si_3N_4 and 240 nm InSb, the transmissivity of the membrane is expected to be on the order of 5.9×10^{-8}. Unlike the semi-transparent PDI pinhole membrane, the PS/PDI membrane is required to be opaque.

This second pinhole membrane was used for all of the PS/PDI measurements reported here. These four pinholes were used in literally thousands of interferogram exposures over the course of two months. For reference, these four pinholes have been here labeled, A, B, C, and D, as indicated in Fig.7. The diffraction characteristics of these pinholes are discussed in Section 6.4.

In this configuration of the PS/PDI for Schwarzschild objective measurement, the image-plane pinholes are manually pre-aligned and remain stationary with respect to the moving test optic. For repeatable pinhole positioning, the pinholes are attached to a kinematic mount that rests on the three balls that define the image-plane. The mount holds the pinholes inclined at 12.1°, normal to the central ray of the off-axis beam. The tops of the balls fit snugly into three shallow, radial "V" grooves on the under-side of the mount, creating three distinct and repeatable positions of the mask, approximately 120° apart. This three-way positioning facilitates measurement of all three sub-apertures of the Schwarzschild objective without modification of the pinhole mounting.

The pattern of the pinhole membranes can be arranged in many ways. Using an array of pinhole/window patterns facilitates wavefront measurement across the field-of-view of the test optic without repositioning the image-plane pinholes. Here, one difficulty is the requisite 12.1° inclination of the pinhole membrane that causes pinholes in an array to occupy different longitudinal planes. At this time, research has been proposed to investigate the importance of keeping the pinholes at normal incidence to the central ray. Until this evaluation has been completed, the inclination of the pinhole plane should be maintained. The first effect of the membrane tilt is that field points separated by 40 μm laterally (a typical distance) differ in longitudinal position by 8.4 μm. With a 10× demagnification optical system, each micron of longitudinal image-plane position change requires a 100 μm adjustment of the object-plane position: a 8.4-μm image-plane change requires a (large) adjustment of 840 μm from the object-plane.

6.2.6 *High-Vacuum-Compatible High-Speed Shutters*

A reliable, high-vacuum-compatible beam-shutter is of prime importance for the EUV interferometer. The shutter, placed beyond the K-B mirrors in a position where the beam size is approximately 4-mm-diameter, protects the critical and sensitive interferometer components from constant, intense EUV exposure. The shutter must be synchronized with the CCD control hardware to prevent exposure during read-out. Two novel shutters have been custom designed and implemented in the interferometry experiments.

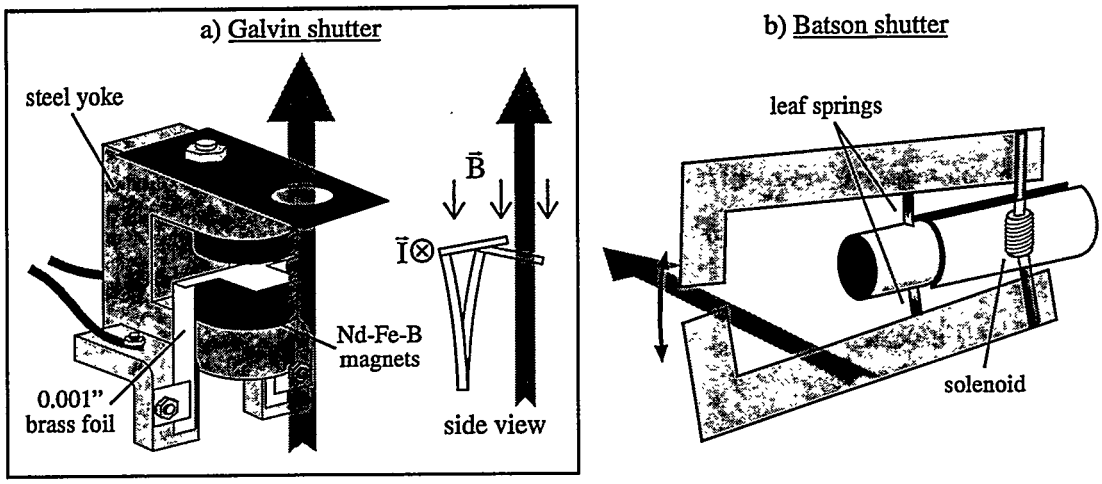

Figure 8. High-vacuum-compatible high speed shutters are required to protect the optical components from constant exposure, and to ensure the proper operation of the CCD detector. Two shutters have been developed for this purpose. a) A shutter designed by James Galvin operates based on the Faraday effect. b) To achieve greater travel and faster operation, a second shutter designed by Philip Batson was installed after the interferometric measurements described in this thesis had been performed.

These are shown in Fig. 8.

A compact shutter designed by James Galvin, shown in Fig. 8(a), operates based on the Faraday effect: a current-carrying shutter flap moves within the strong stationary field created by a pair of strong Nd-Fe-B magnets held in a steel yoke. This particular shutter functioned successfully through months of daily operation, but suffered from a short range of motion (below 4 mm) that caused it to block a portion of the available beam.

In the active area, the measured magnetic field is approximately 0.5 Tesla. The flexible shutter flap is created from a single piece of 1-mil brass foil machined or hand-cut and folded into the proper shape. The shutter has a travel of approximately 3 mm, carries approximately 1-amp peak current, and operates with a minimum useful open time of approximately 50 msec. One or both of the clamps that hold the shutter flap must be electrically isolated from the vacuum chamber.

During the development of the shutter, several conductive non-magnetic materials were evaluated for use as the shutter flap. One-mil-thick (25.4 μm) brass met the criteria for high flexibility, light weight, vacuum compatibility, and shape-retention. One important design flaw was discovered and addressed early on. When the foil was folded sharply near the position where it is required to bend, the joints were observed to fail after only a few hours of operation. This problem was overcome with the design shown in Fig. 8(a), wherein the *legs* of the flap are neither bent sharply nor creased in any way. Bending occurs in a gradual arc along the relatively long length of the foil. There is no stress applied to the fold which causes the flap to project forward at 90°.

One element not shown in Fig. 8(a) is a motion restrictor that limits the backward (into the yoke)

travel of the flap. With the large applied forces and the narrow but deep magnetic gap, this restrictor is required to prevent the shutter flap from sticking to the magnet surfaces. The restrictor consists of a thin glass tube on the end of a wire bent into a "C" shape and epoxied into position.

To achieve greater travel and faster operation, a new shutter designed by Philip Batson was used. The shutter arms open rapidly, pulled by the force of a pair of small magnets inside a solenoid symmetrically placed between the arms. The arms are pulled against the force of a bent leaf-spring that holds the arms closed in the absence of current. The minimum useful exposure time enabled by the shutter is approximately 0.05 seconds.

Once again the arms of the shutter are electrically isolated from the vacuum chamber. In this second implementation a current meter attached between the shutter arms and ground enables the shutter to function as a photocurrent detector. When the EUV beam falls on the closed leaves of the shutter, the current from the shutter is typically on the order of 1 μA.

6.2.7 *Beam Detectors*

Identical to the EUV PDI experiments (Chapter 3), data is recorded with a back-thinned, back-illuminated, un-coated, 1024 × 1024 pixel, 1-square-inch area, 16-bit Tektronix CCD camera optimized for EUV detection. The CCD is mounted at an angle of 12.1° from the vertical to receive the central ray of the test beam at normal incidence. The detector is placed approximately 12 cm beyond the image plane.

Two Hamamatsu GaAsP photodiode detectors are used to monitor the beam flux. The detectors have 5×5-mm^2 area. As mentioned in Section 6.2.3, one detector is held just above the HMF orifice. This detector is primarily used to center the beam within the 1.5-mm-diameter orifice. A second detector is held on a retractable arm in a plane just above the grating stages. This detector measures the beam current *after* the object pinhole and is used to optimize the position of the object pinhole.

6.3 THE TEST WAVE

The simple illumination pattern of the test optic reveals a great deal of information about the quality of the Schwarzschild objective and its multilayer coatings. With no image-plane windows or pinholes, the optic is illuminated at 13.4-nm wavelength using a ~0.5-μm-diameter object pinhole spatial filter. The illumination is recorded with the CCD detector, placed approximately 12 cm beyond the image-plane.

One important characteristic of the Schwarzschild objective is that the concave secondary mirror forms a real image of the primary mirror (the entrance pupil) 7.9 cm beyond the image plane. The image is inverted and is magnified by approximately 3×. Any visible feature of the primary mirror is projected sharply into this plane. Although the CCD camera is placed several centimeters beyond this plane, large

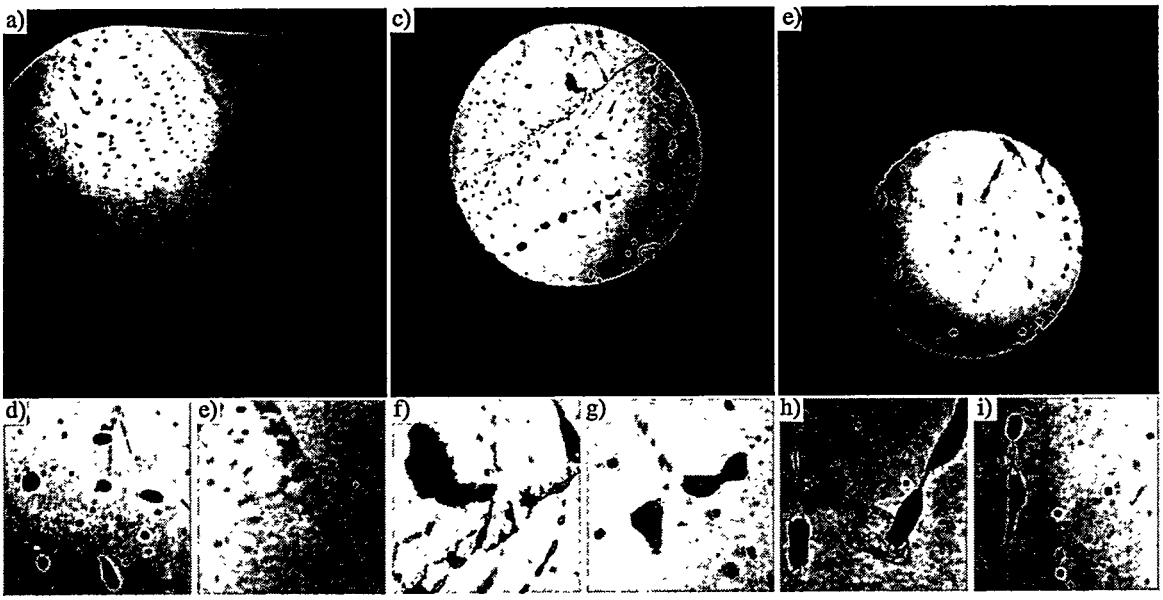

Figure 9. Illumination of the 10× Schwarzschild objective reveals a pattern of defects, or *blemishes,* observable as intensity variations in the test beam. Transmission through the three sub-apertures is shown here as recorded by the CCD camera in 1024×1024-pixel images. (a), (b), and (c) are raw data shown in linear scale. (c) The aperture stop does not fully extend to the edge of the mirror surface, allowing a curved sliver of light to pass. Details of several of the blemish regions are shown in (d) through (i), with (d) and (e) taken from (a), (f) and (g) from (b), and (h) and (i) from (c). Each detail is 120 × 120 pixels, subtending an approximate solid angle of 0.024 rad, or 1.4°, representing an area 510-μm-wide on the primary mirror surface. Bright, thin diffraction *halos* are visible along the sharp boundaries of the blemishes because the CCD is several centimeters beyond the plane in which the concave secondary mirror re-images the primary.

defects on the mirrors appear very distinctly, as is apparent in Fig. 9. The ability to observe these features clearly in the pupil is due to the short wavelength used, the narrow cone of rays, and the relatively large size of the blemishes. The features *are* out of focus in the plane of the CCD, and under careful inspection, a small bright ring is observable around every sharp feature.

6.3.1 *Blemishes*

The presence of numerous blemishes in the test optic could be due to defects in the substrate, contamination of the substrate prior to coating deposition, contamination during deposition, contamination of the coating surface, or a combination of these effects. By eye, several dust particles are visible on the mirror surfaces, but the appearance of these streaks and spots suggests that there may be residue left by a wet cleaning process. One attempt at cleaning using de-ionized nitrogen gas was made, but this yielded little observable difference.

With the grating beamsplitter removed, the isolated test beam passes through the image-plane window. In this configuration, an image of the spatially-filtered test beam is recorded with each interferometric measurement. Test beam images from all three sub-apertures are shown in Fig. 10.

6.3.2 *Illuminating Beam:* In Situ *Pinhole Size Assessment*

The spatially-filtered illuminating beam is the first spherical reference wavefront of the interferom-

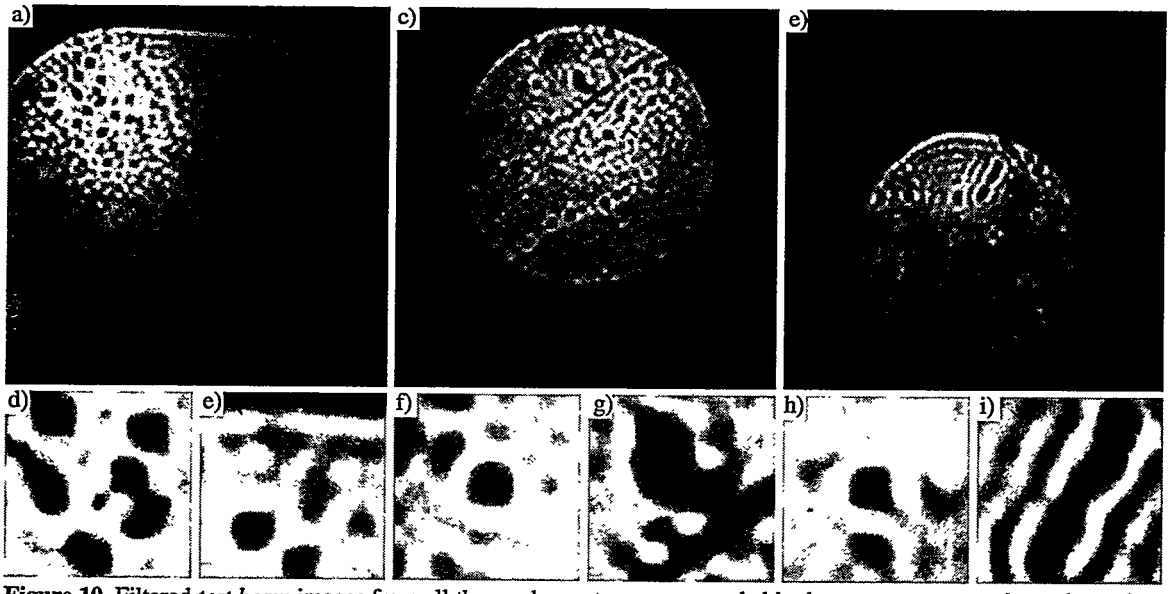

Figure 10. Filtered *test beam* images from all three sub-apertures are recorded in the same manner as those shown in Fig. 9. However, with the PS/PDI image-plane pinholes and windows installed, the test beam is spatially filtered by the 4.5 μm window. As before, the details, (d) through (i) (are 120 × 120 pixels, subtending an approximate solid angle of 0.024 rad, or 1.4°. (d) and (e) are taken from (a), (f) and (g) from (b), and (h) and (i) from (c), although they do not correspond to the same detail regions shown in Fig. 9. The square shape of the spatial filter window is evident in the *rectangular* pattern of ripples that surrounds each defect. This is especially apparent with the smallest "sub-resolution" defects. See Section 5.10 for a discussion of spatial filtering.

eter. Based on observations of the test beam and of the angular rate of intensity fall-off, the size of the object pinhole can be determined approximately. The *actual* size can be determined by other means, such as electron microscopy. However, since the most important property of the pinhole is the quality of the wave diffracted from it, an *effective size* of the pinhole can be defined as the size of the equivalent ideal pinhole that diffracts an Airy-like wave.

By design, the first diffraction minimum of the illuminating beam falls well beyond the NA defined by the entrance pupil. An estimate of the pinhole diameter may be based on the intensity full-width at half-maximum, the known object-side NA angle within the pupil, and an assumption of an Airy-like diffraction pattern. As discussed in Sections 2.3.1 and 4.6.1, the angular distribution of the Airy pattern intensity is

$$I(\alpha/\lambda) \propto \left(\frac{\lambda d}{2\alpha}\right)^2 J_1^2\left(\frac{\pi \alpha d}{\lambda}\right). \tag{1}$$

α is the direction cosine with respect to the central ray. When the half-angle of the intensity half-maximum $\theta_{I/2}$ is known, then the pinhole diameter may be calculated empirically from

$$d = \frac{0.514\lambda}{\sin\theta_{I/2}}, \tag{2}$$

based on Eq. (1). Using the average of two similar measurements of the intensity profile, taken from the

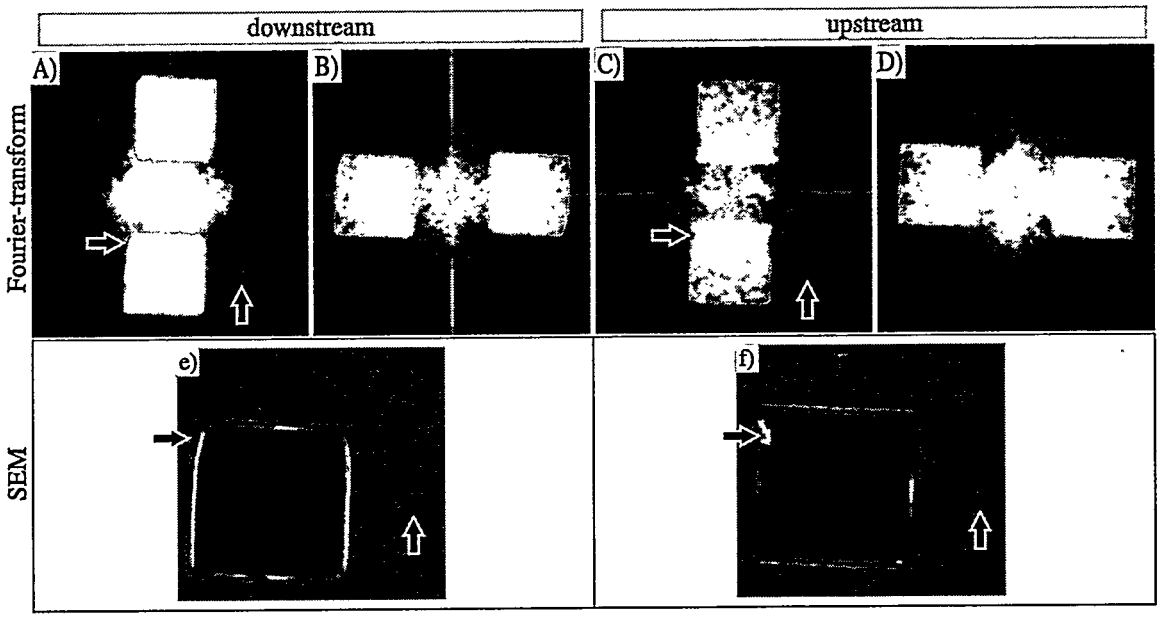

Figure 11. (A) through (D) The patterns of the pinholes and the window are clearly visible in the logarithmically-scaled Fourier-transform of the reference pinhole diffraction patterns. Because the (strictly-real) intensity of the diffraction pattern is measured, the Fourier-transform shows polar symmetry. With a single beam centered on one of the reference pinholes, the leakage of light through the window and the second pinhole illustrates the role of the window as a bandpass filter for the reference beam, allowing a range of mid-to-high spatial-frequencies to pass. Reference pinholes (A) through (D) are featured in (A) through (D) respectively. SEM images of the same pinholes are shown for comparison. Irregularities in the shapes of the windows are clearly visible in the Fourier-domain.

test wave measurements, the effective pinhole diameter is estimated to be 0.76 μm. More than one pinhole was used in the interferometric experiments: after one pinhole had been used to gather the bulk of the interferometric data, several other pinholes were tested. These experiments are discussed in Chapter 8. Experiments to determine the quality of the spatial filtering properties of the entrance pinhole are discussed in Section 8.3.

6.4 THE REFERENCE WAVE

As with the PDI, the quality of the reference wavefront is the most important element for determining the accuracy and precision of the PS/PDI. The size of the reference pinholes largely determines the quality of the spatial filtering they generate. In this section, two ways of determining the effective size of

Table 1. Size determination by SEM and at-wavelength diffraction measurements of the four reference pinholes used in the interferometry experiments.

	SEM			Diffraction		
pinhole	*x*-width	*y*-width	$d = \sqrt{xy}$	*x*-width	*y*-width	diameter
A	137	124	130	168	141	154
B	220	201	210	168	154	161
C	164	171	167	177	173	177
D	163	144	153	172	159	167

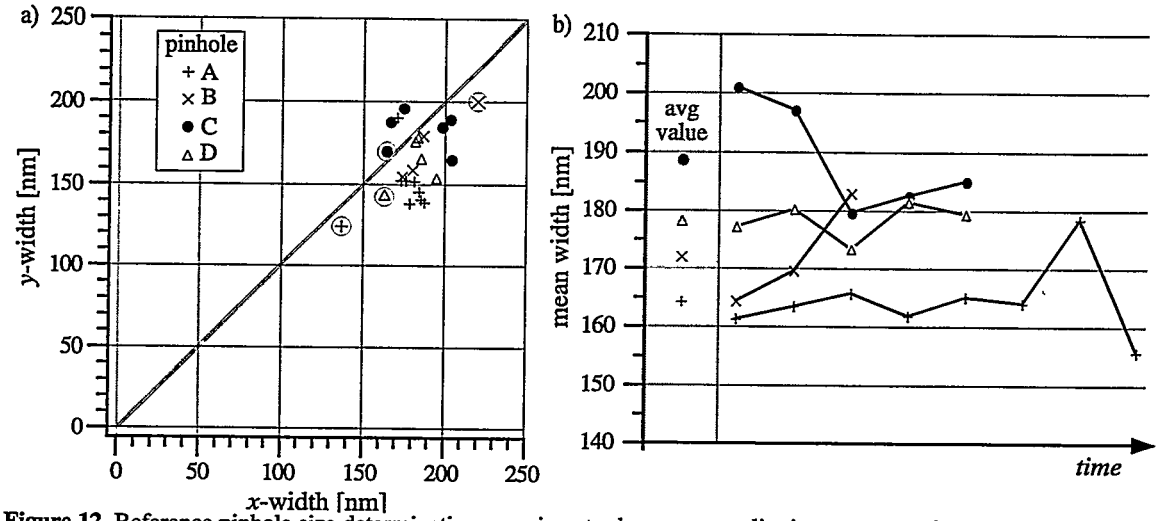

Figure 12. Reference pinhole size determination experiments show poor qualitative agreement between the SEM observations, and the measured pinhole diffraction patterns. The averaged data is shown in Table 1. (a) Separate *x*- and *y*-widths are determined from both the SEM images and the diffraction patterns. Each diffraction measurement is shown in the left graph. The SEM measurements of the same four pinholes are indicated by circled symbols. Over a two month period, diffraction measurements were made occasionally. (b) The time axis indicates only the order in which the diffraction patterns were recorded. The same plotting symbols are used in both graphs.

the reference pinholes are described, and characteristics of the reference waves are discussed. As described in Section 6.2.5, there are four pinholes from one single pinhole membrane under investigation. These pinholes represent two orthogonal directions from two field points. As shown in Fig. 7, the field points are located in the upstream and downstream directions, separated by only 40 μm.

6.4.1 *The PS/PDI Reference Wave*

The reference wave in the PS/PDI is considerably different from that of the PDI because of the way in which it is generated. In the PS/PDI, where a beamsplitter produces multiple focused beams in the image-plane, the beam selected as the test beam passes through a (relatively) large window, while an adjacent beam is brought to focus on the sub-resolution reference pinhole. Regardless of the beam separation and the quality of the optical system under test, there will be some overlap. Typically, the most significant consequence of this is the overlap, or *leakage,* of the reference beam through the large window. Since the window sits in the image-plane and is displaced from the center of the reference beam, it behaves as a bandpass filter allowing a range of mid- to high-spatial-frequencies to be transmitted.

In order to characterize the reference pinholes, experiments were done to investigate their diffraction properties. In these experiments, the grating beamsplitter is removed and a single beam is brought to focus on a pinhole under study. These experiments parallel those reported for the PDI pinholes, Chapter 3.

The measured far-field diffraction patterns may be understood from examination of their Fourier-transforms, shown in Fig. 11. Because only the (strictly-real) intensity of the far-field diffraction pattern is measured, the Fourier-transform is Hermitian — its complex amplitude shows polar symmetry. At the

center of the Fourier-transform pattern is a narrow peak representing the spatial frequency content of the highly filtered beam that passes through the reference pinhole. Figure 11, which is logarithmically scaled and smoothed for display, clearly shows the function of the window as a bandpass filter. For comparison, the SEM image of the pinhole window is shown adjacent to the Fourier-transforms. The shapes of the windows, including irregularities, are clearly reproduced in the Fourier-domain. Even the second, unused pinholes are visible in the Fourier-transform as a faint bright peak.

6.4.2 In Situ *Pinhole Size Assessment*

The sizes of the reference pinholes can be determined in several ways, including SEM and *in situ* diffraction measurements performed *at-wavelength*. While SEM measurements are the most straightforward indicators of size, the widths of the diffraction patterns yield the useful *effective diameters* that would be expected by the assumption of ideal, Airy-like diffraction.

The SEM images of the pinholes (recorded by Larry Murray), taken in reflection mode, are shown in Fig. 11. The maximum widths in the x- and y-directions may be ascertained from the apparent open area of the pinholes. The x- and y-direction widths are shown in Table 1, along with the geometric mean. These two directions are arbitrary, yet provide some qualitative indication of apparent pinhole ellipticity.

The pinhole diameters are also calculable from the diffracted intensity profile in the same manner used for the estimation of the object pinhole diameter in Section 6.3.2. From Eq. (2), the half-angle at half-intensity is used. To calculate this angle, a small sampling of reference pinhole diffraction patterns is made. The angle-to-pixel ratio for the CCD camera is known from the interferometry experiments to be approximately 0.2 mrad per pixel. To calculate the half-angle, the pinhole diffraction patterns are spatially filtered to remove the mid- and high-frequency content. For each image, a contour is generated automatically, tracing the half-maximum of the intensity in approximately 500 points. From these points, the first moments of the distribution are used to determine the *central* points in the x- and y-directions. These are shown in Fig. 12. The mean distance (in pixels) from each contour point to the center is used to calculate the half-angle. Also of interest are the maximum angular widths in the x- and y-directions, given in Table 1. As with SEM analysis, these directions are arbitrarily chosen, yet provide a qualitative indication of any ellipticity in the pinholes.

It is clear from the comparison of these two size-determination methods that the SEM images do *not* provide a good indication of the effective pinhole diameters observed in the diffraction measurements. In fact, the pinhole that appears largest in the SEM images, pinhole B, produces a diffracted wave that is the second-smallest of the four.

6.5 FOURIER-TRANSFORM ALIGNMENT METHOD

Once the illuminating beam is aligned and the object pinhole position is optimized for peak flux, the most difficult procedure is bringing the reference beam onto the tiny reference pinhole, on the order of 100-nm diameter. Alignment proceeds by lateral translation of the test optic, taking advantage of the 10× demagnification to achieve fine adjustment of the lateral beam position in the image-plane. When the system is aligned, or nearly aligned, interference fringes become visible and the alignment proceeds by optimizing the appearance of the fringes, looking for uniformity and complete coverage of the illuminated area. When the system is misaligned, even slightly, the fringe pattern is not visible and there are few clues available to bring the system toward proper alignment.

One somewhat effective method is to observe the *square*-ish ring pattern that surrounds the small blemishes. When the system is properly aligned and the test beam passes through the center of the window, the rings are symmetric top-to-bottom and right-to-left. Using this indicator is equivalent to understanding the Fourier-domain filtering performed by the window.

A much more effective technique uses the Fourier-domain *directly*. Since the recorded intensity is the far-field diffraction pattern of the image-plane field, a simple Fourier-transform provides a mathematical *image* of the field in that plane. For each image recorded, the fast Fourier-transform (FFT) algorithm can be implemented rapidly and the results displayed with logarithmic scale, giving immediate visual feedback on the position of the beam within the window or pinhole. Such a system, developed by the author

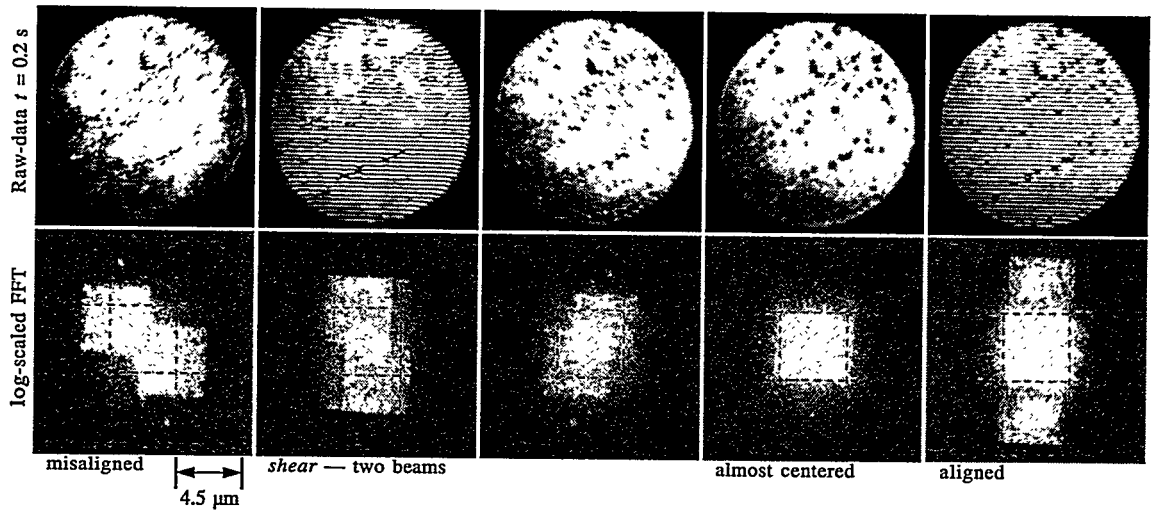

Figure 13. The Fourier-transform alignment method facilitates the otherwise-difficult alignment of the reference beam through the tiny reference pinhole in the image-plane. The raw intensity data collected by the CCD detector (top row), with 0.2 second exposure time and 4 × 4 pixel hardware binning, is the far-field diffraction pattern of the field in the image-plane. As such, the Fourier-transform (bottom row) reveals the distribution of light in the image-plane. Since the real-valued intensity is measured, the Fourier-transform is Hermitian, accounting for the redundant image.

This typical series of images was recorded during system alignment. As the lateral position of the test optic is adjusted, the beam becomes more centered in the window until the PS/PDI fringe pattern is clearly visible. The image marked as "shear" indicates that two beams are passing through the window, similar to a lateral shearing interferometer. However, in this geometry both beams clip the edges of the window and are thus of poor quality.

and successfully implemented as of October 1997, has greatly enhanced the alignment procedure. Images are recorded with sub-1-second exposure times, and the FFT is displayed almost immediately, adjacent to the raw intensity data. As the fringes become visible, the first-order peaks appear above the background.

Since the CCD measures only the (strictly-real) far-field intensity pattern and the phase information is unavailable during the alignment process, the Fourier-spectrum is Hermitian — the complex amplitude of the FFT shows a redundant polar symmetry. Several typical interferogram and Fourier-transform images are shown in Fig. 13.

7

Wavefront Measurements and Imaging

7.1 INTRODUCTION

The central goal of this thesis research is the development and demonstration of at-wavelength EUV interferometry capable of accurately measuring lithographic-quality optical systems. The importance of this capability lies in its the ability to predict imaging performance. In this chapter, wavefront measurements from all three sub-apertures of the 10× Schwarzschild objective are presented. These measurements reveal the nearly diffraction-limited quality of this optical system at the same time as they explore the performance of the interferometer. Subsequent to the interferometric characterization, this optic was used in a series of high-resolution imaging experiments at Sandia National Laboratory.; the results of those experiments are also presented here. As will be discussed, these results show strong agreement with imaging simulations based on the measured wavefront.

7.2 WAVEFRONT MEASUREMENTS

This section contains the wavefront measurements of all three sub-apertures of the 10× Schwarzschild objective. Investigations were conducted in the same way for each sub-aperture, with the Schwarzschild objective simply rotated by 120° about its optical axis to bring the proper sub-aperture into position. Relative to sub-apertures B and C, a large number of data sets were recorded of sub-aperture A at 13.4-nm wavelength. For this reason, estimates of the interferometer's precision are all based on measurements of sub-aperture A.

To measure the system wavefront at a given field point, two phase-shifting measurements are performed using orthogonal fringe directions (i.e. beam separation directions). This is necessary to remove a geometric coma systematic error related to the beam separation (Section 5.5). A pair of orthogonally-aligned grating beamsplitters is used sequentially, to create the two directions of the fringe patterns. The test beam is chosen to be the zeroth-order beam from the grating; it passes through a stationary point in the image-plane window. The reference beam is one of the first-diffracted-order beams from the grating. In each orientation, the reference beam is brought to focus on a reference pinhole that is one of two pinholes placed at 90° with respect to the image-plane window (see Sections 5.11 and 7.2.5 for the design). These two wavefront measurements are combined to remove the geometric coma systematic error using the method described in Section 5.5.2.

From analysis of the four reference pinholes used (two field points were tested), one fact has become clear: because of its large size, pinhole C does not produce a reliable reference wavefront. The wavefront variation observed from this one pinhole renders measurements performed with it unusable. Since individual field-point measurements require the use of *both* pinholes in a pair, data from the *upstream* field point, which use pinhole C, are not presented. In addition, because of the noticeable deteri-

oration in system performance and fringe contrast of the sub-aperture A interferograms that occurred after re-alignment of the system, wavefront data taken after the re-alignment are not included. (This is the "April" data discussed in Section 8.6. The loss of fringe contrast is demonstrated in Section 8.11.)

7.2.1 *Determination of the Raw Phasemap*

Beginning with the raw interferometric data recorded with the CCD camera, the individual exposures are normalized to compensate for the steadily decreasing electron-beam current of the Advanced Light Source. During a measurement series of five interferogram exposures, the current typically decreases by less than 0.5%. Using the least-squares method of phase-shifting analysis (Section 12.2.3) with the Fourier-Transform Method of Phase-Shift Determination (Section 12.4.2), the phase is calculated at every point in the domain. The least-squares technique uses the temporal-domain data to independently calculate the phase at each point. Therefore, it is not necessary to limit the calculations to the sub-region of interest. The modulo 2π phasemaps are unwrapped using the robust Fourier-Transform Guided Unwrapping method (Section 13.5) to overcome the high density of *bad* data points associated with the numerous localized blemishes.

The raw unwrapped phase data is shown in Fig. 2 (in the following section, where the sub-region definition is discussed). From the line-out taken in the middle of the sub-region, a high level of noise is apparent. This characteristic of the raw phase data demonstrates why the simple unwrapping techniques fail. The Fourier-Transform Guided Unwrap method was developed specifically to address this difficulty.

7.2.2 *Establishing a Coordinate System — Sub-Region Definition*

In order to successfully compare or combine measurements performed at different times, it is *essential* to establish a consistent coordinate system fixed to measurable positions in the test optic. Even small displacements or rotations between measurements can yield false wavefront differences. The magnitude of these differences is simply related to the wavefront slope (or *derivative*) at any point of comparison.

Virtually any set of clearly observable fiducial markings in the pupil can in principle serve as a reference for the establishment of a consistent coordinate system. For the measurements of the Schwarzschild objective, the distinctive pattern of blemishes in each aperture *became* the fiducial. Using the isolated test beam images (Section 6.3) recorded concurrently with each phase-shifting data set, a single, universal coordinate system was established for each sub-aperture. First, one test beam image was declared to be the *reference.* Then, using the positions of the blemishes as a guide, test beam images from each data set were aligned until the optimal image translations were ascertained. This optimization was performed *manually* by the author using image subtraction techniques. In the future, this painstaking process could be automated by the introduction of an well-designed fiducial system and by the implementation of a relatively simple software algorithm to compare pairs of test beam images.

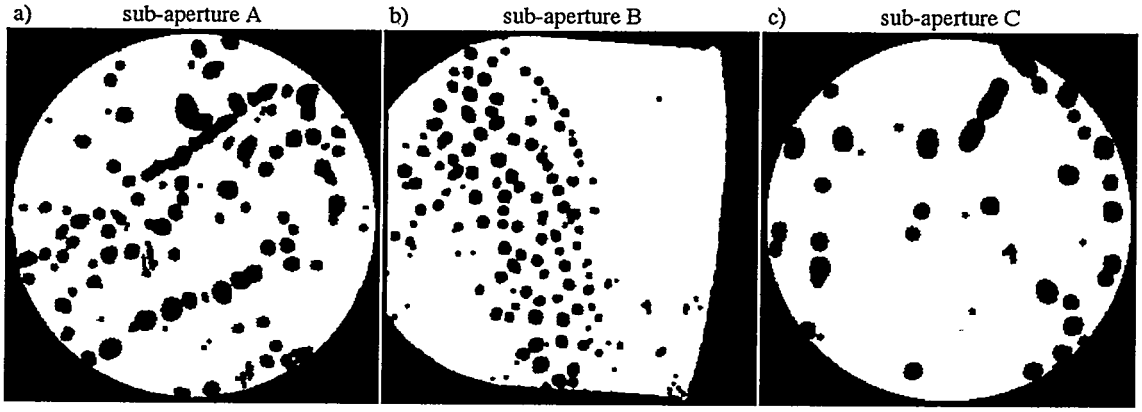

Figure 1. Sub-regions used for data analysis in sub-apertures A, B, and C. The blemish regions are removed automatically based on the mid- to high-spatial frequency intensity variations of the measured test beam. The three sub-regions are 659, 830, and 564 points wide and they contain 279188, 503569, and 224470 valid data points, respectively.

Once the relative positions of the various data sets have been brought into agreement, the next step is the establishment of the sub-region containing the valid data for analysis. Interferometrically there are many ways to determine which data points are valid. Some methods are based on fringe contrast or measurement uncertainty (Robinson 1993): these typically apply a threshold function to establish a minimum contrast allowed for inclusion. In this case, such methods are problematic and ineffective for two reasons: first, edge-effects near the blemishes cause unpredictable results and may unintentionally include bad data points in the sub-region. Second, and more importantly, low fringe contrast alone is not a clear indicator of invalid data. A second class of data validation techniques uses information obtained from the phase unwrapping to determine which points are to be excluded (Huntley 1989, Kreis and Juptner 1989, Robinson 1993, Charette and Hunter 1996). Given the high computational demand of this technique, and the desire for a more straightforward approach based on the exclusion of the blemishes, a different method is required.

Because the fringe coverage is very good across the entire aperture for all of these measurements, the sub-region determination method chosen for this application uses the intensity of the test beam as an indication of data validity. The test beam image is compared to a low-pass-filtered version of itself, and a threshold is applied to the ratio. In this way, the localized blemishes are quickly removed and the abrupt edges of the domain are easily found. Following the determination of valid data points, a circular region reaching almost to the edge of the domain is selected. This region becomes the *unit circle* in the normalized detector coordinate system (Section 5.2.2). Since the sub-apertures are slightly elliptical (Section 6.2.1) and irregular in shape, some points at the edges are trimmed. Figure 1 shows the sub-regions defined for each sub-aperture according to this method. Points included in the analysis are shown in white. The numbers of individual points used in wavefront fitting on sub-apertures A, B, and C are 279188, 503569, and 224470,

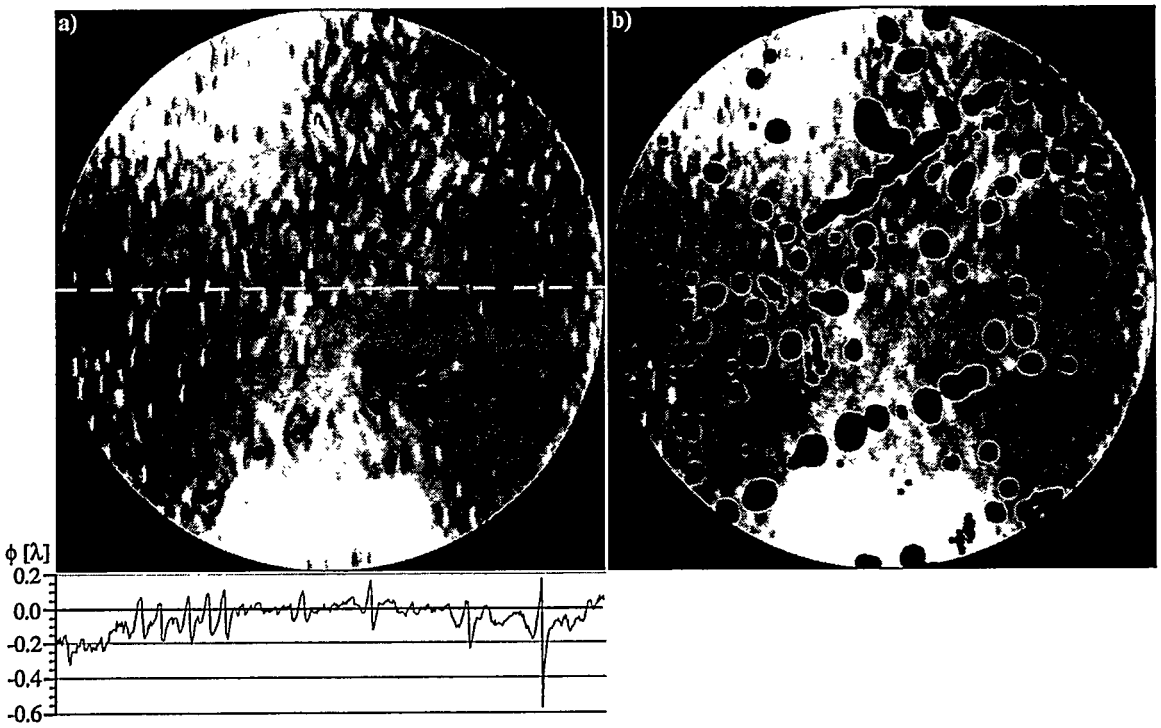

Figure 2. (a) Raw phasemap data from one single phase-shifting series representing sub-aperture A. Only the 659-pixel-wide circular sub-region of data is shown. The line-out below (a) is taken from the middle of the sub-region and shows the magnitude and density of the high-frequency phase components that severely complicate the unwrapping and analysis. The sub-region chosen for analysis eliminates most of the problematic regions, without affecting the measurement of the underlying low-spatial-frequency aberrations. (b) Only the points *included* in the wavefront analysis of this sub-aperture are shown.

respectively. Compare the pattern of these sub-region maps to the test beams shown in Section 6.3.

Once the sub-region is determined, wavefront analysis may be performed. To facilitate understanding of the aberrations present in the system and to reduce the effects of mid- to high-spatial-frequency components, surface fitting to the Zernike polynomials is performed. Figure 2(a) shows a raw unwrapped phasemap from a single phase-shifting series of sub-aperture A; here only the points within the full circular sub-region chosen for analysis are shown. Below Fig. 2(a), the line-out shows the severity of the high-frequency noise present in the raw data. The sub-region chosen for analysis excludes the most problematic points from the raw phasemap. When the troublesome points are excluded, the phasemap appears as in Fig. 2(b).

It is very important to remove bad data points from the sub-regions used for wavefront surface fitting. Wavefront fitting is noticeably affected when these points with their spurious phase values are not removed. The irregular patterns and large numbers of points excluded from the circular sub-regions require that special attention be paid to the polynomials used for the analysis. The Zernike polynomials are *not* orthogonal over these irregular domains, and the simplest methods of polynomial fitting will produce unpredictable results.

7.2.3 *Wavefront Surface Fitting*

Chapter 15 addresses wavefront surface fitting in general, and Section 15.5 describes the Gram-Schmidt process of wavefront surface fitting that is used to fit the conventional set of Zernike polynomials on these irregular domains. Based on the Zernike polynomials, an intermediate set of polynomials is generated that *is* orthogonal over the measurement domain. Once this set is known and the transformation matrix between the two sets has been determined, analysis may be performed with a minimum of uncertainty. The first 37 Zernike polynomial coefficients which describe the low-frequency *figure* aberrations

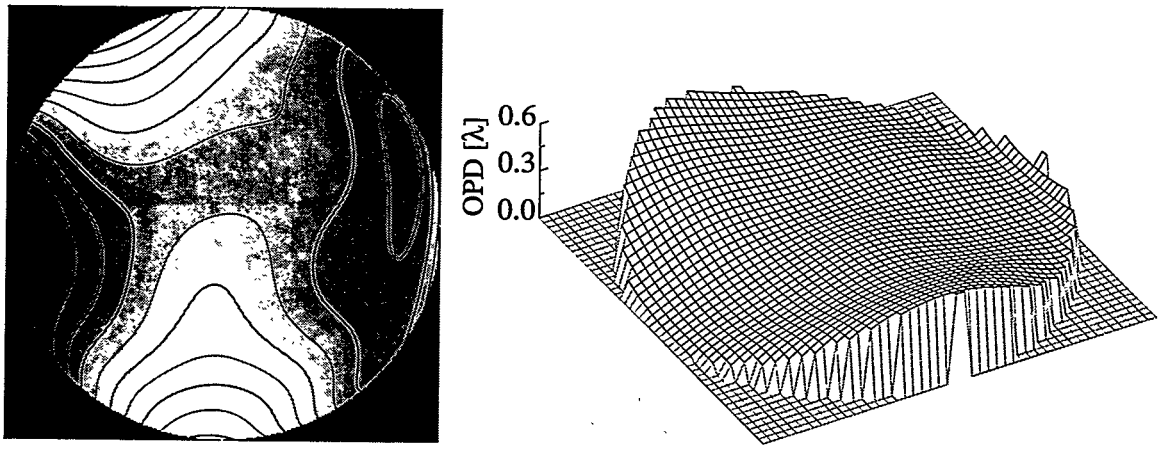

Figure 3. Sub-aperture A. Contour and surface plots of the measured wavefront. The contours are separated by 0.05 waves, or λ/20.

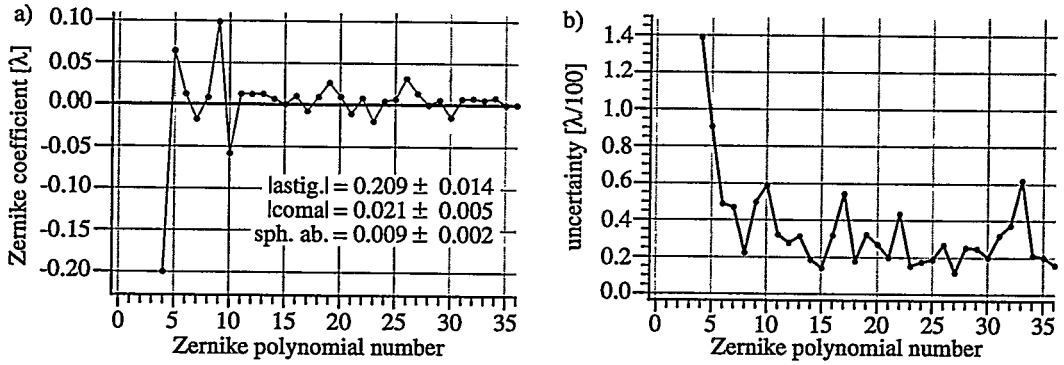

Figure 4. Sub-aperture A. (a) Zernike coefficients are based on 19 phase-shifting measurement series, or 114 individual interferograms. (b) The fitting-coefficient uncertainties are based only on the variations of the measured coefficients from the 19 individual measurements.

Table 1. Sub-aperture A measured wavefront aberration magnitudes. The Zernike coefficient, P-V, and RMS magnitudes with uncertainties are given for each component.

Sub-aperture A: wavefront statistics

σ: 0.099 ± 0.006 λ = 1.32 ± 0.08 nm = λ/10.1 ± λ/166
P-V: 0.593 ± 0.086 λ = 7.94 ± 1.16 nm = λ/1.7 ± λ/12

aberration	Zernike coefficient [λ]	Zernike coefficient [nm]	P-V [λ]	P-V [nm]	RMS [λ]	RMS [nm]
astigmatism	0.209 ± 0.014	2.80 ± 0.19	0.418 ± 0.028	5.60 ± 0.38	0.085 ± 0.006	1.14 ± 0.08
coma	0.021 ± 0.005	0.28 ± 0.07	0.042 ± 0.01	0.56 ± 0.13	0.007 ± 0.002	0.09 ± 0.03
spherical aberration	0.009 ± 0.002	0.12 ± 0.027	0.018 ± 0.004	0.24 ± 0.05	0.004 ± 0.001	0.05 ± 0.01

are calculated for each phase-shifting data set. Comparison and combination of separate measurements are performed using the wavefronts reconstructed from these Zernike coefficients. In this way, spurious mid- and high-spatial-frequency contributions are removed.

7.2.4 *Sub-Aperture A*

Sub-aperture A is considered to be the most important sub-aperture of the 10× Schwarzschild objective. Based on the results of visible light interferometry, performed by Tim Gleason at Telandic, this 0.07 NA sub-aperture was predicted to have nearly diffraction-limited performance.

Nineteen separate phase-shifting measurements, or 114 individual interferogram exposures, are combined to form the wavefront phasemaps shown in Fig. 3. All of these measurements are from the "downstream" field point, using pinholes A and B. The average of twelve measurements from pinhole A are combined with the average of nine measurements from pinhole B to remove the geometric coma systematic error.

The wavefront phasemaps shown in Fig. 3 are generated from the first 37 Zernike polynomials shown

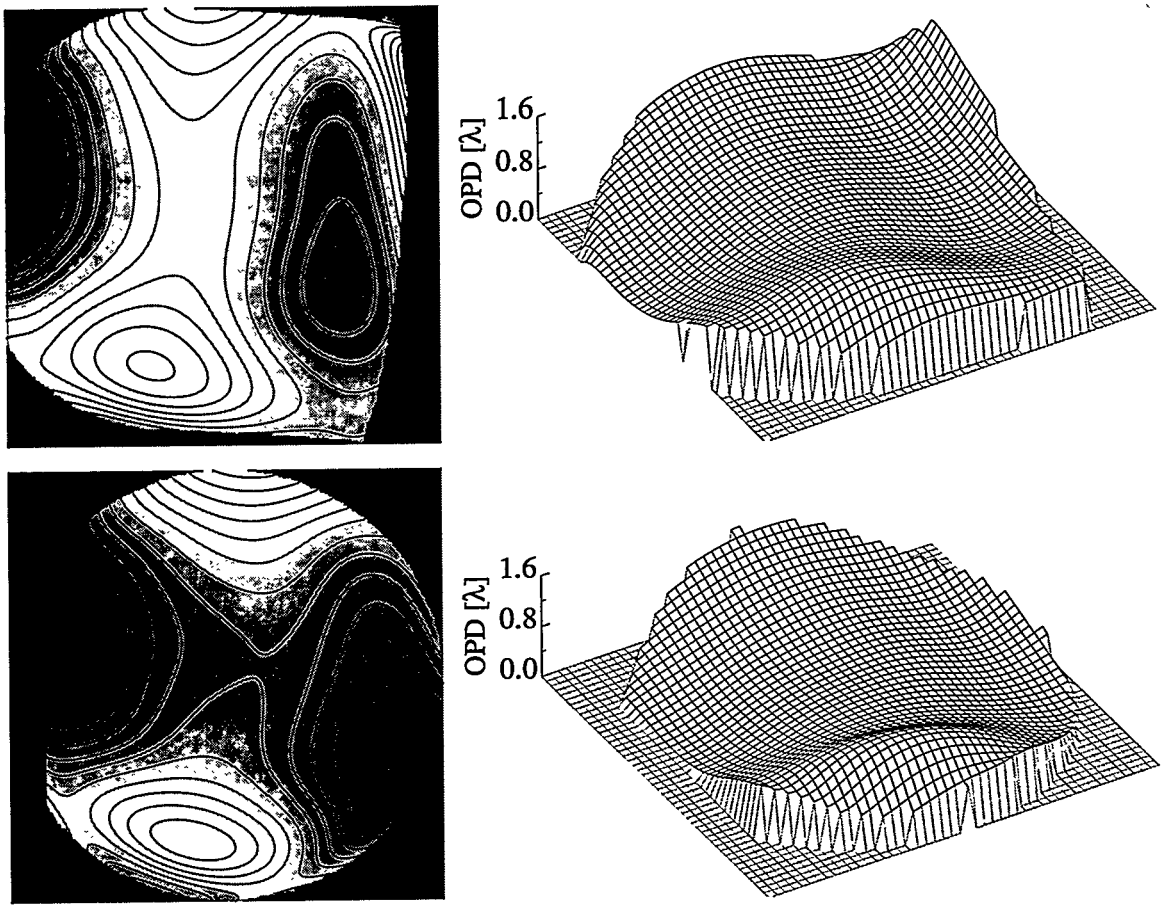

Figure 5. Sub-aperture B. Contour and surface plots of the measured wavefront. (Above) The wavefront over the whole "D"-shaped aperture. (Below) Measurements over a circular sub-region of the full aperture, excluding the inner-most portion. The contours are separated by 0.1 waves, or λ/10.

in Fig. 4(a). The position-dependent piston, tilt, and defocus components are removed from the analysis. Table 1 shows the aberration magnitudes and measurement uncertainties for the low-ordered aberration components. Here, astigmatism is the dominant aberration component, with 0.418 waves P-V, or 0.085 waves RMS.

Qualitative verification of the measured aberrations comes from the imaging experiments performed with this sub-aperture. These experiments are described in Section 7.3.

7.2.5 *Sub-Aperture B*

Sub-aperture B was designed to have a 0.08 NA circular pupil, but the pupil-defining aperture was broken during fabrication and the pupil shape became a "D" facing away from the optic axis of the Schwarzschild objective. Unfortunately, near the outer edge of the aperture, in the area designed to be blocked by the aperture, the wavefront has a high degree of curvature in one direction.This curvature *significantly* complicates interferometric measurement of this sub-aperture.

PS/PDI measurements require that the aberrations be small enough that the test and reference beams are well-separable given the fixed image-plane spacing between the reference pinhole and the window. Where aberrations are large, this separation distance must be increased. Although the 4.5-μm center-to-center spacing of the reference pinhole and window is adequate for the measurement of the other sub-apertures, here it is too narrow. The high curvature of the wavefront along one direction certainly elongates the focal spot in that direction. Since the measurements are performed in two orientations of the beam separation, the problems are limited to the one orientation in which the beam separation is parallel to the beam elongation: this is where the overlap is most severe. In the orthogonal orientation, the overlap is not an impediment to measurement.

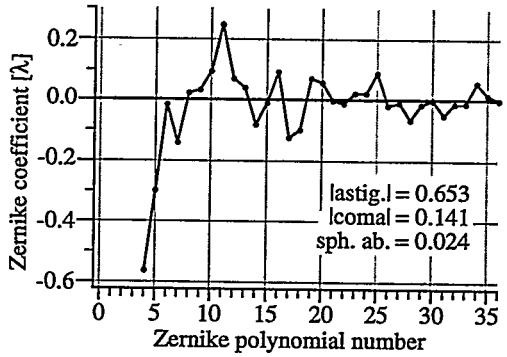

Figure 6. Sub-aperture B. Zernike coefficients based on 9 individual interferograms are reported for a circular sub-region of the "D"-shaped aperture.

Due to a misalignment of the CCD detector, interferometric data is not available for the innermost portion of the aperture. From the available data, two wavefront surfaces are presented in Fig. 5. The upper surface represents the measured

Table 2. Sub-aperture B measured wavefront aberration magnitudes.

Sub-aperture B: wavefront statistics for the full aperture

σ:	0.260 λ =	3.49 nm =	~λ/3.8
P-V:	1.392 λ =	18.65 nm =	~7λ/5

Sub-aperture B: wavefront statistics for the circular sub-aperture

σ:	0.290 λ =	3.88 nm =	~λ/3.4
P-V:	1.344 λ =	18.01 nm =	~4λ/3

	Zernike coefficient		P-V		RMS	
aberration	[λ]	[nm]	[λ]	[nm]	[λ]	[nm]
astigmatism	0.635	8.51	1.270	17.02	0.259	3.47
coma	0.141	1.89	0.282	3.78	0.050	0.67
spherical aberration	0.024	0.32	0.048	0.64	0.011	0.14

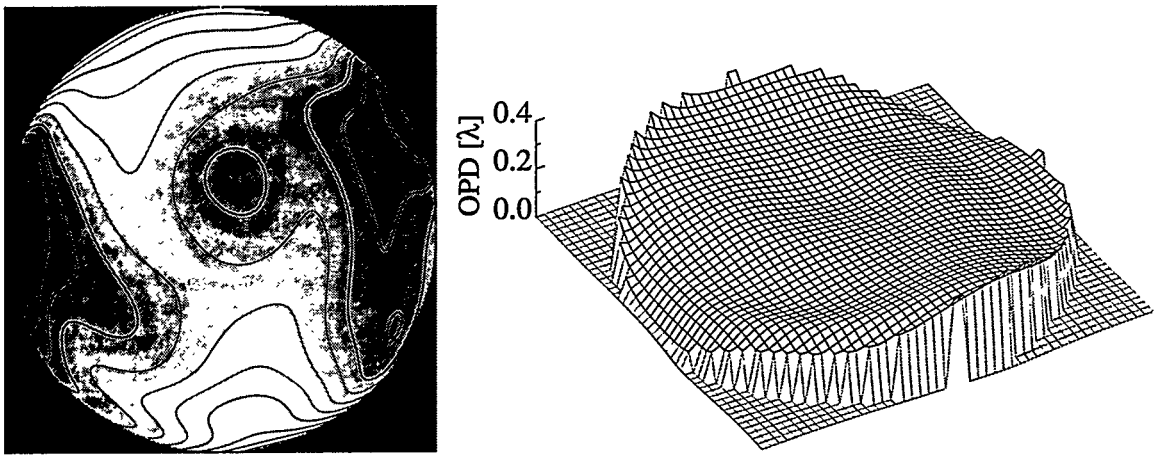

Figure 7. Sub-aperture C. Contour and surface plots of the measured wavefront. The contours are separated by 0.025 waves, or λ/40.

wavefront across the entire "D"-shaped pupil. The lower surface imposes a circular sub-region on the measured domain to approximate the wavefront characteristics that would have been observed if the aperture had not been broken. Wavefront statistics for the circular sub-region are shown in Table 2, based on the Zernike coefficients shown in Fig. 6. No error estimate is given for the Zernike coefficients presented here because only one pair of phase-shifting data series (10 interferograms) was combined to compute the wavefront.

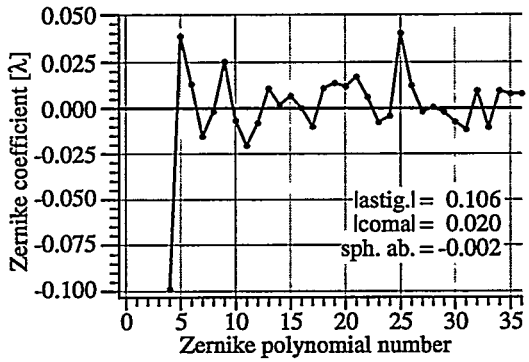

Figure 8. Sub-aperture C. Zernike coefficients are based on 10 individual interferograms in two phase-shifting series.

Table 3. Sub-aperture C measured wavefront aberration magnitudes.

Sub-aperture C: wavefront statistics

σ:	0.048 λ	= 0.64 nm	= ~λ/21
P-V:	0.367 λ	= 4.92 nm	= ~λ/2.7

	Zernike coefficient		P-V		RMS	
aberration	[λ]	[nm]	[λ]	[nm]	[λ]	[nm]
astigmatism	0.106	1.42	0.212	2.84	0.043	0.58
coma	0.020	0.27	0.041	0.54	0.007	0.10
spherical aberration	-0.002	-0.02	-0.003	-0.04	-0.001	-0.01

7.2.6 *Sub-Aperture C*

The third and smallest sub-aperture, designed for 0.06 NA, was found to have the smallest wavefront aberrations of the three sub-apertures tested. The wavefront aberrations are smaller than over any other equivalent 0.06 NA region of the other two sub-apertures. Figure 7 shows the wavefront phasemap. The wavefront statistics are given in Table 3, and the Zernike polynomial coefficients are shown in Fig. 8. Again, no error estimate is given for the Zernike coefficients because only one pair of phase-shifting data series (10 interferograms) was combined to compute the wavefront.

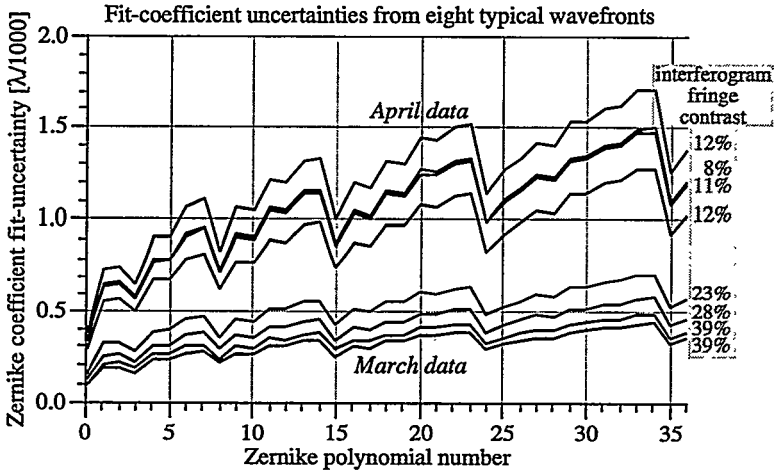

Figure 9. Uncertainties in the wavefront surface fit coefficients are shown for eight typical phase-shifting measurements of sub-aperture A. The uncertainties are based on the fit variance, as described in Section 15.6. The qualitative difference between the March and April measurements is related to an overall decrease in the fringe contrast observed in the April measurements. The fringe contrast in the corresponding interferograms is shown next to each set of uncertainties. The relationship between fringe contrast and coefficient uncertainty is investigated in Section 8.11.

7.2.7 *Measurement Precision*

Estimation of the wavefront measurement precision is performed on several fronts; this is the primary subject of Chapter 8. Experimentally, the dominant effect is the measurement-to-measurement variation that is observed in the wavefront fitting data. The other contribution to the uncertainty comes from the fit-variances related to noise in the raw data. Because there are so many data points under consideration and the data is of relatively high quality after localized blemishes are removed, the contributions from the fit-variances are *significantly* smaller than from the former effect.

Only sub-aperture A was measured a sufficient number of times for an ensemble of measurements to be compiled. The standard deviation for each individual Zernike polynomial coefficient of the measurements made of this sub-aperture is plotted in Fig. 4(b) (Section 7.2.4). With a magnitude of 0.014 waves (0.188 nm, or ~λ/70), the uncertainty is largest in one of the two astigmatism coefficients. For the others, the typical uncertainty values are roughly 0.003 waves (0.040 nm, or ~λ/300).

The less significant contribution to the uncertainties is that associated with the fit-variance, as described in Section 15.6. Here the uncertainties are related to the quality of the fit, dependent essentially on the mid- and high-spatial-frequency noise in the data. As each individual phase-shifting data series is analyzed and the wavefront surface fitting is performed, the uncertainty in each coefficient is calculated.

The coefficient uncertainties for eight typical phase-shifting series from the measurement of sub-aperture A are shown in Fig. 9. There is a clear distinction in the magnitudes of the coefficient uncertainties between the March and April data sets. These two separate sets of measurements are described in Section 8.6. Experimental evidence suggests that the discrepancy is strongly dependent on differences in the observed interferogram fringe contrasts. This point is investigated further in Section 8.11. Only data from the March data sets were used to compile the sub-aperture A phasemap shown in this chapter. For these measurements the *largest* coefficient uncertainty is below 7.5×10^{-4} waves (0.010 nm, or ~λ/1300).

Thus it is clear that the contribution from the fitting uncertainty is *much* less than from the measurement-to-measurement variation. It is important to note here that although the fitting uncertainty in the April data is more than twice as large as in the March data, the measured wavefront difference between the two data sets is only 0.018 waves RMS (0.241 nm, or ~λ/57) and the differences in the measured Zernike coefficients have a typical value below 0.005 waves (0.067 nm, or λ/200) (Section 6.6.2).

7.2.8 *Zonal Fabrication Error*

The presence of astigmatism as the dominant term in each measured sub-aperture suggests a trend characteristic of this annular Schwarzschild objective as a whole. As the system is aligned for the measurement of each sub-aperture, the reference pinhole is placed in the position that produces the best fringe contrast in the interferogram. For an astigmatic wavefront, characterized by a *cylindrically-shaped* aberration, this is the position that *balances* the defocus components in the two orthogonal directions of the astigmatism. Adding a small amount of defocus to the measured wavefront is equivalent to a longitudinal translation of the reference pinhole, placing it closer to the *best focus* in one of the two directions (i.e. the *tangential* or *sagittal* focus).

Figure 10(a) shows the three measured wavefronts rotated into their proper orientation and placed in position within the three-aperture pupil. By adding a small amount of defocus to each measured wavefront and observing the resulting annular pattern, shown in Fig. 10(b), it is possible to argue that the astigmatism measured in each sub-aperture comes from an overall *zonal error* in the optical system. This small error, of magnitude less than λ/2, or ~7 nm, could be a figure error in either of the optical substrates, or could be related to multilayer thickness variations. Verification of an overall zonal error can only be made

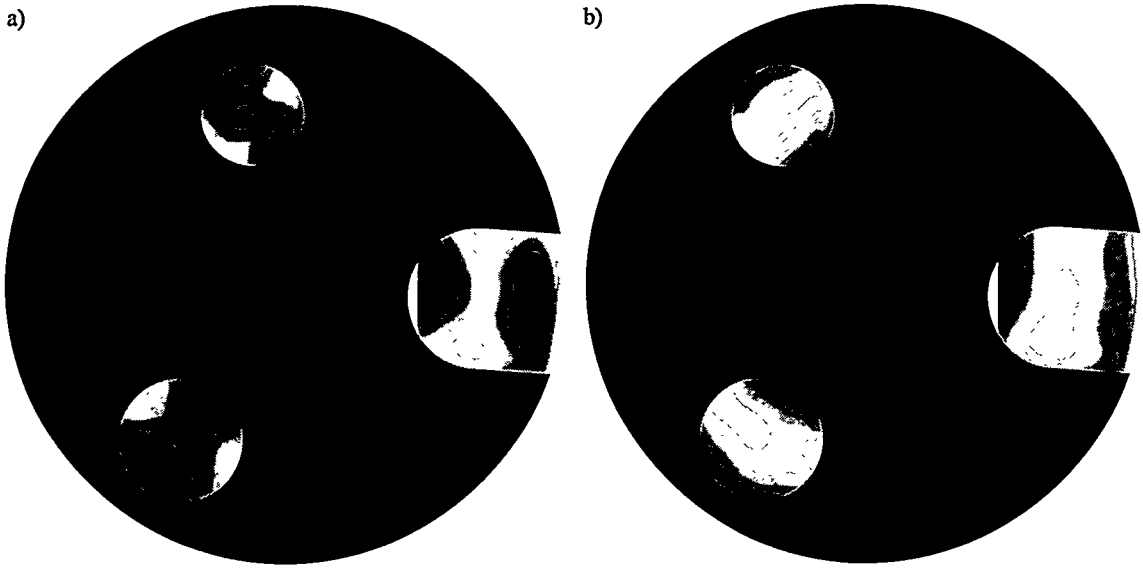

Figure 10. (a) Measured wavefront phasemaps of the three sub-apertures of the 10× Schwarzschild objective oriented and positioned within the pupil-defining aperture. (b) Adding a small amount of defocus to the measured astigmatic phasemaps reveals the possibility of a zonal fabrication error in the annular optic.

by the simultaneous measurement of all three sub-apertures, or by measurements made with very close attention to the absolute coordinates of the reference pinhole. Neither is possible at this point, so the existence of a zonal error can be no more than a reasonable conjecture.

It is much more likely that a zonal error would be caused by an error in the substrate figure than by the multilayers, since any changes in the multilayer thickness capable of producing a $\lambda/2$ phase variation would most likely be accompanied by a loss in reflectivity. Such reflectivity changes are not observed. Furthermore, the multilayer thicknesses were measured after deposition and were observed to meet the design specifications. The substrate figure may not have been measured with an accuracy high enough to observe fabrication errors of this small size.

7.3 IMAGING EXPERIMENTS

At the conclusion of the interferometric measurements, the 10× Schwarzschild objective was brought to Sandia National Laboratory, in Livermore, California, to perform imaging experiments using the 10×I EUV imaging system (Tichenor et al. 1993, 1994), shown schematically in Fig. 11. The "10×I" Schwarzschild objective designed to be used in the Sandia system shares the same optical design as the Berkeley "10×B", and the mechanical housings are similar enough that installation of 10×B in the Sandia system is trivial.

The Sandia system uses a laser-produced plasma source. Light is collected by an ellipsoidal condenser and directed toward the reflective EUV test-pattern mask with a near-45° turning mirror. The system uses Köhler-type illumination with a partial coherence factor near 0.5. As with the interferometry experiments, here too the Schwarzschild objective is oriented vertically and is illuminated from below. A photoresist-coated wafer rests on the three-ball mount at the top of the optic and records the image of the mask. A manually-adjusted translation stage literally pushes the wafer forward in one direction, allowing multiple exposures to be made on a single wafer.

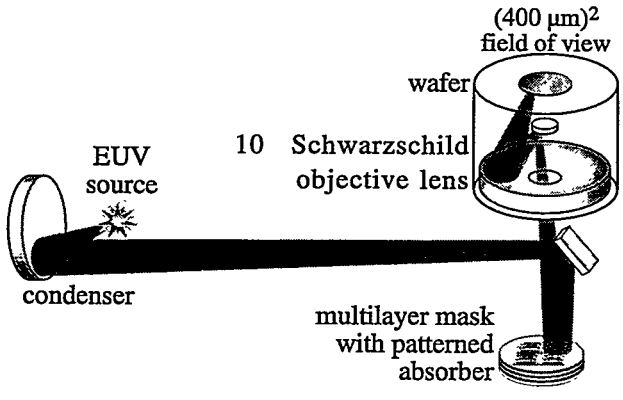

Figure 11. A schematic representation of the key components of the Sandia 10×I EUV imaging system. The system utilizes a laser-plasma source and reflective multilayer-coated optics to illuminate the mask which is patterned on a reflective multilayer-coated substrate. A 10×-demagnification Schwarzschild objective (such as the 10×B, Berkeley objective) is used to project an image of the mask onto a photoresist-coated wafer that rests on a three-ball mount at the top of the objective. The longitudinal (vertical) position of the mask may be adjusted to bring the image of the mask into focus on the wafer. The 10×B objective was brought to Sandia to perform imaging experiments using this system.

7.3.1 *Experimental Results and Predicted Behavior*

Comparison of the recorded results with the predicted performance shows very good agreement. The results of imaging experiments at the resolution limit of the system are presented in this section.

The choice of the negative-tone, chemically-amplified resist SAL 601 was a compromise between sensitivity and resolution. With 100-nm-thick resist the images appear grainy, but the essential features are clearly visible in SEM micrographs. Figure 12 shows a line-and-space pattern of 0.2-μm pitch, where the smallest individual features are 0.1-μm wide.

The performance of the system and the predictive powers of the interferometry are more clearly revealed in images of an *Archimedes star* test pattern, shown in Fig. 13. On a single wafer, images were recorded at multiple focal positions, with a 1-μm increment. Focal adjustments were actually performed by longitudinal translation of the mask in 100-μm steps, which is nearly equivalent to a 1-μm longitudinal translation of the image plane, with a very slight change in the magnification (power).

Sub-aperture A was the only aperture used for these imaging experiments. The wavefront aberrations in this sub-aperture are dominated by astigmatism of 0.418 waves P-V, or 0.085 waves RMS. Astigmatism causes the focusing properties to be different along two orthogonal directions. The primary characteristic of an optical system containing astigmatic aberrations is that the longitudinal positions of best-focusing occur at separate planes for the two directions of the astigmatism. In other words, horizontal and vertical features (for example) form their sharpest images in different planes. This effect is clearly observable in the SEM micrographs of Fig. 13. Here, when the system is a few microns out of focus, the sharpness of the thinnest features is noticeably different in the horizontal and vertical directions. On opposite sides of focus, the two directions reverse roles. The asymmetry of these features in passing through focus can be attributed to an

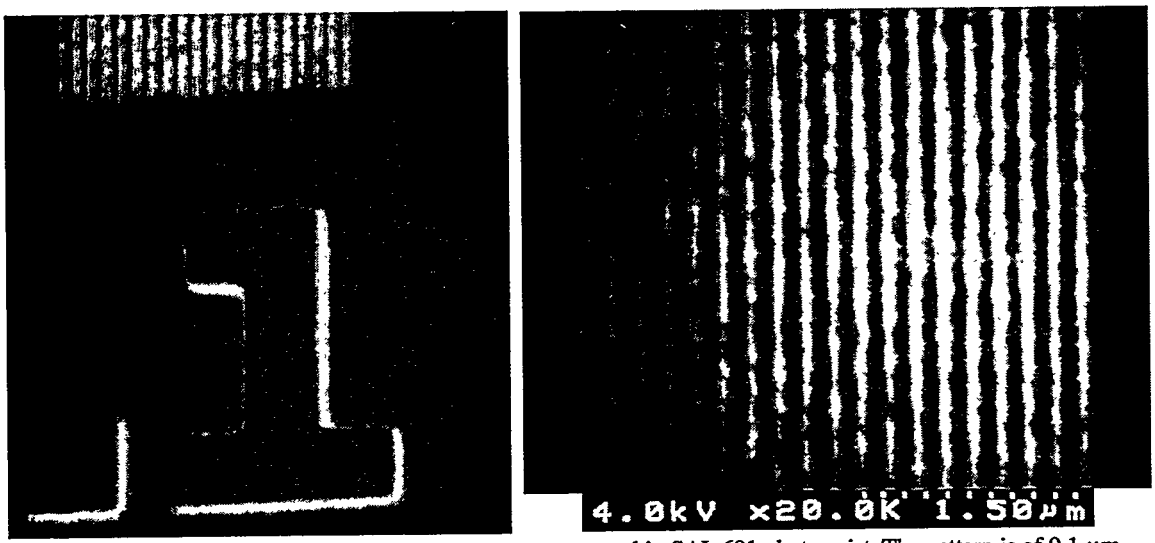

Figure 12. SEM micrographs of a resolution test pattern exposed in SAL 601 photoresist. The pattern is of 0.1-μm lines and spaces. The image on the right is a detail of the region at the top of the image on the left.

unintended difference in the exposure dose.

Based on the measured wavefront at 0.07 NA, an illumination partial coherence factor of 0.5, and 13.4-nm wavelength, detailed calculations were performed to predict the imaging behavior of 10×B (Tejnil et al. 1997) with the Archimedes star resolution test image. These calculations were performed using the SPLAT imaging simulation program developed at the University of California, Berkeley. The simulation yields the predicted field amplitude in the wafer plane. Adjacent to each exposure measurement, Fig. 13 shows several predictions of the imaging quality based on the application of simple threshold values to the predicted field intensity. With a unit intensity bright-field image, the thresholds are intended to simulate the behavior of the resist. Given the limitations of the resist material and the uncertainties in the exposure and development processes, comparison of the simulations with the SEM micrographs shows excellent agreement.

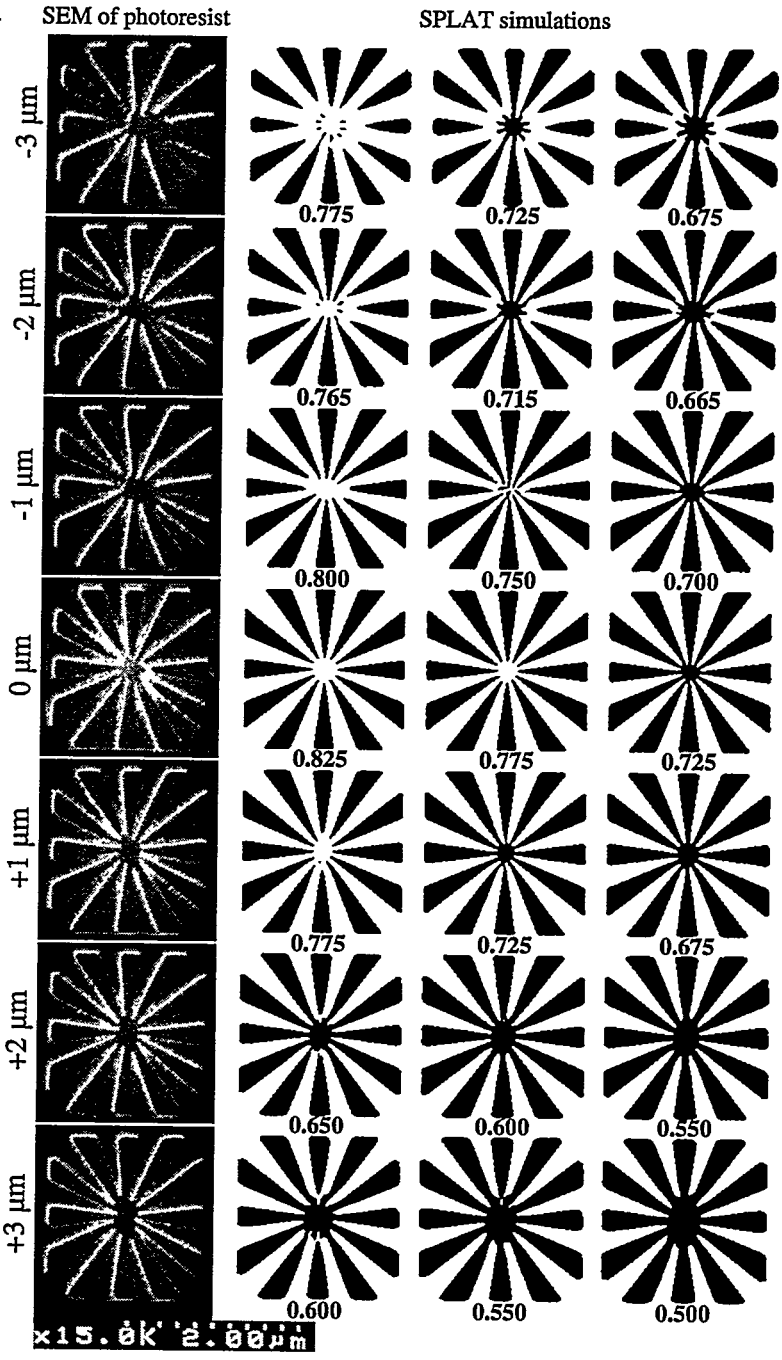

Figure 13. (Left column) SEM micrographs of an *Archimedes star* resolution test pattern, measured at seven positions through-focus. The amount of defocus is indicated at the left of each image. The characteristics of the astigmatic wavefront are clearly observable in the pattern: the horizontal features are sharpest when the system is defocused by 3 µm in the *negative* direction, while the vertical features are sharpest at 3 µm in the *positive* direction. Simulations of the imaging properties are shown to the right of each image. A simple threshold is applied at three levels to the predicted field intensity to model the behavior of the photoresist with different exposure doses. Based on a unit intensity bright field, the threshold values are shown below each simulation image. The qualitative agreement between the predictions and measurements is very good.

8

Interferometer Performance and Characterization

8.1 RANDOM AND SYSTEMATIC ERROR MEASUREMENT

This chapter describes a number of experiments that are performed to characterize the magnitude and effect of random and systematic errors on the performance of the interferometer. Of the random errors, the most significant stem from the spatial filtering of the reference wavefront by the reference pinhole and the spatial filtering of the illumination wavefront by the object pinhole. Direct measurements of these effects place bounds on the system's sensitivity to alignment.

In principle, each optical component of the interferometer is capable of introducing its own systematic error into the wavefront measurements. Both mechanical and optical concerns are paramount. Experiments (described here) are performed to assess the mechanical and thermal stabilities of the system. Systematic errors potentially contributed by the grating beamsplitter are investigated in the comparison of the zero-order reference to the first-order reference PS/PDI configurations. As an indication of the sensitivity of the wavefront measurements, the geometric coma systematic error is examined.

Finally, the analysis methods themselves are investigated: the performance of the complex methods described in Section 12.5 is compared to the conventional, simple methods described in Section 12.2. The Fourier-transform method (Section 11.3) is also compared to the phase-shifting analyses.

In many of the experiments described in this section, the Fourier-transform method of single interferogram analysis is used to extract the wavefront from individual measurements. In nearly all cases described here, the uncertainties introduced by this analysis method are significantly smaller then the effects being measured. Furthermore, fitting the resultant wavefront data to the Zernike polynomials (Chapter 15) reduces noise and high-frequency variations in the data.

8.2 REFERENCE PINHOLE SPATIAL FILTERING

It is known that pinhole size affects the quality of the reference wavefront. While theoretical calculations help to establish the relationship between pinhole size and predicted wavefront quality, the *actual* quality of the spatial filtering can only be assessed *in situ*. One simple way to perform such measurements is by the intentional misalignment of the reference pinhole about the focus of the reference beam. An ideal spatial filter produces a spherical wavefront regardless of how it is illuminated. Experimentally, however, it has been shown that the alignment *does affect* the wavefront measurements. This is not at all unexpected, considering the fact that measured reference pinhole sizes (Section 6.4.2) are larger than the sub-100-nm target size.

Presently, when the interference patterns are recorded fine alignment is performed to optimize the appearance of the fringes, as judged by the operators of the interferometer. Hence, it may be said that the position of the pinhole is arbitrary within a small domain of positions that produce analyzable and reason-

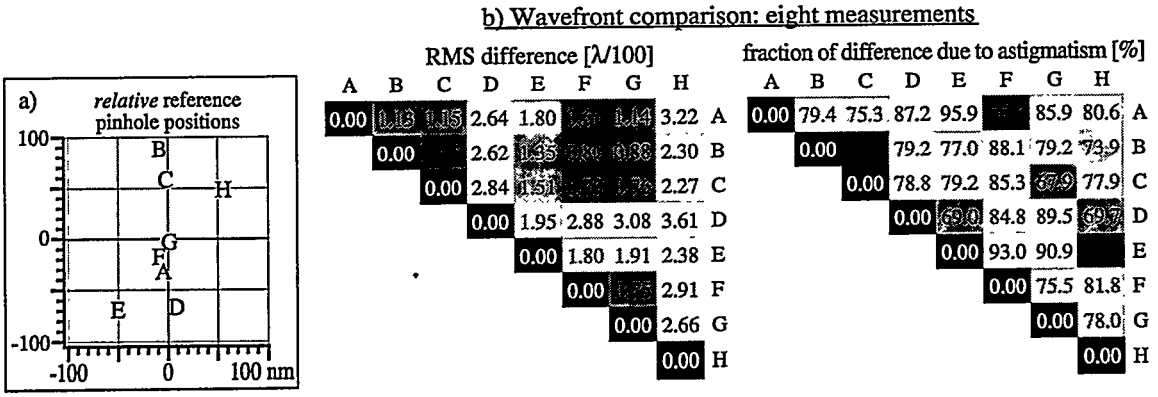

Figure 1. Assessment of the spatial-filtering properties of the reference pinholes is performed by comparing the interferometrically-measured wavefront recorded at several de-optimized pinhole positions within the focus of the reference beam. (a) Small translations produce a measurable change of tilt, allowing the arbitrary *relative* positions of the pinhole to be determined. (b) Analysis of the *difference wavefronts,* computed for all pairs of measurements, indicates the expected variability or uncertainty in the wavefront measurements. The largest reported RMS displacement values of the difference wavefront are on the order of λ/30 and the average value is 0.0186 waves. Most of the RMS difference comes from the astigmatic component. The fraction of the RMS related to astigmatism is also shown. Experimental wavefront variations are expected to be smaller than these values because the reference pinhole position is optimized before measurement.

ably high-quality interferograms. Intentional translation of the pinhole to positions within this small domain gives a qualitative assessment of how sensitive the wavefront measurements are to the position of the reference pinhole.

To establish an upper bound on the wavefront uncertainty, the reference pinhole is moved as far from the optimum as possible without losing the fringe pattern. Experimental uncertainties may thus not be this large in practice.

Figure 1 shows the results of this test as performed using Pinhole D and the 0.07 NA sub-aperture A. The reference pinhole was moved to eight separate arbitrary positions and a single interferogram was recorded at each. Analysis was performed using the Fourier-transform method of single interferogram analysis with a Gaussian filter $1/e^2$ radius of 8 cycles in the spatial-frequency domain. The eight measured wavefronts, labeled A through H, were compared, with the piston, tilt, and defocus terms subtracted. The RMS displacement of the *difference wavefronts* are shown in Fig. 1 for each pair. The largest difference is 0.0361 waves (0.484 nm, or ~λ/28); the average measured difference among all of the comparisons is 0.0186 ± 0.0093 waves (0.249 nm, or ~λ/53).

The relative positions shown in Fig. 1(a) are inferred from the measured tilts and an assumed measurement NA of 0.066 (based on the 0.07 NA sub-aperture and the size of the sub-region used for analysis). The positions are determined from an easily-derived expression: with small NA, the path length difference ΔR is

$$\Delta R[\lambda] = \frac{NA}{\lambda}(x,y)\cdot(Z_1,Z_2)\,. \qquad (1)$$

Z_1 and Z_2 are the Zernike polynomial x- and y-components of the tilt, and (x, y) is the lateral displacement vector. The distribution width of these points indicates that the largest tolerable pinhole displacements are on the order of 175 nm.

The wavefront variation shown here indicates that from any *single* interferogram measurement, an uncertainty of approximately 0.02 waves RMS (0.268 nm, or $\lambda/50$), should be expected. Since the reference pinhole position in the beam is adjusted before each series of measurements, this uncertainty becomes a random error source. The implications of this result for phase-shifting measurements, which incorporate several (typically 5) interferograms together in a single measurement, are not clearly discernable.

Inspection of the individual difference wavefronts reveals that the dominant aberration component is always astigmatism. In general, the disagreements between any two measured wavefronts are dominated by variations in the measured astigmatism. The fraction of astigmatism in the RMS differences is shown in Fig. 1(b) for each measurement pair. These fractions are between 50 and 96%, with most above 75%. This astigmatism problem is discussed in Section 8.13.3.

8.3 OBJECT PINHOLE SPATIAL FILTERING

A similar set of experiments can be performed to assess the quality of the spatial filtering performed by the object pinhole in generating a spherical illuminating wavefront. By incorporating alignment positions far from the optimum, these simple tests provide an upper bound on the expected measurement uncertainty. Although variations from only one component are of interest, these experiments involve two components of the interferometer. When the object pinhole is displaced laterally, the position of the reference beam focus in the image-plane also moves. The sensitivity of the wavefront measurements to the position of the reference pinhole, demonstrated in Section 8.2, necessitates re-optimization of the reference pinhole position for each measurement. Thus there is no simple way to isolate the effect of the object pinhole alone.

These tests were performed using sub-aperture A. The results of two object pinhole displacement experiments are shown in Fig. 2. Once again, the Fourier-transform method of single interferogram analysis is used (Section 8.2). The intensity in a lateral plane near the K-B focus is measured by scanning the object pinhole, using a photodiode to record the transmitted flux at each position. In each test, five object pinhole positions (A through E) are sampled, as shown in the Fig. 2. The stage is calibrated and the positions are known to within 1 μm. As before, the RMS displacement of the *difference wavefronts* are calculated for each pair of measurements, with piston, tilt, and defocus terms removed.

For Test #1, the average RMS difference is 0.0061 ± 0.0013 waves (0.0819 ± 0.0178 nm, or $\sim\lambda/164$). For Test #2, the average is 0.0143 ± 0.0049 waves (0.1918 ± 0.0654 nm, or $\sim\lambda/70$). Since the object

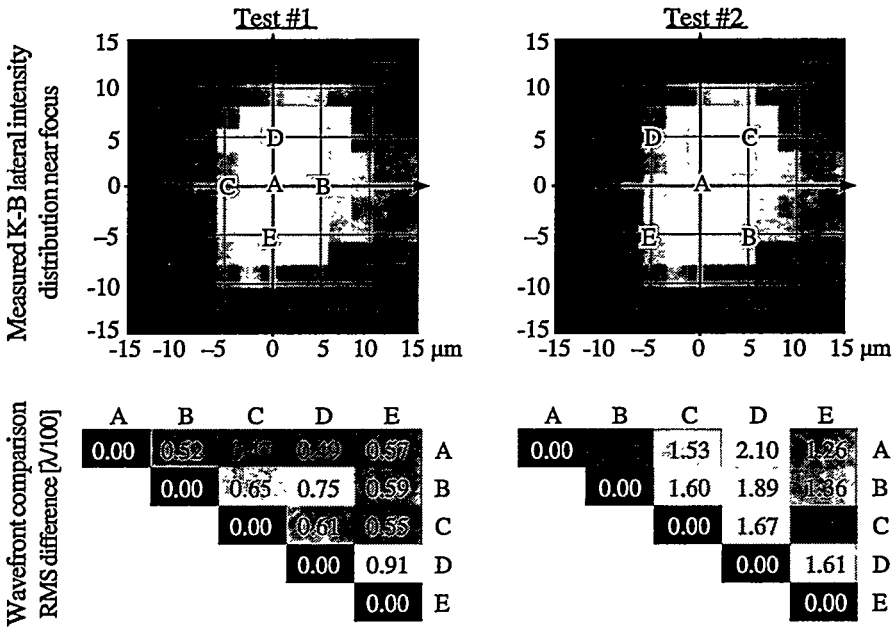

Figure 2. To assess the quality of the object pinhole spatial filter, two separate experiments were performed in which the object pinhole was translated laterally in the vicinity of the K-B focus. (Above) The positions within the measured K-B intensity profile are indicated by the letters A through E in each test. For each measurement, the position of the reference pinhole was re-optimized and the wavefront was calculated. (Below) Comparisons of the wavefront measurement pairs, with piston and tilt removed, are shown in terms of the RMS displacement of the difference wavefronts. The discrepancy in the typical difference-magnitudes observed within each test is attributable to the fact that different object *and* reference pinholes were used in each case.

pinhole position is seldom adjusted during the course of many measurements, this uncertainty enters the experiment as a systematic error source. In practice, the actual wavefront variation will be much smaller than the wavefront variation caused by the intentional displacement of the object pinhole.

8.4 THROUGH-FOCUS EXPERIMENTS

An important test of the spatial filtering properties of the object pinhole is one that examines the dependence of the measured wavefront on the longitudinal, or *focal*, position of the object pinhole. Because the reference pinhole remains stationary in the image-plane, translating the object pinhole causes only the test beam to focus above or below the image-plane.

Since the window is very large compared to the focal spot diameter, within a broad range of focal positions the window transmits the test beam with almost no dependence on the focal position. The tiny reference pinhole, however, defines a stationary center-of-curvature for the reference beam. Thus with their longitudinal centers-of-curvature displaced, the test and reference beams acquire a small amount of *defocus*. The defocus magnitude is easily derived for small NA. In waves, the path-length-difference is

$$\Delta R[\lambda] = \frac{z\,NA^2}{4\lambda} Z_3 . \qquad (2)$$

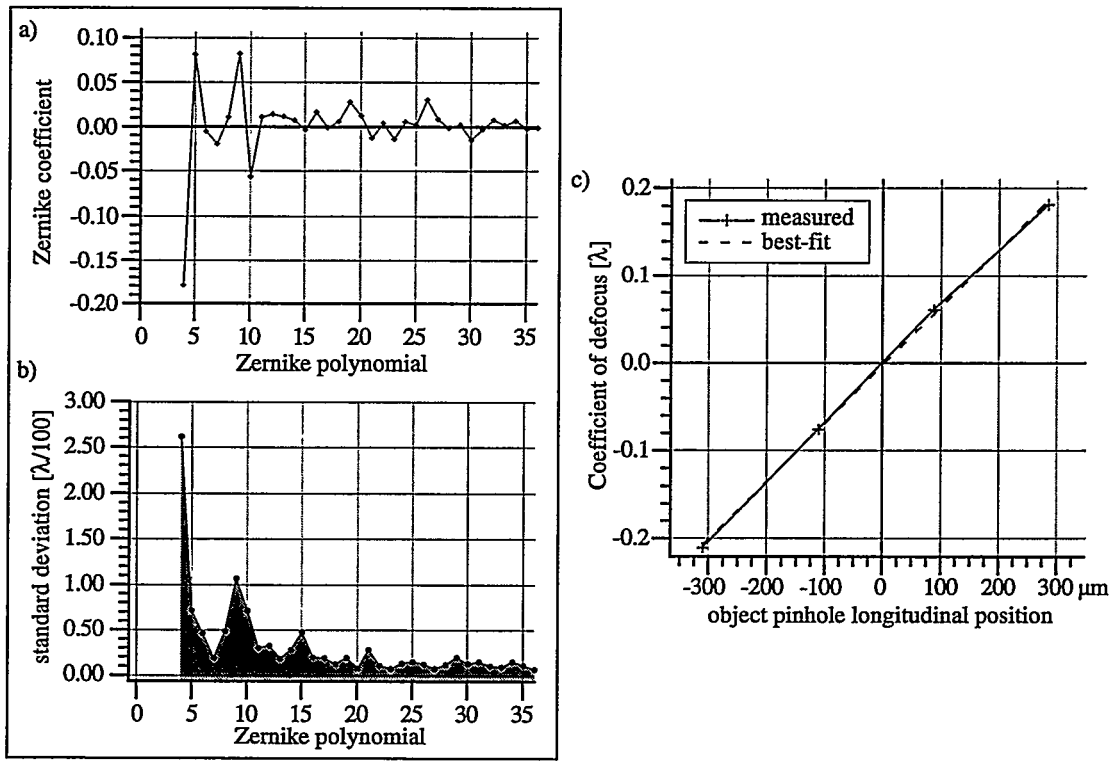

Figure 3. Wavefront measurements recorded as the longitudinal position of the object pinhole is adjusted are used to assess the sensitivity of the system to defocus. For each measurement, the position of the reference pinhole was also re-optimized. (a) A comparison of the Zernike polynomial fits to the four measured wavefronts shows excellent agreement of the aberration coefficients. (b) The magnitude of the differences in these coefficients is shown. The longitudinal position is known via the calibrated stage and the measured defocus, which depends linearly on the longitudinal position. (c) The measured defocus follows the longitudinal position linearly, as expected. However, the slope indicates a *measurement NA* of 0.060 on the image-side, which is smaller than expected.

z is the longitudinal displacement, and Z_3 is the Zernike polynomial corresponding to defocus.

Figure 3 contains the results of this experiment, again performed using sub-aperture A.The object pinhole was translated vertically by a total of 594.5 μm, and four individual interferogram measurements were made. Here, as in Section 8.3, the experiments require re-optimization of the reference pinhole after each longitudinal translation. Thus the added uncertainty introduced by the reference pinhole effects are incorporated in these results. Figure 3(a) shows the average of the measured Zernike polynomial coefficients, excluding piston, tilt, and defocus. The very small standard deviations of each term (determined by the four measurements) are shown in Fig. 3(b).

Figure 3(c) shows the measured Zernike coefficient of defocus versus the longitudinal position of the object pinhole and reveals a discrepancy in the measurement. The slope of the best-fit line is 6.626×10^{-4} waves/μm. Using Eq. (2), at 13.4 nm wavelength, this slope indicates a measurement NA of 0.0060 on the object side or 0.060 on the image-side. Based on the maximum width of the illuminated area in the recorded data (702 pixels) and on the size of the circular sub-region used for analysis (659 pix-

els), the predicted *measurement NA* is 0.066 within this "0.07 NA sub-aperture." At the time these experiments were conducted, the NA was not accurately known from other means; it is therefore possible that the numerical apertures under consideration are actually smaller than expected, by as much as 9%.

8.5 MECHANICAL STABILITY: DRIFT

Care was taken to design the interferometer to be rigid and isolated from vibration. Separate from the motions of the source and the beamline, the most critical positions are the *relative* locations of the object pinhole with respect to the Schwarzschild test optic and of the image plane pinholes. Recalling that the image-plane pinholes are mounted to the test optic, the most likely source of drift in the system is the position of the object pinhole with respect to the test optic. Clearly, the best way to measure the importance of drift in the interferometer system, and probably in *any* interferometer system, is to observe changes in the measured wavefront *in situ.*

Several such experiments were performed; the results of one are shown in Fig. 4. Here, the positions of the pinholes and the test optic are optimized and then not adjusted for ten minutes. A single interferogram measurement is made once every two minutes for a total of six measurements; each wavefront is compared

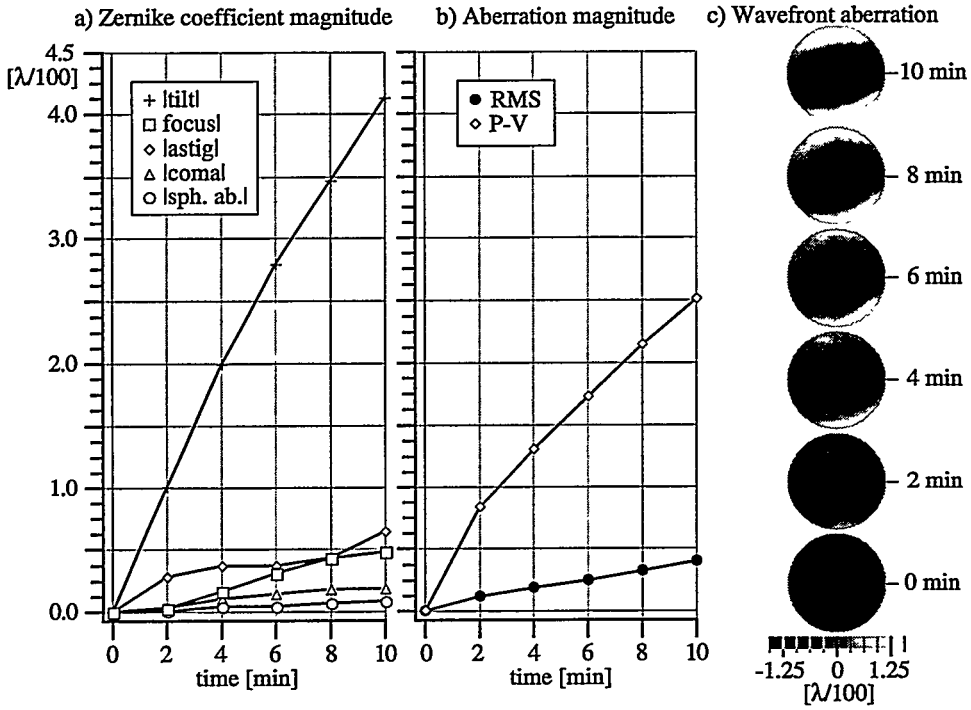

Figure 4. *In situ* measurement of mechanical stability is performed by observing changes in the measured wavefront over time, as the system is left undisturbed in one position. Changes are recorded with respect to the first measured wavefront (time = 0 min). (a) The magnitude of the change in tilt indicates a lateral drift of approximately 90 nm in 10 minutes. (b) With the tilt component removed from the analysis, the RMS and P-V displacements of the measured wavefronts are also shown. In ten minutes, the RMS difference did not exceed λ/200. (c) The difference wavefronts are plotted using a consistent grayscale.

to the first. The wavefronts are calculated using the Fourier-transform method with a narrow Gaussian filter $1/e^2$ width of four cycles in the spatial-frequency domain. The Zernike coefficient magnitudes of the primary aberrations in the difference wavefronts are shown in the Fig. 4(a): by definition, the P-V error from any of these is twice the magnitude of the coefficient. The P-V and RMS wavefront displacements are shown in Fig. 4(b) with the piston and tilt terms removed.

Following Eq. (1), and using the NA value from the defocus experiment (Section 8.4), the measured 4.1×10^{-2} waves of tilt indicate a lateral drift of approximately 90 nm in 10 minutes, or 9 nm/min on the image-side of the optic. The defocus coefficient reached a maximum value of 4.8×10^{-3} waves, which by Eq. (2) indicates a longitudinal shift of 7.2 μm in 10 minutes, or 0.72 μm/min on the object-side of the system.

To correctly replicate the way in which the interferometer has been used, the system was *not* allowed to stabilize after the alignment had been optimized. It is possible that the system drifts most rapidly immediately after it is adjusted, and then reaches a more stable position. Further investigations to characterize the system drift are warranted, but have not yet been performed. The maximum allowable drift rate should be based on the rate of data collection, and on the target accuracy of the measurements.

An important secondary result can also be extracted from this experiment. The clear observation of small, well-behaved incremental changes using single-interferogram analysis methods indicates the high sensitivity of this interferometer, with measurement precision below λ/100. This precision magnitude is supported by other self-consistency tests described in Section 8.10.3.

8.6 OBJECT PINHOLE EXCHANGE AND MEASUREMENT REPEATABILITY

Understanding the performance of the interferometer and the qualities of its components requires evaluation of the wavefront measurements, subject to the exchange of "identical" elements wherever possible. To what extent do the measurements depend on the optical components separate from the optic under test? By performing a series of experiments with a number of different object pinholes, for example, systematic errors potentially introduced by defects in any one pinhole become random errors in the larger data set.

This section describes two important experiments designed to evaluate the object pinholes and the importance of system alignment. Because re-alignment was performed during the evaluation of the multiple-pinhole effects, the results of these two experiments are essentially coupled.

8.6.1 *Multiple Object Pinholes*

More than seven individual object pinholes were used in interferometry experiments. Two pinholes were known to be too large to fill the measurement NA; those measurements are not presented in this section. Five other pinholes, discussed here, are commercially available laser-drilled pinholes designed to be

0.5-μm in diameter. They may in fact be somewhat larger.

One object pinhole was used for numerous measurements of sub-aperture A, referred to here as the "March" data (these experiments were performed in March of 1997). After the March data were recorded, the Schwarzschild objective was re-aligned for measurement of sub-apertures B and C. Then the system was returned to sub-aperture A for repeatability studies. In this position, the "April" data were recorded. Here four different object pinholes were used, not including the pinhole used for the March data.

All of the measurements correspond to sub-aperture A, and were performed using the same image-plane reference pinholes and window. For each pinhole under consideration, all available measurements were combined to form a single set of Zernike polynomial coefficients.

The agreement among the five measurements is presented in Fig. 5. Figure 5(a) shows a plot of the Zernike coefficients measured with each of the five pinholes. The five pinholes are labeled A through E. A alone represents the March data, and B through E represent the April data. The variation in the measured wavefronts is described by the *difference wavefront* statistics calculated for each pair of measurements. Tables of the RMS and P-V displacements of the difference wavefronts are shown in Fig. 5(b).

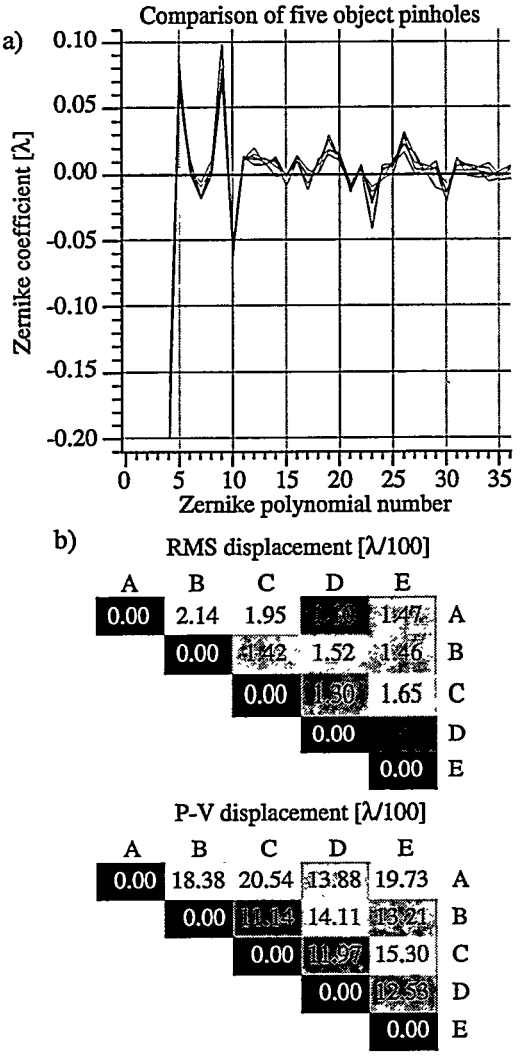

Figure 5. Comparison of wavefront measurements under the exchange of five "0.5-μm" object pinholes. (a) The Zernike polynomial coefficients and (b) the RMS and P-V displacements of the difference wavefronts are shown. Uncertainties are consistent with other measurements requiring re-optimization of the reference pinhole position.

Examining the P-V measurements, one trend is apparent: the agreement is generally better among B through E than it is between A and any of the others. One explanation is the system re-alignment, addressed in the following section. The RMS displacements are all on the order of 0.01 to 0.02 waves, consistent with the variation seen in the reference pinhole displacement experiment, described in Section 8.2.

8.6.2 *System Re-Alignment*

As described above, the Schwarzschild objective was removed from the interferometer chamber and reinstalled several times, including once for each of the three sub-apertures tested. At the time these experiments were conducted, the optic was not kinematically mounted to the translation-stage that controlled its

lateral movement, and the range of stage motion was very limited. (These problems have since been addressed.) This re-alignment procedure required several iterations to bring the position, rotation, and angle of the test optic and the position and angle of the EUV beam into an optimum configuration. A comparison of measurements made before and after re-alignment demonstrates the repeatability of the measurements, as performed from scratch.

As described in the previous section, the comparison between the March and April data (i.e., the comparison of the measurements made before and after re-alignment) was performed using a number of object pinholes. This adds an extra degree of uncertainty to the difference measurement and further explains why this experiment is coupled to the pinhole exchange experiment.

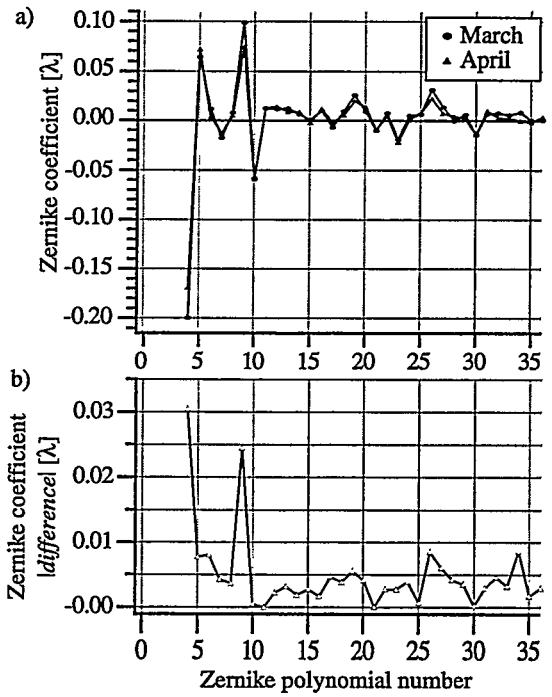

Figure 6. Measurements recorded before and after a complete system re-alignment show excellent agreement. Measurements are also separated by more than two weeks. A comparison (a) of the Zernike polynomial coefficients and (b) the magnitude of their difference.

The comparison is shown in Fig. 6. The two overlapping sets of Zernike polynomial coefficients are shown in 6(a); 6(b) shows the magnitude of the difference. Here the only terms larger than λ/100 are astigmatism Z_4 and the ninth Zernike polynomial, Z_9, which is *triangular astigmatism*. These are also the two aberration components with the largest Zernike polynomial coefficients. The RMS and P-V displacements of the difference wavefront are, respectively, 0.018 and 0.153 waves (0.24 and 2.05 nm, or ~λ/56 and ~λ/6.5). Seventy-four percent of the RMS difference comes from the astigmatic component alone.

8.7. TEMPERATURE MEASUREMENT

An experiment was conducted to gauge the thermal stability of the interferometer chamber over two days of typical operation. The air inside the experimental area of the Advanced Light Source where the interferometer sits is designed to be controlled to ±0.5°C. However, the experimental system sits within 10 m of a large access door that is opened several times per day for several minutes at a time. Concern over the actual chamber temperature prompted this simple study.

A temperature meter was placed in thermal contact with the base of the interferometer chamber and the temperature was recorded intermittently for two days. The results, shown in Fig. 7, verify that the chamber temperature stays within the published specifications of the ALS experimental floor. Additional tempera-

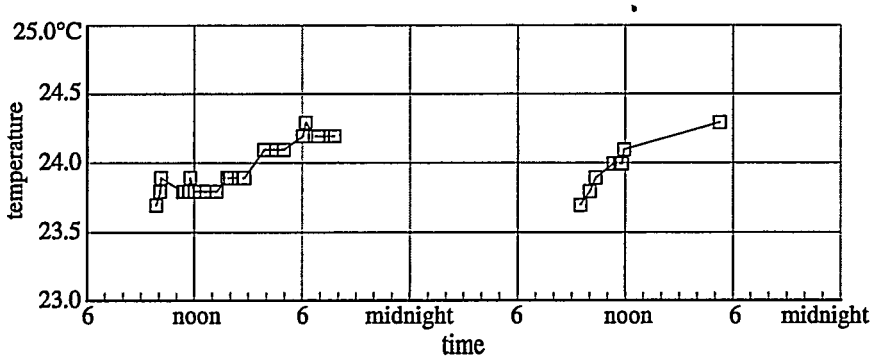

Figure 7. The temperature of the interferometer chamber wall was sampled over a two-day period. These and other measurements (not pictured) show stability to within ±0.5°C with a slow daily rise and nightly fall in temperature.

ture measurements have since been conducted in which the temperature from a number of probes in various positions is recorded automatically at regular intervals. The newer measurements are in good agreement with the data shown here.

8.8 ZEROTH-ORDER REFERENCE VERSUS FIRST-ORDER REFERENCE

A small number of experiments were conducted to measure the difference between the *zeroth-order reference* and the default *first-order reference* configurations of the interferometer. These two very similar modes of operation are defined in Section 4.3 and discussed further in Sections 5.4, 5.8.4, and 5.10. As the names imply, the essential difference is a reversal-of-roles changing which one of the beams from the grating beamsplitter is used as the test beam and which one as the reference beam. By definition, the reference beam is that beam which is brought to focus on the reference pinhole to produce the spherical reference wavefront. Starting in the first-order reference position, a simple 4.5-μm translation of the beam positions in the image-plane brings the zeroth-order beam to focus on the reference pinhole; the *other* first-order beam becomes the test beam.

From a typical, binary transmission grating, the first-order beams are each 40% as intense as the zeroth-order. Spatially filtering a first-order beam in the first-order reference configuration *increases* the intensity discrepancy between the test and reference beams and further reduces the fringe contrast. Evidence of the improvement in fringe contrast offered by the zeroth-order reference configuration is shown in Figs. 8(a) and 8(b). Improved fringe contrast facilitates the analysis.

While intensity-balancing issues motivate the use of the zeroth-order reference configuration, concern for the quality of the grating's diffracted first-order beam is paramount. For this reason, the first-order reference configuration, which filters the diffracted beam, became the default mode of operation.

A comparison of the same wavefronts measured in both configurations is given in Fig. 8(c). Here, the RMS displacements of the difference wavefronts are all less than or equal to 0.0131 waves (0.176 nm, or ~$\lambda/76$). Because reference pinhole re-alignment is required in each case, the uncertainties in these measurements do include the reference pinhole alignment uncertainty discussed in Section 8.2. Since that

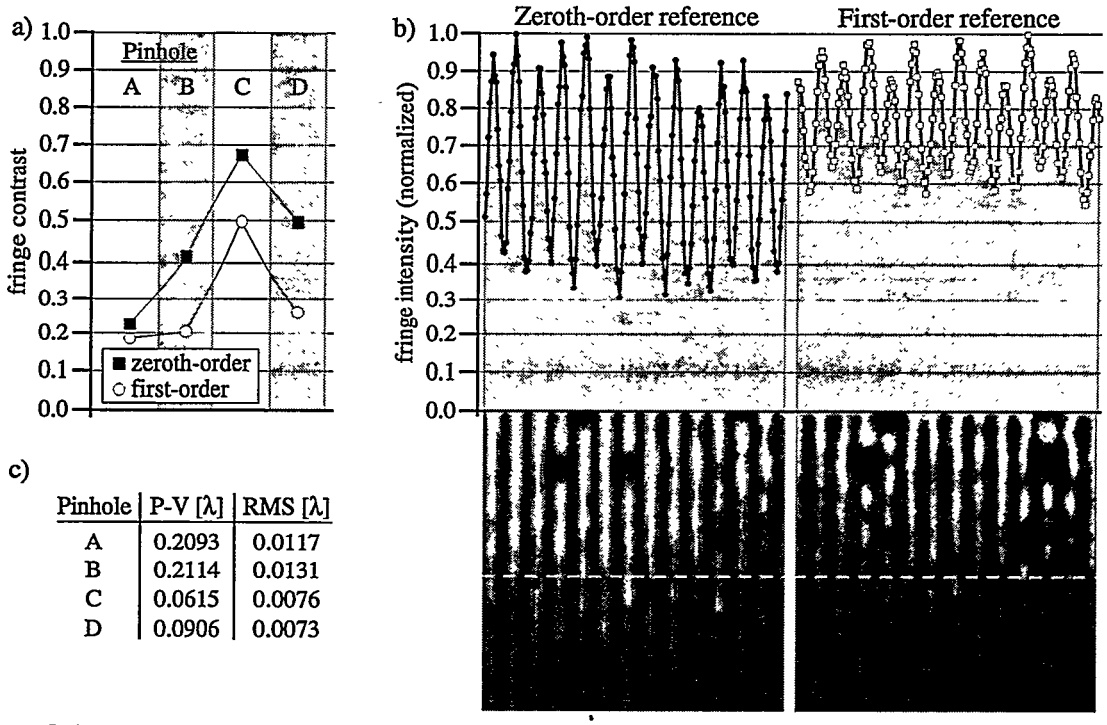

c)

Pinhole	P-V [λ]	RMS [λ]
A	0.2093	0.0117
B	0.2114	0.0131
C	0.0615	0.0076
D	0.0906	0.0073

Figure 8. A comparison of wavefronts measured using the default first-order reference and the zeroth-order reference configurations of the PS/PDI. While the first-order reference configuration uses the zeroth-diffracted-order beam from the grating to ensure a high-quality test beam, the zeroth-order reference configuration offers a significant improvement in fringe contrast by balancing the intensities of the two beams more closely. (a) From each of the four pinholes (A, B, C, and D), the fringe contrast is shown for both configurations. (b) For a comparison, one typical sub-region of the interferogram pattern is shown in detail. The cross-sections taken from the position of the dashed white line reveal both the fringe modulation and the sampling density of the raw data. (c) The RMS and P-V displacements of the difference wavefronts show that the phasemap measurements are nearly indistinguishable within typical measurement uncertainties.

uncertainty is larger than the discrepancy found in this study, it is thus possible that the magnitudes of the wavefront differences between these two configurations are below the measurement uncertainty.

8.9 OBSERVATION OF THE GEOMETRIC COMA SYSTEMATIC ERROR

The small (4.5 μm) image-plane displacement of the test and reference beam centers-of-curvature introduces a geometric coma systematic error that is readily observable in the data (Section 5.5). The clear observation of this very small effect serves to demonstrate the high resolution of the EUV PS/PDI.

The magnitude and direction of the coma systematic error depend linearly on the beam separation. When an isolated wavefront measurement is made, the contribution of this systematic error is unknown. However, when any two such measurements are performed with a rotation or change in the separation, the *wavefront difference* between the two measurements reveals the isolated contribution of the systematic error.

The PS/PDI image-plane spatial filter was designed to facilitate the removal of this systematic error. By performing *two* wavefront measurements using reference pinholes placed 90° apart with respect to the window, the geometric coma is easily identified and removed according to the prescription

Table 1. Difference wavefront statistics from measurements performed in two nearly orthogonal directions. Tilt ($\mathbf{T}_\Delta$) and coma ($\mathbf{C}_\Delta$) for sub-apertures A and C.

	$\lvert\mathbf{T}_\Delta\rvert$		$\lvert\mathbf{C}_\Delta\rvert$	
Sub-aperture	P-V	θ_T	P-V	θ_C
A	62.94 λ = 843.3 nm	46.48°	0.068 λ = 0.92 nm	45.77°
C	55.41 λ = 742.5 nm	46.81°	0.017 λ = 0.23 nm	46.89°

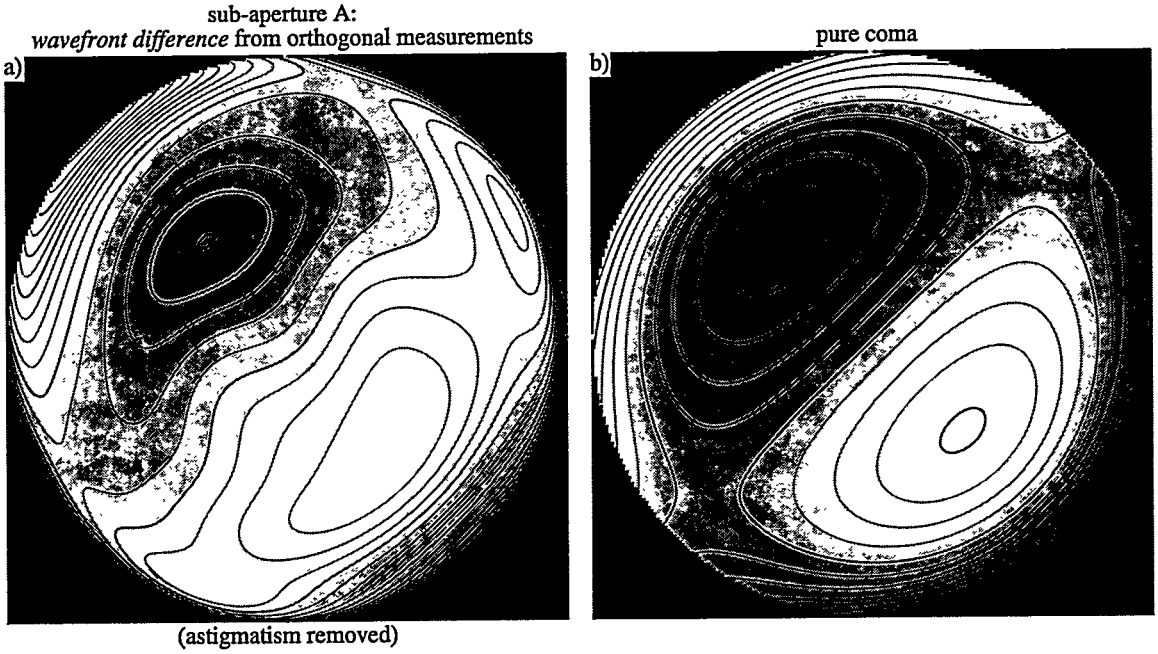

Figure 9. Observation of the geometric coma systematic error can be made by the subtraction of any two measurements in which the beam separation has changed. With the beam separation, and hence the coma, rotated by nearly 90°, the *difference wavefront* shows the coma effect at approximately 45°. Data from sub-aperture A (a) is shown alongside pure coma (b) for comparison. Because the variation of the astigmatism term masks this small effect (less than 1 nm in a 0.07 NA sub-aperture), astigmatism has been subtracted from this figure. The variations in (a) are related to the measurement uncertainties.

described in Section 5.5.2.

The magnitude of the systematic error is small. For the measured difference wavefronts, the *tilt difference vector* $\mathbf{T}_\Delta$ and the *coma difference vector* $\mathbf{C}_\Delta$ are shown in Table 1. Within each sub-aperture, $\mathbf{T}_\Delta$ and $\mathbf{C}_\Delta$ are expected to be parallel; the angles θ_T and θ_C shown in the table demonstrate the agreement with expectations.

Based on measurements from sub-aperture A, Fig. 9(a) shows a difference wavefront obtained by subtracting the average wavefronts measured in the two nearly orthogonal beam separation directions. Because this effect is small relative to the variation in the measured astigmatism, the astigmatism has been removed from the difference wavefront in the creation of this figure. For comparison, Fig. 9(b) shows a *pure* coma aberration aligned in the direction of θ_T.

While the measurements presented for sub-aperture A represent the average of nineteen separate phase-shifting series, those for sub-aperture C come from only *two* measurements, one series in each direc-

tion. Given the small size of the data set, the level of agreement in the difference tilt and coma angles is remarkably high. This agreement both facilitates the removal of the systematic coma and emphasizes the high precision of the individual measurements.

8.10 PHASE-SHIFTING ANALYSIS

Analysis of the EUV phase-shifting PS/PDI data proved to be extremely complicated due to the unreliable positioning of the grating translation stages responsible for controlling the phase-shifting increments. To overcome these difficulties, the author developed the *Fourier-Transform Method of Phase-Shift Determination* (Section 12.4.2) and applied it using the least-squares method of phase-shifting analysis (Section 12.2.3). This section explains the necessity of this new technique and demonstrates the advantages of this method over others, using experimental data. Several available phase recovery techniques for phase-shifting methods of analysis are presented in Chapter 12, along with a discussion of specific advantages and limitations of each. The inherent sensitivity of the least-squares method of phase-shifting analysis is presented at the end of this section, and the implications for polynomial fitting uncertainties are discussed.

8.10.1 *Phase-Calibration Difficulties*

Difficulty in guaranteeing the position of the PS/PDI grating beamsplitter stages plagued the phase-shifting analysis of the interferometric data during the entire course of measurements. For each individual phase-shifting measurement, a series of five to nine (most often, five) interferograms was recorded. After each exposure, the position of the grating was advanced by approximately one-quarter cycle, or 4.5 μm of its 18-μm pitch. The stage motion is calibrated *in situ* by careful observation of the fringe pattern during the motion of the stage over more than 20 cycles (360 μm) of motion. During the measurement of a phase-shifting series, the grating is translated by only one to two cycles total, depending on the number of exposures.

From *all* of the phase-shifting measurements, 951 individual interferograms, or 163 phase-shifting series, were investigated to determine the magnitude of the phase-step errors. The relative *overall phase* of each image was calculated using

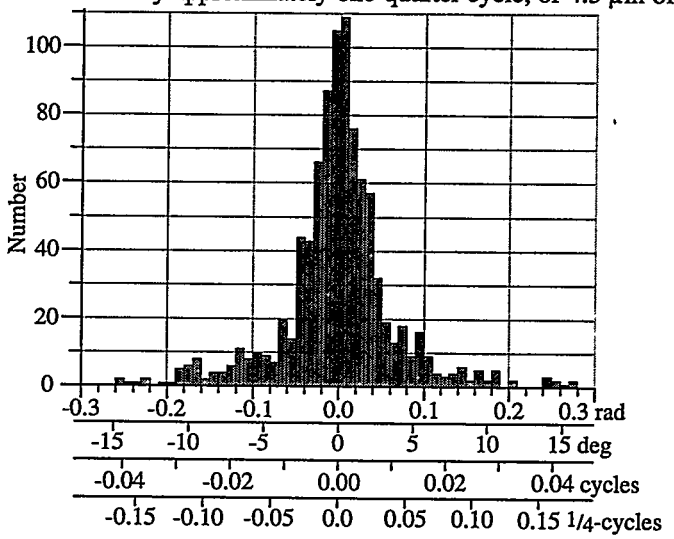

Figure 10. Histogram of phase-step errors, calculated using 927 interferograms, from 163 separate phase-shifting series. Limitations in the grating translation stage lead directly to errors in the phase-increments. The target increment was always one quarter-cycle, or $\pi/2$. The global phase of each interferogram was calculated using the Fourier-Transform Method of Phase-Shift Determination.

the Fourier-Transform Method of Phase-Shift Determination (Section 12.4.2). Then *within* each series the average phase *increment* was subtracted and the distribution about the mean phase-increment was tabulated. A histogram of the phase-step errors is shown in Figure 10. Here the ordinate is given in radians, degrees, cycles, and quarter-cycle steps (the target increment). The full-width at half-maximum of this distribution is approximately 0.07 radians, 4.0 degrees, 0.011 cycles, or 4.4% of the quarter-cycle step.

8.10.2 *Comparison of Phase-Shifting Methods*

Evaluation of the available methods of phase-shifting analysis using experimental EUV data is the most appropriate way to discern the actual benefits and drawbacks each. To illustrate such an investigation, a single phase-shifting measurement series was selected. This series is comprised of nine exposures with an (unintentionally) irregular phase-increment. Elements of this study are shown in Fig. 11. Using data from sub-aperture B, a relatively-clear 160 × 160 pixel sub-region was chosen. Details of four phase-shifted exposures are shown.

The Fourier-Transform Method of Phase-Shift Determination was used to determine the global phase-shift between exposures. Here, the complex phase of the first-order peak in the spatial-frequency spectrum is used to assign a global phase to the interferogram. The average phase increment was found to be 88.0°. The individual steps or step errors are shown in Fig. 11(b).

Seven separate methods of phase-shifting analysis are applied to the raw data. The unwrapped phasemaps from each method are shown with the piston and tilt components removed. The four-step method (Section 12.2.1) uses only the first four exposures. The Hariharan method (Section 12.2.2), utilizing the first five exposures, is applied in two different ways: first, assuming quarter-cycle steps, and second, using the known average 88° phase increment. A nine-step method* was the last of the *simple* methods to be applied. The complex method is applied in three ways, using the global phase increments calculated with the Fourier-Transform Method of Phase-Shift Determination. The least-squares method was applied to three, five, and then all nine exposures.

One characteristic feature exemplifies the main problem associated with the simple techniques: in the presence of phase-step errors, ripples appear in the data at twice the frequency of the fringe pattern. This so-called *fringe print-through,* clearly visible in the first four images of Fig. 11(c), is absent from the three applications of the complex method.

The discrepancies between the individual methods are most clearly revealed in the *difference wavefronts* calculated by subtracting the phasemap of the nine-bucket least-squares algorithm from the

* A *nine-step* phase-retrieval algorithm developed by the author. Quarter-cycle steps are assumed.

$$\phi(x) = \tan^{-1}\left[\frac{2(I_4 - I_6 + I_8 - I_2)}{I_9 - I_1 + 2(I_5 - I_3 - I_7)}\right] \tag{3}$$

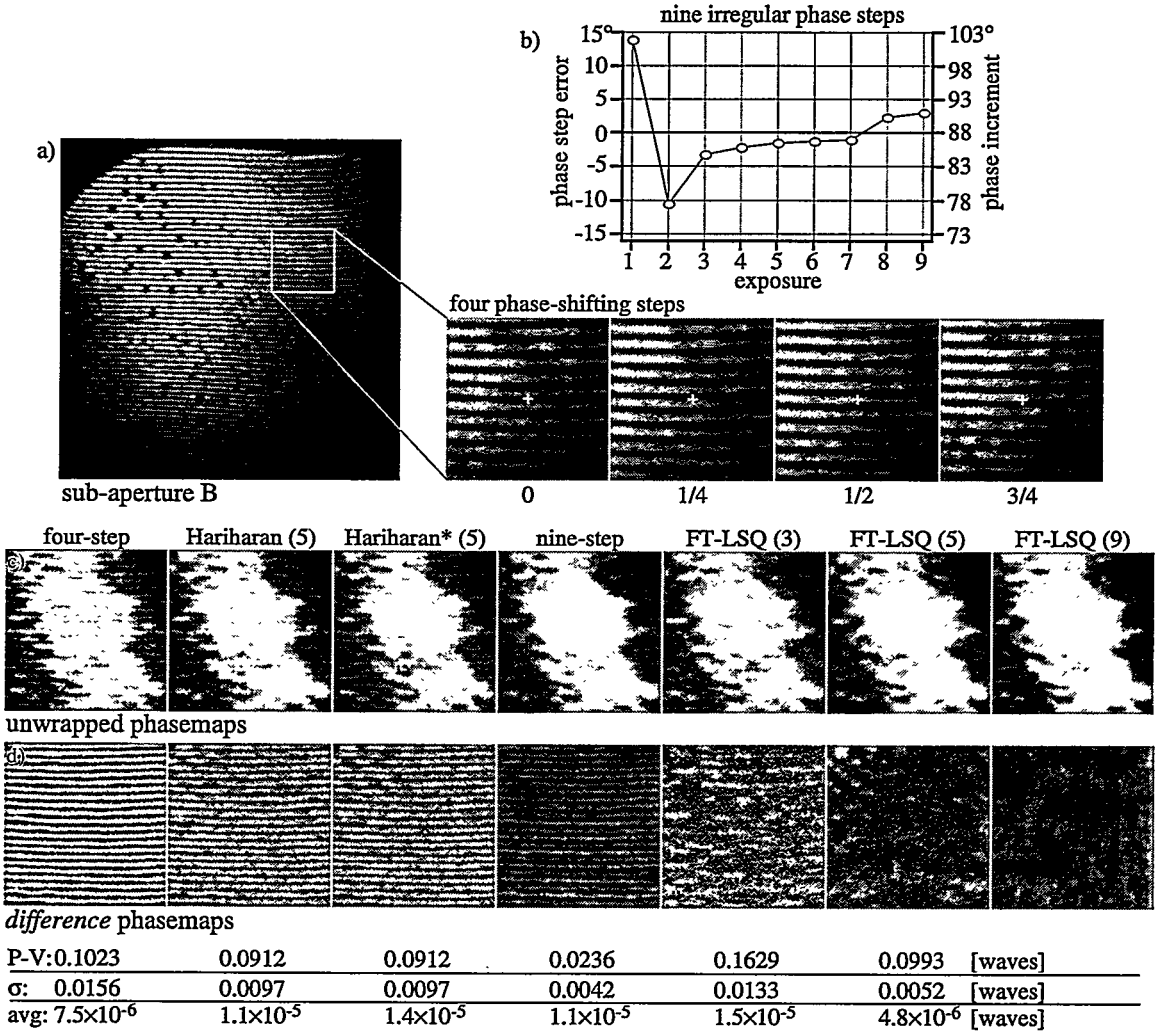

P-V: 0.1023	0.0912	0.0912	0.0236	0.1629	0.0993	[waves]
σ: 0.0156	0.0097	0.0097	0.0042	0.0133	0.0052	[waves]
avg: 7.5×10^{-6}	1.1×10^{-5}	1.4×10^{-5}	1.1×10^{-5}	1.5×10^{-5}	4.8×10^{-6}	[waves]

Figure 11. A number of different phase-shifting analysis techniques, including both simple methods and complex methods developed by the author, are compared in this figure. (a) 160 × 160 pixel details taken from a nine-exposure phase-shifting series are shown. The small white cross indicates the same stationary position in all four images. The data comes from a measurement of sub-aperture B. (b) The irregular phase-increments have an average step size of 88.0°. (c) Unwrapped wavefront phasemaps are presented for seven different methods of phase-shifting analysis. The various methods used different numbers of exposures, as indicated in the names, or parenthetically. (d) Each phasemap is compared to the nine-image least-squares phasemap, and the difference wavefronts are shown. All are plotted using the same grayscale. Displacement statistics for the six comparisons are shown below each image. Double-frequency *fringe print-through* is problematic in the application of the simple techniques. However, the complex least-squares method developed by the author to cope with irregular phase-steps is resistant to this problem.

phasemap of each of the other algorithms. In these difference images, shown in Fig. 11(d), the fringe print-through from the simple techniques and the less-regular difference patterns in the least-squares techniques are clearly visible. Below each image, the difference wavefront statistics are given.

One important statement can be made about all of these measurement techniques: the net phase-errors, or the *average* phase errors, are zero to within the measurement noise level. This is more a property of the periodicity of the fringes than of the analysis methods themselves. Depending on how the piston term is adjusted, in the absence of measurement noise the phasemaps generated by any two analysis meth-

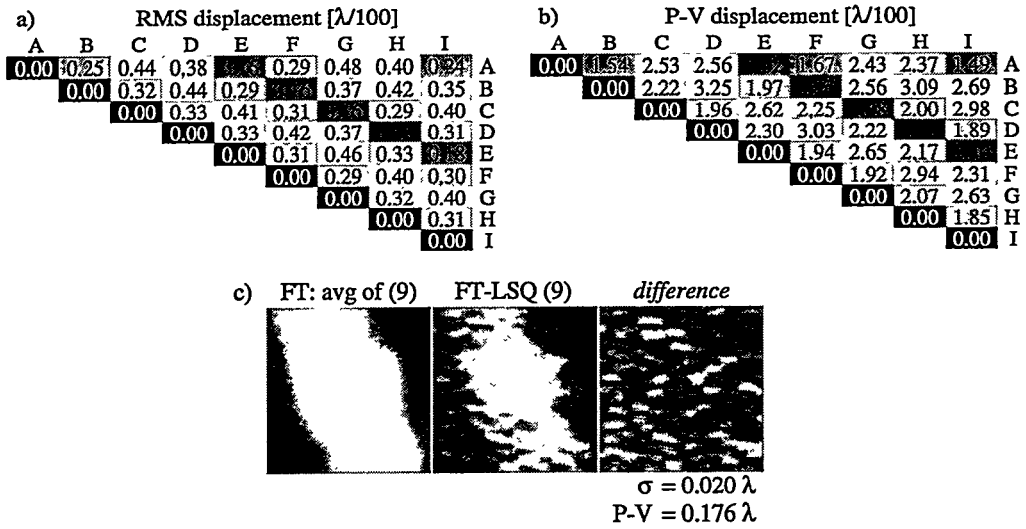

Figure 12. Analysis of the nine individual interferograms in a single phase-shifting series is performed using the Fourier-transform method. (a) and (b) Within a 160 × 160 pixel region, the pairs of measurements are compared to assess the self-consistency of the results. (c) The average wavefront determined from the nine individual measurements is compared to the wavefront calculated using the least-squares method. The difference wavefront reveals the extent of the spatial filtering in the Fourier-transform method, and shows the mid-spatial-frequency content of the measured phasemaps.

ods can be made to agree at one or two points within each cycle of the fringe pattern. Between these points of agreement, individual methods may diverge, as evidenced by the periodicity of the fringe print-through. The implications of this zero average difference are that in cases of high fringe density, some level of fringe print-through can be tolerated without affecting the low-spatial-frequency components of the measured phasemap. However, if the fringe density is sparse, then the phase errors introduced by print-through may dominate the low-spatial-frequency wavefront aberrations, adversely affecting the measurements.

8.10.3 *Fourier-Transform versus Phase-Shifting Methods*

Besides the phase-shifting methods, the other important analysis technique applied to interferometric data is the Fourier-transform method of single interferogram analysis (Section 11.3). This relies on the spatial rather than the temporal domain of measurement. Experience has shown these methods to be very reliable and robust in the presence of noise. They do, however, require the application of spatial filtering to the data and thus suffer from lower spatial-resolution than the phase-shifting methods. Furthermore, spatial filtering causes any abrupt discontinuities in the data to introduce analysis errors within the vicinity surrounding the discontinuity.

To assess the quality of the Fourier-transform method of analysis, two studies were made. The first evaluates the self-consistency of the analyses as applied separately to the nine independent measurements described in the previous section. The second compares this analysis with the least-squares technique. The Fourier-transform method is applied separately to all nine images of the phase-shifting series. To avoid possible edge-effects, the analysis is performed using the entire 1024 × 1024 pixel image, before the

160 × 160 pixel region of study was isolated. For this analysis, a Gaussian filter of radius seven cycles was applied in the spatial-frequency domain.

The nine separate phasemaps calculated with the Fourier-transform method were unwrapped, and the difference wavefronts from all measurement pairs were tabulated. Figures12(a) and 12(b) show the RMS and P-V displacements of these difference wavefronts, respectively. The average of the RMS displacements is 0.0033 ± 0.0009 waves (0.044 ± 0.012 nm, or ~λ/307).

For comparison with the least-squares phase-shifting technique, the average of the nine separate phasemaps was computed. Figure 12(c) shows a side-by-side comparison of this average wavefront with the least-squares result; both are shown with piston and tilt components removed. The difference between the two is also shown. By inspection, the characteristics of the difference clearly reveal the result of spatial filtering and averaging on the Fourier-transform data. Notice that the original fringe pattern, shown in Fig. 11(a), has horizontal fringes, indicating a *vertical* displacement of the test and reference beams in the coordinate system of this measurement. As described in Section 6.4, the overlap of the reference beam through the window causes the latter to behave as a bandpass filter for the former. For this reason, the features observable in the difference phasemap show much higher spatial-frequency content in the vertical direction than in the horizontal direction.

There are two important results here. First, the self-consistency of the Fourier-transform method applied to separate interferograms is measured to be about λ/300 on this domain. Second, the RMS difference between the Fourier-transform method and the phase-shifting analysis is approximately λ/50. That difference is comprised only of mid-to-high spatial-frequency features — features that do not significantly affect the measurement of the low-spatial-frequency aberrations of interest.

The Fourier-transform method of analysis is appropriate for use in most cases where phase-shifting data is not available or where high accuracy with high spatial resolution is not required. Further research is necessary to evaluate the performance of the Fourier-transform method in the vicinity of blemishes or near the edges of the domain, where its performance suffers.

8.10.4 *Sensitivity of Least-Squares Phase-Shifting Analysis*

Additional error sources in the measurements are related to the detection and digitization (discretization) of the interferogram image. In addition to photon shot-noise and noise sources in the detector's amplification electronics, the digitization performed by the detector in the recording of the interferogram should also be considered. The high-spatial-frequency noise effects all play a *very small* role in the wavefront measurements presented in this thesis; however, they may become significant in low-light interferometric applications where high-brightness sources are not available. This section is not intended to

present an exhaustive nor detailed study of noise effects, but instead to give an order-of-magnitude estimate for the ranges in which they become relevant. More detailed and general analysis of these effects has been performed by Koliopoulos (1981) and Brophy (1990).

The relationship between the phase-uncertainty of the *individual* points and the uncertainties of the Zernike polynomial coefficients is described in Section 15.6. When a large number of points N are measured (on the order of 100,000 – 300,000 is typical), the uncertainties of the Zernike coefficients are approximately $1/\sqrt{N}$ times as large as the individual variation; this may be more than 100 times smaller in ideal circumstances.

A pair of simple studies is performed to evaluate the effects of shot-noise and image digitization on the phase measurements conducted with the least-squares technique using five quarter-cycle phase-shifting steps. Here an ideal input wavefront with 20,000 points in a linear slope and a range of one cycle is used as the input. In the first study, to approximately model Poisson statistics of photon-counting the simulated intensity data with 100% fringe contrast is subjected to Gaussian noise of width $\sqrt{N}$. In Fig. 13, the recovered phase is compared to the input phase and the RMS difference is plotted for a range of maximum photon numbers. An empirical formula relating the RMS phase uncertainty σ_ϕ to the peak number of photons N is

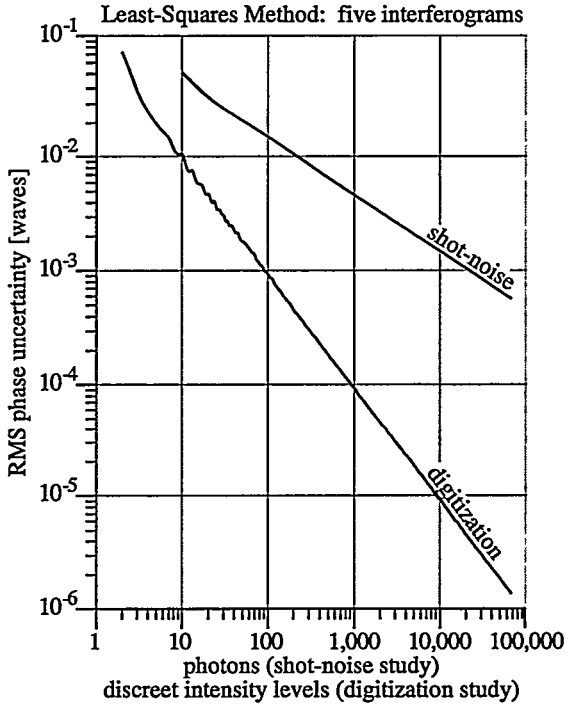

Figure 13. Two empirical investigations of the sensitivity of the least-squares method of phase-recovery to photon shot-noise and image digitization. The abscissa is given in photons for the shot-noise study, and in the number of discreet intensity levels for the digitization study.

$$\sigma_\phi\,[\text{waves}] \approx \frac{1}{6.5\sqrt{N}}. \tag{4}$$

The digitization effect can be isolated from all of the other noise sources. Here D is an integer describing the number of discrete levels present in the fringes with no other noise sources. The RMS phase uncertainty is calculated in the same manner as above, and an empirical expression is obtained relating σ_ϕ to the level of discretization D.

$$\sigma_\phi[\text{waves}] \approx 0.093\,D^{-1} \approx \frac{1}{10.8\,D}. \tag{5}$$

In general, for EUV PS/PDI experiments the target fringe height is set at approximately 1000 counts. The measured detector sensitivity is 0.8 counts per detected photon. With 1000 counts, or 1250 photons, the RMS point-by-point phase uncertainty from shot-noise is approximately 4×10^{-3} waves (0.054 nm, or $\lambda/250$). Discretization with 1000 levels produces a significantly smaller RMS phase uncertainty of 9×10^{-5} waves (0.0012 nm, or ~$\lambda/11{,}000$).

According to the results of this simple analysis, noise and other high-frequency random errors from the detector do not significantly affect the EUV PS/PDI measurements presented in this thesis. Once again, they may become important only when reliable data is required in low-light situations.

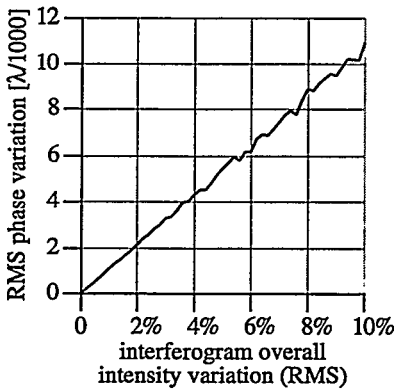

Fig 14. Fluctuations in the overall intensity of the recorded interferograms in a phase-shifting series introduce phase uncertainties into the measurement. This graph shows the results of a simple empirical study conducted to investigate this effect. Within a series of five simulated ideal interferograms, the individual exposure intensities are varied before analysis with the least-squares method is performed.

8.10.5 *Intensity Fluctuations*

Fluctuations in the overall intensity level of the recorded interferograms can introduce measurement uncertainties into phase-shifting analysis. Intensity variations can be caused by fluctuations in the light source, or by the performance of the shutter. While single-interferogram analysis methods are generally unaffected by intensity changes, phase-shifting methods rely on the stability of the system during the multiple exposures of a phase-shifting series.

Similar to the investigations presented in the previous section, a simple empirical study is performed to gauge the sensitivity of the least-squares method of phase-shifting analysis to fluctuations in the overall intensity of the measured interferograms. Once again, an ideal input wavefront with a linear slope and a range of one cycle is used as the input. The simulated phase-shifting interference data is generated for five quarter-cycle phase-steps. Before the analysis is performed, the overall intensity levels of the individual "interferograms" are adjusted by randomly chosen multiples selected from a given Gaussian distribution width. For each distribution width of interest, 500 such analyses are performed and the RMS difference of the calculated phase from the ideal input phase is tabulated. The average of RMS phase difference indicates the expected phase-uncertainty for each intensity distribution width. The results of this investigation are shown in Fig. 14. For intensity variations below 10%,an empirical relation between the RMS phase uncertainty and the RMS overall intensity variation is

$$\sigma_\phi\ [\text{waves}] \approx 1.069\times10^{-3}/(\%\ \text{intensity variation, RMS}) \approx \frac{(\%\ \text{variation})}{936}\ . \qquad (6)$$

In the EUV PS/PDI experiments, the primary source of overall intensity fluctuations is the steady decrease in the electron beam current of the Advanced Light Source. During a typical phase-shifting measurement, the ALS current was observed to decrease by less than 0.5%. As described previously, the beam current is recorded with each exposure, and the images are normalized before the analysis is performed. Intensity variations from the source are therefore limited to less than approximately 0.25%.

A secondary source of intensity fluctuations is the shutter, described in Section 6.2.6. The performance of the shutter used in these experiments is limited to approximately 0.02 seconds. Therefore, with a typical exposure time of five seconds, the fluctuation from the shutter could be as large as 0.4%.

These two sources of intensity fluctuations are predicted to contribute less than 0.001 waves (0.0134 nm, or λ/1000) to the phase uncertainty of the measurements — less than the variations produced by shot-noise at these intensity levels.

8.11 FRINGE CONTRAST AND WAVEFRONT FITTING UNCERTAINTY

The process of wavefront surface fitting used for the analysis of the interferometric data involves the minimization of the *fit variance* based on a finite basis of orthogonal polynomials (Chapter 15). The variance comes from the *residual* wavefront error remaining after the contribution from the polynomial surface fitting has been subtracted from the raw data. The surface fit is constructed from the contributions of each of the orthogonal polynomials in the finite basis; thus, the set of polynomial coefficients is all that is required to reconstruct the fit on a given domain. For the Zernike circle polynomials, typically 37 polynomial components are specified. As described in Section 15.6, the uncertainty in each of these fit-coefficients depends on the magnitude of the variance and on the characteristics of the individual polynomial components.

A large number of wavefront measurements were made of sub-aperture A. Over time, the transmis-

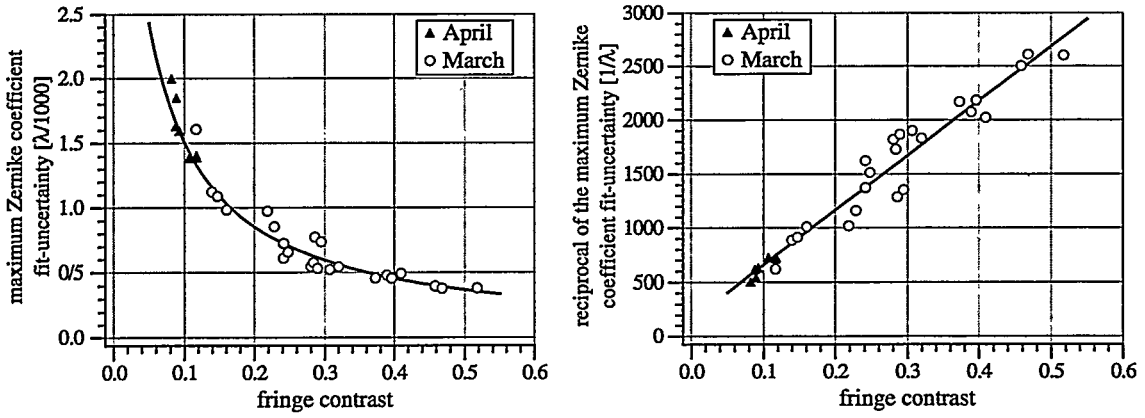

Figure 15. Measured dependence of the largest Zernike coefficient uncertainty on interferogram fringe contrast for 30 separate phase-shifting series. Each series corresponds to the same downstream field point measurement of sub-aperture A. A relative deterioration in fringe contrast observed in the April data sets may be attributable to changes in the reference pinhole transmission.

sion properties of the reference pinholes changed, and the intensity of the reference wave decreased. The loss of fringe contrast accompanying this decrease in reference wave intensity had a significant effect on the fit variance of the individual measurements.

Figure 15 shows a comparison between the measured fringe contrast (calculated with the method described in Appendix A.6) and the largest fitting-coefficient-uncertainty among the 37 Zernike polynomial coefficients, σ_{max}. Thirty phase-shifting series were considered. Note that in these measurements σ_{max} is always attributable to Zernike polynomial numbers 33 and 34, which are high-ordered coma terms. This comparison clearly demonstrates the inverse relationship between σ_{max} and the fringe contrast: the reciprocal of σ_{max} shows a roughly linear dependence on contrast. An empirical relationship that describes this dependence is

$$\sigma_{max} \approx \frac{\lambda}{160 + 5060\, contrast}. \tag{6}$$

Typically, σ_{max} is more than 1.5 times larger than the individual uncertainties of the important lower-ordered aberration components (astigmatism, coma, and spherical aberration).

Fortunately, due to the large number of points used in the fit (279,188) and the relatively high quality of the phase-shifting data available, the coefficient uncertainties related to the surface fitting are *significantly smaller* than the uncertainties related to the measurement-to-measurement variation. For this reason, the uncertainties from the surface fitting are not included in the analysis presented in Section 7.2.4.

8.12 SUMMARY AND CONCLUSIONS

All of the individual experiments described in this chapter demonstrate the precision of the interferometer: reference and object pinhole displacement experiments, mechanical stability tests, pinhole exchange, system re-alignment, and observation of the geometric coma systematic error. All describe experiments that are similar in principle, where two wavefronts are compared by inspection of their differences. Here, the *variations* in the data stand out and are characterized.

The following section contains a brief summary of the main performance evaluation experiments described in this chapter. Following that is a discussion of accuracy and the need for further testing.

8.12.1 *Summary of Precision-Testing Measurements*

- **8.2 Reference pinhole spatial filtering.** Based on measurements made as the reference pinhole is displaced slightly from the optimum position, the expected measurement-to-measurement RMS wavefront variation is 0.019 ± 0.009 waves (0.249 nm, or ~λ/53).
- **8.3 Object pinhole spatial filtering.** In two experiments, lateral translation of the object pinholes produced an RMS wavefront variation of 0.006 ± 0.001 waves (0.082 ± 0.018 nm, or ~λ/164) in the first experiment, and 0.014 ± 0.005 waves (0.192 ± 0.065 nm, or ~λ/70) in the second.
- **8.4 Through-focus experiments.** Small longitudinal translations of the object pinhole adjust the posi-

tion of the reference pinhole through focus. The average of the measured RMS displacements of the difference wavefronts is 0.015 ± 0.007 waves (0.204 ± 0.088 nm, or ~λ/66).

- **8.5 Mechanical stability.** Based on observations of the wavefront changes over ten minutes as the system is held stationary, the interferometer components appear to drift. The image-plane lateral and longitudinal drift rates were approximately 9.0 nm/min and 7.2 nm/min respectively. On the object-side of the optic, these motions would be 90 nm/min laterally and 0.72 μm/min longitudinally.
- **8.6.1 Object pinhole exchange and measurement repeatability.** Five object pinholes were tested in measurement of sub-aperture A. The average of the measured RMS displacements of the difference wavefronts is 0.015 ± 0.004 waves (0.197 ± 0.051 nm, or ~λ/68).
- **8.6.2 System re-alignment.** The test optic was removed from the vacuum chamber and re-aligned from scratch several times. For the two combined measurements of sub-aperture A, the RMS displacement of the difference wavefront is 0.018 waves (0.24 nm, or ~λ/56).
- **8.8 Zeroth-order reference versus first-order reference.** A comparison of the two methods shows an average difference wavefront of RMS displacement 0.010 ± 0.003 waves (0.13 ± 0.04 nm, or ~λ/101).
- **8.11 Fringe contrast and wavefront fitting uncertainty.** A dependence was observed between the measured fringe contrast and the coefficient uncertainties of the Zernike polynomial fit. The largest observed uncertainty of the first 37 coefficients follows $1/\sigma_{max}$ [1/waves] ≈ 160 + 5060 contrast, for contrast values between 10% to 50%. Uncertainties of the low-ordered primary aberrations are approximately two-thirds as large. Typical values range from $2–7\times10^{-4}$ waves ($2.7–9.4\times10^{-3}$, or ~λ/5000-λ/1400).

8.12.2 *Comments*

It is clear from the above measurements that the most significant limitation to the measurement precision is the quality of the reference wavefronts generated by the reference pinhole. Every one of the tests described here incorporates a re-alignment (large or small) or other change that causes the reference pinhole effects to be included in the measurement. Not doing so is unavoidable. By isolating these reference pinhole effects, the reference pinhole spatial filtering experiment indicates that measurement variations on the order of λ/50 RMS should be anticipated.

One of the four pinholes, pinhole C, was found to introduce the largest measurement-to-measurement variation and the least spatial filtering of the four pinholes studied. Yet this pinhole is not much larger than the other pinholes used for these experiments. Here, two conclusions can be drawn: the reference pinhole is the most significant limiting agent in achieving high measurement precision in the EUV PS/PDI; and improvement could be achieved by the use of slightly smaller pinholes. A small sacrifice in fringe contrast brought about by the use of a smaller reference pinhole will not significantly limit the precision of the measurements relative to the other contributing factors.

8.13.3 The Astigmatism Problem

The goal of having an interferometric system for which the accuracy and precision can be specified independently from the characteristics of the optical system under test appears to be thwarted by the diffi-

culty of spatially filtering astigmatism. Without exception, the dominant component of the difference wavefronts in each of the relevant experiments described in this chapter is astigmatism.

Section 4.6.2 gives some insight as to how astigmatism becomes the most difficult aberration to remove by spatial filtering, but it does not provide insight into any one solution more effective than reducing the pinhole size. It appears clear both experimentally and from the simple model that the pinhole size standard for filtering astigmatism is narrower than for any of the other primary aberrations. For this reason, the performance of the system necessarily depends on the constituent aberrations of the test optic.

8.13.4 *Accuracy and the Need for* Two Pinhole *Tests*

In addition to *high precision, high accuracy* is the true goal of interferometric optical system measurement.

In principle, the simple *difference measurements* described in this chapter, in which the system is subjected to slightly different conditions in two measurements, are incapable of detecting systematic errors. The presence of a systematic wavefront figure error would go unnoticed if it were lost in the subtraction of the two measurements being compared.

When the assumption is made that every optical component of the interferometer is capable of contributing systematic errors, then a wide variety of systematic effects and the mechanisms to generate them can be hypothesized. As discussed in Section 5.8, systematic errors introduced directly by defects in the grating beamsplitter can be identified by large translations of the grating, or by grating exchange. More onerous by far are reference wave systematic errors introduced by the object and image-plane spatial filter pinholes. It may be suggested that the particular defects or irregularities of a given pinhole introduce a stable aberration pattern in the reference wavefront it generates. In addition, there may be unknown physical properties of pinhole diffraction (e.g. polarization dependent astigmatism, irregularities caused by non-uniform illumination, etc.) that may create systematic errors of significant magnitude near the target accuracy. Far more simple are geometric systematic errors (Chapter 5) that come from the beam separation (geometric coma), detector misalignment (a source of astigmatism), the use of a planar grating in a spherical beam (grating coma), and the use of a planar detector in a spherical beam (a source of radial distortion).

While some of these systematic effects can be observed and are easily subtracted from the wavefront measurements (e.g. geometric coma), others present a more daunting problem. The importance of identifying these effects cannot be overstated because the accuracy of the interferometer is at stake.

One strategy for overcoming the systematic errors uses a two-pronged approach. First, of the systematic errors that cannot be directly observed, can their *magnitude* be determined? This is the strategy applied to the investigation of the pinhole spatial filtering. For example, what may be manifest as a systematic error in a single measurement becomes a random error when a large number of measurements are

made in ways that induce changes in the "systematic" error. The pinhole translation and pinhole exchange experiments are all examples of this strategy for turning systematic errors into random errors and identifying their magnitude by carefully observing *differences*. The average magnitude of the differences indicates the typical contribution of the systematic error to any single measurement.

The second strategy is to find a way to isolate the systematic effects under consideration. The geometric coma removal is one example of this. Given that the systematic error depends directly on the magnitude and direction of the beam separation, introducing a 90° rotation in the beam separation allows this systematic effect to be identified and quantified.

The identification and isolation of other systematic errors requires a so-called *null test*. In such, every attempt is made to remove the contributions of the test optic from the measurement, and the bare system performance is studied. One way in which this could be achieved in the EUV PS/PDI is by using a *two-pinhole test*, in which a two-pinhole spatial filter is placed in the image plane of the PS/PDI (Goldberg 1997). The image-plane window that transmits the test beam is replaced by a second tiny reference pinhole. The measured interference pattern and wavefront can be compared to those predicted for two ideal pinhole spatial-filters, and systematic errors will be revealed in the difference. Besides the expected tilt and geometric coma, small detector misalignments may be observable in this sensitive technique.

To improve the measurements and broaden the significance of the two-pinhole test, the experiment may be expanded to include a large number of pinhole pairs, in different orientations, and with different separations. Sensitivity to certain geometric errors will be greater in some orientations than in others. In addition, the use of many pinhole pairs provides information on the variation in the spatial filtering properties of the pinholes: the waves diffracted from the pinholes are essentially being "compared" with each measurement.

Some effects may not be observable using the two-pinhole tests. For example, if every pinhole were to create the same kind of aberration in the diffracted reference wave it generates, then a comparison of any two waves by subtraction would reveal nothing. Experiments have been performed to assess the quality of a single reference wave, using shearing techniques to compare the wavefront to an angularly displaced copy of itself. Such measurements could be attempted for the PS/PDI reference waves, but it is not clear that the tests could achieve the desired sub-$\lambda/100$ accuracy that is necessary. Alternatively, rotation of the optical system may help to identify these effects.

9

Chromatic Effects

9.1 INTRODUCTION: 10× SCHWARZSCHILD MULTILAYER COATING PROPERTIES

Measurements of isolated chromatic effects provide perhaps the clearest demonstration of the sensitivity and importance of at-wavelength interferometric testing. The resonant reflective multilayer coatings exhibit a strong wavelength-dependent response in both reflected intensity and phase that occurs separately from the figure of the optical surfaces under test. By tuning the wavelength and performing measurements near the reflectivity peak, these chromatic effects are easily demonstrated and the properties of the multilayers can be studied.

Multilayer response depends critically on the multilayer period, the illumination angle, and the wavelength and polarization of the incident light. As described in Section 6.2.1, the multilayer-coatings are designed for peak reflectivity and wavefront response at 13.4-nm wavelength. The range of angles subtended by the light incident on the primary mirror necessitates the use of a multilayer containing a radial thickness gradient. This design makes the performance of the system very sensitive to changes in wavelength.

This chapter contains measurements of the chromatic response of the multilayer coatings. In addition to the direct demonstration of chromatic aberrations and the sensitivity of the interferometer itself, measurements such as these would be required to understand the system performance in the presence of broadband illumination. For example, understanding imaging performance under broadband illumination requires that both the intensity transmission and the wavefront be considered over the range of illumination wavelengths. A separate section of this chapter addresses measurements made without the wavelength-filtering of the monochromator.

Qualitative wavelength-dependent measurements of chromatic aberrations have been reported previously by Ray-Chaudhuri (1995a). The investigations presented here may be the first high-precision quantitative measurement of such effects.

9.2 WAVELENGTH-DEPENDENCE OF THE TRANSMITTED INTENSITY

The first experimental indications of the presence of chromatic effects related to the multilayer coatings were observable in the transmitted intensity patterns. Figure 1 shows the transmitted intensities for sub-apertures A, B, and C. The data from sub-aperture C were recorded with the sub-aperture defining pupil removed and a large region of the clear aperture visible. These images clearly show the response of the multilayer coatings in a wavelength-dependent, annular pattern. As described in Section 6.2.2, for these measurements the illumination bandwidth set by the monochromator is measured to be below 1-Å full-width at half-maximum.

The areas at the inner and outer edges of the annulus are especially interesting. The periods of the multilayer coatings were designed and measured to be within a thickness tolerance of 0.125 Å over a

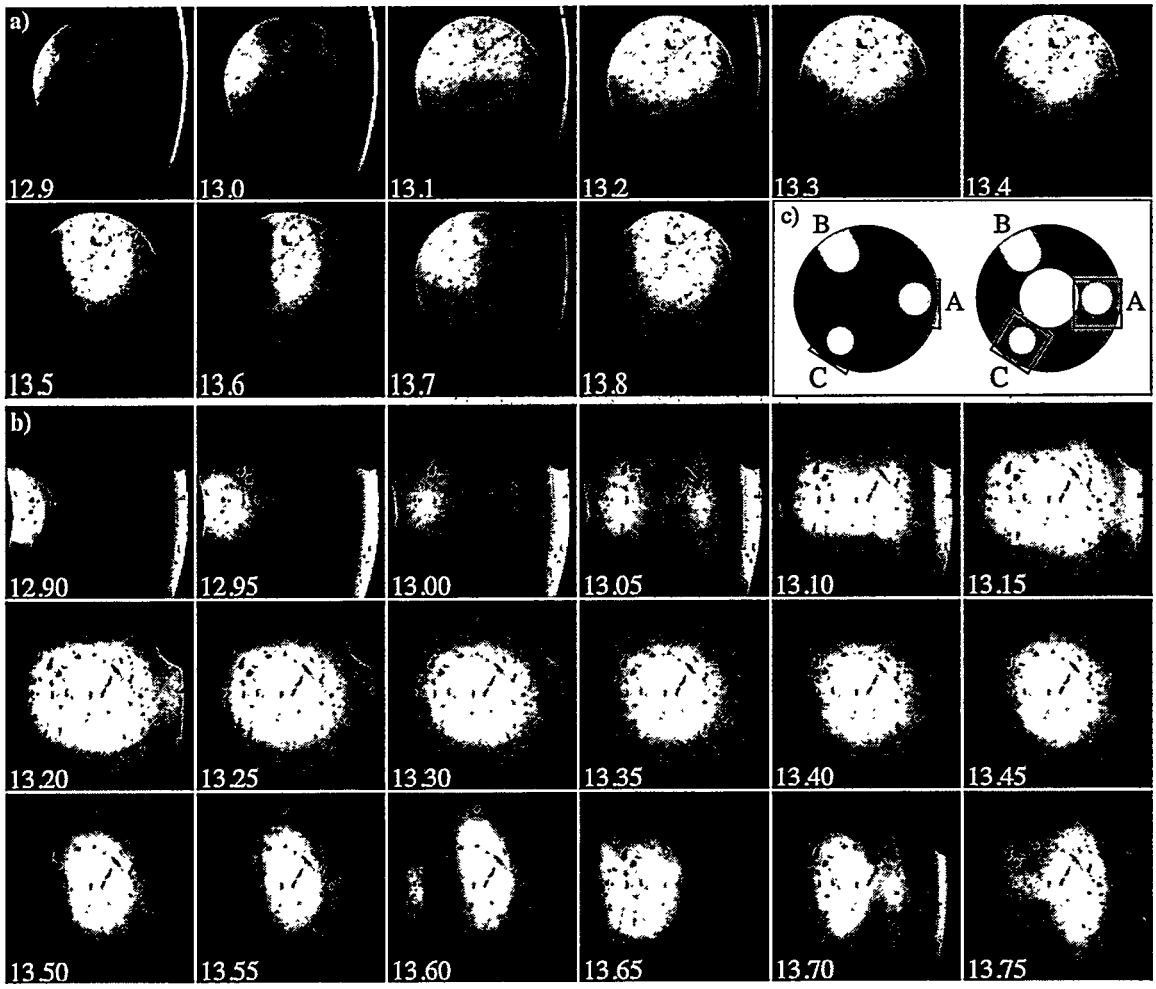

Figure 1. Wavelength-dependent intensity transmission patterns are shown for two sub-apertures of the 10× Schwarzschild objective. (a) Sub-aperture A (0.07 NA) is shown with the aperture-defining stop in place. (b) Sub-aperture C is shown with the stop removed to expose a larger section of the annulus. Illumination wavelengths in nanometers are shown in the lower-left corner of each image. (c) The appearance of the Schwarzschild objective's full annular pupil, with and without the stop, is shown. The square outlines illustrate which two sections of the annulus are shown in (a) and (b). The annular characteristics of the multilayer response are clearly visible in these images.

finite region of the aperture (i.e. a limited range of radii). At the edges where no effort was made to control the period, the reflectivities appear highest at the shorter wavelengths; this indicates *thinner* layers in these regions. Comparison of the measured and theoretical intensity transmission behaviors has been presented elsewhere (Tejnil 1997).

9.3 WAVELENGTH-DEPENDENT WAVEFRONT MEASUREMENTS – CHROMATIC ABERRATIONS

When the PS/PDI is aligned and optimized, experiments to measure the wavelength dependence of the wavefront are very simple to perform: adjustment of the undulator and beamline monochromator tune the illumination wavelength; *very* minor position optimization of the optical components is all that is

Table 1. The wavefront measured at the central wavelength, 13.4 nm, is subtracted from the individual wavefronts measured at each wavelength generating the *difference wavefront*. Statistics of the difference wavefronts are given. The measured change of the focal position is also given.

λ [nm]	P-V [nm]	RMS [nm]	defocus [μm]
13.0	1.70	0.29	1.54
13.1	1.36	0.17	1.62
13.2	1.02	0.13	1.55
13.3	0.48	0.07	0.09
13.4	—	*Central wavelength*	—
13.5	1.65	0.17	0.79
13.6	3.28	0.48	1.28
13.7	2.58	0.34	1.24

required to perform measurements at different wavelengths.

The wavelength-dependent change of the measured wavefronts is a small effect. Its significance becomes most apparent in an examination of the *difference wavefronts* generated by comparison to the wavefront at 13.4-nm wavelength. With the wavefronts scaled in nanometers (rather than in waves), pairs of measured wavefront profiles are compared. The measured wavefronts from sub-aperture A are reconstructed from the first 37 Zernike polynomials to isolate the low-spatial-frequency figure changes of interest.

The difference wavefronts are shown in Fig. 2. In Fig. 2(a), the difference wavefronts are individually scaled from black to white. In 2(b), the eight difference wavefronts are all represented on the same grayscale. The relevant statistics of these difference wavefronts are presented in Table 1. One noteworthy effect is the apparent change in the focal position at each wavelength. On either side of the central wavelength (13.4 nm), the focal shift occurs in the same longitudinal direction. Defocus is not included in the difference wavefronts of Fig. 2 or in the wavefront statistics reported in Table 1.

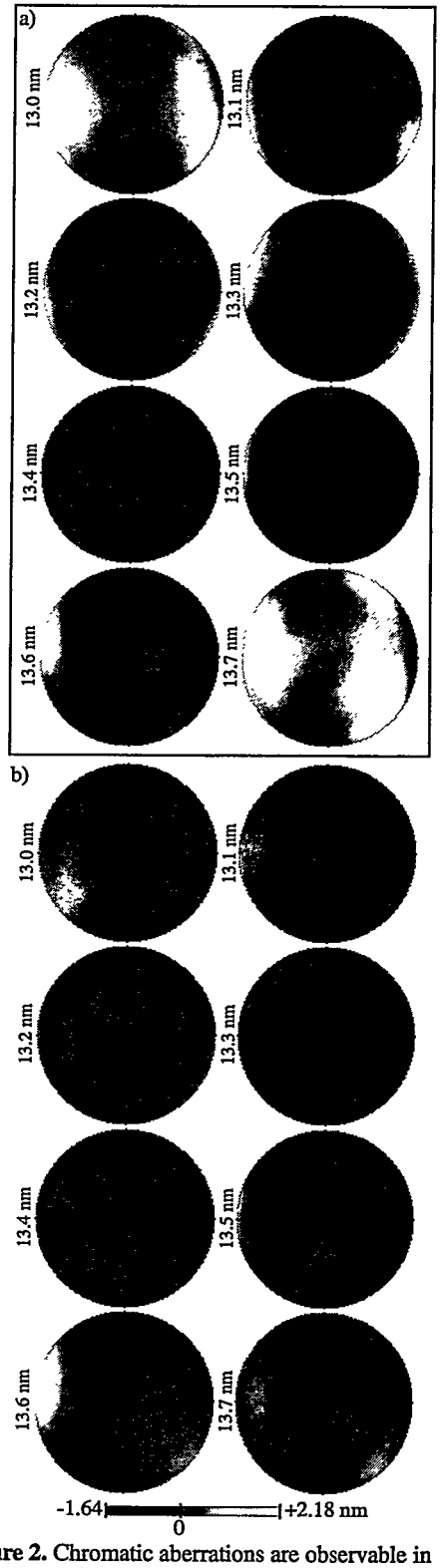

Figure 2. Chromatic aberrations are observable in the variation of the difference wavefronts measured over a range of wavelengths. These are generated by comparison of the wavefronts to the wavefront measured at the design wavelength, 13.4 nm. (a) individually scaled images. (b) all wavefronts are shown on the same scale grayscale.

9.4 BROADBAND ILLUMINATION

To illuminate the system with relatively broadband illumination, the monochromator's planar grating may be

adjusted to give a specular (zeroth-diffractive-order) reflection. In this configuration, the bandwidth is primarily determined by the undulator: with 55 magnetic periods, the natural bandwidth of the undulator radiation into the first harmonic is $\lambda/\Delta\lambda \approx 55$, or 0.24 nm at 13.4-nm wavelength.The total flux reaching the K-B mirrors does not increase noticeably because the blazed grating diffracts very efficiently into its first diffractive order.

With a measured bandwidth of 0.9 nm (6.7%), the near-45° multilayer-coated turning mirror does not significantly filter the beam. Here, the term *broadband* is used to denote the case where the zeroth-order reflection from the monochromator is used — not to indicate the presence of *truly* broadband light.

A series of interferometric experiments was performed with the beamline in this *no monochromator* configuration. The experiments were all conducted using sub-aperture C (0.06 NA) of the Schwarzschild objective. Experiments with the standard beamline configuration, using the first diffractive order from the monochromator, were conducted immediately following the broadband experiments, with no physical changes made to the interferometer.

9.4.1 *Wavefront Measurements with* Broadband Illumination

Comparison of the wavefront data measured both with and *without* the monochromator shows agreement to well within the expected uncertainty. The wavefront in the *no monochromator* case was calculated from three phase-shifting series. Compared to the measured wavefront at 13.4-nm wavelength, the difference wavefront, reconstructed from the first 37 Zernike polynomials, shows an RMS wavefront displacement of 0.011 waves (0.147 nm, or ~λ/90) and peak-to-valley displacement of 0.108 waves (1.45 nm, or ~λ/9). Based on these values, the two measurements are indistinguishable within the uncertainties typically observed in this interferometer.

9.4.2 *Wavefront and Intensity Measurements in the Zeroth-Order Reference Configuration*

In the presence of broadband illumination, the zeroth-order reference configuration of the PS/PDI is predicted to behave differently from the default first-order reference configuration. As described in Section 5.4, the wavelength-dependent diffraction angle of the grating beamsplitter separates the available wavelength components laterally in the image-plane. The position of the zeroth-order focus remains stationary, affected only by the chromatic aberrations in the test optic. Yet in the first-order reference configuration, where the pinhole sits in the grating's first-order beam, it functions as a monochromator – based on the geometry, it transmits some wavelength components more efficiently than others. The test beam is transmitted through the window and may contain a much broader bandwidth than the reference beam. Alternately, in the zeroth-order reference configuration the various wavelength components are not distributed laterally in vicinity of the reference pinhole, and (dependent on the chromatic aberrations of the test optic) the reference beam is broadband. The test beam in this configuration *also* contains the available

wavelength components, transmitted through the large window.

With broadband illumination, a comparison is made of the wavefront measurements from these two configurations. The two tests were performed consecutively; wavefront measurements from single phase-shifting series are compared here. The difference wavefronts, compared assuming 13.4-nm central wavelength, show an RMS displacement of 0.010 waves (0.134 nm, or ~λ/100) and P-V displacement of 0.122 waves (1.635 nm, or ~λ/8). Hence, the wavefront measurements are again indistinguishable within the typical uncertainties.

From these two configurations, the transmitted intensity is expected to be higher in the first-order reference configuration because *all* of the wavelength components of the test beam are transmitted to reach the detector. The fringe contrast is affected by three independent considerations: the relative intensity of the first-order beams is estimated to be approximately 40% of the zeroth-order beam; the spatial filtering of the reference pinhole significantly reduces the intensity of the reference beam; and, since interference fringes are only produced by the interference of like-wavelength components, a mismatch of the bandwidths of the two beams reduces the observed fringe contrast. Given these considerations, the zeroth-order reference configuration may be expected to produce greater fringe contrast.

After compensating for the decreasing intensity of the synchrotron illumination, the total measured signal is 2.4 times higher in the first-order reference than in the zeroth-order reference configuration. The overall fringe contrast is measured to be 22% with the first-order reference, compared to 41% with the zeroth-order reference configurations.

These particular intensity and fringe contrast measurements depend too strongly on the transmission properties of the reference pinhole to carry broad implications for the benefits of one configuration over the other. Furthermore, the quality of the optical system plays an important role in determining the maximum achievable fringe contrast from the PS/PDI. More investigation is needed to establish the advantages and disadvantages of these two arrangements. However, the consistency among the wavefront measurements indicates that the interferometer system is very tolerant of the bandwidth of the illumination.

9.5 VISIBLE-LIGHT

Observations of the intensity transmission of the 10× Schwarzschild objective were made at visible-light wavelengths. As described in Section 6.2.3, HeNe laser light was introduced via a fiber-optic line directly into the HMF. Spatial filtering was performed by the fiber's polished tip, and the illumination over-filled the NA significantly. The intensity transmission data is shown in Fig. 3 adjacent to a similar EUV image at 13.4-nm wavelength.

A special visible light PS/PDI image-plane pinhole membrane was fabricated, and one series of

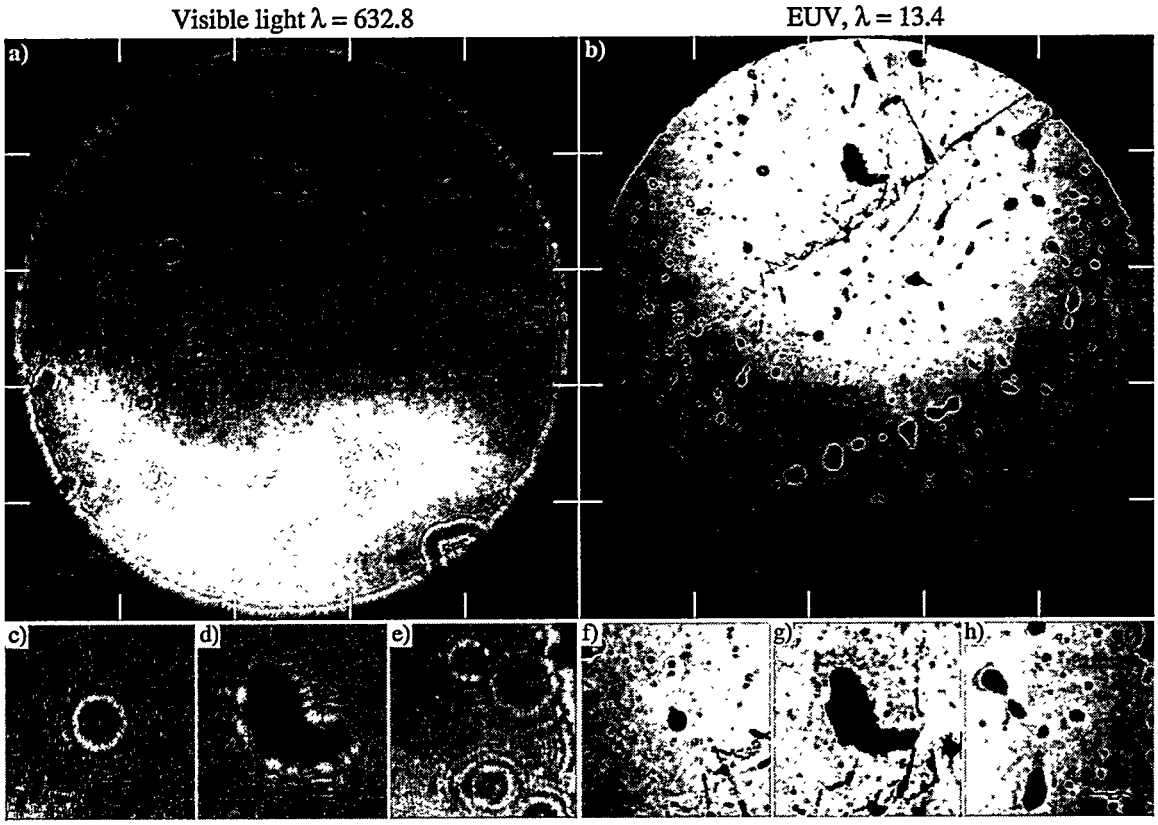

Figure 3. Side-by-side comparison of the transmitted intensity measured at a visible-light wavelength (a), 632.8 nm, and the EUV design wavelength (b), 13.4 nm. Three regions are shown in detail for visible-light, (c) through (e), and for EUV, (f) through (h). The detector is well beyond the plane in which the pupil is re-imaged by the secondary, and diffraction affects the two wavelengths to a much different extent. Only some of the blemishes observable at EUV wavelengths are seen in the visible light image, demonstrating important differences in these two methods of inspection. The bright patch of light in the lower portion of the visible-light image is caused by an unintentional reflection in the vacuum chamber.

experiments was conducted as a demonstration of PS/PDI interferometry at visible-light wavelengths. Because of the large diffraction angles from the grating beamsplitter used in the EUV experiments, a coarser grating was chosen. This ensures that the zeroth- and first-order beams fall within the acceptance angle of the object-side NA and reduces the fringe density in the interferogram. In these experiments, a simple mechanical limitation prevented the fiber-tip from reaching the object plane. As a result, the measurements were hampered by an unacceptable amount of defocus. Figure 4 shows one interferogram pat-

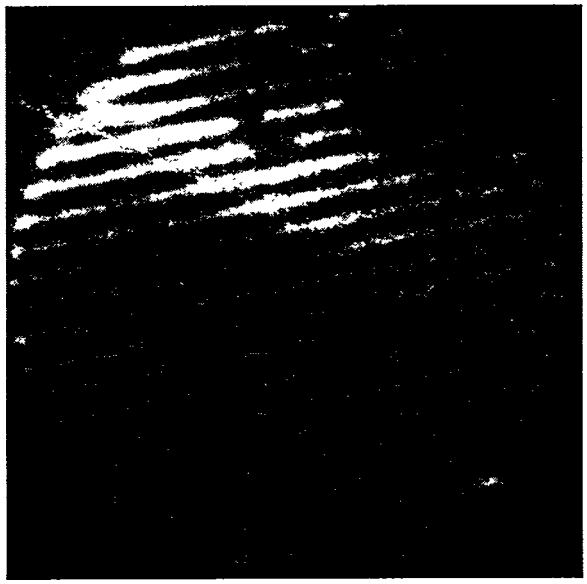

Figure 4. A visible-light PS/PDI interferogram of sub-aperture A. The grating beamsplitter used in this image is more coarse than the one used for EUV interferometry, leading to a lower fringe density.

tern from this demonstration experiment.

The development of a concomitant capability high-accuracy visible-light interferometry capability is highly desirable for many reasons. System alignment could be performed while the components inside the chamber are accessible, before the system is brought under vacuum. Furthermore, direct comparisons could be made between the wavefront measurements performed at EUV and visible wavelengths.

One major difficulty in this effort is the presence of systematic errors that depend on the image-plane beam separation. For example, the magnitudes of the systematic coma effect (Section 5.5) and the astigmatism related to detector alignment (Section 5.6) depend linearly on this separation. At nearly fifty times the EUV wavelength, the beam separation required for the visible-light measurements makes these systematic effects more than an order of magnitude larger than the small aberrations of interest. Further research is required to identify ways to address these problems. One solution may be to use a different common-path interferometer, such as the LSI (Chapter 4) or the conventional PDI, both of which are easier to develop and operate at visible-light wavelengths than for the EUV.

IV. INTERFEROGRAM ANALYSIS

10

Interferogram Analysis Overview

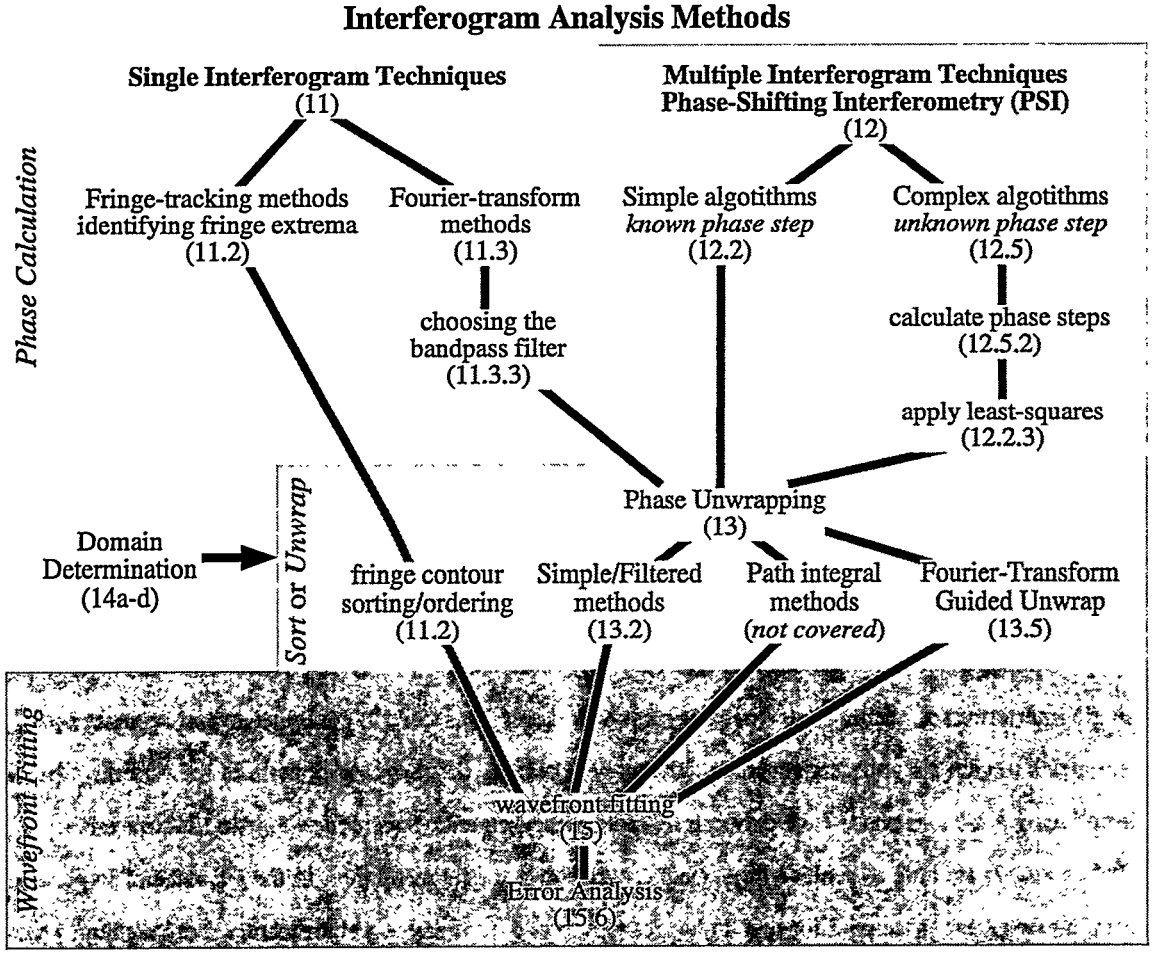

Figure 1. Flowchart-outline of the interferogram analysis methods discussed in this dissertation. The chapter and section of each subject are shown in parentheses.

10. INTERFEROGRAM ANALYSIS OVERVIEW

> "In any interferometric optical testing procedure the main objective is to determine the shape of the wavefront measured with respect to a best fit sphere." (Malacara and DeVore 1992)

Fundamentally, interferogram analysis is the solution of an inverse problem for which more than half of the information is missing and the data is coarsely sampled. An intensity *fringe pattern* is recorded at a location removed from the optical system under test, and the central question is, what electric field in the exit pupil produced the measured intensity distribution?

This section, comprised of Chapters 10 through 15, is dedicated to the practical solution of this inverse problem, with specific attention paid to interferogram analysis of EUV interferometric data. The goal is to retrieve the wavefront produced by the optical system under test. Following some simplifying assumptions, this difficult inverse problem becomes tractable and yields to rapid automated analysis methods.

Historically, methods for interferogram analysis have been divided into two main categories by their use of either single or multiple recorded interferogram images. Figure 1 outlines some of the available methods and shows in which section of this thesis they are discussed.

The *single interferogram analysis techniques* (Chapter 11) use either the fringe profiles or a Fourier-domain analysis of the intensity data to recover the phase. The *Fourier-transform method* is resistant to noise and can be highly efficient and very simple to apply. However, it suffers from low spatial-resolution and can be vulnerable to errors in the presence of abrupt features in the data.

Although more time-consuming and generally more challenging to implement than those involving a single interferogram, the *multiple interferogram techniques* (Chapter 12) combine several separate measurements to gain a significant statistical advantage. Utilizing the *temporal* domain of measurement by introducing a relative phase-shift between separate measurements, these Phase Shifting Interferometry (PSI) methods are able to achieve high accuracy *and* high spatial resolution. In the presence of imperfect data, however, the price paid for this higher resolution and accuracy is a significantly more difficult process of analysis, required to be robust in the presence of noise.

Once the phase is known, most analysis techniques require one further, critical step. Typically, the phase is only measured to within an integer multiple of 2π, and for each fringe in the interference pattern there can be an accompanying 2π discontinuity contour. To remove the presence of these discontinuities, the data must undergo a process called *phase unwrapping*. Although innocuous in appearance, the process of phase unwrapping (Chapter 13) is in itself a challenging inverse-problem and, in the opinion of the author, is the most difficult aspect of interferogram analysis. The literature is filled with phase unwrapping techniques for all occasions, and there appears to be little agreement as to the best approach.

After the wavefront phase has been successfully unwrapped, interpretation of the data often

requires that the measured surfaces be cast into a convenient set of orthogonal surface polynomials, such as the Zernike polynomials (Chapters 14 and 15). Once a coordinate system has been established for the data, the surface fitting can proceed in several ways, with some methods more appropriate for accurate analysis than others.

The procedures and techniques described in these chapters cover the process of interferogram analysis from start to finish, following several different paths. More than just a recitation of available methods, these chapters also introduce several novel procedures developed by the author, including the *Fourier-Transform Method of Phase-Shift Determination* (Chapter 12), developed to address difficulties with phase shift calibration, and the *Fourier-Transform Guided Unwrap Method* (Chapter 13), created and successfully employed to overcome significant high- and mid-spatial-frequency noise in the raw phase data. In addition, to facilitate accurate wavefront surface fitting and representation in terms of the aberration polynomials, an expedient Gram-Schmidt orthogonalization process (Chapter 15) is described.

11

Single Interferogram Analysis Methods

11.1 INTRODUCTION

Several methods of single-interferogram analysis are available when phase-shifting methods cannot be applied. Procedures that determine the positions of the fringe maxima or minima, or that utilize Fourier-domain processing, all rely on the same assumption: intensity variations caused by the *phase* of the test beam can be separated from those caused by the *amplitude* alone. Although this assumption makes these analysis methods highly sensitive to amplitude fluctuations that distort fringe positions, proper filtering of the interferogram data can greatly enhance the reliability of single interferogram analysis methods. This section provides a description of several of these methods and discusses their application.

The methods that scan the interferogram searching for local maxima, minima, or zero-crossings of the derivative are known as *fringe-tracking* or *fringe-center* techniques. Often the discrete derivative of the interferogram data is used to locate these contours of constant phase, each separated from the next by one wavelength. After the distinct phase contours are properly ordered, a (typically sparse) representation of the wavefront surface emerges. A wide variety of intensity-based fringe-tracking strategies are discussed by Yatagai (1993). In general, fringe-tracking methods suffer from non-uniform spatial sampling, and risk overlooking sub-wavelength variations in phase.

Since the advent of computer-aided data collection and image -processing in the last few decades, fringe-tracking techniques have become less widely used. Other techniques now offer significantly higher resolution and accuracy. Historically, however, the fringe-tracking methods have proven very successful, and thus merit a brief discussion here. These straightforward methods were applied at the earliest stages of this EUV interferometry research.

A separate class of procedures, the *Fourier-transform techniques,* utilize the spatial-frequency domain to separate low-to-mid spatial-frequency *phase* modulations of interest from lower-frequency *amplitude* modulations and high-frequency noise. Typically a spatial carrier-frequency is introduced to facilitate this Fourier-domain separation. The Fourier-transform method, first described by Takeda et al. (1981), has spawned a great number of adaptations and related techniques. The fundamental aspects of the Fourier-transform method are described in this chapter, with emphasis placed on the practical application of these methods to EUV interferometry.

11.1.1 *The Monotonic Phase Requirement*

Although the various fringe-tracking and Fourier-transform methods differ greatly in their approach and implementation, both types impose one important requirement on the measured wavefront phase.

> Proper analysis requires that *all* intensity maxima and minima represent points where the local phase is separated from other minima/maxima by an integral number of 2π cycles (or wavelengths, λ).

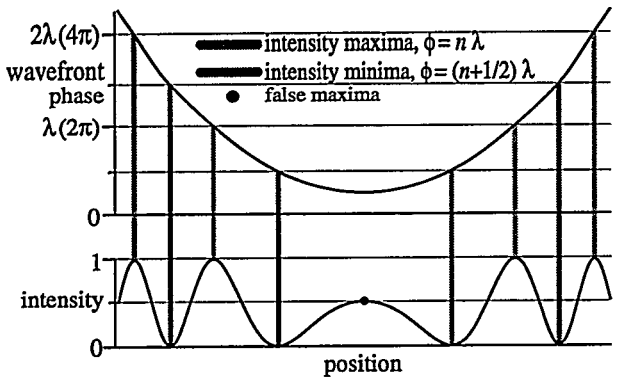

Figure 1. Interferogram intensity extrema occur when either of two conditions are met: the phase equals a multiple of nπ or the phase function itself reaches a maximum or minimum. To guarantee successful analysis, the singe interferogram techniques require that the latter case, illustrated by the central point of the graph, never occurs within the measurement domain. The figure shows the correspondence between each intensity extrema and the phase function.

This requirement removes potential ambiguities from the data. In some cases, filtering must be used to remove the isolated, spurious local maxima created by high-frequency noise. Excluding such noise, this rule applies mainly to low-spatial-frequency variations.

Consider Fig. 1, in which this requirement is violated and such phase ambiguity is illustrated. This figure is based on the one-dimensional expression

$$I(x) = A + B\cos\left[\phi(x)\right], \tag{1}$$

with $A = B = 1/2$ and a parabolic phase function. (This discussion can easily be extended to two dimensions, where a similar rule applies.) All but one of the local minima and maxima are seen to correspond to points where the phase crosses $\phi(x) = n\lambda/2$ waves (or $n\pi$ radians). Notice that in the center of the graph the local intensity maximum (indicated by a gray circle) corresponds to a local minima of the phase function, and *not* to a specific multiple of $\lambda/2$ in phase. Such a *false maximum* can confuse the fringe tracking analysis methods: it may be counted erroneously as a position where $\phi = n\lambda/2$ waves.

This requirement can be illustrated mathematically. From Eq. (1), the condition for an intensity extrema is

$$\frac{dI(x)}{dx} = 0 = -B\frac{d\phi(x)}{dx}\sin\left[\phi(x)\right]. \tag{2}$$

This condition is satisfied in two cases: first, where the phase function has a minimum or maximum

$$\frac{d\phi(x)}{dx} = 0, \tag{3}$$

and second, where the phase function crosses $n\pi$ radians, (or $n\lambda/2$ waves).

$$\sin\left[\phi(x)\right] = 0 \;\Rightarrow\; \phi(x) = n\pi \text{ [radians]} = \frac{n\lambda}{2} \text{ [waves]}. \tag{4}$$

In order to guarantee that over the measurement domain the *only* extrema come from $\phi(x)$ crossing $n\lambda/2$ waves, there must exist no point in the domain at which Eq. (3) is satisfied. This brings us to three *equivalent* requirements on $\phi(x)$.

1. $\phi(x)$ must not contain an extrema within the domain of measurement.
2. $\phi(x)$ must be *monotonic* within the measurement domain.
3. $d\phi(x)/dx \neq 0$ within the measurement domain. In two-dimensions, this requirement is $\nabla\phi \neq 0$.

A spatial carrier-frequency, or *tilt*, is introduced to satisfy this monotonic phase requirement. Beginning with a phase function $\phi_o(x)$ containing zero average slope, add or subtract a tilt component kx.

$$\phi(x) = \phi_o(x) - kx. \tag{5}$$

Using requirement 3 above, one statement of the monotonic phase requirement becomes

$$\frac{d\phi_o(x)}{dx} < k. \tag{6}$$

The test wavefront slope must neither equal nor exceed the slope of the carrier-frequency wave.

Experimentally, this places more of a requirement on the carrier-frequency than it does on the test wavefront. The carrier-frequency can usually be controlled to some extent, while the test wavefront is determined by the optical system being measured.

This slope restriction alone does *not* place a limitation on the highest measurable spatial-frequency of the test wavefront. In principle, high-frequency components of small phase amplitude *can* be measured as long as the slope does not exceed k. For example, if the phase function $\phi_o(x)$ contains a single spatial-frequency component k_A such that

$$\phi_o(x) = A\sin(k_A x) \tag{7}$$

then the limitation on the amplitude A imposed by Eq. (6) is

$$A < \frac{k}{k_A}. \tag{8}$$

In practice, there will be a wide range of spatial frequencies and amplitudes present in $\phi_o(x)$. This simplistic model requires that high-frequency components have smaller magnitude than the low-frequency components, to impose an upper limit on the phase *slope*.

The limitation on the highest allowable slope comes from the Nyquist limit (Nyquist 1928). In principle, the sampling density cannot be lower than two points per fringe or the pattern will be unmeasurable. The width of the detector elements may also contribute to a reduction in measurable fringe contrast if the fringe density is too high. There are sub-Nyquist interferometry (SNI) methods that rely on *a priori* wavefront information (Greivenkamp 1987).

11.2 APPLICATION OF THE FRINGE-TRACKING METHODS

This section is a brief digression into the application of fringe-tracking methods of interferogram fringe pattern analysis. These methods were used in the early stages of the EUV interferometry research,

applied only to the Fresnel zone plate measurements. (Once the more sophisticated Fourier-transform methods of single interferogram analysis were successfully implemented, they quickly replaced fringe-tracking.)

Assume, for the purposes of this discussion, that a spatial carrier-frequency has been introduced to generate a fringe pattern with a generally-horizontal fringe orientation. Contours of constant phase chosen for analysis may be those of the intensity *maxima*, the *minima*, or the so-called *zero-crossings*. The zero crossings are the inflection-point contours of the fringes.

One procedure for locating the fringe maxima uses the discrete derivative of the intensity along each column. Consider an interferogram $I(x, y)$ on a rectangular grid of size $N_x \times N_y$.

Procedure 1: Fringe-Tracking Method Using Fringe Maxima.

1. Loop i from 1 to N_x
2. $d(j) \equiv I(i, j+1) - I(i, j)$ *(single-column discreet derivative)*
3. $j^* \equiv \{j \mid d(j) \geq 0 \text{ AND } d(j+1) < 0\}$ *(set containing locations of the maxima)*

3a $j^* \equiv \{j \mid d(j) \leq 0 \text{ AND } d(j+1) > 0\}$ *(alternately, the minima may be used)*

4. Add points $\{(i, j^*)\}$ to the set of maxima from which the contours are constructed.

4a. [Optional] Keep track of the *order* of these points vertically.

4b. [Optional] Use polynomial fitting of the neighboring points to more accurately locate the individual maxima, allowing the elements of j^* to take non-integral values.

5. Sort (order) the contour data into separate, "continuous" contours.

In Step 2, the maxima are identified as points where the derivative goes from non-negative to negative. Of course, noisy data can generate spurious maxima; the data may require filtering in the vertical direction. The median filter and various other low-pass filters have been recommended (Yatagai 1993).

Sorting the contour data means identifying the contour-line to which each maxima point belongs. This procedure is also called *fringe ordering*. When the contour lines are unbroken and span the width of the array, as is the case in Fig. 2(b), this exercise is almost trivial to perform. However, if the data exists on a limited sub-region, if contours are discontinuous, or if the contours deviate significantly from a pre-

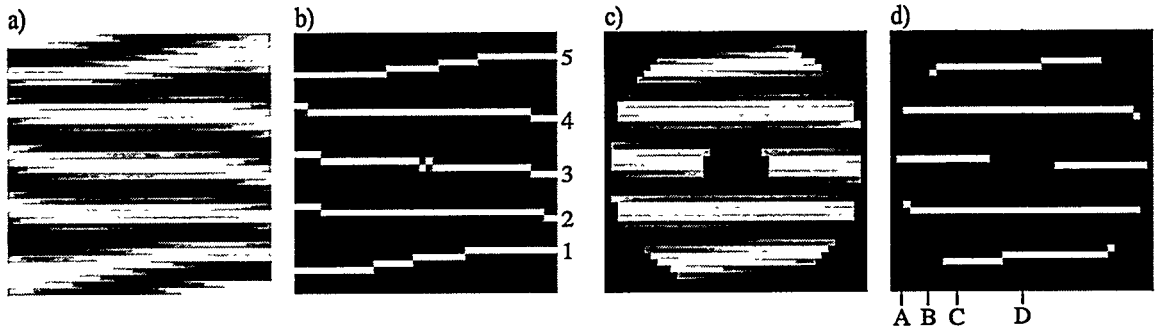

Figure 2. Illustration of the fringe-tracking method, with sorting. The vertical-direction derivative is used to locate the extrema of the interferograms in (a) and (c). The positions of these extrema, shown in (b) and (d), trace contours of constant path-length-difference between the two interfering beams. Each contour is separated from the next by one wavelength of path-length-difference. Analysis requires that each contour be regarded separately from its neighbors in a process known as *sorting*. Numbers indicate the index of the sorted contours. When the contours span the width of the domain, sorting by examination of the columns is trivial. However, when the domain does not reach the edges of the array or contains obstructions, automated sorting procedures become complex.

dictable direction, then the sorting algorithm may require a flexible approach. Fig. 2(d) shows a case where a flexible sorting routine is required. Notice here that scanning upward (or downward) along the columns indicated by the lines A, B, C, and D, a simple contour-counting algorithm would erroneously attribute adjacent maxima points to different contours. If the fringes do not reach the edge of the measurement domain, care must also be taken to avoid falsely attributing maxima or minima to points near the domain edges.

One severe limitation of the fringe-tracking techniques is the relative sparseness of the sampled wavefront contour data. If the fringe separation corresponds to N pixels on average in the detector measurement domain, then the coverage of the measurements is approximately $1/N$ of the total number of available points. Although this may be *thousands* of points, since those points are arranged along narrow stripes, the surface fitting and subsequent wavefront reconstruction may yield spurious wavefront curvature in regions not covered by the contours.

The decision on whether to use the maxima, minima, or zero-crossings depends on several competing factors. In the presence of noise, the signal-to-noise ratio is often highest at the peaks of the intensity pattern. Based on this alone, maxima location would appear to be more accurate than minima location. Complicating this assumption is the fact that variations of the background intensity or of the fringe amplitude can shift the locations of the extrema. These competing concerns must be addressed in choosing the best algorithm.

11.3 FOURIER-TRANSFORM METHODS

Since the early part of the 1980s, Fourier-transform techniques for interferogram fringe pattern analysis and wavefront recovery have gained widespread acceptance as the leading methods for single-interferogram analysis (Takeda et al. 1981, Nugent 1985, Bone et al. 1986, Kreis 1986, Roddier and Roddier 1987). In addition to their versatility and ease of application, the Fourier-transform techniques hold other, more significant advantages over the fringe-center methods. These Fourier methods often contain spatial-frequency filtering as one component of their application, and are thus more resistant to the presence of high-frequency noise, low-frequency background variation, and low-frequency fringe-amplitude variations. Furthermore, these methods generate wavefront data over the entire measurement domain, unlike the sparsely-sampling fringe-center methods.

In this thesis, Fourier-transform methods are used in the analysis of all of the Fresnel zoneplate data (Chapter 3) and for various measurements of the Schwarzschild objective where phase-shifting data is unavailable (Chapter 8).

The Fourier-transform methods are easily understood from consideration of the spatial-frequency-

spectrum of the interferogram data. To begin, the *real* one- or two-dimensional interferogram data is represented by additive and multiplicative intensity components. These components of the fringe modulation represent the stationary and the modulated intensity, respectively. As in the other single-interferogram techniques, a spatial carrier-frequency $\mathbf{k}_o$ is introduced to facilitate analysis.

$$I(\mathbf{r}) = A(\mathbf{r}) + B(\mathbf{r})\cos\left[\phi_o(\mathbf{r}) + \mathbf{k}_o \cdot \mathbf{r}\right], \quad \text{with } A, B, \phi_o \in R\,. \tag{9}$$

Successful implementation of the Fourier-transform techniques relies on frequency-domain separation of the interferogram *phase* modulation from the *amplitude* modulation. This requirement puts limitations on each term of the interferogram as represented in Eq. (9), and on the spatial carrier-frequency, as well. $A(\mathbf{r})$, $B(\mathbf{r})$, and $\phi(\mathbf{r})$ may contain both low- and high-frequency variations, but there must be a range of spatial frequencies over which these functions are *quiet* (arbitrarily small in magnitude). The spatial carrier-frequency is used to shift the phase-variations of interest into this *quiet* region of the domain. The range of phase modulation spatial frequencies that is available for accurate analysis is primarily determined by the spatial-frequency *width* of the quiet region.

Since the two terms in Eq. (9) are additive, it is always possible to attribute all of the high-frequency variations in the interferogram to $A(\mathbf{r})$ alone. (This is not true for phase-shifting analysis (Chapter 12), in which the stationary components are separable from the modulated components of the intensity.)

To facilitate the Fourier-domain representation of the interferogram, the cosine may be separated as follows.

$$I(\mathbf{r}) = A(\mathbf{r}) + \tfrac{1}{2}B(\mathbf{r})e^{i\left[\phi_o(\mathbf{r}) + \mathbf{k}_o \cdot \mathbf{r}\right]} + \tfrac{1}{2}B(\mathbf{r})e^{-i\left[\phi_o(\mathbf{r}) + \mathbf{k}_o \cdot \mathbf{r}\right]}, \tag{10}$$

$$I(\mathbf{r}) = A(\mathbf{r}) + C(\mathbf{r})e^{i\mathbf{k}_o \cdot \mathbf{r}} + C^*(\mathbf{r})e^{-i\mathbf{k}_o \cdot \mathbf{r}}, \tag{11}$$

where

$$C(\mathbf{r}) \equiv \tfrac{1}{2}B(\mathbf{r})e^{i\phi_o(\mathbf{r})} \tag{12}$$

and * indicates the *complex conjugate*. From Eq. (11), the Fourier-transform of the interferogram may be written

$$i(\mathbf{k}) = a(\mathbf{k}) + c(\mathbf{k} - \mathbf{k}_o) + c^*(\mathbf{k} + \mathbf{k}_o)\,. \tag{13}$$

Here, functions denoted by upper case letters are used to indicate the *spatial* (measurement) domain, and lower-case letters denote the Fourier-transform of each. (The definition of the discrete Fourier-transform, as applied to interferogram data, is discussed in Section 11.3.2.) The phase information we seek is contained in $c(\mathbf{k} - \mathbf{k}_o)$, or equivalently in $c^*(\mathbf{k} + \mathbf{k}_o)$. The addition of the carrier-frequency facilitates the separation of either $c(\mathbf{k} - \mathbf{k}_o)$ or $c^*(\mathbf{k} + \mathbf{k}_o)$ from the other components of the spatial-frequency spectrum. $c(\mathbf{k} - \mathbf{k}_o)$ and $c^*(\mathbf{k} + \mathbf{k}_o)$ form separate *side-lobes* centered on $\mathbf{k}_o$ and $-\mathbf{k}_o$ respectively. The isolation of one side-lobe is our immediate goal.

Since $I(\mathbf{r})$ is real, its Fourier-transform $i(\mathbf{k})$ is *Hermitian*, indicating

$$i(\mathbf{k}) = i^*(-\mathbf{k}) . \tag{14}$$

The amplitude of the spatial-frequency spectrum $|i(\mathbf{k})|$ has polar symmetry about the central, zero-frequency component. $a(\mathbf{k})$ is also Hermitian and typically contains a strong peak near zero-frequency, related to the overall intensity of the recorded interferogram.

Depending on the phase aberrations present in the system under test, c and c^* typically consist of a narrow peak near zero-frequency. The presence of the carrier-frequency shifts c and c^* by $\mathbf{k}_o$ and $-\mathbf{k}_o$, respectively, where they can be isolated from the other spatial-frequency-domain components of the spectrum.

Applying to $i(\mathbf{k})$ a bandpass-filter centered about $\mathbf{k}_o$ (alternately, about $-\mathbf{k}_o$) in the spatial-frequency domain achieves several of our goals. One of the components $c(\mathbf{k} - \mathbf{k}_o)$ or $c^*(\mathbf{k} + \mathbf{k}_o)$ is isolated from the rest of the frequency spectrum. Symbolically,

$$i'(\mathbf{k}) \equiv Filtered_{\mathbf{k}_o}\left\{i(\mathbf{k})\right\} = Filtered_{\mathbf{k}_o}\left\{a(\mathbf{k}) + c(\mathbf{k}-\mathbf{k}_o) + c^*(\mathbf{k}+\mathbf{k}_o)\right\} \approx c(\mathbf{k}-\mathbf{k}_o) . \tag{15}$$

Filtering destroys the Hermiticity of $i(\mathbf{k})$, and Fourier-inversion of $i'(\mathbf{k})$ produces an approximation to the complex function $C(\mathbf{r})$. $C(\mathbf{r})$ is only approximately known due to the necessary spatial-frequency-domain filtering and the possible overlap of $a(\mathbf{k})$ and $c^*(\mathbf{k})$. Filtering strategies are discussed in Section 11.3.3. Fourier-inversion of the filtered interferogram returns us to the spatial domain.

$$\mathcal{F}^{-1}\left\{i'(\mathbf{k})\right\} \approx C(\mathbf{r})e^{i\mathbf{k}_o\cdot\mathbf{r}} = \tfrac{1}{2}B(\mathbf{r})e^{i\phi_o(\mathbf{r})+i\mathbf{k}_o\cdot\mathbf{r}} . \tag{16}$$

The wavefront phase information is contained in the exponential term. Here there are several equivalent ways of determining $\phi_o(\mathbf{r})$.

$$\phi_o(\mathbf{r}) + \mathbf{k}_o\cdot\mathbf{r} = \tan^{-1}\left(\frac{\mathrm{Im}\{C(\mathbf{r})\}}{\mathrm{Re}\{C(\mathbf{r})\}}\right) = \tan^{-1}\left(\mathrm{Im}\{C(\mathbf{r})\},\ \mathrm{Re}\{C(\mathbf{r})\}\right) = \tan^{-1}[C(\mathbf{r})] , \tag{17a, b, c}$$

or, equivalently,

$$\phi_o(\mathbf{r}) + \mathbf{k}_o\cdot\mathbf{r} = \mathrm{Im}\{\ln[C(\mathbf{r})]\} . \tag{17d}$$

Note that the additive term $\mathbf{k}_o\cdot\mathbf{r}$ behaves simply as a removable wavefront *tilt* added to the phase function of interest. Regarding the arctangent, certain computer applications require the input arguments to be provided in one of the equivalent formats shown in Eqns. (17a) through (17c).

Since the arctangent and the complex logarithm are periodic functions, $\phi_o(\mathbf{r})$ is only determined to within a multiple of π or 2π. Equation (17a) returns $\phi_o(\mathbf{r})$ as a modulo π function, while Eqns. (17b) through (17d) return $\phi_o(\mathbf{r})$ modulo 2π. This common aspect of interferogram analysis leads to the necessity of *phase unwrapping* to remove the ambiguity caused by this loss of information, and to re-create a continuous wavefront. Phase unwrapping is the subject of Chapter 13.

Regarding the Fourier-inverse-transform of Eq. (16), Nugent (1985) recommends the optional step of *shifting* the filtered interferogram $i'(\mathbf{k})$ by $\pm\mathbf{k}_o$ to shift one of the symmetric $c(\mathbf{k})$ lobes to the zero-fre-

quency position *before* the inverse transform is performed. In so doing, the bandpass filter will be centered on the zero-frequency, and all or most of the tilt will be removed. The difference here is mainly cosmetic. If the carrier-frequency is precisely known, then $\phi_o(\mathbf{r})$ may be recovered directly from the methods of Eqns. (17a) through (17d). When $\mathbf{k}_o$ is known only approximately, the shift in the spatial-frequency-domain reduces the amount of wavefront tilt added to $\phi_o(\mathbf{r})$, and potentially eliminates a large number of wrapping transitions caused by the modulo 2π reconstruction of $\phi_o(\mathbf{r})$.

Now that the mathematical framework has been established, the following two sections address issues related to the practical application of the Fourier-transform method. The first section briefly discusses the discrete Fourier-transform (DFT), and the second addresses the selection of the Fourier-domain filter used in the Fourier-transform method.

11.3.1 *The Discrete Fourier-Transform*

Interferogram measurements are generally collected on a square-grid, discrete domain. Consequently, all Fourier-transform operations required by the methods described in the previous section are performed on this domain. In order to study the application of various Fourier-domain filters, we begin with the conventional definition of the discrete Fourier-transform (DFT) (Conte and de Boor 1980:277-83). For an arbitrary function $G(\mathbf{r})$, with $\mathbf{r} \equiv (x, y)$, defined on the discrete, two-dimensional, $N \times N$ domain, the Fourier-transform operation is defined as

$$\mathcal{F}\{G(\mathbf{r})\} \equiv g(\mathbf{k}) \equiv \sum_{\substack{x=0 \\ y=0}}^{N-1} G(\mathbf{r}) \exp\left[\frac{i2\pi}{N}(\mathbf{k}\cdot\mathbf{r})\right], \tag{18}$$

or, equivalently,

$$\mathcal{F}\{G(x,y)\} \equiv g(k_x,k_y) \equiv \sum_{\substack{x=0 \\ y=0}}^{N-1} G(x,y) \exp\left[\frac{i2\pi}{N}(k_x x + k_y y)\right]. \tag{19}$$

Here, upper-case functions denote the spatial domain, while their lower-case counterparts refer to the domain of spatial-frequencies. The position vector in the spatial-frequency domain $\mathbf{k}$ is defined in *cycles*. The inverse transform is defined as

$$\mathcal{F}^{-1}\{g(\mathbf{k})\} \equiv G(\mathbf{r}) \equiv \frac{1}{N^2} \sum_{\substack{k_x=0 \\ k_y=0}}^{N-1} g(\mathbf{k}) \exp\left[-\frac{i2\pi}{N}(\mathbf{k}\cdot\mathbf{r})\right], \tag{20}$$

with an analogous expression for $\mathcal{F}^{-1}\{g(x, y)\}$. The coefficient $1/N^2$ in the definition of the inverse transform guarantees that

$$\mathcal{F}^{-1}\{\mathcal{F}\{G(\mathbf{r})\}\} = G(\mathbf{r}). \tag{21}$$

Note: In many circumstances, computational efficiency is greatly enhanced by the application of the so-called *fast Fourier-transform* (FFT). The FFT algorithm optimizes the computation of the discrete Fourier-transform, although mathematically it is identical to the DFT.

11.3.2 *Analogy Between the Continuous Fourier-Transform and the DFT*

The DFT is actually a special case of the continuous Fourier-transform; considering it as such simplifies the description of filtering presented in the following section. For an arbitrary function $H(\mathbf{r})$ defined in the x-y plane, and periodic in x and y with period N, the Fourier transform of $H(\mathbf{r})$ is

$$\mathcal{F}\{H(\mathbf{r})\} \equiv h(\mathbf{k}) \equiv \int_{x=0}^{N} \int_{y=0}^{N} H(\mathbf{r}) \exp\left[\frac{i2\pi}{N}(\mathbf{k}\cdot\mathbf{r})\right] d\mathbf{r}. \tag{22}$$

In the conventional definition, the argument of the exponential is $i\mathbf{k}\cdot\mathbf{r}$. Here, for analogy with the DFT case, the coefficient $2\pi/N$ has been extracted from $\mathbf{k}$, making $\mathbf{k}$ equivalent to $\boldsymbol{f}$ in the common definition.

The *comb* function helps to make the transition between the continuous and the discrete domains. The comb function may be defined in two similar ways:

$$\mathrm{comb}(x) \equiv \begin{cases} 1, & x \in \textit{Integers} \\ 0, & \text{otherwise} \end{cases}, \quad \text{or} \quad \mathrm{comb}(x) \equiv \sum_{n=-\infty}^{\infty} \delta(x-n). \tag{23}$$

It is easily shown that the Fourier-transform of the comb function in one dimension is

$$\mathcal{F}\{\mathrm{comb}(x)\} = \sum_{n=-\infty}^{\infty} \delta(k-n). \tag{24}$$

Again, a comb function in the spatial-frequency domain. A direct analogy extends to two dimensions where

$$\mathrm{comb}(\mathbf{r}) \equiv \mathrm{comb}(x,y) \equiv \sum_{n_x=-\infty}^{\infty} \sum_{n_y=-\infty}^{\infty} \delta(x-n_x)\delta(y-n_y), \tag{25}$$

and

$$\mathcal{F}\{\mathrm{comb}(\mathbf{r})\} \equiv \sum_{n_x=-\infty}^{\infty} \sum_{n_y=-\infty}^{\infty} \delta(k_x-n_x)\delta(k_y-n_y). \tag{26}$$

When the comb function is included in the Fourier-transform, the continuous Fourier-transform integral reduces to the DFT summation in Eq. (18). By the Convolution Theorem (Goodman 1988:10), including the comb function with an arbitrary function in a continuous Fourier-transform produces the Fourier-transform of the arbitrary function, defined only at discrete positions. This important result enables us to simplify the discussion of bandpass and other filters applied within the Fourier-transform method of analysis: the discrete Fourier-transforms follow their continuous counterparts, but are defined only on a square-grid, discrete domain.

11.3.3 *Spatial-Frequency-Domain Filtering*

Extraction of phase information using the Fourier-transform methods of interferogram analysis requires the application of bandpass filters in the spatial-frequency domain. Selection of the *optimum* filter is a highly complicated process that may in fact require a case-by-case approach. However, several of the

most important filter characteristics can be identified and enumerated. This section defines general criteria for filter selection, and investigates the application of a Gaussian filter of arbitrary width.

11.3.3.1 ***General Filter Requirements*** Three general filter requirements are discussed in this section.

1. Side-lobe isolation.
2. Use of symmetric, real filter functions.
3. Smoothly varying filter amplitude (optional).

Define $t(\mathbf{k})$ as a filter function in the spatial-frequency domain. $T(\mathbf{r})$ and $t(\mathbf{k})$ are a corresponding Fourier-transform pair, with $T(\mathbf{r})$ defined in the spatial domain of measurement. The filter is applied by multiplying the spatial-frequency spectrum by the frequency-shifted filter function.

1. Side-lobe isolation. The foremost goal of the filter is to isolate one of the side-lobes of the spatial-frequency spectrum, containing $c(\mathbf{k}-\mathbf{k}_o)$, or $c^*(\mathbf{k}+\mathbf{k}_o)$, as described in Section 11.3. These symmetric lobes contain the phase information of interest. The magnitude and direction of the displacement is determined by the spatial carrier-frequency $\mathbf{k}_o$.

The minimum requirement for side-lobe isolation, recommended by some authors (Macy 1983, Kreis and Juptner 1989) is a simple *half-plane filter*, displaced slightly from the central frequency to transmit only one side-lobe. In this simple case, the high-frequency information (including noise) is preserved in the measured phase data.

A different approach is to transmit only a bounded region centered on one of the side-lobes. Examples of bounded filters are the *circular* (or *elliptical*) *top-hat* filter and the *Gaussian* filter, which, although technically *not* bounded, decays rapidly toward zero over a short distance from the side-lobe center. In the displacement direction (parallel to $\mathbf{k}_o$), the size is constrained by the separation of the side-lobe and central-lobe. This situation is *directly* analogous to the design considerations of the physical spatial filter window in the PS/PDI (Section 5.10). There is no such filter size constraint in the complementary (perpendicular) direction. In the $\mathbf{k}_o$ direction, the maximum allowable size is constrained by the width of the central lobe. Clearly, larger filter widths allow the transmission of relatively more high-spatial-frequency information; but to avoid overlap, filter radii larger than $|\mathbf{k}_o|/2$ should not be used. When measurements are primarily concerned with only the lowest spatial-frequency aberrations, a very *narrow* filter can be highly effective at significantly reducing noise.

When using a bounded filter function, the filter should be centered on the side-lobe peak (i.e. centered on $\pm\mathbf{k}_o$) to avoid *introducing* phase errors into the calculation. When $\mathbf{k}_o$ is not known in advance, it may be determined approximately by searching the spatial-frequency spectrum for a peak absolute value (or peak square-modulus), excluding from the search a small domain centered about the zero-frequency peak. Of course, since the spatial-frequency spectrum is Hermitian, there will be two peaks, one of which must be selected.

2. Use of symmetric, real functions. When selecting a filter, it is helpful to remember that the complex function of interest, $C(\mathbf{r})$ from Eq. (12), will be convolved with $T(\mathbf{r})$ by the filtering process. $t(\mathbf{k})$ must be carefully selected to ensure that $T(\mathbf{r})$ does not *introduce* phase effects into the data. Requiring $T(\mathbf{r})$ to be symmetric and real (except possibly for a leading complex constant) imposes the requirement that $t(\mathbf{k})$ also be symmetric and real. The simple half-plane filter described above is actually just a large rectangular window filter defined on the periodic domain and displaced from the central frequency. The top-hat and Gaussian filters are also symmetric filters displaced by $\pm\mathbf{k}_o$.

3. Smoothly varying amplitude. This optional requirement is imposed to reduce *ringing* introduced by the filtering process. Filters with sharp features (high slope, or discontinuities) in the spatial-frequency domain may *create* phase oscillations in the measurement. A discontinuity in $t(\mathbf{k})$, for example, may introduce alternating positive and negative lobes into $T(\mathbf{r})$ and, by convolution of $C(\mathbf{r})$ with these alternating lobes, cause ringing near any sharp feature in the data. Experience has shown that ringing plagues the use of both the half-plane (rectangular) filter and the top-hat filter. The Gaussian filter is a logical choice to eliminate the ringing problem: its transform is also Gaussian and contains no alternating lobes.

11.3.3.2 *The Gaussian Filter*

For this discussion, a Gaussian filter is defined in the continuous spatial-frequency domain in two dimensions as

$$t_G(\mathbf{k}) \equiv e^{-(\mathbf{k}/\kappa)^2}. \tag{27}$$

The radius κ at which the $1/e$ amplitude is reached is called the *width* of the filter. The two-dimensional Gaussian filter is separable into a product of two one-dimensional filters defined for any two perpendicular directions. A rotationally symmetric *circular* Gaussian filter, with two equivalent axes, may be defined. In other cases, it may be desirable to define an *elliptical* filter with two widths corresponding to the "semi-major" and "semi-minor" axes.

It is easily shown in one dimension that the continuous Fourier-inverse-transform of the Gaussian filter $t_G(k)$ is also Gaussian. Neglecting leading coefficients not important to this discussion, we have

$$t_G(k) \equiv \exp\left[-\left(\frac{k}{\kappa}\right)^2\right] \;\Rightarrow\; T_G(x) \propto \exp\left[-\left(\frac{x}{N/\pi\kappa}\right)^2\right]. \tag{28}$$

The width in the spatial domain $N/\pi\kappa$ is inversely related to the width in the spatial-frequency domain, as expected. This shows that a *narrow* Gaussian spatial-frequency-domain filter convolves the phase data with a *broad* Gaussian function and vice versa.

The application of circular Gaussian filters in the Fourier-transform method of interferogram analysis is illustrated in Fig. 3. Here, six filters of varying widths are separately used in the analysis of a simulated

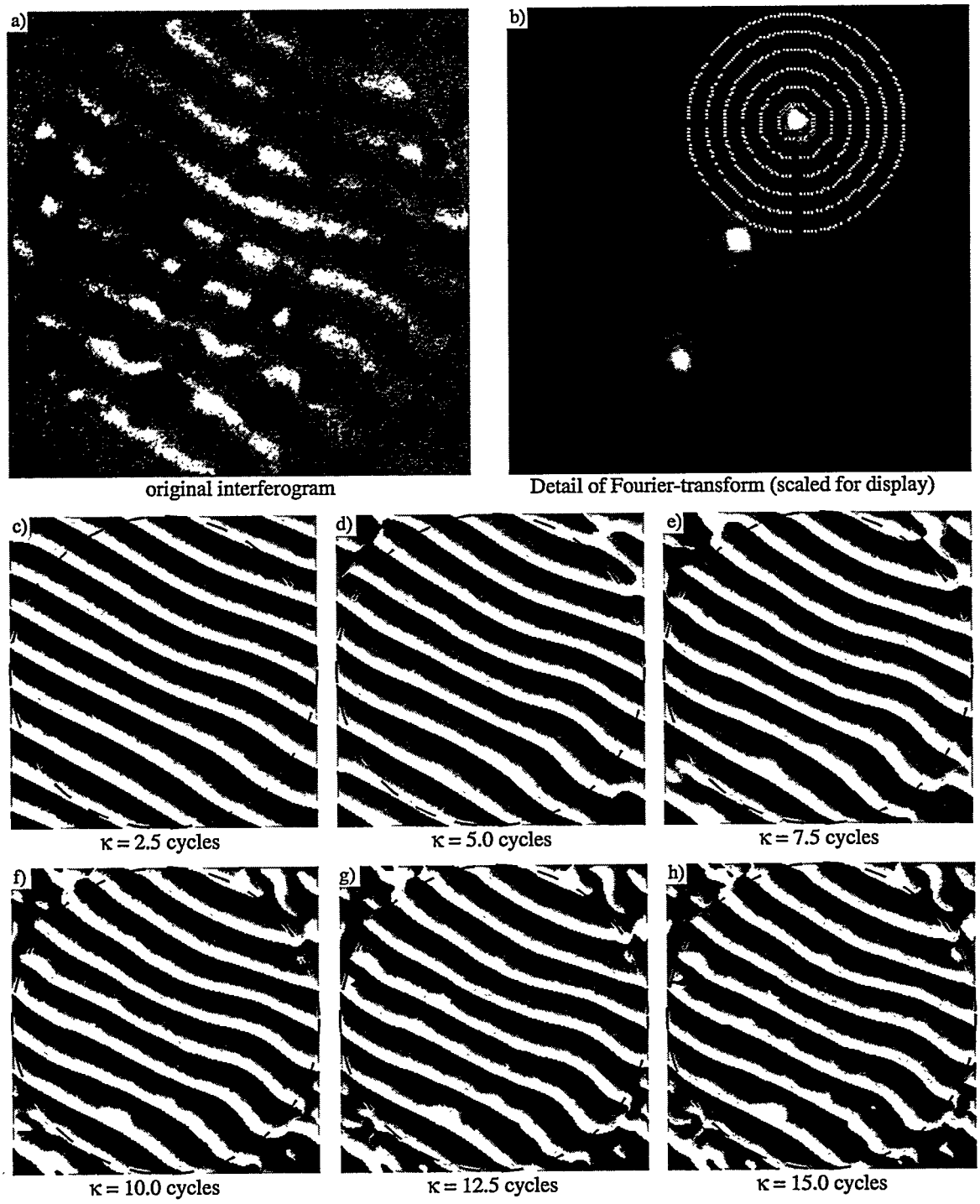

Figure 3. Illustration of the Fourier-transform method of single-interferogram phase-retrieval. The simulated interferogram (a) contains wavefront aberrations, noise, background variation, and blemishes. A Gaussian filter is applied to the spatial-frequency-spectrum (b) to isolate one of the side-lobes. Here, for purposes of illustration, six different filters of varying radius are used. The spectral width of the six filters is indicated by the concentric circles in (b). The modulo 2π phase functions are shown in (c) through (h) for each filter width. Notice that (c), at 2.5-cycles wide, is clearly *over-filtered*, while (g) and (h) are *under-filtered*, enabling the blemishes to cause serious phase errors that will complicate the unwrapping process.

interferogram pattern. The 256 × 256 pixel interference pattern contains numerous imperfections common to experimental data. The curvature of the fringes indicates imperfections in the underlying wavefront. Both high-frequency random noise and a low-frequency additive background intensity are present. To simulate blemishes in the test optic or on the detector, the interferogram is multiplied by a randomly-generated, high-contrast, mid-spatial-frequency pattern.

The interferogram is shown in Fig. 3(a) and a detail of the central portion of the spatial-frequency-spectrum is shown in 3(b), logarithmically scaled for display. The concentric dashed circles placed on the first-quadrant side-lobe of Fig. 3(b) indicate the widths of six different Gaussian filters used in the analysis. For each filter, the wrapped phasemap, calculated using the Fourier-transform method, is shown in Figs. 3(c) through 3(h).

The phase-discontinuities on the wrapped phasemaps follow the fringes closely over the circular measurement domain. Notice that in Figs. 3(c) through 3(e), where heavy filtering (a narrow filter) is applied, the mid-spatial-frequency blemishes and the high-frequency noise are effectively removed from the analysis. In 3(c), with the strongest filter, the calculated phase clearly fails to match the curvature of the wavefront seen in the raw fringe pattern. As the filter width is increased in 3(f) through 3(h), more frequency information is preserved. Effects related to the blemishes are first clearly visible in 3(f). In 3(g) and 3(h), the filtered region in the spatial-frequency domain begins to overlap both the central lobe and the side-lobe. Here, the phase-slope between the discontinuities appears to be non-linear. Also, the blemishes begin to create singular discontinuities in the phasemap. Observe the cusp created by the blemish just to the left of the image center. Such a cusp will create phase-unwrapping difficulties when the conventional phase-unwrapping methods are applied.

One procedure for the implementation of the Fourier-transform method of interferogram analysis, using a Gaussian filter, may now be outlined (Procedure 2). Begin with a square, $N \times N$ interferogram $I_o(x, y)$. The Gaussian filter here defined in Step 5 may be replaced by any other suitable filter. There are several nearly-equivalent representations of the arctangent application in Step 8. Alternatively, it may be represented by $\tan^{-1}\{\mathrm{Im}[I_1(x, y)], \mathrm{Re}[I_1(x, y)]\}$, $\tan^{-1}\{\mathrm{Im}[I_1(x, y)]/\mathrm{Re}[I_1(x, y)]\}$, or $\mathrm{Im}\{\log[I_1(x, y)]\}$.

Procedure 2: The Fourier-Transform Method

1. $f(i, j) \equiv \mathcal{F}\{I_o(x, y)\}$	*(perform the FFT or DFT operation)*
2. $f_1(i, j) \equiv f(i, j) * \{1 - \exp[-(i^2 + j^2)/2^2]\}$	*(define a copy of the frequency spectrum; use a Gaussian filter to eliminate central lobe)*
3. $(i_m, j_m) \equiv$ location of maximum of $\lvert f_1(i, j)\rvert$	*(locate side-lobe peak: there are two, pick one)*
4. $\kappa \equiv 10$	*(define a Gaussian filter width κ. 10 cycles is arbitrary)*
5. $t_G(i, j) \equiv \exp[-(i^2 + j^2)/\kappa^2]$	*(define the Gaussian filter)*
6. $c(i, j) \equiv t_G(i - i_m, j - j_m) * f(i, j)$	*(to isolate one side-lobe, apply the filter, shifted to the location of the side-lobe maximum)*
7. $I_1(x, y) \equiv \mathcal{F}^{-1}\{c(i, j)\}$	*(inverse transform)*
8. $\phi(x, y) \equiv \tan^{-1}\{I_1(x, y)\}$	*(determine phase)*

For clarity, Procedure 2 was written in an expanded form, with each term defined in a separate step. All of the steps may be combined into one *transform-filter-transform* representation, provided that the position of the side-lobe maximum is known in advance.

Procedure 2a: Concise Fourier-Transform Method

1. $\phi(x, y) \equiv \tan^{-1}\left[\mathcal{F}^{-1}\left\{\exp\{-[(i-i_m)^2 + (j-j_m)^2]/\kappa^2\} * \mathcal{F}\{I_o(x, y)\}\right\}\right]$

12

Phase-Shifting Interferometry

12.1 INTRODUCTION

The addition of computers and computer-controlled equipment into the fields of interferometry and optical testing opens the door to a new, powerful class of data-gathering and analysis methods known collectively as *Phase-Shifting Interferometry* (PSI). This chapter introduces some of the basic and extremely useful PSI algorithms and then describes a novel, versatile approach designed specifically to overcome limitations of the first implementation of the EUV PS/PDI described in this thesis.

Although highly effective in some instances, single-interferogram analysis methods are fraught with restrictions and limitations (Chapter 11). Because the single-interferogram techniques rely on the location of "fringe-centers," they are caught in a trade-off between precision and the desire for a high number of sampled data points. Most of these methods can only operate under conditions of high wavefront tilt, where the addition of a spatial-carrier-frequency is required to remove phase ambiguities. In other cases, the requirement is that there be no closed fringe contours. When only one interferogram is collected, additional information is required to determine the overall *sign* or *polarity* of the wavefront (i.e., concave or convex).

PSI overcomes many of the problems that plague single-interferogram analysis methods. PSI, which was first described by Carré in 1966 and fully developed in the 1970s (Crane 1969; Bruning et al. 1974; Wyant 1975), utilizes the *temporal domain* to collect a series of interferograms where only the reference phase of the interferometer is adjusted. Using the multiple interferograms, the wavefront phase is recovered at *each point* in the domain independently from its neighbors. The addition of a spatial-carrier-frequency is not required, the necessity of finding fringe-center locations is eliminated, and the wavefront polarity may be found unambiguously. Furthermore, using only the time-domain to find the phase at each point enhances the potential for high-spatial-frequency measurement. Unlike the single-interferogram techniques, PSI is capable of overcoming spatial variations in the detector response (sensitivity).

There are many available ways to implement the reference phase-shift required by PSI. One of the most common is by translation of a mirror in one arm of an Twyman-Green or Mach-Zender interferometer (Soobitsky 1986; Hayes 1989). The angle of a tilted, plane-parallel, transparent plate placed in the reference beam can be adjusted to induce a path-length change (Wyant and Shagam 1978). Alternatively, a small change of the optical frequency may be used in some cases to produce the required phase-change. The method used in the EUV PS/PDI is the translation of a grating through the beam of light, such that the diffracted beams acquire a phase-shift relative to the *undiffracted,* zeroth-order beam.

However the phase-shift is implemented, the analysis methods are similar. It is most convenient to describe the measured interferogram intensity with two terms: a *stationary* term and a *modulated* or *phase-dependent* term representing the fringes and their amplitude modulation.

$$I(\mathbf{r},t) = A(\mathbf{r}) + B(\mathbf{r})\cos\left[\phi(\mathbf{r}) + \Delta(t)\right]. \tag{1}$$

In Eq. (1), the relative phase-shift between the test and reference beams is absorbed into the time-dependent term $\Delta(t)$. When a finite number of images are recorded, and the system is held stationary during measurement, the individual interferograms can be written as

$$I_n(\mathbf{r}) = A(\mathbf{r}) + B(\mathbf{r})\cos\left[\phi(\mathbf{r}) + \Delta_n\right] \tag{2}$$

The following sections of this chapter are dedicated to the phase-retrieval problem: finding $\phi(\mathbf{r})$ given a series of recorded interferograms. There are limitless varieties of phase-shifting algorithms tailored to meet the specific demands of a wide range of experimental conditions. As mentioned previously, each of these methods utilizes the *temporal* domain to achieve a relative phase shift between the test and reference waves while all other experimental conditions are held stable.

In principle, the analytic solution of Eq. (2) with its three unknowns requires that three or more interferograms be included in the analysis. In most cases, numerous solutions exist; considerable research has been dedicated to finding optimum methods of analysis in a variety of experimental conditions. A few of the most basic algorithms are presented here to demonstrate the available means of reducing experimental uncertainties. These methods, based on strict assumptions about the linear or non-linear phase-steps, are here referred to as the *simple techniques*. In contrast, the *complex techniques* presented in Section 12.4 make no such assumptions about the phase-shifts. The complex techniques are used exclusively in the analysis of phase-shifted EUV PS/PDI data described in this thesis.

12.2 SIMPLE PHASE-SHIFTING TECHNIQUES

Three of the simple phase-shifting techniques are presented in this section, followed by a comparison of their sensitivities to phase-shifting calibration errors. This discussion reveals how small refinements in the analysis can greatly improve the ability of these techniques to overcome some experimental limitations, specifically phase-shifting calibration errors. However, this discussion also illustrates the inadequacy of these methods when faced with large or unpredictable calibration errors. The sections on the complex phase-shifting techniques address these issues.

12.2.1 *The Four-Step Algorithm*

The *four-step algorithm* (Greivenkamp and Bruning 1992:510-513) is a good place to begin the discussion of PSI analysis methods, because among available algorithms it is perhaps easiest to understand. Assume that four interferograms are collected with a relative phase-step of $\pi/2$ between each. The four interferograms may be expressed as

$$\begin{aligned} I_1(\mathbf{x}) &= A(\mathbf{x}) + B(\mathbf{x})\cos[\phi(\mathbf{x})] &&= A(\mathbf{x}) + B(\mathbf{x})\cos[\phi(\mathbf{x})] \\ I_2(\mathbf{x}) &= A(\mathbf{x}) + B(\mathbf{x})\cos[\phi(\mathbf{x}) + \tfrac{\pi}{2}] &&= A(\mathbf{x}) - B(\mathbf{x})\sin[\phi(\mathbf{x})] \\ I_3(\mathbf{x}) &= A(\mathbf{x}) + B(\mathbf{x})\cos[\phi(\mathbf{x}) + \pi] &&= A(\mathbf{x}) - B(\mathbf{x})\cos[\phi(\mathbf{x})] \\ I_4(\mathbf{x}) &= A(\mathbf{x}) + B(\mathbf{x})\cos[\phi(\mathbf{x}) + \tfrac{3\pi}{2}] &&= A(\mathbf{x}) + B(\mathbf{x})\sin[\phi(\mathbf{x})] \end{aligned} \tag{3}$$

Extracting $\phi(x)$ from the set of measurements above is straightforward. One analytic solution is

$$\phi(\mathbf{x}) = \tan^{-1}\left[\frac{I_4 - I_2}{I_1 - I_3}\right], \text{ or } \phi(\mathbf{x}) = \tan^{-1}(I_4 - I_2, I_1 - I_3). \tag{4}$$

For clarity, the spatial dependence of the interferograms I_n is implied, but not written explicitly here. Notice that subtraction within both the numerator and denominator removes the stationary, additive component $A(x)$, while division eliminates the multiplicative term $B(x)$. In this way, $\phi(x)$ modulo 2π, or $\phi(x)$ modulo π is obtained.

Often the *fringe modulation* or *fringe contrast* is of interest. Here, $\gamma(x)$ is defined as the ratio of the amplitude of the modulated intensity to the (temporal-domain) average intensity at a given point **x**.

$$\gamma(\mathbf{x}) \equiv \frac{B(\mathbf{x})}{A(\mathbf{x})}. \tag{5}$$

It can be shown that in the Four-Step algorithm, the modulation is

$$\gamma(\mathbf{x}) = \frac{2\sqrt{(I_4 - I_2)^2 + (I_1 - I_3)^2}}{I_1 + I_2 + I_3 + I_4}. \tag{6}$$

12.2.2 *The Hariharan Five-Step Algorithm*

When more than three phase-shifted interferograms are collected, there exist multiple ways available to extract $\phi(x)$ from the data analytically. The *Hariharan algorithm* for five steps (Hariharan 1987) in particular, chooses a solution with reduced sensitivity to phase-shift calibration errors. (Error analysis is discussed in Section 12.3.) The Hariharan method uses five images with a linear, relative phase-step α between frames. Define Δ as a vector of phase-step values.

$$\Delta = (-2\alpha, -\alpha, 0, \alpha, 2\alpha), \tag{7}$$

$$\begin{aligned} I_1(\mathbf{x}) &= A(\mathbf{x}) + B(\mathbf{x})\cos[\phi(\mathbf{x}) + \Delta_1] &&= A(\mathbf{x}) + B(\mathbf{x})[\cos\phi(\mathbf{x})\cos 2\alpha + \sin\phi(\mathbf{x})\sin 2\alpha] \\ I_2(\mathbf{x}) &= A(\mathbf{x}) + B(\mathbf{x})\cos[\phi(\mathbf{x}) + \Delta_2] &&= A(\mathbf{x}) + B(\mathbf{x})[\cos\phi(\mathbf{x})\cos 2\alpha + \sin\phi(\mathbf{x})\sin 2\alpha] \\ I_3(\mathbf{x}) &= A(\mathbf{x}) + B(\mathbf{x})\cos[\phi(\mathbf{x}) + \Delta_3] &&= A(\mathbf{x}) + B(\mathbf{x})\cos\phi(\mathbf{x}) \\ I_4(\mathbf{x}) &= A(\mathbf{x}) + B(\mathbf{x})\cos[\phi(\mathbf{x}) + \Delta_4] &&= A(\mathbf{x}) + B(\mathbf{x})[\cos\phi(\mathbf{x})\cos\alpha - \sin\phi(\mathbf{x})\sin\alpha] \\ I_5(\mathbf{x}) &= A(\mathbf{x}) + B(\mathbf{x})\cos[\phi(\mathbf{x}) + \Delta_5] &&= A(\mathbf{x}) + B(\mathbf{x})[\cos\phi(\mathbf{x})\cos 2\alpha - \sin\phi(\mathbf{x})\sin 2\alpha] \end{aligned} \tag{8}$$

These expressions are combined to form

$$\tan\phi(\mathbf{x}) = \frac{2\sin\alpha\,(I_2 - I_4)}{2I_3 - I_5 - I_1}. \tag{9}$$

The optimum choice of α occurs where the method is least sensitive to errors in α. Differentiating the right-hand-side of Eq. (9) with respect to α, it is easily shown that the minimum of the derivative occurs where $\alpha = \pi/2$. With this quarter-cycle phase-step, the phase and modulation expressions are

$$\phi(\mathbf{x}) = \tan^{-1}\left[\frac{2(I_2 - I_4)}{2I_3 - I_5 - I_1}\right], \text{ or } \phi(\mathbf{x}) = \tan^{-1}\left[2(I_2 - I_4), 2I_3 - I_5 - I_1\right], \tag{10}$$

and

$$\gamma(\mathbf{x}) = \frac{3\sqrt{4(I_4 - I_2)^2 + (I_1 + I_5 - 2I_3)^2}}{2(I_1 + I_2 + 2I_3 + I_4 + I_5)}. \tag{11}$$

With $\alpha = \pi/2$, the first and last interferograms are nominally the same. However, to preserve the insensitivity to calibration errors, this assumption is not imposed in the analysis. Notice again that subtraction within the numerator and denominator removes the additive term, while the division eliminates the multiplicative term.

12.2.3 *The Least-Squares Algorithm*

One pragmatic approach is the *least-squares algorithm* (Bruning et al. 1974, Greivenkamp 1984), in which $N \geq 3$ interferograms are combined using arbitrary, known phase-shifts. Although this method is not optimized against linear phase-shift calibration errors in the same way that other methods are, by allowing arbitrary phase-steps it proves to be the most versatile of the phase-shifting analysis algorithms described here. This versatility will be utilized by the complex techniques described in Section 12.4.

When the phase-shifts are known by some external means, application of this method is straightforward. For N measured interferograms, the phase-steps are

$$\Delta = (\Delta_1, \Delta_2, \ldots, \Delta_N). \tag{13}$$

The n-th interferogram may be written in the conventional way, and then expanded as follows:

$$I_n(\mathbf{x}) = A(\mathbf{x}) + B(\mathbf{x})\cos\left[\phi(\mathbf{x}) + \Delta_n\right] = a_0(\mathbf{x}) + a_1(\mathbf{x})\cos\Delta_n + a_2(\mathbf{x})\sin\Delta_n. \tag{13}$$

Here, the phase-steps Δ_n have been separated from the unknown phase $\phi(x)$ using the definitions

$$\begin{cases} a_0(\mathbf{x}) \equiv A(\mathbf{x}) \\ a_1(\mathbf{x}) \equiv B(\mathbf{x})\cos\phi(\mathbf{x}) \\ a_2(\mathbf{x}) \equiv -B(\mathbf{x})\sin\phi(\mathbf{x}) \end{cases}. \tag{14}$$

These are the three unknowns for which we must solve. Since the phase-steps are known, the $\sin\Delta_i$ and $\cos\Delta_i$ terms are simply the scalar coefficients of the unknown $a_1(x)$ and $a_2(x)$ in Eq. 13, and are identical for all points x in the measurement domain.

Applying the method of least-squares separately at each point x_i of $\mathbf{x}$, the goal is to minimize the *error function* $E^2(x_i)$, defined as

$$E_i^2 \equiv E^2(x_i) \equiv \sum_{n=1}^{N} \left[I_n(x_i) - a_0(x_i) - a_1(x_i)\cos\Delta_n - a_2(x_i)\sin\Delta_n \right]^2 . \tag{15}$$

The error function is related to the *fit variance*, where it is assumed that each measurement $I_i(x_i)$ contains the same uncertainty.

At each x_i, $E^2(x_i)$ is minimized by differentiating Eq. (15) with respect to the three unknowns a_0, a_1, and a_2. The resultant expression may be written in matrix form

$$\begin{bmatrix} N & \Sigma\cos\Delta_n & \Sigma\sin\Delta_n \\ \Sigma\cos\Delta_n & \Sigma\cos^2\Delta_n & \Sigma\cos\Delta_n\sin\Delta_n \\ \Sigma\sin\Delta_n & \Sigma\cos\Delta_n\sin\Delta_n & \Sigma\sin^2\Delta_n \end{bmatrix} \begin{bmatrix} a_0(x_i) \\ a_1(x_i) \\ a_2(x_i) \end{bmatrix} = \begin{bmatrix} \Sigma I_n(x_i) \\ \Sigma I_n(x_i)\cos\Delta_n \\ \Sigma I_n(x_i)\sin\Delta_n \end{bmatrix}, \tag{16a}$$

$$A(\Delta)\mathbf{a}(x_i) = \mathbf{b}(x_i, \Delta) . \tag{16b}$$

Here, Σ is a shorthand notation representing the sum over the N measurements, with n as the summation index. The symmetric matrix $\mathbf{A}(\Delta)$, called the *curvature matrix*, depends only on the known phase-shifts, while the vector $\mathbf{b}(x_i, \Delta)$ contains the measured interferogram data. $\mathbf{A}(\Delta)$ may be calculated just once, yet the calculation of $\mathbf{b}(x_i, \Delta)$ must be done separately at every point in the measurement domain. The solution for the coefficient vector $\mathbf{a}(x_i)$ requires inverting $\mathbf{A}(\Delta)$, and pre-multiplying both sides of Eq. (16b).

$$\mathbf{a}(x_i) = A^{-1}(\Delta)\mathbf{b}(x_i, \Delta) \tag{17}$$

When there are three or more unique phase steps, the rows will be independent and $\mathbf{A}(\Delta)$ will be invertible. Once $\mathbf{a}(x_i)$ is known, the phase $\phi(x_i)$ and modulation $\gamma(x_i)$ are easily found. Over the whole domain,

$$\phi(\mathbf{x}) = \tan^{-1}\left[\frac{-a_2(\mathbf{x})}{a_1(\mathbf{x})}\right], \text{ or } \phi(\mathbf{x}) = \tan^{-1}\left[-a_2(\mathbf{x}), a_1(\mathbf{x})\right], \tag{18}$$

and

$$\gamma(\mathbf{x}) \equiv \frac{\sqrt{a_1^2(\mathbf{x}) + a_2^2(\mathbf{x})}}{a_0(\mathbf{x})} . \tag{19}$$

The sensitivity of the least-squares method with $\pi/2$ phase steps is discussed in Section 8.10.4.

12.3 LINEAR PHASE-SHIFTING CALIBRATION ERRORS AND THE SIMPLE ALGORITHMS

One important source of measurement errors facing every type of phase-shifting analysis is phase-step calibration errors. Any means used to generate the relative phase-shift is vulnerable to errors in the step-increments induced by inaccuracies, non-linearities, and random noise in the components. For instance, a stage that is perfectly repeatable and linear may be mis-calibrated by several percent; a stage driven over relatively long distances by piezoelectric transducers may exhibit non-linearities; and the finite precision of translation stages may introduce random errors into the positioning.

Many of the simple analysis techniques attempt to compensate for and reduce sensitivity to phase-shifting errors in a number of ways. When the phase-errors are small, the phase-shift may be modeled using a power-series expansion about their intended values. The first-order model describes the ideal phase-shift, plus a linear error. Note that the phase *step* or phase *increment* is simply the discrete derivative of the phase itself. Thus, an error that is *linear* in phase is equivalent to a *constant* offset (calibration error) in the step.

Consider the effects of a linear phase calibration error on the simple algorithms described in Section 12.2. Here, assume that the experimental phase-increment α' is related to the *target* phase increment α by a constant offset ε.

$$\alpha' = \alpha + \varepsilon, \tag{20}$$

making the phase steps

$$\Delta = (0, \alpha', 2\alpha', \ldots, n\alpha', \ldots) = (0, \alpha + \varepsilon, 2\alpha + 2\varepsilon, \ldots, n\alpha + n\varepsilon, \ldots). \tag{21}$$

"Propagating" the small error ε through the Four-Step algorithm with $\alpha = \pi/2$ yields a phase error $\Delta\phi' \equiv (\phi' - \phi - \text{constant})$ of

$$\text{Four-Step algorithm:} \qquad \Delta\phi' = \tfrac{1}{2}\cos(2\phi)\varepsilon - \tfrac{1}{8}\sin(4\phi)\varepsilon^2 + O[\varepsilon^3]. \tag{22}$$

Notice that the phase error is periodic in multiples of ϕ and has first-order dependence on ε. This commonly observed behavior is called *fringe print-through* because the fringe pattern (or harmonics of it) are visible in the phasemap. (Section 8.10.4 gives an experimental example of fringe print-through.) A constant phase term with ε-dependence was removed from Eq. (2) because it depends only on a constant offset in the phase-step definition.

Similar analysis conducted on the Hariharan algorithm shows a very different result.

$$\text{Hariharan algorithm:} \qquad \Delta\phi' = \tfrac{1}{4}\sin(2\phi)\varepsilon^2 + O[\varepsilon^4]. \tag{23}$$

While again the error is periodic in multiples of ϕ, the dependence on the phase-step error ε has now been reduced to second-order. This dependence is illustrated in Fig. 1. The collection of one additional interferogram (five instead of four) has improved the uncertainty of the phase recovery significantly.

Note on Print-through. The significance of fringe print-through depends on several factors, including the amplitude and spatial-frequency of the error term $\Delta\phi'$. From the two examples presented, it is clear that the spatial-frequency of the print-through is related to harmonics of the fringe period. When high fringe density makes the spatial-frequency of the print-through much higher than the low-spatial-frequency of the aberrations of interest, then the print-through errors average to zero over a typical length scale. In that case the significance of fringe print-through is greatly reduced. Unfortunately, this averaging cannot occur for low fringe densities. Hence print-through can be a very serious problem, and great care

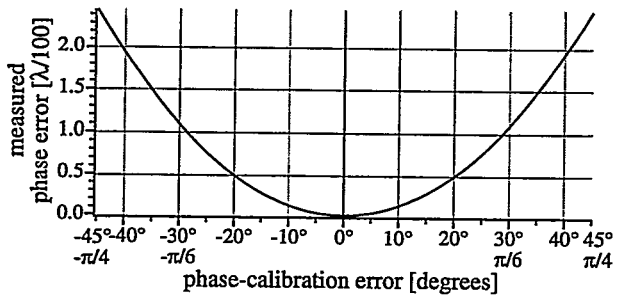

Figure 1. The effect of phase-step calibration errors on the Hariharan method of phase-retrieval. Designed to reduce sensitivity to calibration errors, the Hariharan method shows a maximum error of approximately 0.01 λ (waves) for calibration errors below 30° per step. Not shown in this figure is the periodic dependence of the measurement error on the wavefront phase.

must be taken to eliminate it. Section 8.10.2 reports experimental observation and elimination of fringe print-through with EUV PS/PDI data.

Numerous phase-shifting analysis techniques have been developed to reduce sensitivity to linear phase-step calibration errors (Creath 1986, Schmit and Creath 1992). Still other methods seek higher accuracy by modeling non-linear phase-increments (de Groot 1995). Analysis in the temporal domain provides insight into the behavior and facilitates the development of these advanced methods. By utilizing more phase-steps, and by finding alternate analytical solutions, the number of possible phase-recovery techniques is truly limitless.

Aside from the expense in time, collecting increasing numbers of interferograms for analysis is beneficial in virtually all circumstances. In addition to the potential for compensation of the effects of phase-calibration errors, having more data helps reduces sensitivity to noise. However, regarding phase-step calibration errors, each additional phase-step introduces one more degree of freedom. In principle, it requires a polynomial of order $(N-1)$ to model the behavior of N arbitrary phase steps. Given N interferograms, and N unknown phase-steps, we are faced with a system of $N+3$ variables, but only N equations (A, B, and ϕ are the extra three variables).

This is where the simplified models of the phase-step errors becomes necessary. For small phase-step errors and carefully chosen phase-retrieval algorithms, fringe print-through can be minimized. However, if the phase errors are large and unpredictable, then adding more interferograms to the analysis may not overcome the problem. EUV interferometry of the 10× Schwarzschild objective, described in this thesis, was faced with the latter circumstance; a different approach, capable of utilizing data collected with irregular phase-increments was required. A novel method, developed by the author to meet these needs, is presented in Section 12.5.2.

12.4 COMPLEX PHASE-SHIFTING TECHNIQUES

The simple phase-shifting techniques impose a linear or non-linear phase-step model on the data analysis. Optimization of these methods proceeds from the point of view that the incremental collection of

more interferograms enables the compensation of more non-linear phase-shifting effects. However, as stated previously, when the phase-shift errors are large and unpredictable, the inclusion of more phase-steps may not improve the analysis. This latter, difficult experimental circumstance arose in the EUV PS/PDI research, and prompted the author to develop a complex phase-shifting technique that has been implemented with great success.

Due to the limitations of the translation stages used to position the grating beam-splitter/phase-shifting element, the phase-shifting steps were neither linear nor predictable. Errors as large as 0.04 cycles, or 16% of the target $\pi/2$ phase increment, were routinely observed. Analysis using the simple techniques is compromised by the presence of significant fringe-print-through (Section 8.10.4).

A separate approach to interferogram analysis in the presence of high phase-shift uncertainty is to use the available data to determine the *phase-steps* themselves prior to or concurrently with the analysis of the phase at each point. One stated advantage of the phase-shifting algorithms is their individual treatment of each point in the measurement domain. Yet, while the phase function $\phi(\mathbf{x})$ is local, the phase-steps Δ are global and in principle affect all measurement points equally. Determination of the phase-steps must be possible.

Formulated, as before, with N interferograms, and N *unknown* phase steps Δ,

$$\Delta = (\Delta_1, \Delta_2, \cdots, \Delta_N), \tag{24}$$

and the n-th interferogram is written as

$$I_n(\mathbf{x}) = A(\mathbf{x}) + B(\mathbf{x})\cos[\phi(\mathbf{x}) + \Delta_n]. \tag{25}$$

At each domain point, there is a set of N equations, with $N + 3$ unknowns (A, B, ϕ, and $\Delta_1, \ldots, \Delta_N$), making direct solution impossible. However, by utilizing all or a subset of the domain points (there are often hundreds of thousands), there exist a number of available strategies for determining Δ. Determining Δ is the key to the complex phase-shifting techniques. Once Δ is known, application of the least-squares algorithm to recover the phase $\phi(\mathbf{x})$ is trivial.

12.4.1 *Global Least-Squares*

One iterative method, described by Han and Kim (1994), seeks to minimize a global error function with respect to the three unknowns at each point, and the N phase-shifts. Following the least-squares algorithm of Section 12.2.3, the error function is defined individually for each domain point as

$$E_i^2 \equiv E^2(x_i) \equiv \sum_{n=1}^{N} \left[I_n(x_i) - a_0(x_i) - a_1(x_i)\cos\Delta_n - a_2(x_i)\sin\Delta_n \right]^2. \tag{26}$$

Now, allowing the phase steps Δ_n to be chosen freely, a *global error function* E^2 takes the form

$$E^2(\Delta,\mathbf{x}) \equiv \sum_{i=0}^{N_i} E_i^2 = \sum_{i=0}^{N_i}\sum_{n=1}^{N}\left[I_n(x_i) - a_0(x_i) - a_1(x_i)\cos\Delta_n - a_2(x_i)\sin\Delta_n\right]^2 . \tag{27}$$

Here N_i is the number of domain points used in this calculation. Because the phase steps Δ_n appear as the arguments of cosine and sine in Eq. (27), solution will require a *non-linear least-squares* approach. For any given set of phase-shifts Δ, solution of the other three unknowns follows the linear least-squares algorithm described previously, and the global error function is easily calculated. Starting with an initial *guess* for the values of Δ (e.g. $\Delta_n = n\pi/2$), the individual phase-shifts may be given small increments so as to minimize E^2 globally.

Because Δ_n and ϕ appear together in the argument of the cosine in Eq. (25), there is ambiguity in the definition of a *zero reference* phase point. This indicates that there are infinite degenerate solutions available. By defining the first phase position as *zero*, $\Delta_0 \equiv 0$, and defining all other phase steps with respect to it, we can exploit this ambiguity and remove one degree of freedom from the calculation. Solution proceeds as a minimization of E^2 in an $(N-1)$-dimensional space.

Global minimization should produce the optimum set of fit parameters. Although the authors of this method claim successful minimization is easily accomplished, experience with the implementation of this algorithm using a wide variety of minimization algorithms has shown otherwise. Inherent in Eq. (27) is a *high-degree of interdependence* among the individual phase-shifts Δ_n, leading to instability in the solution algorithm. Changing one of the phase-shift parameters by a small amount requires that each of the others must also be adjusted to minimize the error function. Perhaps if the initial guess is very close to the minimizing solution, then the problem can be made linear in the variations of Δ. Such considerations are beyond the scope of this thesis. Otherwise, a superior method must be found.

12.4.2 *The Fourier-Transform Method of Phase-Shift Determination*

With all other experimental conditions held fixed, the relative phase increments generated in phase-shifting interferometry are easily and accurately discernible in the Fourier-domain in the presence of a spatial-carrier-frequency. This section describes a novel yet very simple method of utilizing the spatial-frequency-domain information to discover the individual relative phase-increments from a phase-shifting series of interferograms. The application of this method and a comparison to other phase-shifting methods of analysis are presented in Section 8.10.2.

Many interferometric techniques, including the PS/PDI, require the introduction of a spatial-carrier-frequency, that is, *tilt fringes*. The PS/PDI acquires tilt as a by-product of the required beam-separation in the image-plane. In addition, *all* of the single-interferogram analysis methods discussed in Chapter 11 require the introduction of a significant amount of tilt. For successful analysis, the Fourier-transform

methods of single interferogram analysis require the presence of a spatial-carrier-frequency to adequately separate and isolate one of the information-carrying side-lobes.

As before, the expression for the n-th interferogram in a series may be written as

$$I_n(\mathbf{r}) = A(\mathbf{r}) + B(\mathbf{r})\cos\left[\phi(\mathbf{r}) + \Delta_n\right] = A(\mathbf{r}) + B(\mathbf{r})\cos\left[\phi(\mathbf{r}) + \mathbf{k}_o \cdot \mathbf{r} + \Delta_n\right], \tag{28a}$$

where

$$\phi(\mathbf{r}) \equiv \phi_o(\mathbf{r}) + \mathbf{k}_o \cdot \mathbf{r}. \tag{28b}$$

Here, following the discussion of Section 11.3, the general expression of the wavefront phase is represented by three separate terms: the *piston* term Δ_n contains all constant offsets; all *tilt* components, including the spatial-carrier-frequency, are collected in $\mathbf{k}_o \cdot \mathbf{r}$; $\phi_o(\mathbf{r})$ is comprised of all of the higher-ordered aberrations that are of interest to the interferometric measurements. By this definition, the piston and tilt components of $\phi_o(\mathbf{r})$ are identically zero.

Neglecting for the moment the presence of the discretely sampled domain, the Fourier-transform of $I_n(\mathbf{r})$ will be simplified by expansion of the cosine term:

$$I_n(\mathbf{r}) = A(\mathbf{r}) + B(\mathbf{r})\cos\left[\phi_o(\mathbf{r}) + \mathbf{k}_o \cdot \mathbf{r} + \Delta_n\right] = A(\mathbf{r}) + \tfrac{1}{2}B(\mathbf{r})e^{i\left[\phi_o(\mathbf{r}) + \mathbf{k}_o \cdot \mathbf{r} + \Delta_n\right]} + \tfrac{1}{2}B(\mathbf{r})e^{-i\left[\phi_o(\mathbf{r}) + \mathbf{k}_o \cdot \mathbf{r} + \Delta_n\right]}. \tag{29}$$

$$I_n(\mathbf{r}) = A(\mathbf{r}) + e^{i\Delta_n}C(\mathbf{r})e^{i\mathbf{k}_o \cdot \mathbf{r}} + e^{-i\Delta_n}C^*(\mathbf{r})e^{-i\mathbf{k}_o \cdot \mathbf{r}}, \tag{30}$$

where

$$C(\mathbf{r}) \equiv \tfrac{1}{2}B(\mathbf{r})e^{i\phi_o(\mathbf{r})}. \tag{31}$$

and * indicates the complex conjugate.

The Fourier-transform of $I_n(\mathbf{r})$ is $i_n(\mathbf{k})$, given by

$$\mathcal{F}\left\{I_n(\mathbf{r})\right\} = i_n(\mathbf{k}) = a(\mathbf{k}) + e^{i\Delta_n}c(\mathbf{k} - \mathbf{k}_o) + e^{-i\Delta_n}c^*(\mathbf{k} + \mathbf{k}_o). \tag{32}$$

By the same assumptions made in Section 11.3 regarding the spatial-frequency content of $A(\mathbf{r})$, $B(\mathbf{r})$ and $\phi(\mathbf{r})$, $a(\mathbf{k})$ and $c(\mathbf{k})$ both peak about the zero-frequency. Furthermore, although $a(\mathbf{k})$ may contain high-frequency and low-frequency components, it is assumed to be *quiet* in the vicinity of $\mathbf{k}_o$. The presence of the spatial-carrier-frequency displaces c and c^* and creates a Hermitian distribution with a zero-frequency peak and two side-lobes centered about $\mathbf{k}_o$ and $-\mathbf{k}_o$ respectively.

At the carrier-frequency

$$i_n(\mathbf{k}_o) = a(\mathbf{k}_o) + e^{i\Delta_n}c(0) + e^{-i\Delta_n}c^*(2\mathbf{k}_o). \tag{33}$$

$i_n(\mathbf{k}_o)$ is dominated by one of the side-lobes, and may be written as

$$i_n(\mathbf{k}_o) \approx e^{i\Delta_n}c(0). \tag{34}$$

Equation (33) enables us to access the individual *global* phase-steps Δ_n to within an arbitrary and unimportant offset angle.

$$\Delta_n \approx \tan^{-1}\left[i_n(\mathbf{k}_o)\right], \text{ or } \Delta_n \approx \mathrm{Im}\left\{\ln\left[i_n(\mathbf{k}_o)\right]\right\}. \tag{35}$$

At this point, the individual phase-steps can be calculated and applied to the phase recovery as described previously. The additional additive phase angle determined by the complex constant $c(0)$ may be absorbed into the piston term in the analysis. Calculation of the individual phase-steps requires only that the Fourier-transform be calculated at one point, the carrier-frequency.

The following two sections introduce a method of carrier-frequency determination and assess the quality of the approximation made in Eqns. (34) and (35) and the effect of the discrete domain.

12.4.2.1 ***Carrier-Frequency Determination***

The Fourier-transform method of phase-shift determination requires knowledge of the carrier-frequency $\mathbf{k}_o$. Experimentally, there are several ways of various complexity to determine $\mathbf{k}_o$ from the data. To implement these procedures, no wavefront aberration information is needed, and the entire interferogram is not required. If fact, these methods work best when only a sub-domain of the interferogram with complete fringe-coverage is used.

The most direct carrier-frequency determination method finds $\mathbf{k}_o$ approximately by locating the side-lobe peak in the spatial-frequency domain. In fact this required step is performed in the Fourier-transform method of single interferogram analysis (Section 11.3). When the side-lobe peak is located within the discrete Fourier-transform (DFT) spectrum, the uncertainty due to the discretization is one-half of the discretization size — typically, this is 0.5 cycles. This uncertainty can be reduced to any arbitrary size by increasing the resolution of the discrete spatial-frequency domain in the calculation.

A second two-step method uses the measured wavefront slope to determine the carrier-frequency. First, the Fourier-transform method of single-interferogram analysis is applied to a single interferogram in the series and a modulo 2π wavefront phasemap is generated. Heavy spatial-filtering can be used to simplify this procedure. After the phasemap is unwrapped, polynomial fitting procedures can be used to determine the components of *tilt* in the x- and y-directions. Let $\mathbf{t}$ be the tilt vector defined as

$$\mathbf{t} \equiv (x\text{-tilt}, y\text{-tilt}). \tag{36}$$

Here, the *magnitude* of $\mathbf{t}$ is defined as half of the peak-to-valley amplitude of the wavefront phase it describes. In this case, $\mathbf{k}_o$ is easily found.

$$\mathbf{k}_o = 2\mathbf{t}. \tag{37}$$

However $\mathbf{k}_o$ is calculated, there may be some uncertainty. Assume that while $\mathbf{k}_o$ is the *true* carrier-frequency, attempts to calculate $\mathbf{k}_o$ yield the value $\mathbf{k}'$ where

$$\mathbf{k}' \equiv \mathbf{k}_o + \boldsymbol{\varepsilon}. \tag{38}$$

$\boldsymbol{\varepsilon}$ is a vector in the spatial-frequency domain of magnitude much less than $\mathbf{k}_o$. The dependence of the

phase determination on $\boldsymbol{\varepsilon}$ can be seen from Eq. (33), with $\mathbf{k}'$ replacing $\mathbf{k}_o$:

$$\begin{aligned} i_n(\mathbf{k}') &= i_n(\mathbf{k}_o+\boldsymbol{\varepsilon}) = a(k_o+\boldsymbol{\varepsilon}) + e^{i\Delta_n}c(\boldsymbol{\varepsilon}) + e^{-i\Delta_n}c^*(2\mathbf{k}_o+\boldsymbol{\varepsilon}) \\ &\approx e^{i\Delta_n}c(\boldsymbol{\varepsilon}) \end{aligned} \tag{39}$$

The approximations of Eqns. (34) and (35) are still valid, but with a different leading constant. Depending on $\boldsymbol{\varepsilon}$, the magnitude of $c(\boldsymbol{\varepsilon})$ may be less than $c(0)$. The implications of this are discussed in the following section.

12.4.2.2 *Error Estimation*

The accuracy of phase-shift determination using the spatial-frequency-domain depends on the relative amplitudes of the functions $c(\mathbf{k}-\mathbf{k}_o)$, $c^*(\mathbf{k}+\mathbf{k}_o)$, and $a(\mathbf{k})$, near $\mathbf{k} = \mathbf{k}_o$. The phase of interest Δ_n is found in the coefficient of $c(\mathbf{k}-\mathbf{k}_o)$ in Eq. (33) and is given approximately by Eq. (35). The error in this approximation cannot be determined while $c(\mathbf{k})$ and $a(\mathbf{k})$ are unknown. However, by examining the data in a phase-shifting series an estimate of the error magnitude is easily made.

For an individual phase-step, the three quantities $c(\mathbf{k}-\mathbf{k}_o)$, $c^*(\mathbf{k}+\mathbf{k}_o)$, and $a(\mathbf{k})$ plus the Δ_n-dependent complex coefficients found in Eq. (33) may be regarded as complex scalars, or vectors in the complex plane. Assuming that all other experimental conditions are held fixed while the phase-shifting is implemented, only the unit-magnitude coefficients of $c(\mathbf{k}-\mathbf{k}_o)$ and $c^*(\mathbf{k}+\mathbf{k}_o)$ are affected. To separate the one term of interest from the other two, define two complex constants p and q.

$$\begin{aligned} p &\equiv e^{i\Delta_n}c(0) \\ q &\equiv a(\mathbf{k}_o) + e^{-i\Delta_n}c^*(2\mathbf{k}_o) \\ i_n(\mathbf{k}_o) &= p+q \end{aligned} \tag{40a, b, c}$$

p represents the phase of the side-lobe peak. q is the magnitude of the additional components. In most experimental situations of interest, it is safe to assume that $p >> q$ and that the phases of p and q are independent.

Figure 2 shows a representation of p for six 60°-phase-steps in the complex plane. Only the resultant vectors are measurable. The largest phase error (between p and the measured value of $i(\mathbf{k}_o)$) occurs when q is perpendicular to p. When q is significantly smaller than p, the maximum magnitude of the error in the measured phase $\delta\Delta_n$ is approximately

$$\delta\Delta_n \leq |p|/|q| \,. \tag{41}$$

Since the $\delta\Delta_n$ depends on the ratio of $|q|$ to $|p|$, minimization of the error can occur in two ways. $|p|$ is increased by ensuring that the calculated carrier-frequency occurs at the peak value of the spatial-frequency domain side-lobe $c(\mathbf{k}-\mathbf{k}_o)$. $|q|$ depends on the mid-spatial-frequency content of $c^*(\mathbf{k})$ and $a(\mathbf{k})$, and can

only be minimized by guaranteeing that the spatial-carrier-frequency in use is of sufficient magnitude for this to be true. Improvements in fringe contrast reduce the relative magnitude of $a(\mathbf{k})$ and improve the ratio.

Although the magnitude of q is unknown, it may be estimated from the data. The variation in the measured magnitude of $i_n(\mathbf{k}_o)$ is related to the magnitude of q. This variation is represented by the gray ring in Fig. 2. The outer and inner radii of the ring are determined by $\max\{|p-q|\}$ and $\min\{|p-q|\}$, respectively. $i_n(\mathbf{k}_o)$ is maximum when p and q have the same phase, and minimum when p and q are 180° out of phase. The limitation of this estimation is that for a small sampling of phase-shift steps, there is no guarantee that the maximum and minimum values of $i_n(\mathbf{k}_o)$ will be achieved.

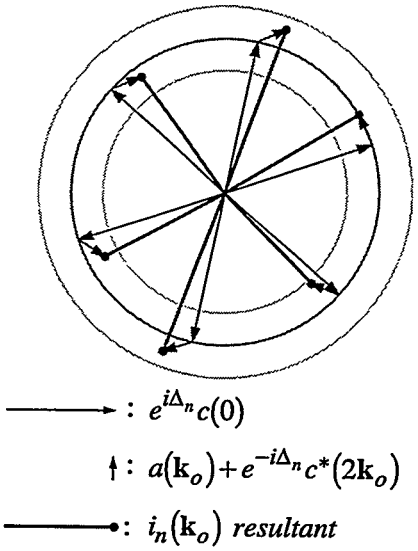

Figure 2. A complex-plane representation of the side-lobe peak p, for six phase-shifting steps of 60°. The measured phase at the carrier frequency $i(\mathbf{k}_o)$ is dominated by p, but is affected by the non-zero magnitude of the other spatial-frequency-domain components q. q causes errors in the phase-determination. The gray ring shows that the maximum and minimum measured values of $i(\mathbf{k}_o)$ can be used to estimate q.

$$|q| \gtrsim \tfrac{1}{2}\left[\max\left\{\left|i_n(\mathbf{k}_o)\right|\right\} - \min\left\{\left|i_n(\mathbf{k}_o)\right|\right\}\right]. \tag{42}$$

Combining Eqns. (41) and (42), based on the measured data the estimated uncertainty in any given phase-step is

$$\delta\Delta_n \gtrsim \frac{1}{2|p|}\left[\max\left\{\left|i_n(\mathbf{k}_o)\right|\right\} - \min\left\{\left|i_n(\mathbf{k}_o)\right|\right\}\right] \approx \frac{\left[\max\left\{\left|i_n(\mathbf{k}_o)\right|\right\} - \min\left\{\left|i_n(\mathbf{k}_o)\right|\right\}\right]}{2\left|\overline{i_n(\mathbf{k}_o)}\right|}. \tag{43}$$

13

Phase Unwrapping

13.1 INTRODUCTION

Due to the periodic nature of interference fringes, and the absence of an absolute reference point in phase, nearly all modern interferogram analysis phase-recovery methods are only capable of determining the wavefront phase to within an arbitrary multiple of 2π (occasionally, only to within a multiple of π). This limitation does not, however, restrict measurement to optical path differences (OPDs) of less than half of a wavelength: usually, there is sufficient information to reconstruct the original continuous wavefront from the available discontinuous data.

This chapter describes several approaches for solving this important inverse problem, and presents two novel methods. One method is designed to overcome the difficulties presented by numerous, isolated regions containing no valid data. A second, very general and robust method is capable of operating in low signal-to-noise applications and, where valid data exists, in isolated, discontiguous regions.

13.1.1 *Unwrapping Overview*

For reasons addressed in Chapter 12, many phase-retrieval methods combine several separate interference patterns and utilize a relation based on an arctangent to recover the wavefront phase. Other methods, based on Fourier-domain analysis, also utilize an arctangent.

In general, the calculated phase $\phi'(\mathbf{r})$ may be written as a functional, combining N separately measured interferograms $\{I_1, \ldots, I_N\}$:

$$\phi'(\mathbf{r}) = \tan^{-1}\left\{F\left[I_1(\mathbf{r}), I_2(\mathbf{r}), \cdots, I_N(\mathbf{r})\right]\right\}. \tag{1}$$

Each point in $\phi'(\mathbf{r})$ is related to the actual wavefront $\phi(\mathbf{r})$ by an arbitrary number of 2π steps. $\phi'(\mathbf{r})$ is called a *modulo 2π phasemap* and is related to the actual wavefront phase by the relation

$$\phi'(\mathbf{r}) = \phi(\mathbf{r}) \bmod 2\pi. \tag{2}$$

Here the modulus function is defined as the remainder after the largest integer multiple of 2π less than or equal to $\phi(\mathbf{r})$ has been subtracted. Figure 1 illustrates this point in one dimension, showing both the original wavefront and the modulo 2π measured wavefront.

Equation (2) forms the basis of one of the most important and often extremely difficult inverse problems in modern interferogram analysis: the modulo 2π phasemap must be used to reconstruct the

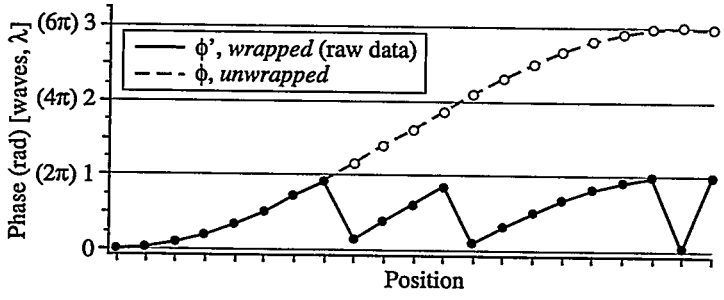

Figure 1. Although the test wavefront is continuous (dashed line), the raw phase data from interferogram analysis is typically modulo 2π, or modulo λ. The goal of *phase unwrapping* is to reconstruct the original continuous wavefront from the raw data.

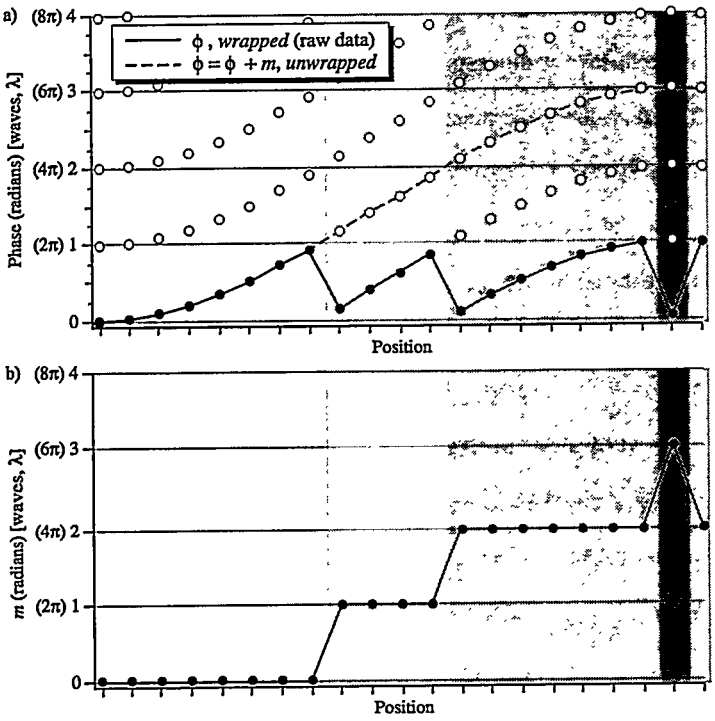

Figure 2. Reconstruction of the test wavefront from the wrapped raw data requires that each point be incremented by an integral number of wavelengths (2π radians), to achieve a surface free of discontinuities. (a) Based on the raw data (black circles) the hollow circles represent the available choices for each point in the reconstruction. (b) The calculated increments are stored in the array m.

actual wavefront, such that $\phi(\mathbf{r})$ is the surface of least curvature, with its 2π discontinuities removed by the reconstruction.

While an obvious approach may simply require the addition of 2π steps wherever a discontinuity is detected, the problem becomes complicated in the presence of noise, or where the data exists in disjoint regions. Another source of difficulty arises when the spatial-frequency of the fringes approaches the Nyquist limit (Nyquist 1928), and the local wavefront slope exceeds individual steps of π *continuously*. Such extreme cases, not discussed here, may require *a priori* information and utilize the so-called Sub-Nyquist Interferometry (SNI) methods developed by Grievenkamp (1987).

In each method presented here, the goal is to determine empirically the function $m(\mathbf{r})$ that solves

$$\phi(\mathbf{r}) = \phi'(\mathbf{r}) + m(\mathbf{r}), \text{ where } m(\mathbf{r}) = 2\pi n(\mathbf{r}), \; n \in \textit{Integers}\,. \tag{3}$$

Fig. 2 shows the role of $m(\mathbf{r})$.

13.1.2 *Notation*

A change of units simplifies our notation considerably. Using *wavelength* units rather than *radians* to describe the wavefront phase $\phi(\mathbf{r})$ and $\phi'(\mathbf{r})$ enables $m(\mathbf{r})$ to take integer values. For this notation, Eqns. (2) and (3) must be re-written as

$$\phi'(\mathbf{r}) = \phi(\mathbf{r}) \bmod 1\,, \tag{4}$$

and

$$\phi(\mathbf{r}) = \phi'(\mathbf{r}) + m(\mathbf{r}), \; m(\mathbf{r}) \in \textit{Integers}\,. \tag{5}$$

The modulo 1 function retains only the fractional part of $\phi(\mathbf{r})$, between 0 and 1, *including* zero. Here, $\phi'(\mathbf{r})$ is referred to as the *modulo* λ *phasemap*.

13.2 SIMPLE UNWRAP METHODS

Under favorable circumstances, procedures for unwrapping *modulo 2π phasemaps* (or *modulo λ phasemaps*, in wavelength units) are often very straightforward, iterative techniques. Complicated versatile and robust algorithms are often built on the careful application of the simple techniques. This section presents several general unwrapping methods of increasing complexity and usefulness. First, a one-dimensional treatment is presented and then is expanded to two dimensions. Next, the problem is generalized to withstand the presence of noise and to include arbitrary "continuous" aperture shapes. The specific continuity requirements are carefully described for each method.

As discussed in Section 13.1.1, the goal of phase unwrapping is to find the function $m(\mathbf{r})$, which is used to reconstruct the smooth phasemap $\phi(\mathbf{r})$ from the (potentially) discontinuous modulo λ phasemap $\phi'(\mathbf{r})$. From the previous section, the function is defined in the following way, in wavelength units:

$$\phi(\mathbf{r}) = \phi'(\mathbf{r}) + m(\mathbf{r}),\ m(\mathbf{r}) \in \textit{Integers}\,. \tag{6}$$

One assumption of the following discussions is that we have no *a priori* knowledge of the uncertainty of any individual data point relative to the others. Some phase-unwrapping methods utilize varied data-validation techniques (Huntley 1989, Quiroga and Bernabeu 1994, Stephenson 1994, Charette and Hunter 1996) to eliminate spurious points or regions from further calculations. Here the assumption will be that *bad* points coexists with the rest of the data.

13.2.1 *One-Dimensional Unwrapping*

In principle, the discontinuities in $\phi'(x)$ are limited to a finite number of points. Excluding these points, $\phi'(x)$ and $\phi(x)$ are related by a (piecewise continuous) constant offset, and thus have the same derivative. Numerically, the discontinuities in $\phi'(x)$ are easily detected by examining the behavior of the discrete derivative of $\phi'(x)$, defined as

$$\frac{d\phi'}{dx} \equiv \frac{\phi'(x+1) - \phi'(x)}{1} = \phi'(x+1) - \phi'(x),\ \text{where } x = 0,\ 1,\ 2,\ \cdots \tag{7}$$

For the purposes of this discussion, the term *derivative* refers to this discrete approximation. Discontinuities are present wherever the magnitude of the derivative exceeds a given threshold.

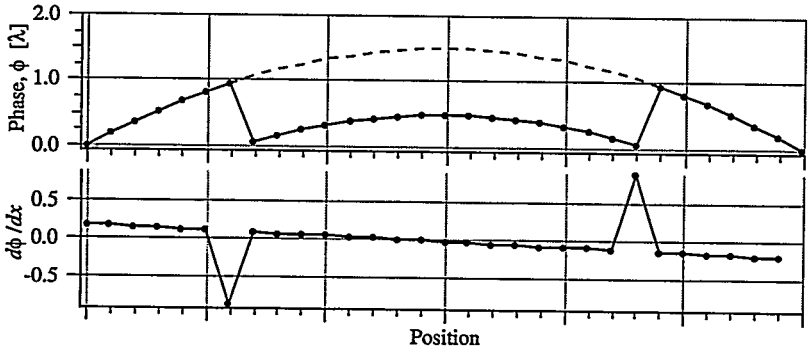

Figure 3. Modulo λ raw phase data ϕ' and the discrete derivative $d\phi'/dx$ as defined in Eq. (7) are shown to illustrate the use of the derivative in locating the phase discontinuities.Where the magnitude of the derivative exceeds a threshold value (e.g. 0.5 waves), a discontinuity is detected. The sign of the derivative is also used in the reconstruction.

Figure 3 shows the behavior of $\phi(x)$, $\phi'(x)$, and $d\phi'/dx$, where $d\phi'/dx$ is defined on the discrete domain, with x as the index of the point. Where the magnitude of the derivative exceeds 0.5 (waves), a discontinuity is present. The sign of the derivative reveals whether the step is up or down.

To construct $m(x)$ from $\phi'(x)$ and $d\phi'/dx$, one may scan across the domain of N points and increment $m(x)$ according to the following procedure.

Procedure 1: Basic One-Dimensional Unwrap

1. Loop i from 1 to $(N\text{-}1)$
2. $\quad \Delta_x = \phi'(i+1) - \phi'(i)$ *(horizontal discrete derivative)*
3. $\quad$ IF $|\Delta_x| > 0.5$ THEN
4. $\quad\quad m(i+1 \text{ to } N) \leftarrow m(i+1 \text{ to } N) - \text{sign}(\Delta_x)$ *(shift all points from $i+1$ to end of row)*

The sign function is defined as

$$sign(x) \equiv \begin{cases} -1, & x < 0 \\ 0, & x = 0 \\ +1, & x > 0 \end{cases} . \tag{8}$$

The arrow operation "←" indicates: *replace the quantity on the left with the quantity on the right.* (This operation is straightforward to perform on a computer.) In Step 4, all of the points in $m(x)$ that *follow* a discontinuity are affected. The use of the sign function, defined in Eq. (8), implements an increasing *or decreasing* step where appropriate.

The *threshold value* on the magnitude of the derivative (here defined as 0.5 in Step 3) determines the maximum allowable wavefront slope for proper reconstruction. Any slope greater than this value is identified as a discontinuity where the phase is wrapped.

Application Note. In experimental applications, one fact about this unwrap method is abundantly clear: Procedure 1 is very vulnerable to bad data. A single "error" can create an erroneous offset in all of the subsequent data. It is possible to incorporate several neighboring points into the derivative calculation in order to overcome the effects of a single spurious data point. In such cases, care must be taken to properly handle discontinuities when they occur at the edges of a domain. Methods of this sort can also be effective where the wavefront slope is large.

Another approach is to pre-filter the data before unwrapping, either in one- or two-dimensions. Simple *smoothing* or *averaging* filters should be avoided because they improperly smooth the necessarily sharp 2π phase-discontinuities and may reduce their magnitude below the threshold required for detection. Furthermore, smoothing causes a loss of high-frequency information that may be of interest. In the presence of an isolated bad point, a *smoothing* filter will decrease the magnitude of the difference by distributing the magnitude among a neighborhood of adjacent points.

Some authors have recommended the median filter (Freiden 1981, Crennell 1993) as one capable

of reducing isolated *bad points* while preserving the sharpness of the phase discontinuities. Since a median filter samples a small neighborhood of points and replaces the value at the center with the median value of the group, it can bring an isolated bad point into agreement with its neighbors without affecting adjacent points. This is a very important advantage of the median filter.

13.2.2 *Two-Dimensional Unwrapping*

Two-dimensional unwrapping is required for most interferogram wavefront analysis. It may be considered as the direct extension of one-dimensional unwrapping to rows *and* columns of data. First, the x-direction derivative is used to implement the horizontal row unwrapping of Procedure 1. In the absence of noise, this ensures the continuity of ϕ in the x-direction only. A second step then utilizes the y-direction derivative to increment entire rows. During the procedure, it may occur that the magnitudes of some discontinuities become larger than 1.5. In these cases, the required increments (or decrements) of m become greater than 1. Any row-incrementing routine must address this issue either by using multiple unwrapping "passes" through the data or by sensing the magnitude of each required increment.

Note that for the purpose of phase unwrapping on a two-dimensional data set, the x-direction is chosen arbitrarily. Clearly, when the orientation of the unwrapping procedure is rotated by 90°, the resultant phasemap must be the same to within a constant multiple of λ. Separately unwrapping in two orientations can be used as a method of data validation. A comparison can be used to quickly identify problematic regions.

The most basic procedure for two-dimensional unwrapping is outlined below. As a simplified notation, an asterisk used as an index represents an entire row or column of the domain. For instance, $\phi'(*,2)$ is the entire second row, and $\phi'(3,*)$ is the third column.

Procedure 2: Basic Two-Dimensional Unwrap

1. Loop j from 1 to N
2. Implement Procedure 1: on each row $\phi'(*, j)$ *(1-D unwrap)*
3. Choose a single column, $x = x_o$, to use as a *guide* for vertical unwrapping
4. Loop j from 2 to N
5. $\Delta_y = \phi'(x_o, j) - \phi'(x_o, j-1)$ *(vertical derivative)*
6. IF $|\Delta_y| > 0.5$ THEN
7. $m(*, j) \leftarrow m(*, j) - \text{sign}(\Delta_y) * \text{floor}(|\Delta_y|)$ *(shift row)*

The function floor(x) is defined as the greatest integer less than or equal to x.

The most significant limitation of Procedure 2 is that just one column is arbitrarily chosen as a guide for the vertical unwrapping. As with the one-dimensional unwrapping of Procedure 1, a single bad data point in this particular column affects the subsequent unwrapping of all of the rows.

Experience has shown that simple methods of filtering the derivative can substantially improve unwrapping results in the presence of noise. If the row increment is based instead on the *average vertical*

derivative across the width of the array, then many more points are considered, reducing the effects of a single bad data point. However, it is quite possible for one or several points very far in magnitude from the neighboring values to strongly influence the average derivative.

A superior filter is the median. When the *median vertical derivative* is used, a large number of *bad* data points, or several points that are far from their neighboring values, will not affect the calculated derivative. In this way, the effects of bad data points do not propagate as easily into other rows.

A method for incorporating the median in the vertical unwrap is given in Procedure 3.

Procedure 3: Two-Dimensional Unwrap with a Median Filter

1. Loop j from 1 to N
2. Implement Procedure 1: on each row $\phi'(*, j)$ (*1-D unwrap*)
3. Loop j from 2 to N
4. $\Delta_y \equiv \text{median}\{\phi'(*, j) - \phi'(*, j-1)\}$ (*median difference*)
5. IF $|\Delta_y| > 0.5$ THEN
6. $m(*, j) \leftarrow m(*, j) - \text{sign}(\Delta_y) * \text{floor}(|\Delta_y|)$ (*shift row*)

13.2.3 *Unwrapping on Sub-Domains*

Interferogram fringe patterns are often collected on a sub-region of a detector array. Consequently, the relevant regions containing phase information are sub-regions of a larger available domain. A broad class of versatile phase unwrapping algorithms accommodates the arbitrary positions and shapes of these domains, and avoids the inclusion of points from outside of the valid sub-region.

In this section two methods are presented for addressing sub-domain unwrapping. The first method places strict requirements on the shape of the sub-region and is therefore limited in its applicability. The second, more general method extends the capabilities of the first to a wider variety of sub-region shapes.

For the purposes of this discussion, the selection of the sub-domain of interest must be done prior to the unwrapping calculation. This may be done in a number of ways: manual methods, involving user-interactive procedures, or automatic methods, in which an investigation of signal-to-noise or some other relevant property helps to identify the sub-regions of valid data. As mentioned previously, some calculation-intensive methods are capable of validating data *during* the analysis. It is not be necessary to address those methods here.

We can describe sub-regions of interest with the definition of a special binary function $o(\mathbf{r})$ across the full domain of measurement. $o(\mathbf{r})$ is used throughout this discussion.

$$o(\mathbf{r}) \equiv \begin{cases} 1, & \forall\, \mathbf{r} \in \text{sub-region} \\ 0, & \forall\, \mathbf{r} \notin \text{sub-region} \end{cases}. \tag{9}$$

Sub-Domain Unwrapping: Method 1

This method places two requirements on the shape of the sub-region.

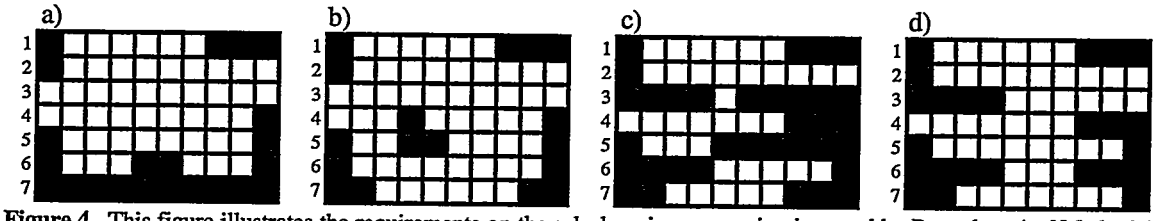

Figure 4. This figure illustrates the requirements on the sub-domain unwrapping imposed by Procedure 4 of Method 1. White squares belong to the sub-domain of interest. Row 6 of (a) is discontinuous. Likewise, rows 4 and 5 are discontinuous in (b). All of the rows of (c) are continuous, yet vertical connectedness is violated by rows 5 and 6, which share no common columns. (d) satisfies both of the requirements and is a valid sub-domain for unwrapping by Method 1.

1. **Row Continuity**: The horizontal path between any two points in the same row within the sub-domain must not include any points outside the domain. That is, the horizontal rows of the sub-region must not be discontinuous.
2. **Vertical Connectedness**: Any two adjacent rows within the sub-domain must contain at least one column in common.

Figure 4 illustrates these requirements.

Procedure 4 is a modification of the median-filtered two-dimensional unwrapping Procedure 3, refined to include only points within the sub-domain defined by $o(\mathbf{r})$.

Procedure 4: Two-Dimensional Median-filtered Unwrap on a Sub-Domain

1. Loop j from 1 to N
2. Implement Procedure 1, on each row $\phi'(*, j)$ *(1-D unwrap)*
3. Loop j from 2 to N
4. $i^* \equiv \{i \mid o(i,j) = 1 \text{ AND } o(i,j-1) = 1\}$ *(vertical connectedness)*
5. IF $i^* \neq \varnothing$ THEN *(note: $\varnothing$ denotes the* empty set*)*
6. $\Delta_y \equiv \text{median}\{\phi'(i^*, j) - \phi'(i^*, j-1)\}$ *(median difference)*
7. IF $|\Delta_y| > 0.5$ THEN
8. $m(*, j) \leftarrow m(*, j) - \text{sign}(\Delta_y) * \text{floor}(|\Delta_y|)$ *(shift row)*

The symbol $\varnothing$ denotes the *empty set.*

It is not necessary, to restrict the row-unwrapping of Step 2 to include only points within the sub-region, points outside of the sub-region will be ignored by the use of i^* in Step 6. Between every pair of adjacent rows, the median difference Δ_y calculated in Step 6 is based only on those pairs of points that share a column. This is illustrated in Fig. 5. The arrows indicate which pair of rows is being compared. In the figure, the elements that would be used in the calculation of Δ_y are marked with an "X". Note that if a row contains no valid points of the sub-region, no calculation is performed. By the two requirements above, it is clear that this only occurs at the bottom row and at the first empty row above the sub-region.

By invoking median filtering in Step 6, Procedure 4 is more resistant to noise than Procedure 3.

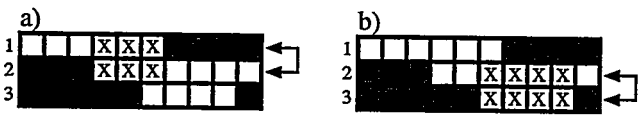

Figure 5. In Procedure 4, Step 6, the median difference between two rows (a vertical derivative) is calculated using only points from columns common to both rows. Here the arrows indicate which two rows are being compared, and the "X" symbols mark the specific points that are used.

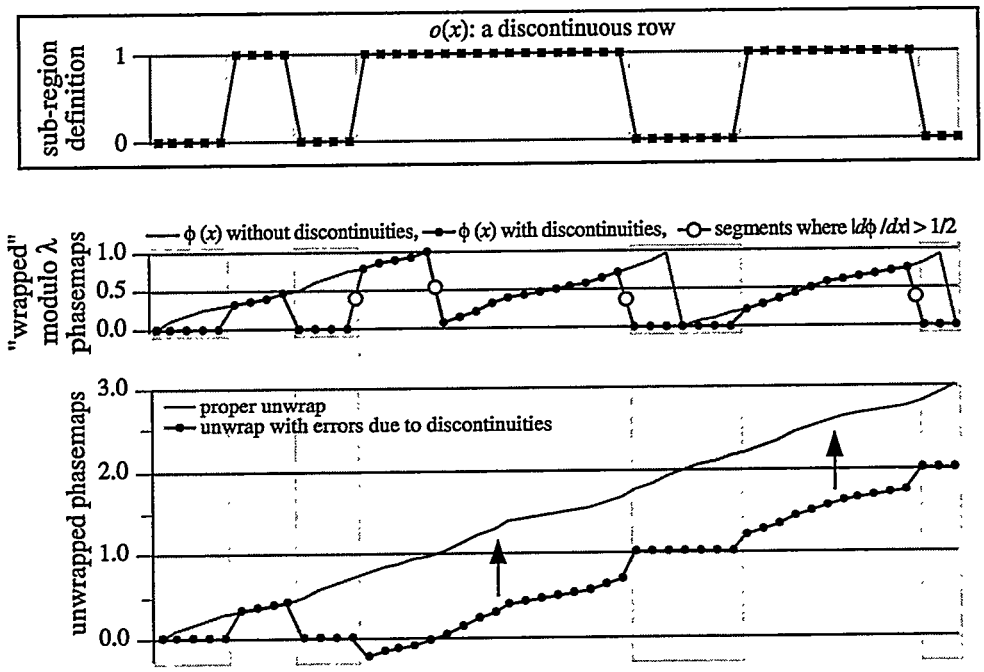

Figure 6. Row unwrapping in the presence of discontinuities can lead to unwrapping errors. The domain is defined by the binary function $o(x)$, shown in the top plot. $o(x) = 1$ for points within the domain. The middle plot shows a modulo λ raw phasemap (dots), set to zero within the discontinuities. The solid grey line shows what the raw phasemap would be if the obstructions were removed. The hollow circles indicate the places where magnitude of the derivative exceeds 0.5, triggering a phase increment in the unwrapping algorithm. The bottom plot compares the unsuccessfully unwrapped phasemap (dots) with the ideal case (grey line). Here, errors are caused by phase-wrapping occurring within the obstruction, *and* by the obstruction itself.

However, the application of Procedure 4 is limited to special kinds of sub-regions. For example, it is incapable of properly unwrapping in the presence of row discontinuities; Fig. 6 illustrates why. There are two kinds of errors that can be introduced when this procedure is followed in the presence of discontinuities. One type of error arises when a phase-wrap occurs *within* a discontinuity. The second type causes a phase-step to be assigned (correctly or erroneously) *because of* the discontinuity, wherever the magnitude of the derivative exceeds 0.5 (waves); these points are indicated in the figure by hollow circles.

It is possible to improve Procedure 4 to identify and correctly account for horizontal discontinuities. Therefore, sub-regions containing "holes" can be properly unwrapped. This method is outlined in Procedure 5.

The less-restrictive sub-region requirements for Procedure 5 are as follows.

1. **Row Continuity** is required only of the *first row.* The horizontal path between any two points in first row of the sub-domain must not include any points outside of the sub-domain. That is, the first row of the sub-region must be continuous.
2. **Vertical Connectedness:** Any two adjacent rows within the sub-domain must contain at least one column in common. Further, if a row *is* discontinuous, then each separate, continuous part of the row must be vertically connected to the *previous* row by at least one point within the sub-domain.

These two requirements are illustrated in Figure 7.

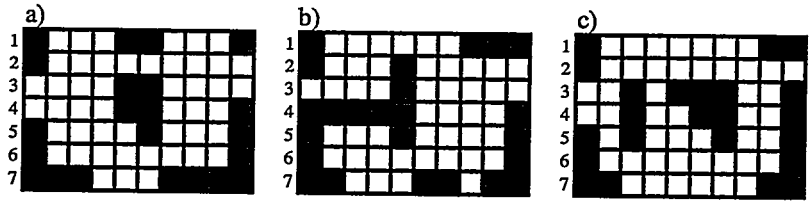

Figure 7. These three figures illustrate the requirements imposed on the sub-domain shape by Procedure 5. Row 1 of (a) is discontinuous and so violates the first requirement. (b) The segment on the left side of row 5 is not vertically connected with the rows above it. (c) Both requirements are satisfied. This illustrates how this method can successfully address surrounded obstructions in the centers of sub-domains.

Procedure 5 Two-dimensional Median-filtered Unwrap on a General Sub-Domain

1. Loop j from 1 to N
2. Implement Procedure 1, on each row $\phi'(*, j)$ *(1-D unwrap)*
3. Loop j from 2 to N
4. $c \equiv$ number of separate, continuous regions in row $\phi'(*, j)$
5. Loop k from 1 to c
6. $i_k \equiv \{i \mid i \in$ the k^{th} continuous region of $o(*, j) = 1\}$
7. $i_k^* \equiv \{i_k \mid o(i_k, j) = 1$ AND $o(i_k, j-1) = 1\}$ *(vertical connectedness)*
8. If $i_k^* \neq \varnothing$ then
9. $\Delta_y^k \equiv \text{median}\{\phi'(i_k^*, j) - \phi'(i_k^*, j-1)\}$ *(median difference)*
10. IF $|\Delta_y| > 0.5$ THEN
11. $m(i_k, j) \leftarrow m(i_k, j) - \text{sign}(\Delta_y^k) * \text{floor}(|\Delta_y^k|)$ *(shift row)*

There are a number of simple ways to count the separate continuous regions of a given row and identify their endpoints, as required by Steps 4 and 6. Besides scanning the individual pixels, the discrete derivative of the sub-region-defining function $o(x, y)$ can be used. Recalling that $o = 1$ for points within the sub-region and $o = 0$ for points outside of the sub-region,

$$\frac{do(x,y)}{dx} = o(x+1,y) - o(x,y) = \begin{cases} 1, & \text{at the point } \textit{before} \text{ the start of a new continuous region} \\ -1, & \text{at the last point of a continuous region} \\ 0, & \text{at any other point} \end{cases} . \quad (10)$$

Since this derivative is undefined at the edges of the domain, edge points must be considered separately. This problem is easily averted by padding the rows with a leading and a trailing zero.

Step 6 identifies the x-indices of points within the row's separate, continuous regions, one region at a time. It should be noted that these regions may be as small as one column wide. Step 7 then determines which of these points can be used in the calculation of the median difference Dyk. If |Dykl exceeds 0.5 (waves), then all of the points within the particular continuous sub-region of the row are incremented by the appropriate integer to make the median difference less than 0.5 in wavelength units.

13.3 UNWRAPPING ISOLATED BAD REGIONS: PHASEMAP *CLEANING*

The unwrapping procedures presented in the previous sections have various amounts of resistance to noise in the raw phase data. By using filtered comparisons of adjacent rows, the more sophisticated

procedures attempt to stem the vertical propagation of errors. However, no attempt is made to limit horizontal error propagation within the rows. As a result, an imperfectly unwrapped phasemap may contain isolated points, horizontal lines, or whole regions of data that are *shifted* by an integral number of wavelengths away from a position that would provide the best agreement with adjacent data.

This very succinct procedure introduces a method that has been successfully used to *clean* unwrapping errors.

Procedure 6: Phasemap Cleaning

1. Break the interferogram into N rectangular tiles: name the individual tile domains D_n.
2. Loop n from 1 to N
3. $m_n \equiv \text{median}[\phi(D_n)]$ (*tile median*)
4. $\Delta(D_n) \equiv \text{round}[\phi(D_n) - m_n]$ (*point-by-point comparison*)
5. $d \equiv \text{round}(m_n - m_{n-1})$ (*adjacent tile comparison*)
6. $\phi'(D_n) \equiv \phi(D_n) - \Delta(D_n) - d$ (*tile cleaning*)

First the interferogram is broken into individual tiles. Then each point in the domain is compared to the tile median with the round(x) function. By definition, round(x) returns the closest integer to x. The two-dimensional array $\Delta(D_n)$ is non-zero at any point that differs from the median by more than 0.5 waves. Similarly, this tile is compared to an adjacent *previously examined* tile (represented symbolically by the n–1 index), again using the round(x) function to calculate the scalar d. Finally, a new phase function ϕ' is calculated for the tile.

One significant aspect of this procedure is the use of the round(x) function rather than a comparative IF ··· THEN statement to identify the points that are more than 0.5 waves from the median. Rounding, which speeds-up and simplifies the procedure, is used again in Section 13.4 for Guided Unwrapping.

Refinements. There are several refinements of the basic method that can improve the results significantly. In the presence of high wavefront slope, or *tilt*, points at the edges of the tile may differ substantially from the median value. For this case, two possible solutions are as follows. First, choose a small tile size, or choose the length and width of the tile based on the mean wavefront slope in the x and y directions respectively — small tile for high slope. Another approach is to calculate and subtract the mean tilt within each tile, then calculate the median, repair the bad points, and, finally, replace the tilt that has been removed. This method makes the use of larger tile sizes possible.

Selecting the optimum tile size is a very difficult matter. Isolated points and lines are the easiest problems to repair. However, when a whole region is collectively shifted, a small tile may become engulfed. For example, the tile may fall completely within the shifted region, and the program may not recognize its displacement from the adjacent phase values. Therefore, the optimum tile size must not be smaller than any shifted regions. At the same time, if the wavefront curvature is large, the tile must not exceed the length-scale of wavefront variations under investigation. Otherwise, the curvature may impair

the proper calculation of the median. The comparison of the median values of adjacent tiles is intended to reduce the limitations of using small tiles. If a *cleaned* tile is compared to the previously-cleaned adjacent tile, then the cleaning process becomes analogous to the simple unwrapping process, performed on the tiles rather than on the individual pixels (i.e. the tiles become *super-pixels*).

Another improvement on these methods is to be aware of which points *within* a tile belong to the measurement domain and which points do not. Rectangular tiles will overlap irregular domain boundaries. The exclusion of points that fall outside of the domain may yield a median value more characteristic of the data within a tile.

A last approach is to perform the cleaning multiple times, using different tile sizes. Doing so, however, runs the risk of *introducing* unwrapping errors into a clean phasemap. To reduce the likelihood of this problem, two cleaning procedures can be performed *in parallel* and then compared for inconsistencies.

Special Note. At this point, the "cookbook" nature of these unwrapping "recipes" is certainly evident. Procedures and variations of procedures fill the literature, and there appears to be little agreement on which is the most reliable, most computationally efficient, and fastest method to use in arbitrary circumstances. The following sections on Guided Unwrapping seek to overcome these limitations by using an entirely different approach that has proved the most successful in EUV interferometry applications.

13.4 GUIDED UNWRAPPING

Unwrapping noisy data is perhaps the single most daunting task facing many interferogram analysis applications, and it was certainly a significant problem for the EUV interferometry experiments as described in this thesis. The unwrapping procedures presented in the previous sections utilize adaptable filtering methods to overcome some of the limiting effects of noise. These methods inevitably fall short of the mark and leave the unwrapped phasemaps with errors introduced by noisy data. Attempts to clean the unwrapped phasemaps improve the situation, but are not always reliable.

A completely different approach is the use of *a priori* wavefront information during the unwrapping procedure. Obviously, if the final result is already known, the unwrapping is trivial. However, when the wavefront is known only *approximately*, then the information contained in the approximate wavefront can be used to *guide* the unwrapping procedure with great success. In the guided unwrap, all of the high-frequency information in the raw data is preserved. Perhaps the most significant advantage of the guided unwrap is its ability to unwrap in the presence of obstructed regions and regions containing no valid data. Discontiguous sub-regions, for example, can be unwrapped without any special considerations. Unlike the previous unwrapping methods, guided unwrapping is equally applicable to any one- or two-dimensional domain because there is *no reliance* on neighboring data.

The concept of guided unwrapping is used in Sub-Nyquist Interferometry (Greivenkamp 1987) designed for cases in which the wavefront slope exceeds 0.5 waves per step (Nyquist limit), where conventional unwrapping methods fail. Here, a similar idea is exploited to overcome noise. How the *a priori* information is obtained is not important here. (Section 13.5 discusses a novel approach to ascertain the approximate wavefront required for guided unwrapping.)

The most simple guided unwrapping procedures are described in Procedures 1a and 1b below. Suppose that the *a priori* wavefront information is contained in the function $\Gamma(\mathbf{r})$ over the measurement domain. Using the raw phase data $\phi(\mathbf{r})$, the most simple guided unwrapping procedure utilizes the function round(x) in a way that is similar to the phasemap cleaning procedures in Section 13.3 of this chapter.

Procedure 1a: Guided Unwrapping

1. $m(\mathbf{r}) \equiv \text{round}[\Gamma(\mathbf{r}) - \phi(\mathbf{r})]$ (*difference rounded to nearest integer*)
2. $\phi'(\mathbf{r}) \equiv \phi(\mathbf{r}) + m(\mathbf{r})$ (*adjust raw phasemap into agreement with the guide*)

More succinctly, this procedure may be written in one single step.

Procedure 1b: One-Step Guided Unwrapping

1. $\phi'(\mathbf{r}) \equiv \phi(\mathbf{r}) + \text{round}[\Gamma(\mathbf{r}) - \phi(\mathbf{r})]$

As in the unwrapping techniques presented in the previous sections, integer (wavelength) steps are added or subtracted from the raw data to produce the unwrapped phasemap. As before, the function $m(\mathbf{r})$ (Procedure 1a only) contains the required integer phase steps in wavelength units. Notice, however, that in

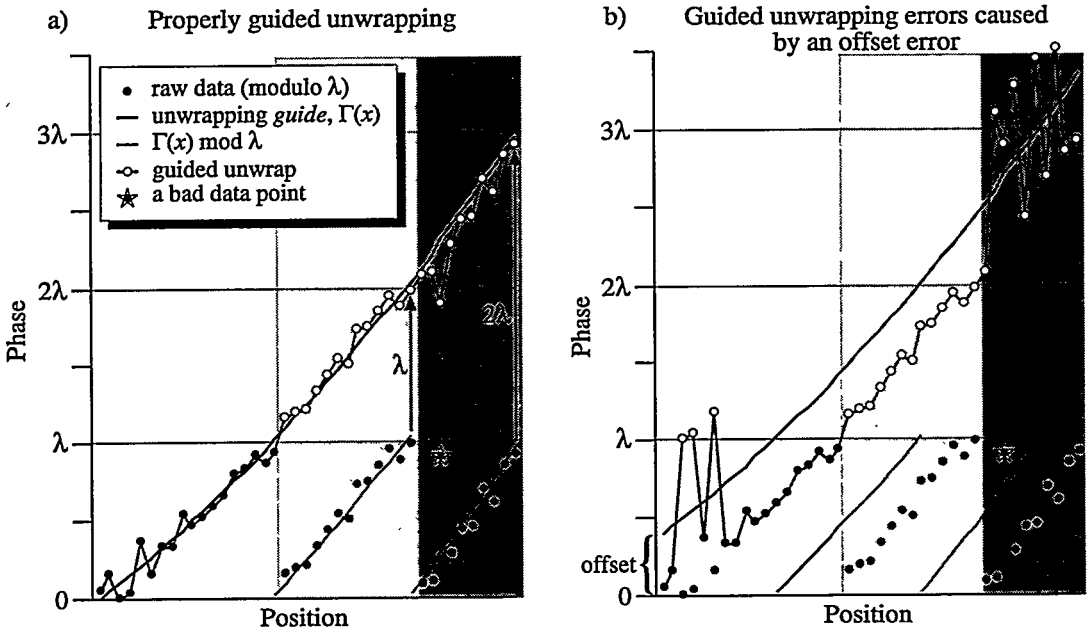

Figure 8. Guided unwrapping works successfully when the guide is approximately separated from the raw data by an integral number of wavelengths, as shown in (a). When there is a fractional offset, however, the proper increment for the raw data becomes ambiguous. In (b) the offset is approximately 0.5 waves. Small variations in the raw data cause the increment to fluctuate by one wave for adjacent points. This kind of guided unwrapping error is addressed by Procedures 2a and 2b.

contrast to the previous methods these procedures pay *no attention* to the locations of the discrete phase-wrapped steps present in the raw data. In fact it is not even necessary to differentiate between points that are inside or outside of the measurement domain: points outside of the domain are not included in subsequent analysis.

At this point, Procedures 1a and 1b contain one subtle oversight that can lead to unwrapping errors. Figure 8 illustrates two examples of the guided unwrapping procedures given in Procedures 1a and 1b above. Under ideal circumstances, shown in Fig. 8(a), the raw data $\phi(x)$ is brought into the best possible agreement with the unwrapping guide $\Gamma(x)$. Figure 8(b), however, illustrates a serious problem that occurs when there is a fractional *offset* between the raw data and the unwrap guide. In this case, there can be ambiguity in the unwrapping. Usually, individual data points are incremented to bring them as close to the guide as possible; but when the offset is close to 0.5 waves, small variations in the raw data can induce differences of one wave in the guided unwrap.

Procedures 2a and 2b, below, overcome the offset problem. The solution presented here is to compute the offset before the guided unwrap is performed. In the presence of noisy data this calculation requires some filtering, and the median filter again proves very useful. Here, it is very important to restrict $\mathbf{r}$ to points within the measurement domain D, this ensures that the median difference is a meaningful value (not based on invalid data from outside of the domain).

Procedure 2a: Guided Unwrapping with Offset Removal, Method 1

1. $\Delta \equiv \text{median}\{[\Gamma(D) - \phi(D)] - \text{round}[\Gamma(D) - \phi(D)]\}$	*(calculate offset)*
2. $m(\mathbf{r}) \equiv \text{round}[\Gamma(\mathbf{r}) - \phi(\mathbf{r}) - \Delta]$	*(difference rounded to nearest integer)*
3. $\phi'(\mathbf{r}) \equiv \phi(\mathbf{r}) + m(\mathbf{r})$	*(adjust into agreement with guide)*

An equivalent yet slightly more succinct implementation of Step 1 above uses the *modulo* operation to perform the rounding and subtraction in one step. There is, however, one minor catch: the modulo operation becomes non-periodic at $x = 0$. Any problem this aspect of the modulo operation may cause may be avoided by ensuring that the difference between Γ and ϕ is positive-definite: a large number L may be added to Γ during the modulo operation.

Procedure 2b: Guided Unwrapping with Offset Removal, Method 2

1. $L \equiv$ *any* integer greater than $-\min\{\Gamma(D) - \phi(D)\}$	*(e.g. choose 10,000)*
2. $\Delta \equiv \text{median}\{[L + \Gamma(D) - \phi(D)] \bmod 1\}$	*(calculate offset)*
3. $m(\mathbf{r}) \equiv \text{round}[\Gamma(\mathbf{r}) - \phi(\mathbf{r}) - \Delta]$	*(difference rounded to nearest integer)*
4. $\phi'(\mathbf{r}) \equiv \phi(\mathbf{r}) + m(\mathbf{r})$	*(adjust into agreement with guide)*

Both Procedures 2a and 2b may be simplified slightly by the combination of the last two steps into one single step, as was done in Procedure 1b.

13.5 FOURIER-TRANSFORM GUIDED UNWRAP

The guided unwrapping technique presented in Section 13.4 combines the desirable attributes of simplicity, speed, and high-reliability. The difficulty lies in obtaining the *a priori* approximation to the unwrapped wavefront being measured. This section presents a novel method of synthesizing the best attributes of two existing methods to produce a new unwrapping procedure called the *Fourier-Transform Guided Unwrap.*

In essence, the powerful spatial-filtering capability of the Fourier-transform technique is used to generate an *a priori* wavefront phasemap containing only low-spatial-frequency information. When used as an unwrapping guide for raw phase data generated by another means (e.g. phase-shifting), otherwise difficult unwrapping procedures are greatly simplified. Depending on the degree of spatial-filtering used in the Fourier-transform procedure, the presence of obstructions and blemishes can be easily overcome. An outline of the main procedure and a note on its application are presented here.

Begin with a raw phasemap $\phi(\mathbf{r})$ and one recorded interferogram $I(\mathbf{r})$ (which may be from of a series of interferograms).

Procedure 1: Fourier-Transform Guided Unwrap

1. Apply the Fourier-transform method (Section 11.3) with *heavy filtering* to the interferogram $I(\mathbf{r})$. This produces a wrapped phasemap $\phi_\gamma(\mathbf{r})$.
2. Unwrap $\phi_\gamma(\mathbf{r})$ to produce the wavefront guide $\Gamma(\mathbf{r})$.
3. Apply guided unwrapping (Procedure 2b) to the raw data $\phi(\mathbf{r})$ using $\Gamma(\mathbf{r})$ as the guide.

Application Notes. Choosing the proper amount of spatial-filtering depends on three main attributes: the characteristics of the obscured regions, the amplitude and spatial-frequency of the noise present in the interferogram, and the curvature of the wavefront under test. With enough spatial filtering, isolated blemishes nearly vanish; even obstructions that cut the measurement domain into multiple disjoint subdomains can be overcome, because the underlying phase can be made continuous across the blemishes and obscurations. When heavy filtering is applied, noise and other discontinuities are removed and unwrapping the guided wavefront becomes very simple. One cause for concern in the application of this method is the presence of highly-curved sections of the wavefront under test. Even in optical systems of high-quality, regions of high curvature may be present at the borders of the measurement domain as a result of diffraction. High-spatial-frequency components of small amplitude and low-spatial-frequency components of large amplitude are *both* attenuated by heavy filtering. The result may be a wavefront guide that fails to approximate the wavefront under test in some regions. The only straightforward solution in these cases is to relax the filtering until the problem is alleviated. It may occur, however, that the relaxation required to include all of the highly-curved wavefront components *undoes* the advantages that this method provides.

The problem of high wavefront curvature was identified in the discussion of single interferogram analysis (Chapter 11). High curvature violates the *monotonic phase requirement* described in Section 1.1.1 for single interferogram analysis and makes the application of filtering problematic. Hence the Fourier-Transform Guided Unwrapping Method is best suited to those cases for which the Fourier-transform methods of phase-retrieval are able to provide a low-spatial-frequency approximation to the wavefront under study. Where it is applicable, its strong advantages are that it is able to withstand isolated bad regions and discontinuities in the sub-region and to preserve the high-spatial-frequency content of the raw data without propagating phase-unwrapping errors throughout the data.

14

Aberration Polynomials

14.1 INTRODUCTION

Aberration polynomials are used to describe the continuous shape of the deformations of an optical wavefront, with respect to an ideal, often spherical, reference surface. While the shape of the aperture under study often dictates the appropriate set of polynomials, it is generally advantageous to use an *orthogonal* basis set. Such a set of polynomials not only enables the decomposition of a wavefront into experimentally meaningful constituent parts, but also facilitates numerical analysis of the measured data.

The most widely adopted representation for circular apertures is the basis set of *Zernike circular polynomials* Z_n^l of n-th degree (Zernike 1934, Zernike and Nijobar 1954). The Zernike polynomials are only orthogonal for circular apertures. Other polynomial sets include Zernike-Tatian (Fischer et al. 1993), Zernike-Mahajan (Mahajan 1994) for annular apertures, or Legendre polynomials for rectangular apertures.

This chapter presents the main representations of the aberration polynomials that are used to describe the interferometrically-measured wavefront data.

14.2 ZERNIKE POLYNOMIALS

Much has been written about the derivation and utility of the Zernike circular polynomials (several excellent references are Born and Wolf 1980:464-68, Malacara and deVore 1992, Carpio and Malacara 1994). This section presents, without proofs, only a brief overview of the most important aspects of the Zernike polynomials. There are many notation systems available for representing the Zernike polynomials; this chapter describes the notation used throughout this thesis.

The Zernike polynomials are obtained from the following two properties (Bathia and Wolf 1952, 1954; Born and Wolf 1980:464):

1. **Orthogonality.** The polynomials are orthogonal over the unit circle. Using the *Kronecker delta* symbol δ_{ij},

$$\int_0^1 \int_0^{2\pi} Z_n^l Z_{n'}^{l'*} \rho \, d\rho \, d\phi = \frac{\pi}{n+1} \delta_{nn'} \, \delta_{ll'} . \tag{1}$$

2. **Rotation.** The mathematical form of the polynomial is preserved when a rotation with a pivot at the center of the circle is applied to the function. By this property, the complex function Z_n^l may be separated into radial and azimuthal functions of the variables ρ and ϕ respectively, as follows:

$$Z_n^l = R_n^l(\rho) e^{il\phi} . \tag{2}$$

n is the degree of the polynomial, and l is the angular-dependence parameter. $|l|$ is the minimum exponent of the polynomials R_n^l. n and l are either both even or both odd; thus $n - l$ is always even.

The radial polynomials satisfy the relations:

$$R_n^l = R_n^{-l} = R_n^{|l|}. \tag{3}$$

$$\int_0^1 R_n^l R_{n'}^l \rho d\rho = \frac{1}{2(n+1)} \delta_{nn'}, \tag{4}$$

and can be generated by the expression

$$R_n^{n-2m}(\rho) = \sum_{s=0}^{m} (-1)^s \frac{(n-s)!}{s!(m-s)!(n-m-s)!} \rho^{n-2s}. \tag{5}$$

Since the azimuthal functions $e^{il\phi}$ are already orthogonal, any two R_n^l polynomials will be orthogonal if they do not have the same l.

A set of *real* polynomials Z_n^l may be written based on the complex U_n^l as

$$U_n^l = \begin{cases} \frac{1}{2}\left(Z_n^l + Z_n^{-l}\right) = R_n^l(\rho)\cos l\phi, & \text{for } l \le 0 \\ \frac{1}{2i}\left(Z_n^l - Z_n^{-l}\right) = R_n^l(\rho)\sin l\phi, & \text{for } l > 0 \end{cases}, \tag{6}$$

satisfying the condition

$$\int_0^1 \int_0^{2\pi} U_n^l U_{n'}^{l'} \rho \, d\rho \, d\phi = \frac{\pi}{2(n+1)} \delta_{nn'} \, \delta_{ll'}. \tag{7}$$

Using the fact that $n \ge 0$ and $n - l$ is even, modify the definition of the azimuthal component of U_n^l to form U_n^m.

$$m \equiv \frac{n-l}{2}, \text{ or } l = n - 2m, \tag{8}$$

now

$$U_n^m = A_n^m R_n^{n-2m} \begin{Bmatrix} \sin \\ \cos \end{Bmatrix} (n-2m)\phi. \tag{9}$$

where sine is used for $n - 2m > 0$ and cosine for $n - 2m \le 0$. With the addition of a convenient numbering system, these become the familiar Zernike polynomials.

14.3 NUMBERING CONVENTION AND COEFFICIENTS

Throughout the body of this text, the following conventions for the representation of Zernike polynomials are maintained.

• **Numbering convention.** An ordering system has been devised (Code V Reference Manual) to label the Zernike polynomials using a single, positive integer j to replace the pair $\{n, m\}$.

$$Z_j \rightarrow Z_n^m. \tag{10}$$

In the description of low-spatial-frequency optical aberrations, it is common to specify a set of 37 Zernike polynomials (0 through 36). The conventional ordering is shown in Table 1. Figure 1 shows a graphical representation of the first 37 Zernike polynomials.

Table 1: Single index notation for the Zernike polynomials.

j	(n, m)	j	(n, m)	j	(n, m)	j	(n, m)
0	(0, 0)	9	(3, 3)	18	(5, 3)	27	(6, 4)
1	(1, 1)	10	(3, -3)	19	(5,-3)	28	(6, -4)
2	(1, -1)	11	(4, 2)	20	(6, 2)	29	(7, 3)
3	(2, 0)	12	(4, -2)	21	(6,-2)	30	(7, -3)
4	(2, 2)	13	(5, 1)	22	(7, 1)	31	(8, 2)
5	(2, -2)	14	(5, -1)	23	(7,-1)	32	(8, -2)
6	(3, 1)	15	(6, 0)	24	(8, 0)	33	(9, 1)
7	(3, -1)	16	(4, 4)	25	(5, 5)	34	(9, -1)
8	(4, 0)	17	(4, -4)	26	(5,-5)	35	(10, 0)
						36	(12, 0)

• **Real quantities.** The polynomials described are *strictly real* quantities based on the set U_n^m from Eqns. (7) and (9). As described in the following sections, the symbol Z_j is used to represent individual, real, Zernike polynomials of the variables (ρ, ϕ), with $\rho \in [0, 1]$, and $\phi \in [0, 2\pi)$.

• **Leading coefficients.** There are two common conventions for the leading coefficients of the Zernike polynomials. Throughout this thesis, the leading coefficients of each Zernike polynomial are set to unity — not including the individual coefficients of the radial terms ρ^n that appear in each polynomial term. The Zernike polynomials are *bounded* on the range [–1, 1]. This convenient definition allows the immediate description of the magnitude of individual wavefront aberrations.

The second common convention in use sets the leading coefficients equal to the *variances* of the individual terms (excluding the constant *piston* term.) That is, Z_j is defined with a leading coefficient that satisfies

$$\left(Variance_j\right)^2 = \sigma_j^2 = \int_0^1 \int_0^{2\pi} Z_j^2 \, \rho \, d\rho \, d\phi \quad . \tag{11}$$

Although this definition simplifies the calculation of wavefront variance when the Zernike coefficients are known, it complicates the rapid interpretation of aberration magnitudes by the inclusion of (*mathematically*) irrational coefficients in each term.

14.3.1 *Vector Representation of Zernike Coefficient Pairs*

In several circumstances, pairing Zernike polynomials that share the same radial dependence is extremely useful in the concise representation of wavefront aberrations. This is especially true in the description of systematic errors (Chapters 5 and 8) where the rotational orientation of a given effect is independent of the coordinate system used for measurement. Throughout this thesis, a vector notation for *coefficient pairing* is utilized.

For example, wavefront *tilt* and *coma* are represented by the coefficient pairs (a_1, a_2) and (a_6, a_7) of the Zernike series respectively. In both cases, the two Zernike polynomials they modify have have $\cos\theta$ dependence in the first term and $\sin\theta$ dependence in the second term. This lends itself to a simple vector notation as follows

$$\text{Tilt, } \mathbf{T} \equiv (a_1, a_2), \text{ and Coma, } \mathbf{C} \equiv (a_6, a_7). \tag{12}$$

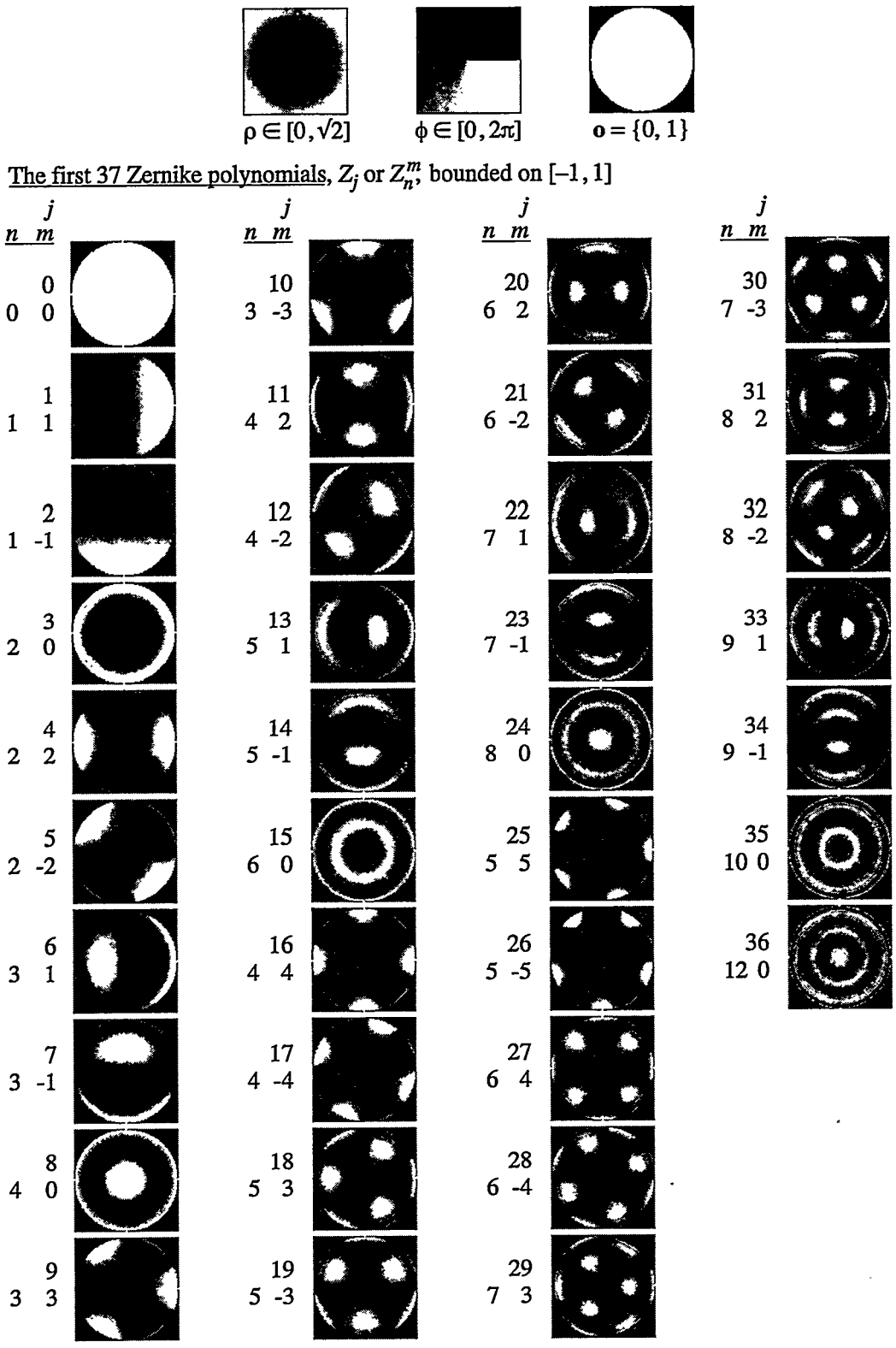

Figure 1. A graphical representation of the first 37 Zernike polynomials (0 through 36) and the three square arrays used to generate them. ρ is the radius array, φ is the azimuthal angle defined counter-clockwise from the x-axis, and **o** is the binary sub-domain-defining array which represents the unit circle on the rectangular grid. Points outside of the sub-domain are undefined. Adjacent to each Zernike term are the two-index and the single-index representations.

14.4 WAVEFRONT REPRESENTATION WITH THE VECTOR NOTATION

A wavefront $W(\rho, \phi)$ may be represented by a finite set of $(M+1)$ Zernike polynomials.

$$W(\rho,\phi)=\sum_{j=0}^{M} a_j Z_j(\rho,\phi). \tag{13}$$

On a discrete set of N points $\{\boldsymbol{\rho}_n\}$ or $\{(\rho_n, \phi_n)\}$ in an aperture domain A, for each point we have

$$W(\boldsymbol{\rho}_n)\equiv W_n=\sum_{j=0}^{M} a_j Z_j(\boldsymbol{\rho}_n). \tag{14}$$

A more compact *vector notation* describes a point in the wavefront at position $\boldsymbol{\rho}_n$ as a vector on a basis of Zernike polynomials.

$$W_n=\begin{bmatrix}a_0 \cdots a_M\end{bmatrix}\begin{bmatrix}Z_0(\boldsymbol{\rho}_n)\\ \vdots \\ Z_M(\boldsymbol{\rho}_n)\end{bmatrix}, \text{ or equivalently, } W_n=\begin{bmatrix}Z_0(\boldsymbol{\rho}_n)\cdots Z_M(\boldsymbol{\rho}_n)\end{bmatrix}\begin{bmatrix}a_0\\ \vdots \\ a_M\end{bmatrix}. \tag{15}$$

On the finite set of N points $\{\boldsymbol{\rho}_n\}$, the wavefront W_n may be written as a column vector. Equation (15) becomes

$$\begin{bmatrix}W_1\\ \vdots \\ W_N\end{bmatrix}=\begin{bmatrix}Z_0(\boldsymbol{\rho}_1) & \cdots & Z_M(\boldsymbol{\rho}_1)\\ \vdots & & \vdots \\ Z_0(\boldsymbol{\rho}_N) & \cdots & Z_M(\boldsymbol{\rho}_N)\end{bmatrix}\begin{bmatrix}a_0\\ \vdots \\ a_M\end{bmatrix}. \tag{16}$$

The dimension of the matrix in Eq. (16) is $M \times N$.

Within this notation, there are now several "vectors" we can define: the wavefront $\mathbf{W}$ has a value for each point in the domain; each Zernike polynomial term $\mathbf{Z}_j$ may be represented as a vector across the domain; for a given domain, there is a vector $\mathbf{Z}^M$ defined on the finite Zernike polynomial basis, spanning the space defined by the first $M+1$ polynomials; and there is a coefficient vector $\mathbf{a}$ of $M+1$ elements.

$$\mathbf{W}\equiv\begin{bmatrix}W_1 \cdots W_N\end{bmatrix}, \tag{17a}$$

$$\mathbf{Z}_j\equiv\begin{bmatrix}Z_j(\boldsymbol{\rho}_1)\cdots Z_j(\boldsymbol{\rho}_N)\end{bmatrix}, \text{ and } \hat{\mathbf{Z}}\equiv\begin{bmatrix}Z_0(\boldsymbol{\rho}_1) & \cdots & Z_M(\boldsymbol{\rho}_1)\\ \vdots & & \vdots \\ Z_0(\boldsymbol{\rho}_N) & \cdots & Z_M(\boldsymbol{\rho}_N)\end{bmatrix}=\begin{bmatrix}\mathbf{Z}_0 \cdots \mathbf{Z}_M\end{bmatrix}, \tag{17b}$$

$$a\equiv\begin{bmatrix}a_0 \cdots a_M\end{bmatrix}. \tag{17c}$$

Several of the above expressions may now be re-written in this compact vector form. The wavefront representation from Eq. (16) becomes

$$\mathbf{W}^T=\hat{\mathbf{Z}}\mathbf{a}^T, \text{ or } \mathbf{W}=\mathbf{a}\hat{\mathbf{Z}}^T. \tag{18}$$

As usual, the superscript T indicates the transpose of a vector or matrix. In the conventional notation,the orthogonality condition is

$$\sum_{n=0}^{N} Z_j(\rho_n) Z_k(\rho_n) \propto \delta_{jk}. \tag{19}$$

In vector notation, the orthogonality condition may be written as

$$\mathbf{Z}_j \mathbf{Z}_k^T \propto \delta_{jk}. \tag{20}$$

To study the variance of a given fit (Chapter 15), we require the definition of a *vector norm* across the set of N measured points.

$$\|\mathbf{W}\|^2 = \sum_{n=1}^{N} W_n^2 = \mathbf{W}\mathbf{W}^T. \tag{21}$$

14.5 REPRESENTATION OF THE ZERNIKE POLYNOMIALS ON A SQUARE GRID DOMAIN

The first step in the analysis of a digitized wavefront must be the establishment of a consistent coordinate system used in all stages of the analysis. Modern detector designs make the establishment of a rectangular Cartesian coordinate system a natural choice. Appropriate to the Zernike polynomials on a circular aperture will be a representation of the *unit circle* within the chosen domain. However, *any* contiguous or disjointed domain(s) of points may be used once an appropriate coordinate system has been established. This step may appear trivial, but there are subtleties in the procedure worthy of discussion. Carpio and Malacara (1993) have suggested a method of representing the Zernike polynomials in Cartesian coordinates. The method described here uses a direct representation of the polar coordinates on a square-grid domain.

Beginning with a square $N \times N$ domain of points D, our goal is to establish three array variables shared by all analysis procedures: $\boldsymbol{\rho}$, $\boldsymbol{\phi}$, and $\mathbf{o}$. For each point in D, $\boldsymbol{\rho}$ is the distance from the center, $\boldsymbol{\phi}$ is an azimuthal angle defined counter-clockwise from the x-axis, and $\mathbf{o}$ is a binary array describing which points are in the unit circle ($o = 1$) and which points lie outside ($o = 0$). As an intermediate step, define the array variables $\mathbf{x}$ and $\mathbf{y}$ in the following way. These array variables are linear and are bounded on the range [–1, 1].

$$\begin{cases} \mathbf{x}(1,*) = -1, & \mathbf{x}(N,*) = 1 \\ \mathbf{y}(*,1) = -1, & \mathbf{y}(*,N) = 1 \end{cases}. \tag{22}$$

Here * represents all columns (or rows) from 1 to N. $\mathbf{x}$ and $\mathbf{y}$ are shown in Figure 2 for an 8×8 array. This very small array is used only to illustrate the method; the EUV interferograms studied in this thesis actually occupy domain sizes from 225×225 to 860×860 pixels.

Many computer programming environments are capable of correctly rendering an arctangent into all four quadrants, using both x and y as input arguments, and yielding an angle modulo 2π. Computer systems without such capacity use the *ratio* of y to x as a single input argument and angles are returned modulo π, because sign information is lost in the division. In either case, $\boldsymbol{\phi}$ should be defined in the straightforward

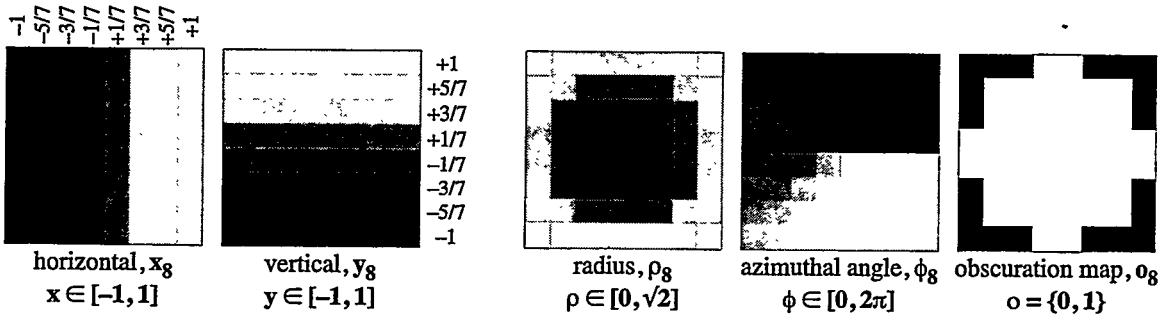

Figure 2. Definition of ρ and ϕ proceeds from the definition of the intermediate arrays **x** and **y**, illustrated in this example of an 8×8 square grid domain. In experimental applications, these arrays are typically hundreds of elements wide and contain tens of thousands of domain points.

manner, on the range $[0, 2\pi]$.

$$\phi = \tan^{-1}(\mathbf{y}, \mathbf{x}), \quad \text{typical modulo } 2\pi \text{ format}, \tag{23a}$$

$$\phi = \tan^{-1}\left(\frac{\mathbf{y}}{\mathbf{x}}\right), \quad \text{alternate modulo } \pi \text{ format}. \tag{23b}$$

The definition of ρ requires the most care. The most simple definition of ρ is

$$\rho = \sqrt{\mathbf{x}^2 + \mathbf{y}^2}. \tag{24}$$

This definition will be modified below for *even-N* arrays, .

It is very important to decide *where* the coordinate of a point resides within each square pixel. For symmetry reasons, we choose the *center of the square* as the locus of its coordinates. This choice maintains both 90° rotational symmetry and reflection symmetry about the two axes, but affects odd- and even-sized arrays differently.

One fact is immediately:apparent in the even-N case there is no single pixel corresponding to the origin, and no individual row or column corresponding to the *x*- or *y*-axis. This difference from the *odd-N* case does not affect measurements in any significant way.

Proper treatment of the points at the edges of the domain is the most important aspect of the definition of ρ. With **o** defined as

$$o = \begin{cases} 1, & \rho \le 1 \\ 0, & \rho > 0 \end{cases}, \tag{25}$$

care must be taken to ensure that the non-zero points of **o** extend to the edges of the domain. Based solely on Eqns. (24) and (25), this condition would not be met for the even-N arrays. The two points at the center of any side have $\rho > 1$ and would be excluded, leaving empty rows and columns along each edge. The following "fix" compensates for this problem by adjusting the definition of ρ for even-N arrays:

$$\text{IF } N \text{ is even THEN } \rho' \equiv \frac{\rho}{\max\{\rho(*,0)\}}. \tag{26}$$

After this normalization, with ρ redefined as ρ', the maximum value of ρ along the edges is identically *one.*

To illustrate the differences between the even and odd array definitions, Fig. 3 shows the appearance of **o** for an 8×8 and a 9×9 domain. After applying the "renormalization" of Eq. (26) to the even-sized array, the included points of **o** (that is, the non-zero points) reach the edges of the domain.

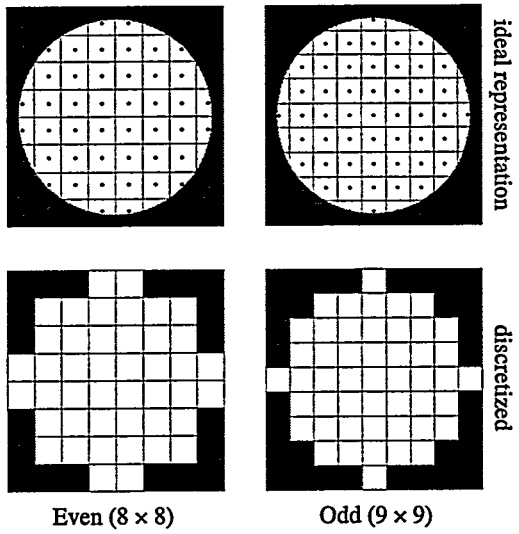

Figure 3. The definition of the radius array ρ depends critically on how the unit circle is defined, and care must be taken to ensure proper behavior at the edges of the domain. This figure illustrates how the ideal representation translates into symmetric even-sized and odd-sized discrete domains. It is important for the domain points to reach the edges of the domain at the points where $\rho = 1$. This condition is guaranteed for even-sized arrays by making the modification in Eq. (26).

14.5.1 *Note on Distortion*

The definition of the coordinate system variables ρ and ϕ presents an opportunity to include compensation for some geometrical systematic errors directly in the analysis. For example, the radial distortion related to the geometry of a planar detector array in a spherical beam (Section 5.12) can, in principle, be compensated for *automatically* by re-defining the radial coordinate ρ. In this particular case, a radial position ρ in the *Detector Coordinate System* corresponds to a polar angle $\gamma(\rho)$ in the spherical *Beam Coordinate System.* By replacing ρ with $\gamma(\rho)$ in the coordinate system definition, all measurements will automatically be made in the Beam Coordinate System.

This treatment is not required; coordinate transformations can be done after the data has been analyzed. However, this process can be simplified by building the transformation into the radial coordinate. This is especially true of the representation of a measured wavefront using the Zernike polynomial series, in which a coordinate *and coefficient* transformation in the presence of a non-linear radius is challenging.

15

Wavefront Surface Fitting

15.1 INTRODUCTION

Once the raw interferogram data has been processed and an unwrapped wavefront phasemap has been produced, the wavefront may be interpreted as the composition of individual, constituent wavefront aberrations. Reconstruction of the raw wavefront data from a limited number of these constituent aberrations also serves as a method of filtering the data to contain only the lowest-spatial-frequency components. The goal of this chapter is to describe several methods of wavefront analysis leading to the development of a novel, expedient variation of a well-established polynomial fitting technique.

The conventional measure of the *goodness of a fit* is based on the minimization of the function χ^2, defined as the ratio of the estimated variance to the parent variance times the number of degrees of freedom ν (Bevington 1969:188). The parent variance is characteristic of the spread of the data about the parent distribution, for which the estimated variance of the fit describes both the spread of the data and the precision of the fit.

The individual uncertainty of *each* individual data point σ_n is included in the definition of χ^2. This fact adds *significant* complication to wavefront surface fitting computations if simplifying assumptions are not made. For instance, the basis set of orthogonal polynomials on the measurement domain must be defined to be orthogonal in the presence of a non-uniform weighting function based on these individual uncertainties.

One simplifying assumption that is often appropriate in interferogram analysis is that the uncertainties of the phase measurements are equal to a constant σ across the measurement domain. (The domain is defined to include only valid data points.) Where this assumption is applicable, the function χ^2 is simply proportional to the fit variance (defined in the following section). Thus the method of wavefront surface fitting described in this chapter is essentially a minimization of the fit variance, based on the raw wavefront data and an appropriate basis set of aberration polynomials. This chapter describes methods that are general and may be applied to the orthogonalization of any arbitrary set of basis polynomials on a given domain.

15.1.1 *Note on Numbering Conventions*

For consistency with the Zernike polynomial basis, all polynomial basis "vectors" are numbered starting from 0; that is, X_0 is the "first" polynomial of an arbitrary basis. When polynomials up to and including X_M are used, then there are M+1 basis vectors. In regard to the Zernike basis, typically polynomials Z_0 through Z_{36} are used to describe aberrations in imaging systems. These constitute the well-known "first 37 Zernike polynomials."

However, on the discrete *measurement* domain, the N measured data points are numbered from 1 to N. Thus, the position vectors ρ_1 through ρ_N describe the measurement domain.

15.2 MINIMIZING THE FIT VARIANCE

The process of wavefront surface fitting described here is based on minimization of the *fit variance*. The fit variance is defined for a measured wavefront **W** and a fit **W′** based on an arbitrary, *finite* set of basis polynomials $\{\mathbf{X}_j\}$. The chosen set $\{\mathbf{X}_j\}$ may be any convenient set and need not be orthogonal. The following discussion is based on the method described by Fischer et al. (1993), and uses the vector notation described in Chapter 14.

In general, surface fitting on a basis of polynomial functions may be represented as

$$\mathbf{W}' = \sum_{j=0}^{M} c_j \mathbf{X}_j = \mathbf{c}\hat{\mathbf{X}}^T . \tag{1}$$

The individual vectors $\mathbf{X}_j$ range over the set of N measurement points. The set $\{c_j\}$ are the scalar polynomial coefficients and form the elements of the coefficient vector **c**. Over a discrete domain, where the fit variance is defined (Bevington 1969:137) as

$$s^2 \equiv \frac{1}{N-M-1}\sum_{n=1}^{N}\left(W'_n - W_n\right)^2 = \frac{1}{N-M-1}\left\|\mathbf{W}'-\mathbf{W}\right\|^2 . \tag{2}$$

N is the number of points in the measurement domain, and $(M+1)$ is the number of parameters used in the fit **W′**.

Inserting the wavefront fit of Eq. (1) into Eq. (2), we define for convenience a scalar quantity S proportional to the variance (and also proportional to χ^2):

$$S = (N-M-1)s^2 = \left\|\mathbf{c}\hat{\mathbf{X}}^T - \mathbf{W}\right\|^2 . \tag{3}$$

The minimization of s^2 (or, analogously, of S) is based on the selection of the optimum set of coefficients **c**. If a perfect fit were possible, S would equal zero. Since there will always be a difference between the measured wavefront and the wavefront reconstructed from the fit, S will be non-zero. The optimization thus requires finding a global minimum of S with respect to each coefficient c_k. This minimum occurs when the partial derivative of S with respect to each c_k is zero.

$$0 = \frac{\partial S}{\partial c_k} = \frac{\partial}{\partial c_k}\left\|\mathbf{c}\hat{\mathbf{X}}^T - \mathbf{W}\right\|^2 = 2\left(\mathbf{c}\hat{\mathbf{X}}^T - \mathbf{W}\right)\mathbf{X}_k^T . \tag{4}$$

Thus, for each k,

$$\mathbf{c}\hat{\mathbf{X}}^T\mathbf{X}_k^T = \mathbf{W}\mathbf{X}_k^T . \tag{5}$$

Equation (5) may be generalized for all k as follows:

$$\mathbf{c}\hat{\mathbf{X}}^T\hat{\mathbf{X}} = \mathbf{W}\hat{\mathbf{X}}, \text{ or } \sigma^2\mathbf{c}\boldsymbol{\alpha} = \mathbf{W}\hat{\mathbf{X}} . \tag{6a}$$

using the definition

$$\boldsymbol{\alpha} \equiv \frac{1}{\sigma^2}\hat{\mathbf{X}}^T\hat{\mathbf{X}} . \tag{6b}$$

As described earlier, σ is the (uniform) uncertainty of each data point in the measured wavefront. The symmetric matrix α is called the *curvature matrix* because it is related to the curvature of S (or s^2, or χ^2) in coefficient space. For clarity, Eq. (6a) may be expanded and re-arranged in matrix form:

$$\begin{bmatrix} \mathbf{X}_0\mathbf{X}_0^T & \cdots & \mathbf{X}_M\mathbf{X}_0^T \\ \vdots & & \vdots \\ \mathbf{X}_0\mathbf{X}_M^T & \cdots & \mathbf{X}_M\mathbf{X}_M^T \end{bmatrix} \begin{bmatrix} c_0 \\ \vdots \\ c_M \end{bmatrix} = \begin{bmatrix} \mathbf{W}\mathbf{X}_0^T \\ \vdots \\ \mathbf{W}\mathbf{X}_M^T \end{bmatrix}. \tag{7}$$

It is important to note that the curvature matrix has *no dependence* on the measured data. The matrix depends on the *domain* of the data, but not on the measured values. The measurements are contained in $\mathbf{W}$, on the right-hand-side of Eqns. (5) through (7). This fact may be exploited to improve computational efficiency in situations where many separate wavefront measurements are performed on the same domain.

Solving for $\mathbf{c}$ may proceed in one of three ways. One way is to assume that the polynomials $\{\mathbf{X}_j\}$ are orthogonal. If there are enough sampled points in the domain, this may be a good approximation; but it can introduce significant errors, especially for the coefficients of the higher-ordered polynomial terms. A second method requires the inversion of the curvature matrix. Great care must be taken because such inversions are notoriously ill-conditioned (Conte and de Boor 1980:249) and therefore extremely sensitive to small changes in the input conditions. The third and most sound method is to perform a transformation to a polynomial basis that is orthogonal over the domain, where the curvature matrix becomes diagonal, and makes solution straightforward. This third approach is typically accomplished using the Gram-Schmidt method (Wang and Silva 1980, Fischer et al. 1993). All three methods are discussed in detail in the following sections; error estimation is discussed in Section 15.6.

15.3 ORTHOGONAL BASIS ASSUMPTION

The minimization problem is particularly simple when the polynomials $\{\mathbf{X}_j\}$ are orthogonal over the measurement domain. The curvature matrix in Eq. (7) becomes diagonal, and the solution is

$$\mathbf{c} = \begin{bmatrix} \dfrac{\mathbf{W}\mathbf{X}_0^T}{\|\mathbf{X}_0\|^2} & \cdots & \dfrac{\mathbf{W}\mathbf{X}_M^T}{\|\mathbf{X}_M\|^2} \end{bmatrix}. \tag{8}$$

This is essentially the *projection* of the measured data $\mathbf{W}$ onto the orthogonal basis set. This approach requires the fewest calculations, and computationally may be the fastest method to perform.

When the discretized domain is a close approximation to an unobstructed circular aperture and when only the lowest-ordered terms are of interest, this method may work quite well. However, experience has shown that significant errors should be expected for certain polynomial terms. We here define a given term as *unbalanced* if the sum (or integral) of the term over the domain is not zero; equivalently, such a term

fails to meet the orthogonality condition that its scalar product with the (constant) *piston* term is zero.

$$\mathbf{Z}_j\mathbf{Z}_0^T \neq 0, \text{ or } \sum_{n=1}^{N} Z_j(\rho_n) \neq 0, \text{ when } j \neq 0 \;\Rightarrow\; \mathbf{Z}_j \text{ is unbalanced.} \tag{9}$$

For example, consider a measured wavefront **W** consisting only of a non-zero constant (piston) over the domain. The solution of **c** in Eq. (8) would yield erroneous, non-zero coefficients for any term that is unbalanced.

Specific polynomials that routinely cause difficulty are the cylindrically symmetric terms (defocus, spherical aberration, etc.) and those with 3θ or 5θ angular dependence. Because they do not match the symmetry of the rectangularly gridded domain, these terms are usually unbalanced. Over an unobstructed and symmetric aperture, the terms with θ or 2θ angular dependence (tilt, astigmatism, and coma) *are* usually balanced and orthogonal because they match the symmetry of the domain.

15.4 MATRIX INVERSION METHOD

To solve for **c** using matrix inversion, post-multiply both sides of Eqns. (6b) or (7) by the inverse of the matrix on the left-hand-side (the curvature matrix):

$$\mathbf{c} = \mathbf{W}\hat{\mathbf{X}}\left(\hat{\mathbf{X}}^T\hat{\mathbf{X}}\right)^{-1}, \text{ or } \mathbf{c} = \sigma^2\mathbf{W}\hat{\mathbf{X}}\boldsymbol{\varepsilon}, \tag{10}$$

using the definition

$$\boldsymbol{\varepsilon} \equiv \boldsymbol{\alpha}^{-1} = \left(\frac{1}{\sigma^2}\hat{\mathbf{X}}^T\hat{\mathbf{X}}\right)^{-1} = \sigma^2\left(\hat{\mathbf{X}}^T\hat{\mathbf{X}}\right)^{-1}. \tag{11}$$

The inverse $\boldsymbol{\varepsilon}$ of the curvature matrix $\boldsymbol{\alpha}$ is also a symmetric matrix. This matrix is called the *error matrix* for its role in error estimation, described in Section15.6.

The reliability of the matrix inversion must be determined on a case-by-case basis. Great care must be taken to ensure that the matrix is not ill-conditioned. Experience has shown that the matrix inversion methods are typically unreliable, owing primarily to the fact that the aberration polynomials, defined on the discrete domain, are not orthogonal. The presence of these *unbalanced* polynomials leads to non-zero off-diagonal elements in $\hat{\mathbf{X}}^T\hat{\mathbf{X}}$, making the matrix ill-conditioned.

15.5 GRAM-SCHMIDT METHODS OF ORTHOGONALIZATION

Beginning with a convenient set of M arbitrary polynomials on the measurement domain $\{\mathbf{X}_j\}$, the goal is to find an orthogonal basis set of M polynomials $\{\mathbf{Y}_j\}$ and the transformation matrix between the two. A measured wavefront is fit on the orthogonal polynomial basis to reduce the uncertainties in the fitting procedure. Often, the orthogonal set $\{\mathbf{Y}_j\}$ is only used as an intermediate part of the wavefront fitting and the final results are given as a coefficient vector **c** defined on the convenient basis $\{\mathbf{X}_j\}$.

$\{\mathbf{X}_j\}$ *convenient* basis	**c** coefficient vector in **X**-space.
$\{\mathbf{Y}_j\}$ *orthogonal* basis, calculated from $\{\mathbf{X}_j\}$	**b** coefficient vector in **Y**-space.

The Gram-Schmidt method of basis orthogonalization is recursive: each successive polynomial $\mathbf{Y}_j$ is added to the previous (j-1) polynomials in such a way that all of the terms $\{\mathbf{Y}_j\}$ are mutually orthogonal. Each $\mathbf{Y}_j$ begins with $\mathbf{X}_j$. Then a linear combination of the previous polynomials is found such that subtraction from $\mathbf{X}_j$ yields a new orthogonal polynomial.

It is worth reiterating that the new set of polynomials and the accompanying transformation matrix are determined only by the *domain* of the data, and not by the measured wavefront. While the determination of the new basis may be computationally intensive, this basis set and transformation matrix may be calculated once and stored for future, rapid application to a series of related measurements.

Two Gram-Schmidt methods are presented here, differing only in the way the transformation matrix is determined. In both, the transformation matrix is developed in parallel with the calculation of the new orthogonal set: the individual projections become the elements of the transformation matrix. The method which appears in the literature (Wang and Silva 1980, Fischer et al. 1993) requires that this lower-triangular transformation matrix be inverted (typically by the method of back-substitution) to determine the coefficients of the *original* polynomials from those of the *new* orthogonal polynomials. In a new, more efficient approach introduced here (Section 15.5.2), the projections are used to develop the inverted matrix *directly*.

15.5.1 *Gram-Schmidt: Conventional Method*

The orthogonalization process begins with the definition

$$\mathbf{Y}_0 \equiv \mathbf{X}_0 . \tag{12}$$

Then each successive term $\mathbf{Y}_j$ is projected onto the new basis and the subtraction of this projection from $\mathbf{X}_j$ yields a new orthogonal polynomial; the individual projections become the elements of a transformation matrix.

$$\mathbf{Y}_j = \mathbf{X}_j - \sum_{s=0}^{j-1} \frac{\mathbf{X}_j \mathbf{Y}_s^T}{\mathbf{Y}_s \mathbf{Y}_s^T} \mathbf{Y}_s = \mathbf{X}_j - \sum_{s=0}^{j-1} \frac{\mathbf{X}_j \mathbf{Y}_s^T}{\|\mathbf{Y}_s\|^2} \mathbf{Y}_s, \quad \mathrm{j} > 0 . \tag{13}$$

The off-diagonal elements of this transformation matrix may be read directly from Eq (13), as the scalar coefficients of $\mathbf{Y}_s$. As an intermediate step we define the matrix **D**, with off-diagonal elements D_{js}.

$$D_{js} \equiv \frac{\mathbf{X}_j \mathbf{Y}_s^T}{\|\mathbf{Y}_s\|^2}, \quad \mathrm{j} > \mathrm{s} . \tag{14}$$

This allows us to write

$$\mathbf{Y}_j \equiv \mathbf{X}_j - \sum_{s=0}^{j-1} D_{js}\mathbf{Y}_s . \tag{15}$$

These two basis sets form equivalent representations of an arbitrary wavefront $\mathbf{W}'$,.

$$\mathbf{W}' = \mathbf{c}\hat{\mathbf{X}}^T = \mathbf{b}\hat{\mathbf{Y}}^T . \tag{16}$$

Since the set of polynomials $\{\mathbf{Y}_j\}$ is orthogonal, we may apply Eq. (8) to find **b**, substituting **b** for **c** and $\mathbf{Y}_j$ for $\mathbf{X}_j$,

$$\mathbf{b} = \left[\frac{\mathbf{W}\mathbf{Y}_0^T}{\|\mathbf{Y}_0\|^2} \quad \cdots \quad \frac{\mathbf{W}\mathbf{Y}_M^T}{\|\mathbf{Y}_M\|^2} \right]. \tag{17}$$

Finding the coefficients **c** requires back-substitution. Beginning with Eq. (16) in matrix form,

$$\begin{bmatrix} \mathbf{Y}_0 \\ \vdots \\ \mathbf{Y}_M \end{bmatrix} = \begin{bmatrix} \mathbf{X}_0 \\ \vdots \\ \mathbf{X}_M \end{bmatrix} - \begin{bmatrix} 0 & \cdots & & & 0 \\ D_{10} & 0 & \cdots & & 0 \\ D_{20} & D_{21} & 0 & \cdots & 0 \\ \vdots & \vdots & & \ddots & \\ D_{M0} & D_{M1} & \cdots & D_{MM-1} & 0 \end{bmatrix} \begin{bmatrix} \mathbf{Y}_0 \\ \vdots \\ \mathbf{Y}_M \end{bmatrix}, \tag{18a}$$

$$\hat{\mathbf{Y}}^T = \hat{\mathbf{X}}^T - \mathbf{D}\hat{\mathbf{Y}}^T . \tag{18b}$$

Using **D** to represent the matrix with the elements D_{js} and **I** as an $M \times M$ identity matrix, Eq. (18b) can be solved for **Y**:

$$\hat{\mathbf{Y}}^T = (\mathbf{I}+\mathbf{D})^{-1}\hat{\mathbf{X}}^T \equiv \mathbf{G}\hat{\mathbf{X}}^T . \tag{19a}$$

Here, the transformation matrix **G** is defined as

$$\mathbf{G} \equiv (\mathbf{I}+\mathbf{D})^{-1} . \tag{19b}$$

Substituting Eq. (19a) into Eq. (16), the coefficients are related by

$$\mathbf{c} = \mathbf{b}(\mathbf{I}+\mathbf{D})^{-1} = \mathbf{b}\mathbf{G} . \tag{20}$$

Here again, care must be taken in the inversion to ensure that the matrix is not ill-conditioned.

15.5.2 *A More Expedient Method*

A more expedient method proceeds in the same way as the Conventional Method, presented above. The difference is in the way the transformation matrix is developed from the projections. The transformation matrix **G** enables us to determine the orthogonal polynomials $\{\mathbf{Y}_j\}$ from the arbitrary set $\{\mathbf{X}_j\}$, and also provides a means to rapidly transform coefficients of $\{\mathbf{Y}_j\}$ to coefficients of $\{\mathbf{X}_j\}$. The definition and utility of **G** are shown in Eqns (19) and (20). Expanding Eq. (19a) into a summation,

$$\mathbf{Y}_j = \sum_{m=0}^{M} G_{mj}\mathbf{X}_m . \tag{21}$$

To begin, the first polynomials of each basis are made equivalent, as before. The first diagonal matrix element G_{00} is set to 1 to reflect this equality.

$$\mathbf{Y}_0 \equiv \mathbf{X}_0. \tag{22}$$

$$G_{00} = 1. \tag{23}$$

Recursively, as before, the next polynomials $\mathbf{Y}_{j>1}$ are formed from $\{\mathbf{X}_s\}$, subtracting the projection of $\mathbf{X}_j$ onto the previously calculated $\{\mathbf{Y}_{s<j}\}$.

$$\mathbf{Y}_j = \mathbf{X}_j - \sum_{s=0}^{j-1} \frac{\mathbf{X}_j \mathbf{Y}_s^T}{\mathbf{Y}_s \mathbf{Y}_s^T} \mathbf{Y}_s = \mathbf{X}_j - \sum_{s=0}^{j-1} \frac{\mathbf{X}_j \mathbf{Y}_s^T}{\|\mathbf{Y}_s\|^2} \mathbf{Y}_s, \quad \mathrm{j} > 0. \tag{24}$$

However, since we are interested in keeping the expression in terms of $\{\mathbf{X}_j\}$, we substitute the previously calculated $\mathbf{Y}_s$ into Eq. (24), as follows:

$$\mathbf{Y}_j = \mathbf{X}_j - \sum_{s=0}^{j-1} \frac{\mathbf{X}_j \left(\sum_{t=0}^{s} \frac{G_{st} \mathbf{X}_t}{\|\mathbf{X}_t\|^2} \right)^T}{\|\mathbf{Y}_s\|^2} \left(\sum_{t=0}^{s} \frac{G_{st} \mathbf{X}_t}{\|\mathbf{X}_t\|^2} \right), \quad \mathrm{j} > 0. \tag{25}$$

$\|\mathbf{Y}_s\|^2$ is simply a constant that can be calculated once for each s. While on paper this may look *more* complicated than the Conventional Method, it is in fact very straightforward to implement in a computer program. Utilizing matrix row-arithmetic, we have a procedure as follows.

Performing row-arithmetic (Step 6) as the $\{\mathbf{Y}_j\}$ polynomials are calculated enables us to calculate the transformation matrix directly, without subsequent back-substitution. To improve computational efficiency, the norm of each of the polynomials $\mathbf{Y}_s$ should be calculated only once and stored for repeated future use.

For wavefront fitting, the coefficients **b** of $\{\mathbf{Y}_j\}$ are determined as before, from Eq. (17). Now, the computation of the coefficients **c** of $\{\mathbf{X}_j\}$ requires *no matrix inversion.* Since **G** is determined directly, from the orthogonalization procedure, Eq. (19a) can be used to compute the orthogonal basis polynomials from the original basis and Eq. (20) allows the coefficients of $\{\mathbf{X}_j\}$ to be determined from the coefficients of $\{\mathbf{Y}_j\}$.

Procedure: Expedient Gram-Schmidt Orthogonalization

1. $G_{00} \equiv 1$
2. Loop j from 1 to M
3. $G_{jj} \equiv 1$
4. Loop s from 0 to (j-1)
5. $\mathbf{Y}_s = [\mathbf{G}]_{\mathrm{row}\ s} \hat{\mathbf{X}}^T$
6. $[G]_{row\,j} \leftarrow [G]_{row\,j} - \frac{\mathbf{X}_j \mathbf{Y}_s^T}{\|\mathbf{Y}_s\|^2} [G]_{row\,s}$

15.6 WAVEFRONT FITTING ERROR ANALYSIS

In general, interferogram wavefront surface fitting error analysis proceeds along several fronts. One goal is to describe the success of a reconstructed-wavefront fit in accurately representing the raw data. A second issue is specifying the agreement among a series of similar measurements, and third is understanding the inherent limitations on the measurement precision, based on the known or measured uncertainties in each element of the system. This particular section addresses only the quality of the polynomial wavefront fitting, based on a measured wavefront phasemap and a given or a calculated basis of polynomial functions. First, the general approach, applicable to any of the previously described methods, will be explained; the error estimation is significantly simplified in those analysis methods that employ the Gram-Schmidt orthogonalization.

The most convenient starting point is to determine the uncertainties in the fitting coefficients **b** of the orthogonal basis $\{\mathbf{Y}_j\}$. Following the conventional method of error propagation with Gaussian error distributions, the estimated uncertainty $\sigma_{b_j}^2$ in an individual fitting coefficient b_j is given by a sum of squares of the individual uncertainty contributions of each point in the measurement domain.

$$\sigma_{b_j}^2 = \sum_{n=1}^{N}\left[\sigma_n^2\left(\frac{\partial b_j}{\partial W_n}\right)^2\right] = \sigma^2\sum_{n=1}^{N}\left(\frac{\partial b_j}{\partial W_n}\right)^2 . \tag{26}$$

σ_n is the estimated uncertainty in the measurement of an individual wavefront point. By a previous assumption (Section 15.1), the individual uncertainties are considered to be equivalent and equal to σ over the domain of valid data points. The partial derivative may be evaluated from Eq. (10), modified for **b** and $\hat{\mathbf{Y}}^T$. Here $\boldsymbol{\varepsilon}$ is evaluated for $\{\mathbf{Y}_j\}$, the basis under consideration.

$$\mathbf{b} = \mathbf{W}\hat{\mathbf{Y}}\left(\hat{\mathbf{Y}}^T\hat{\mathbf{Y}}\right)^{-1} = \sigma^2\mathbf{W}\hat{\mathbf{Y}}\boldsymbol{\varepsilon}, \text{ with } \boldsymbol{\varepsilon} \equiv \sigma^2\left(\hat{\mathbf{Y}}^T\hat{\mathbf{Y}}\right)^{-1}. \tag{27) and (28}$$

$$\left(\frac{\partial b_j}{\partial W_n}\right) = \frac{1}{\sigma^2}\sum_{k=0}^{M}\varepsilon_{jk}Y_k(\boldsymbol{\rho}_n). \tag{29}$$

Substituting Eq. (28) into Eq. (26), the expression for the uncertainties reduces considerably:

$$\sigma_{b_j}^2 = \frac{1}{\sigma^2}\sum_{k=0}^{M}\sum_{m=0}^{M}\varepsilon_{jk}\varepsilon_{jm}\sum_{n=1}^{N}Y_k(\boldsymbol{\rho}_n)Y_m(\boldsymbol{\rho}_n) = \sum_{k=0}^{M}\sum_{m=0}^{M}\varepsilon_{jk}\varepsilon_{jm}\alpha_{km} . \tag{30}$$

Recalling the definition of the curvature matrix $\boldsymbol{\alpha}$ for the basis $\{\mathbf{Y}_j\}$,

$$\boldsymbol{\alpha} \equiv \frac{1}{\sigma^2}\left(\hat{\mathbf{Y}}^T\hat{\mathbf{Y}}\right), \tag{31}$$

and the fact that the error matrix $\boldsymbol{\varepsilon}$ is the inverse of $\boldsymbol{\alpha}$,

$$\sigma_{b_j}^2 = \sum_{k=0}^{M}\varepsilon_{jk}\sum_{m=0}^{M}\varepsilon_{jm}\alpha_{km} = \sum_{k=0}^{M}\varepsilon_{jk}\delta_{jk} = \varepsilon_{jj}, \tag{32}$$

$$\sigma_{b_j}^2 = \varepsilon_{jj} \equiv \sigma^2 \left[\left(\hat{\mathbf{Y}}^T \hat{\mathbf{Y}} \right)^{-1} \right]_{jj} . \tag{33}$$

When the measurement uncertainty σ of each point is unknown, it may be estimated from the variance of the fit (Bevington 1969:154) as follows.

$$\sigma_n^2 \approx \sigma^2 \approx s^2 \equiv \frac{1}{N-M-1} \left\| \mathbf{W}' - \mathbf{W} \right\|^2 . \tag{34}$$

As before, N is the number of points in the measurement domain, $(M+1)$ is the number of parameters used in the fit, and $\mathbf{W}'$ is the wavefront fit reconstructed from the coefficient vector $\mathbf{b}$. Combining Eqns. (33) and (34), the estimated uncertainty in an individual fit coefficient b_j is

$$\sigma_{b_j}^2 = \varepsilon_{jj} = \frac{\left\| \mathbf{W}' - \mathbf{W} \right\|^2}{N-M-1} \left[\left(\hat{\mathbf{Y}}^T \hat{\mathbf{Y}} \right)^{-1} \right]_{jj} . \tag{35}$$

Up to this point, the orthogonality of the polynomial basis has not been considered; thus the error estimation method up through Equation (34) is generally applicable to any polynomial basis and any set of fit coefficients. When $\{\mathbf{Y}_j\}$ *is* an orthogonal basis, then the curvature matrix $\boldsymbol{\alpha}$ and its inverse the error matrix $\boldsymbol{\varepsilon}$ are both diagonal, making the matrix inversion trivial. Equation (33) reduces to these equivalent expressions.

$$\sigma_{b_j}^2 = \varepsilon_{jj} = \frac{\sigma^2}{\mathbf{Y}_j \mathbf{Y}_j^T} = \frac{\sigma^2}{\left\| \mathbf{Y}_j \right\|^2} = \frac{1}{N-M-1} \frac{\left\| \mathbf{W}' - \mathbf{W} \right\|^2}{\left\| \mathbf{Y}_j \right\|^2} = \frac{1}{N-M-1} \frac{\left\| \mathbf{b}\hat{\mathbf{Y}}^T - \mathbf{W} \right\|^2}{\left\| \mathbf{Y}_j \right\|^2} . \tag{36}$$

Here, the estimated uncertainties in the fit coefficients of the orthogonal basis polynomials are easily calculated. However, the orthogonal basis $\{\mathbf{Y}_j\}$ is often used only as an intermediate step in the calculation of the fit coefficients of the more convenient basis $\{\mathbf{X}_j\}$, from which the orthogonal basis was calculated. Since the transformation between the two bases is known, calculation of the estimated uncertainties in the original basis coefficients is very straightforward. $\mathbf{G}$ is determined during the calculation of the orthogonal basis. From the definition of $\mathbf{G}$, Eq. (19a),

$$\mathbf{c} = \mathbf{bG} \;\Rightarrow\; c_j = \sum_{k=0}^{M} b_k G_{jk} . \tag{37}$$

Using the method of error propagation and the fact that $\mathbf{G}$ has no dependence on the measured wavefront,

$$\sigma_{c_j}^2 = \sum_{k=0}^{M} \sigma_{b_k}^2 \left(\frac{\partial c_j}{\partial b_k} \right)^2 = \sum_{k=0}^{M} \sigma_{b_k}^2 G_{jk}^2 . \tag{38}$$

From Eq. (10) $\sigma_{b_k}^2$ is known in terms of $\{\mathbf{Y}_j\}$. This is easily converted to $\{\mathbf{X}_j\}$:

$$\sigma_{c_j}^2 = \sigma^2 \sum_{k=0}^{M} \frac{G_{jk}^2}{\left\|\mathbf{Y}_k\right\|^2} = \sigma^2 \sum_{k=0}^{M} \frac{G_{jk}^2}{\left\|[G]_{\text{row } k} \hat{\mathbf{X}}^T\right\|^2} = \sigma^2 \sum_{k=0}^{M} \frac{G_{jk}^2}{\left\|\sum_{l=0}^{M} G_{lk} \mathbf{X}_l\right\|^2}. \tag{39}$$

From this expression, the uncertainties in the fitting coefficients of the convenient basis are easily calculated.

V. CONCLUSION

CONCLUSION

It is widely agreed in the lithography community that at-wavelength interferometric testing is a fundamental requirement in optical system evaluation. As advances in circuit fabrication technology press the field toward shorter wavelengths and ever-tighter optical tolerances, nowhere are the metrology challenges now as great as for EUV. After several years of work in the development of EUV interferometry as a part of the ongoing research in EUV lithography and related technologies, the success and utility of this research have been amply demonstrated.

Following initial measurements of high-resolution EUV Fresnel zoneplate lenses which revealed the limitations of the conventional point diffraction interferometer, a novel, more sophisticated and improved *phase-shifting* point diffraction interferometer was developed. The latter design was implemented for the at-wavelength measurement of a lithographic-quality EUV 10× Schwarzschild objective. These studies showed nearly diffraction-limited characteristics of the low-spatial-frequency wavefront aberrations, accompanied by a high density of mid-spatial-frequency defects in the multilayer coatings.

Overcoming experimental difficulties necessitated the development of several new interferogram-analysis phase-retrieval methods. Problems in controlling the phase-increment used in phase-shifting analysis were overcome by the development of a novel approach, called the the *Fourier-Transform Method of Phase Shift Determination*. This general method improves the accuracy of phase-shifting analysis considerably by using the phase of the Fourier-domain first-order peak to determine the relative phase-increments, eliminating the common problem of fringe print-through.

The presence of the defects posed significant complications for the data analysis, especially the phase-unwrapping. The concept of guided unwrapping used in sub-Nyquist interferometry was successfully adapted to this problem in a novel approach called the *Fourier-Transform Guided Unwrap*. First, a low-spatial-frequency approximation to the unwrapped wavefront is found using the Fourier-transform method with strong spatial-filtering. The approximation is filtered strongly enough to bridge obstructions or localized regions of invalid data. The approximate wavefront is then used as a *guide* to properly unwrap the raw phase data, preserving all of the original high-spatial-frequency content.

A third new technique is a variation of the well-established method of Gram-Schmidt orthogonalization used for wavefront surface fitting to the Zernike circle polynomials. The improvement enables the calculation of an important polynomial basis transformation matrix without the necessity of performing a matrix inversion operation.

Used in the rapid alignment of the interferometer, the *Fourier-Transform Alignment Method* developed and implemented by the author simplifies the difficult task of positioning a 100-nm pinhole onto the

center of a sub-200-nm focused EUV beam. Using the measured diffraction pattern, or an interferogram recorded by the CCD, the Fourier-transform is rapidly computed, scaled, and displayed, revealing the intensity pattern of test and reference beams in the image-plane. With a continuously-updating display, the two beams can be positioned much more easily than is possible without this tool.

In an effort to evaluate the performance of the interferometer and to characterize the error sources, measurement precision was investigated in a variety of ways. Each individual experiment was designed to isolate (as well as possible) the effects of a single component of the system or of a specific measurement configuration. These experiments reveal that the most significant contributors to measurement uncertainty are the 100-nm-scale reference pinholes used to generate the spherical reference wavefronts. Yet measurements that sought to *intentionally* induce random errors by displacing the reference pinhole far from the optimum position were only able to create small RMS wavefront differences, on the order of 0.02 waves. Every other component performed significantly better than this.

The pinholes are the most critical elements of the PS/PDI, and the ultimate performance will be limited by their quality. Measurement uncertainties show that the quality of the reference wave is affected by the aberrations of the optical system under test. Thus, the importance of adequate spatial filtering increases with the magnitude of the aberrations in the test system. At the time these experiments were conducted, adequately small reference pinholes were not available. The pinholes used were not smaller than 130 nm; yet studies here indicate that the optimum pinhole size for providing adequate spatial-filtering without sacrificing intensity transmission should be below 100 nm.

As a qualitative verification of accuracy, the Schwarzschild objective was used in a series of imaging experiments. Favorable comparisons of the resolution-test-pattern images with the predicted performance indicate that the systematic measurement errors must be small in comparison to the measured wavefront.

The first direct quantitative measurements of significant chromatic aberrations near the 13.4-nm peak wavelength of the Schwarzschild objective's multilayer coatings demonstrate both the importance and sensitivity of at-wavelength inspection. Interferometric wavefront measurements provide detailed quantitative information about broad areas of the surface in ways that high-accuracy reflectometry cannot.

Future work. While the development of high-accuracy and high-precision EUV interferometric capability may meet or exceed the requirements of EUV lithography, its existence cannot guarantee that optical fabrication and multilayer deposition technologies will reach *their* target specifications. One of the most challenging issues is the mid- to high-spatial frequency roughness present in the substrates and multilayers, causing an unacceptable amount of scattering.

As part of this dissertation research, studies have been made to evaluate the relative merits of dif-

ferent configurations of the PS/PDI interferometer. These studies include estimates of the relative efficiencies. With the required development of high power EUV sources for lithography may come the opportunity to create *in situ* EUV interferometry, allowing precision focusing and system alignment to be performed on a production-level tool in a fabrication environment. The high efficiency of the PS/PDI interferometer, the accuracy it provides, and the ease and reliability of the data analysis relative to competing designs make the PS/PDI a candidate for such an *in situ* inspection tool.

The concurrent development of state-of-the-art visible-light interferometry capable of achieving measurement tolerances in the same range as EUV interferometry (Sommargren 1996a, 1996b) meets the current need for a test that can be performed during the optical fabrication process and before the deposition of multilayer coatings. Eventually, comparisons of EUV and visible-light measurements of the same optical systems will yield substantial information about the properties of the multilayer coatings. Yet the investigations of this thesis indicate that at-wavelength testing will probably never be displaced entirely: the multilayer response depends critically on wavelength and other properties that cannot be reliably measured with visible-light.

There are several important areas of research that require more careful investigations, beyond the scope of this thesis. Accuracy is by far the most prized attribute of an interferometric system. The development of routine null-testing (via two-pinhole tests, or by other means) to quantify the systematic error contributions and to establish the accuracy limits is an essential component of reliable interferometry and must be integrated into future interferometer designs.

Further investigations of pinhole diffraction, both experimental and theoretical, are essential to the continued development of point diffraction interferometry. It may be discovered that some absorber materials simply function better than others in generating the reference wave. Also, controlling the thickness of the absorber may be a way to achieve high wavefront quality where small pinholes are unavailable. Determining the optimum pinholes size for the measurement of optical systems with NA higher than 0.1 is another challenging area of research; the compromise between transmitted intensity, wavefront quality, and fabrication issues yields many unanswered research questions.

Continued development of the PS/PDI spatial-filter window-and-pinhole geometry may yield improved measurement schemes suited to a variety of optical systems. Certain design optimizations can simplify the experimental apparatus or facilitate the identification and removal of geometrical systematic errors.

Relevant to the adaptation of the PS/PDI to a compact laser-plasma EUV source are experiments that investigate the relationship between measurement uncertainties, noise, and flux requirements. These experiments can be performed using the synchrotron source with limited exposure times.

Closing remarks. It is my sincere hope that the investigations presented in this dissertation will establish a framework for future research on the PS/PDI or related interferometers. The studies of Chapter 5, in particular, are intended to identify the most important systematic measurement effects in a way that is as general and accessible as possible. The material presented here may aid in identifying the most important design issues for the application of the PS/PDI to the measurement of an arbitrary optical system — be that an EUV optical system with sub-nanometer fabrication tolerances, or a radio telescope with square-meters of collection area. The new methods of interferogram analysis and wavefront surface fitting are very general and may find useful application in a wide range of interferometric systems.

Independent of the status of EUV lithography as a candidate technology for mass-production, the research described here may create new opportunities for the evaluation of high-resolution systems at short wavelength. The high degree of coherence that has been demonstrated in these measurements also reflects favorably on future experiments with coherent EUV radiation using a high-brightness synchrotron light source.

Appendix

A.1 EUV OPTICAL CONSTANTS

The EUV region of the spectrum (nominally 5-20-nm wavelength, or 50-200 eV) is characterized by high absorption in all materials. An empirical understanding of the interaction of EUV light and matter begins with the complex index of refraction. Since the index is close to unity for all materials across the EUV spectral range, a convenient notation is used:

$$n = 1 - \delta + i\beta \tag{1}$$

δ and β are real, empirical constants that have been measured and tabulated for a vast range of materials, over a broad range of wavelengths (Henke et al. 1992). δ represents the *refractive component* of the index, and β is the *extinction coefficient*, related to the absorptivity of the material. The propagation of plane-wave monochromatic light within an isotropic and homogeneous material may be expressed for an arbitrary polarization component as a scalar electric field amplitude E, oscillating with angular frequency ω and initial field amplitude E_o.

$$E(\mathbf{r},t) = E_o e^{-i(\omega t - \mathbf{k}\cdot\mathbf{r})}. \tag{2}$$

The phase velocity may be expressed in terms of the magnitude of the wavevector $\mathbf{k}$ and the complex index of refraction

$$v_{phase} = \frac{\omega}{k} = \frac{c}{n} = \frac{c}{1-\delta+i\beta}. \tag{3}$$

Thus

$$k = \frac{\omega}{c} n = \frac{\omega}{c}(1-\delta+i\beta). \tag{4}$$

Using the translational invariance of the plane wave field, perpendicular to the propagation direction, we define $\mathbf{k}$ in the x-direction and define $\mathbf{r} = x\hat{\mathbf{x}}$. Thus, $\mathbf{k}\cdot\mathbf{r} = kx$, and we have a one-dimensional representation of the field

$$E(\mathbf{r},t) = E(x,t). \tag{5a}$$

$$E(x,t) = E_o \exp\left\{-i\left[\omega t - \frac{\omega}{c}(1-\delta+i\beta)x\right]\right\} \tag{5b}$$

$$= E_o \exp\left[-i\omega t + i\tfrac{2\pi}{\lambda}x\right]\exp\left[-i\tfrac{2\pi}{\lambda}\delta x\right]\exp\left[-\tfrac{2\pi}{\lambda}\beta x\right] \tag{5c}$$

$$= E_o \exp(-i\omega t)\exp\left[i\tfrac{2\pi}{\lambda}(1-\delta)x\right]\exp\left[-\tfrac{2\pi}{\lambda}\beta x\right]. \tag{5d}$$

λ is the free-space wavelength. The extinction in material is described by the electric field intensity

$$I(x) = n\left|E(x,t)\right|^2 \equiv I(0)\exp\left[-\tfrac{4\pi}{\lambda}\beta x\right]. \tag{6}$$

The $1/e$ intensity transmission depth, or *absorption length*, is

$$x_{\frac{1}{e}} \equiv l_{abs} \equiv \frac{1}{4\pi\beta}. \tag{7}$$

An analogous depth may be defined to describe the length of material required to produce a phase change

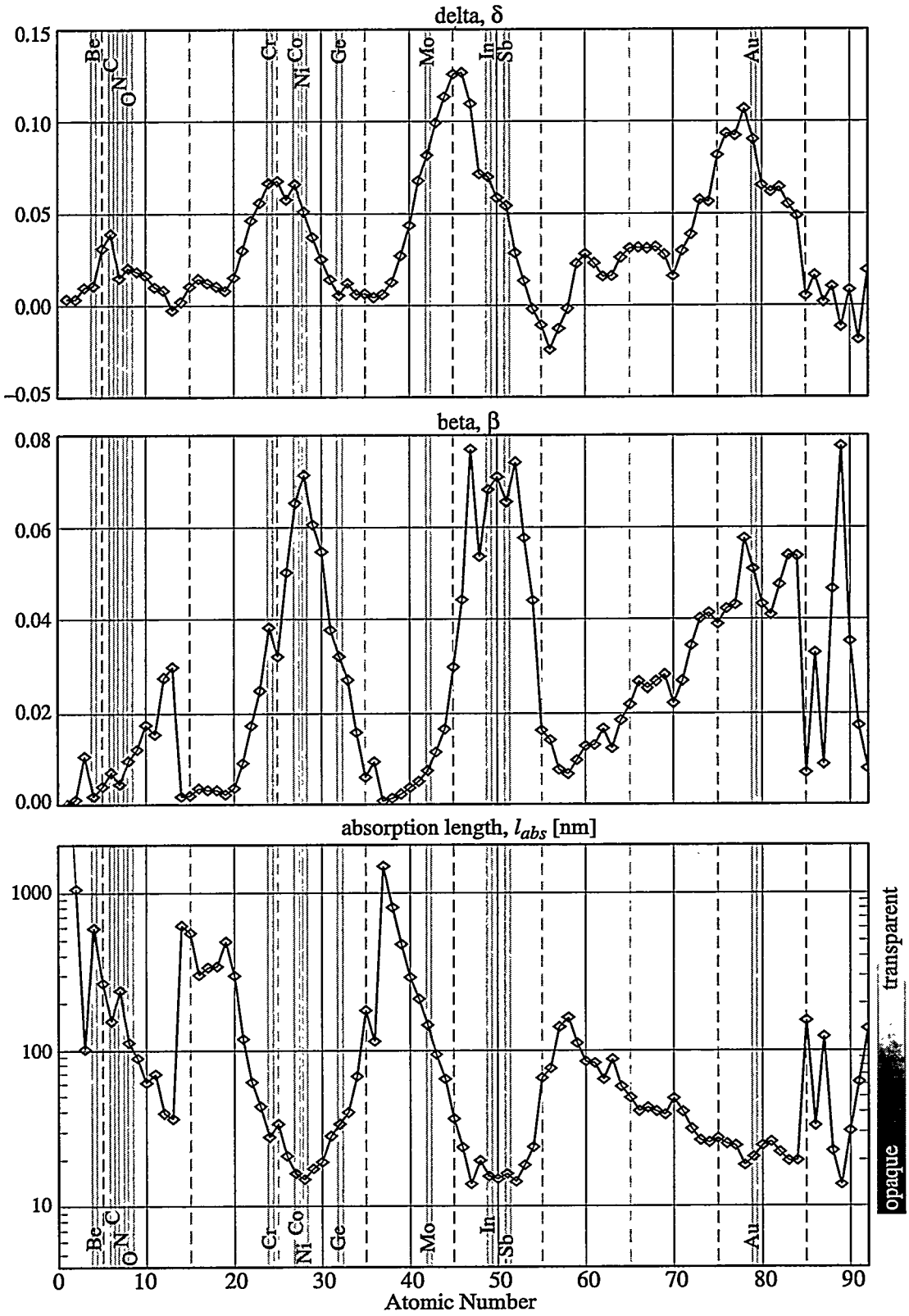

Figure 1. Optical properties of elemental solids at 13.4 nm wavelength (92.5 eV). The index of refraction n is defined in terms of the refractive, *real* component $1 - \delta$ and the absorptive, *imaginary* component $i\beta$. The absorption length l_{abs}, defined as the $1/e$ intensity transmission depth, is inversely related to β.

Table 1. Optical properties of selected materials commonly used in EUV applications at 13.4 nm wavelength.

Material	density, ρ [g/cm³]	δ	β	l_{abs} [nm]
Ag	10.5	0.110161	0.0772735	13.8
Ni	8.902	0.051499	0.0716041	14.9
InSb	7.31	0.064686	0.0699965	15.2
In	7.31	0.070171	0.0682527	15.6
Sb	6.691	0.054474	0.0655745	16.3
Co	8.9	0.066056	0.0653061	16.3
Cr	7.19	0.066673	0.0381981	27.9
Ge	5.323	0.005387	0.0318920	33.4
Si_3N_4	3.44	0.025675	0.0091366	116.7
Mo	10.22	0.076553	0.0073536	145.0
C*	2.2	0.037853	0.0067466	158.1
Si	2.33	0.000069	0.0018211	585.5
Be	1.848	0.010844	0.0017982	593.0
O_2*	1.43×10^{-3}	0.000026	0.0000119	89524.7
N_2*	1.25×10^{-3}	0.000023	0.0000068	155741.6

* Carbon density is given for graphite. Oxygen and nitrogen densities are for the gas-phase at STP.

of 2π relative to vacuum propagation. By inspection, from Eq. 5(d) this phase length is given by

$$x_{2\pi} \equiv l_{phase} \equiv \frac{\lambda}{d}. \tag{8}$$

Figure 1 shows the real and imaginary components of the index of refraction for a wide range of elemental solids at 13.4 nm wavelength (92.5 eV). Several materials commonly used in EUV applications are highlighted in the figure, and are listed in Table 1, also for 13.4 nm wavelength.

A.2 EUV OPTICAL SYSTEMS

In general, optical imaging systems function by generating an optical path-length-difference between rays travelling separate paths. There are numerous strategies employed in generating the path-length-difference; the most important to consider are *refractive, reflective,* and *diffractive* systems. This brief section addresses the application of these strategies to EUV wavelengths.

Refractive optics exploit the difference of the refractive index of one material relative to another (or to vacuum) to achieve an optical path-length-difference. Because of the strong absorption at EUV wavelengths for all materials, refractive optical systems pay much too high a price in intensity attenuation to achieve a small change in path length. With the exception of a few limited cases (including phase-shifting elements), refractive optics at EUV wavelengths are not feasible.

Reflective elements for EUV optical systems fall into two main categories: glancing incidence optics, which exploit the phenomena of *total external reflection*, and multilayer optics, which function by creating a resonant standing-wave field in a thin-film stack.

Glancing incidence optical systems are widely used in EUV, soft X-ray, and hard X-ray applications. They possess several advantages for special applications and are invaluable components of synchrotron beamlines. Often comprised of thin substrates bent or polished into a curved profile, glancing incidence optics exploit the high EUV reflectivities that can be achieved when the glancing angles of incidence are limited to a narrow range above zero. Since the real part of the index of refraction is *less than one* for many materials in this energy regime, the phenomenon of high glancing-incidence reflectivity is most easily understood as a *total internal reflection* but with the light propagating in vacuum or air.

Below the *critical angle* of incidence θ_c, defined from the plane of the interface, very high reflectivities may be achieved. θ_c is the angle at and below which the incident field does not propagate into the medium, but rather propagates along the interface. For EUV and X-ray materials for which δ and β are small,

$$\theta_c = (2\delta)^{1/2}. \tag{9}$$

By distributing the incident light over large surface areas, glancing incidence optical systems demonstrate strong advantages in high-incident-power applications such as synchrotron beamlines. The profiles of the optical surfaces are vulnerable to thermal expansion, making cooling an issue of critical importance. By water-cooling the optical substrates and holders, heat from the absorbed power can be removed.

Multilayer-coatings designed for high-reflectivity at near-normal incidence *are* the key enabling technology that has led to the development of EUV lithography as a viable candidate for the 0.1 μm generation of circuit fabrication and beyond. These systems rely heavily on state-of-the-art optical surface figuring and polishing, and on the development of an optical-coating deposition capability that meets the extraordinarily strict tolerances inherent in these systems. Yet multilayer-coatings provide the freedom to design very sophisticated large-scale optical systems with high-resolution over a large field of view, as is required in lithographic applications. Some important properties of multilayers are addressed in Appendix A.3.

While glancing-incidence reflective optics dominate high-incident-power applications, multilayer systems are currently being developed to address the requirements of lithography. High-resolution EUV applications are now dominated by diffractive optics such as Fresnel zoneplate lenses. Created holographically or, more commonly, by taking advantage of other high-resolution lithographic techniques such as electron-beam lithography, these patterned elements typically function as the hologram of a simple singlet lens. The principles of Fresnel zoneplate operation are described in Appendix A.4.

A.3 REFLECTIVE MULTILAYER COATINGS FOR EUV

Multilayer reflection is a resonance phenomenon. When the wavelength, angle, and polarization of the incident field match the resonance conditions determined by the bi-layer period, layer thicknesses and optical properties of the two materials in the multilayer, strong EUV reflectivities may be achieved, *even*

though the materials are highly absorptive (Stearns et al. 1993). At resonance (peak reflectivity), a standing wave is formed matching the period of the multilayers. Typically the node is formed within the absorptive material and the anti-node within the less-absorptive material. Conditions for high reflectivity exploit the index of refraction *difference* between two materials; the best multilayer material pairs are those for which index difference is large yet neither material is highly absorptive. The materials pair that has been most widely used for EUV near-normal-incidence multilayers near 13-nm wavelength are molybdenum and silicon.

The very resonance properties that enable multilayers to function at normal incidence with high EUV reflectivity also subject them to *extreme* sensitivity to fabrication errors. When the conditions for resonance are not met, the reflected intensity suffers. Of equal or possibly *greater* importance to high-performance imaging systems is the change of phase experienced by the reflected wave. As described in this appendix, even small changes in the multilayer period, or *d-spacing*, can have a dramatic impact on the reflected phase in systems designed for diffraction-limited performance.

To illustrate this extreme sensitivity, the dependence of the reflected intensity and phase of 13.4-nm-wavelength light were calculated and are shown in Fig. 2. (The reflection-phase is shown *relative* to the phase at peak reflectivity.) These simple calculations are based on the method described by Born and Wolf (1980:51-70) for periodically stratified media, with 40 Mo/Si layer pairs. Although the individual layers are approximately only 15 atoms thick, and interfacial diffusion cannot be avoided, the naïve assumption of perfectly abrupt interfaces made in these calculations does not change the outcome significantly.

The optimal layer thicknesses were determined empirically by the author based on normal-incidence reflectivity, using the optical constants recommended by Erik Gullikson (personal communication). The individual layer thicknesses were 4.125 nm of Si and 2.722 nm of Mo. The total bi-layer period d_o is 6.847 nm, and the ratio γ of Mo thickness to the total bi-layer thickness is 0.3975. The peak normal-incidence reflectivity is calculated to be 71.8%.

In the top row of Fig. 2, the multilayer-reflection properties are shown near normal incidence. Dependence on wavelength, layer thickness, and angle are shown. $\Delta d/d_o$ represents a uniform, fractional change in layer thickness about the optimal value. The most significant phase effect that is evident in these plots is the reflected phase change of π-radians that occurs as the parameter under consideration passes through resonance. Across the resonance peak, the phase-dependence is nearly linear with an approximate slope of π divided by the width of the peak.

Two useful empirical formulas describe the phase-dependence near peak reflectivity.

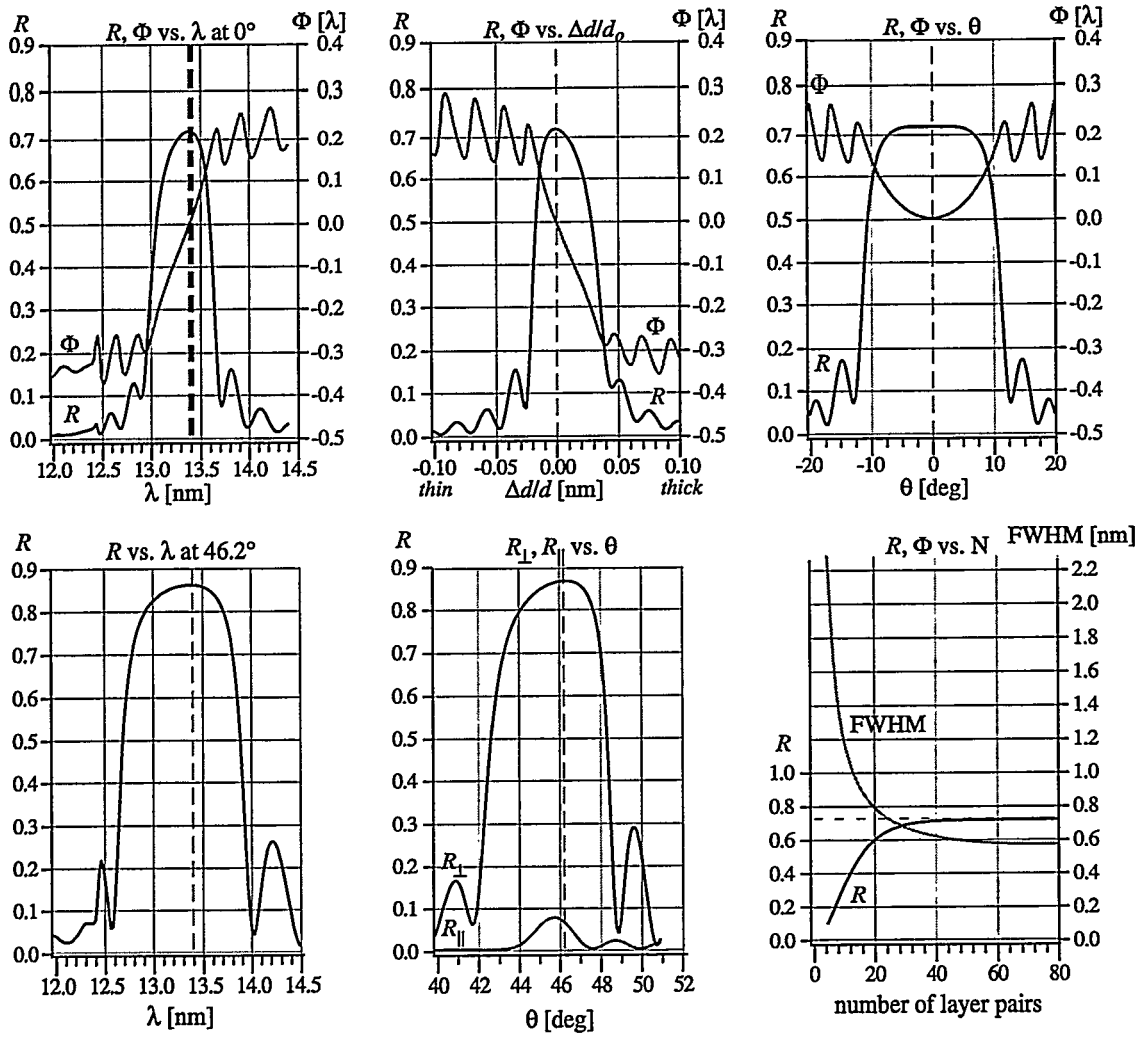

Figure 2. Ideal reflection properties of Mo/Si multilayer mirrors at normal incidence and 46.2° incidence for 13.4 nm wavelength. Optical properties and layer thicknesses are given in the text.

• Dependence of the reflected phase ϕ on incidence angle θ:

$$\phi \text{ [waves]} \approx 1.24\times10^{-3}\ \theta^2 \text{ [deg}^2\text{]}. \tag{10}$$

• Dependence of the reflected phase ϕ on layer thickness error $\Delta d/d_o$:

$$\phi \text{ [waves]} \approx -7.49\ (\Delta d/d_o). \tag{11}$$

Equation (10) is given to demonstrate the magnitude of the angular phase dependence near normal incidence. For most practical purposes, *true* normal-incidence mirrors are of little use — reflective imaging systems *must* contain a finite angle of incidence and a range of angles related to the curvature and size of the surfaces.

The first two graphs of the second row of Fig. 2 model the behavior of the near-45° turning mirror that deflects light vertically toward the object plane of the Schwarzschild objective. The design angle of incidence is 46.2°, and the Mo/Si mirror has 20 layer pairs. The polarizing property of this mirror is evi-

dent in the large difference between the *perpendicular* (TE) and the *parallel* (TM) component reflectivities. The last graph of the lower row shows the dependence of the reflectivity and the full-width at half-maximum bandwidth ($\Delta\lambda$) on the number of layer pairs.

A.3.1 *Fabrication Tolerances*

The tight wavefront tolerances of lithographic-quality EUV imaging systems place extremely high demands on the fabrication of the optical substrates and on the deposition of the multilayers. Small layer thickness errors become multiplied by the number of layer pairs to create larger effects. It is an important and revealing exercise to consider the separate contributions of the geometric path-length-change with the change in phase upon reflection that occurs when the layer thickness is varied.

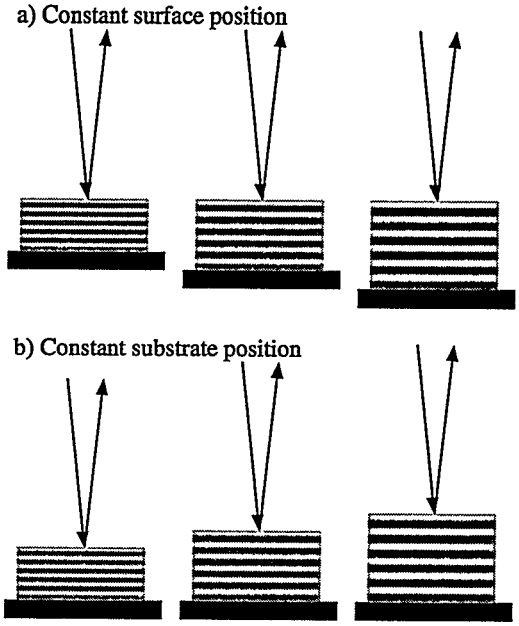

Figure 3. Two models for studying multilayer reflectivity, relevant to fabrication and metrology. (a) When the top surface is measured with visible-light interferometry *after* multilayer deposition, this model isolates the reflected phase effects seen only by the EUV light. (b) When the substrate position is known *before* multilayer deposition, this model is useful in setting layer thickness tolerances: Here the geometric path-length change and the reflected phase change are combined.

Consider two related models to describe this effect. These are shown in Figs. 3(a) and 3(b) First, the *constant surface position* model assumes that the position of the top-most layer surface is fixed in space. Here the measured phase variation with changing layer thickness is the same as the empirical expression given in Eq. (11). The relevance of this model comes from the comparison of visible-light and EUV interferometric measurements of the same optical system. With the assumption that the visible-light measurements are sensitive only to the position of the top surface, the difference between the two measurements is related to the thickness-dependent phase effects that are only observable *at-wavelength* (with EUV light).

Second is the *constant substrate position* model. When interferometric characterization is performed *prior* to the deposition of the multilayers, then the final surface profile may be inferred from the predicted multilayer coating thickness. Thickness errors in this model contribute both a geometric path-length change *and* the thickness-dependent phase change. The net phase change ϕ is thus the sum of a geometric component $\phi_{geometric}$ and the reflected-phase component. For N bi-layers of a multilayer with period length d_o, the optical path length changes by twice the height of the stack on reflection. Defining

Δd as the change from the optimal thickness d_o, and removing a constant phase term gives

$$\phi_{geometric}\ [\text{waves}] = 2N\ (\Delta d)/\lambda. \tag{13}$$

The reflected phase is described by Eq. (11). Combining these gives the net phase change

$$\phi\ [\text{waves}] = 2N\ (\Delta d)/\lambda - 7.49\ (\Delta d/d_o). \tag{14}$$

d_o is roughly $\lambda/2$ — the empirical value calculated earlier is $\lambda/1.957$. Inserting this into Eq. 13 gives

$$\phi\ [\text{waves}] = (1.022N - 7.49)\ (\Delta d/d_o) \approx (N - 7.5)\ (\Delta d/d_o). \tag{15}$$

This important result has the following implications. First, the geometric and the reflection components partially compensate each other: they are nearly balanced when N is seven or eight bi-layers. Typically, 40 layer pairs are used. In that case ϕ [waves] $\approx 33.4\ (\Delta d/d_o)$, and the contribution from the geometric term is roughly 5.5 times larger than the reflection term. The second, serious implication of this result is the tight tolerance it places on the layer thicknesses. Here, for phase changes less than $\lambda/20$, the thickness must be controlled to ±0.15%. To achieve $\lambda/50$, the thickness must be controlled to ±0.06%. At this point in time, it is not entirely clear that such tolerances are achievable, or even measurable.

A.4 FRESNEL ZONEPLATE LENSES

The Fresnel zoneplate lenses used in EUV applications and studied interferometrically in this thesis are essentially binary holograms of simple singlet lenses. Consisting of a patterned absorber layer on a thin support membrane, these elements operate in transmission and behave similarly to their conventional refractive counterparts. The zoneplate consists of a circularly symmetric pattern of alternating transparent and opaque concentric rings. The ring spacing decreases with increasing radius, and light diffracted by the zoneplate is directed toward or away from one single point on axis, different for each diffracted order.

Several excellent sources exists with descriptions of zoneplate theory, behavior, and fabrication (Sussman 1960, Hecht 1987:445-57). This appendix is intended to provide only a few important highlights, following the notation of Hecht (1987). Consider a zoneplate designed for point-to-point imaging. The object distance ρ_0 and image distance r_0 are on opposite sides of the screen where the zoneplate is defined. This

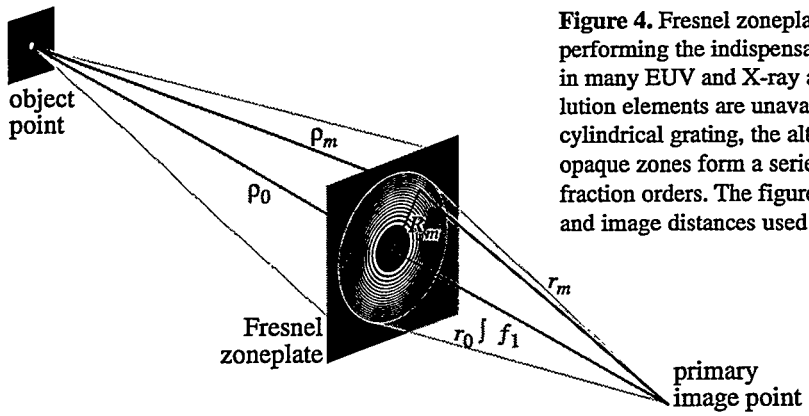

Figure 4. Fresnel zoneplate lenses operate by diffraction, performing the indispensable role of a simple refractive lens in many EUV and X-ray applications where other high resolution elements are unavailable. Essentially consisting of a cylindrical grating, the alternating pattern of transparent and opaque zones form a series of converging and diverging diffraction orders. The figure shows the definition of the object and image distances used in the zoneplate description.

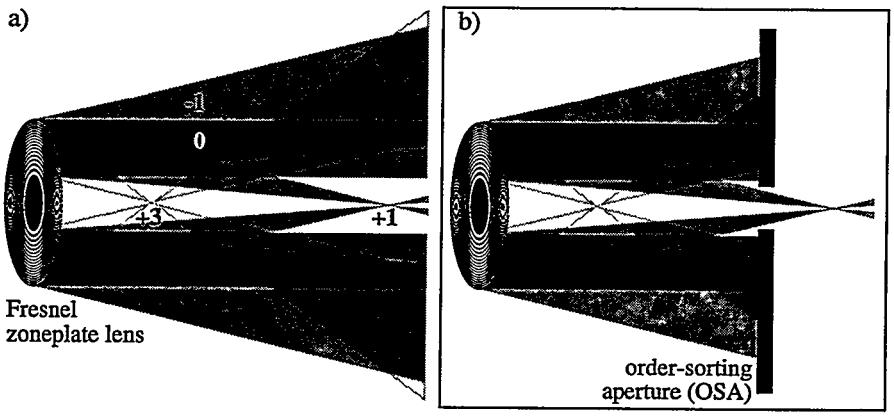

Figure 5. (a) A Fresnel zoneplate lens diffracts light into a series of converging and diverging diffraction orders. Only orders -1 through +3 are shown. Besides the "undiffracted" zeroth-order, even orders are absent. (b) Because of the overlapping orders, imaging applications usually require the use of an order sorting aperture that, if placed appropriately, can be used to transmit only the first-order converging light.

geometry is shown in Fig. 4. The individual zones are defined to diffract the diverging light from the object point to the primary image point in such a way that the light transmitted through each *open* zone adds *in phase*. Mathematically, this requirement indicates that the path-length difference between each open zone is λ; including the opaque zones, the path length difference between adjacent zones is $\lambda/2$.

$$(\rho_m + r_m) - (\rho_0 + r_0) = m\lambda/2. \tag{16}$$

With the zone radii defined as R_m, clearly $\rho_m = (\rho_0 + R_m)^{1/2}$ and $r_m = (r_0 + R_m)^{1/2}$. Assuming that the zoneplate radius is much smaller than the object and image distances and keeping only the first two terms in the expansions of ρ_m and r_m gives the relation

$$\left(\frac{1}{\rho_0} + \frac{1}{r_0}\right) = \frac{m\lambda}{R_m^2}. \tag{17}$$

Under plane-wave illumination, the object distance ρ_0 is extended to infinity. f_1 is defined as the primary focal length r_0, and the radius of the m-th zone is

$$R_m^2 = m f_1 \lambda. \tag{18}$$

Thus the zone placement radii are proportional to the square-root of m. For a given optical design, the main constraint on the size of the zoneplate is often dictated by the resolution limit of the zoneplate fabrication technique.

One important difference between the diffractive zoneplate and the conventional lens is the presence of numerous diffraction orders, as shown in Fig. 5(a). Analogous to the diffraction from a linear grating, a series of orders is diffracted into different directions; but in the case of the zoneplate, these multiple orders form a series of converging and diverging beams. The focal lengths f_m of the various beams occur at positive (converging) and negative (diverging) harmonics of the primary focal length.

$$f_m = f_1/m, \text{ for } m \in [\cdots -2, -1, 1, 2, \cdots], \text{ and } f_0 = \infty. \tag{19}$$

For a binary zoneplate, the even diffraction orders are absent.

When the zoneplate is used as a concentrating element designed to focus light to a certain point, other orders besides the first-order may often be ignored; their intensities are significantly less than that of the focused order at the primary focal position. However, in imaging applications, the various orders may suffer significant overlap, causing confusion in the recorded image. A practical remedy for this problem is the judicious placement of an *order-sorting aperture* (OSA) as shown in Fig. 5(b). When combined with an opaque central stop, as shown in the figure, the OSA may be placed in such a way that only the first-order beam is transmitted. The available space, or *working distance,* between the OSA and the primary focus may be smaller than is apparent due to the thickness of the OSA pinhole and the desire to provide as much longitudinal room near the focus as possible.

A.5 FRINGE CONTRAST AND MODULATION

The *contrast, modulation,* or *visibility* of a fringe pattern can be defined in several ways. These terms are used interchangably, and the definitions used in this thesis are presented here. A convenient description of an interference pattern separates the *stationary intensity* I_A from the *modulated intensity* I_B, with implicit spatial variation. Given a relative phase Φ between the amplitudes, the spatially varying intensity is

$$I = I_A + I_B \cos\Phi . \tag{20}$$

Since the intensity is non-negative, the average magnitude of I_A can never be less than that of I_B. When the electric field amplitudes of two interfering waves E_C and E_D are known, then neglecting the leading coefficients, the intensity can be written as

$$I = |E_C + E_D|^2 = |E_C|^2 + |E_D|^2 + 2|E_C E_D|\cos\Phi . \tag{21}$$

Hence, by equivalence to Eq. (20),

$$I_A = |E_C|^2 + |E_D|^2 \text{ and } I_B = 2|E_C E_D| . \tag{22}$$

The *fringe modulation* γ is defined as the ratio of the modulated to the stationary intensities:

$$\gamma \equiv \frac{I_B}{I_A} \in [0, 1] . \tag{23}$$

Following Michelson, the fringe *visibility* or *contrast* is defined (Born and Wolf 1980:267) as

$$C \equiv \frac{I_{max} - I_{min}}{I_{max} + I_{min}} . \tag{24}$$

which, for the representation of the interferogram in Eq. (20), becomes

$$C=\frac{(I_A+I_B)-(I_A-I_B)}{(I_A+I_B)+(I_A-I_B)}=\frac{I_B}{I_A}=\gamma\,. \tag{25}$$

identical to the fringe modulation.

A.6 FOURIER-TRANSFORM METHOD OF FRINGE CONTRAST DETERMINATION

Fringe contrast plays an important role in the signal-to-noise ratio of the interferometric data (see Section 8.11). As a quantitative indicator of data quality (or system alignment), it is important to establish a consistent contrast measurement method. One simple method proposed here and applied throughout this thesis uses Fourier-domain analysis of the data to quickly compare the intensities of the zeroth- and first-order frequency components of the recorded intensity.

The application of this method closely parallels the Fourier-transform method of interferogram analysis, described in Chapter 11. The goal here is to determine the relative intensities of the zeroth- and first-order components of the spatial-frequency spectrum so that the fringe contrast may be found. Parseval's Theorem is invoked to relate the *energy content* of the spatial and spatial-frequency domain representations of the interferogram.

This method follows the spatial-frequency domain description of the interferogram presented in Section 11.3. The interferogram is represented as

$$I(\mathbf{r})=A(\mathbf{r})+B(\mathbf{r})\cos\left[\phi(\mathbf{r})-\mathbf{k}_o\cdot\mathbf{r}\right],\ \text{with}\ A,\ B,\phi\ \in\ R\ . \tag{26}$$

For the purposes of this discussion, the following simplification is useful:

$$I(\mathbf{r})=A+B\cos\left[\phi(\mathbf{r})-\mathbf{k}_o\cdot\mathbf{r}\right]. \tag{27}$$

A and B here are not actually constant, but may be considered to have only low-spatial frequency attributes. To facilitate the Fourier-domain representation of the interferogram, the cosine may be separated as follows:

$$I(\mathbf{r})=A+\tfrac{1}{2}Be^{i\phi(\mathbf{r})}e^{i\mathbf{k}_o\cdot\mathbf{r}}+\tfrac{1}{2}Be^{-i\phi(\mathbf{r})}e^{-i\mathbf{k}_o\cdot\mathbf{r}}=A+C(\mathbf{r})e^{i\mathbf{k}_o\cdot\mathbf{r}}+C^*(\mathbf{r})e^{-i\mathbf{k}_o\cdot\mathbf{r}}, \tag{28}$$

where

$$C(\mathbf{r})\equiv\tfrac{1}{2}Be^{i\phi(\mathbf{r})}, \tag{29}$$

and * indicates the complex conjugate. By inspection, the Fourier-transform of the interferogram may be written

$$i(\mathbf{k})=a(\mathbf{k})+c(\mathbf{k}-\mathbf{k}_o)+c^*(\mathbf{k}+\mathbf{k}_o), \tag{30}$$

where $a(\mathbf{k})$ is approximately equal to $A\delta(\mathbf{k})$.

Now, similar to the Fourier-transform method, the zeroth- and first-order peaks are isolated from the rest of the spectrum, but here the *energy content* within a spatial-frequency radius κ is the quantity of interest.

The same assumptions about the separability of the peaks are made as with the Fourier-transform method of interferogram analysis. By Parseval's Theorem (Born and Wolf 1980:385, Goodman 1988:10), the zeroth-order components of the spatial and spatial-frequency domains are related.

$$\int |A|^2 d\mathbf{r} = \int |a(\mathbf{k})|^2 d\mathbf{k}. \tag{31}$$

Within κ, the approximate relationship holds

$$A^2 \propto \int_{|\mathbf{k}|<\kappa} |a(\mathbf{k})|^2 d\mathbf{k}, \tag{32}$$

and the constant of proportionality is simply $\int d\mathbf{r}$. A is found from the square-root of the expression in Eq. (32). The first-order term is now found in a similar manner. Once again invoking Parseval's Theorem,

$$\int \left|\tfrac{1}{2} B e^{i\phi(\mathbf{r})}\right|^2 d\mathbf{r} = \int |c(\mathbf{k})|^2 d\mathbf{k}. \tag{33}$$

This allows us to write

$$\left(\tfrac{1}{2}B\right)^2 \int d\mathbf{r} = \int_{|\mathbf{k}|<\kappa} |c(\mathbf{k})|^2 d\mathbf{k} = \int_{|\mathbf{k}-\mathbf{k}_o|<\kappa} |c(\mathbf{k}-\mathbf{k}_o)|^2 d\mathbf{k}. \tag{34}$$

To within the same constant of proportionality as for A ($\int d\mathbf{r}$), B can be found

$$B \propto 2\left(\sqrt{\int_{|\mathbf{k}-\mathbf{k}_o|<\kappa} |c(\mathbf{k}-\mathbf{k}_o)|^2 d\mathbf{k}}\right). \tag{35}$$

The factor of two comes from the definition of B and from the fact that the energy in the first-order is divided equally between the equivalent symmetric peaks in the spatial-frequency domain.

Since, by assumption, the three components of the spatial-frequency spectrum are separable, the expressions for A and B can be re-written using $i(\mathbf{k})$. The ratio of B to A gives the scalar *global fringe contrast* for an interferogram.

$$contrast = 2\sqrt{\frac{\int_{|\mathbf{k}-\mathbf{k}_o|<\kappa} |i(\mathbf{k})|^2 d\mathbf{k}}{\int_{|\mathbf{k}|<\kappa} |i(\mathbf{k})|^2 d\mathbf{k}}}. \tag{36}$$

This expression is easily implemented on a computer. Using the standard mathematical Fast Fourier Transform (FFT), locating the first-order peak (i.e. determining $\mathbf{k}_o$) proceeds by searching for the maximum absolute value in a region that excludes the central, zero-frequency peak. An exclusion radius of 30 cycles was chosen for typical EUV PS/PDI interferograms but would be different if a smaller sub-region of the data were being evaluated. Depending on the combined characteristics of the illuminating beam and of the test optical system, a small radius must be chosen that is large enough to encircle nearly all of the

zeroth- or first-order components in the spatial-frequency domain. To avoid overlap, this radius must not be larger than half of the "distance" between the first-order peak and the central frequency. A radius of ten cycles was chosen for these EUV interferometry experiments.

A.7 READING ZERNIKE COEFFICIENT PLOTS

Throughout this thesis, wavefront phasemap data is represented using the coefficients of the first 37 terms of the Zernike polynomial series, representing the best fit surface to the data. As described in Chapter 14, each term represents one orthogonal aberration polynomial component. Of the first 37, there are seven cylindrically symmetric terms and fifteen pairs of terms that share the same radial dependence but have $\cos(m\phi)$ and $\sin(m\phi)$ angular dependence.

Figure 6 is designed to serve as a *key* for identifying the various polynomial terms from the Zernike coefficient plots. For the PS/PDI data, the first four Zernike polynomial components are the position-dependent terms which depend only on the measurement and *not* on the optic under test. These are the *piston, tilt,* and *defocus* components, and they are typically excluded from the graphs.

Note that there is no significance to the line that connects the individual points in the plot. Its presence only aids in distinguishing one point from the next.

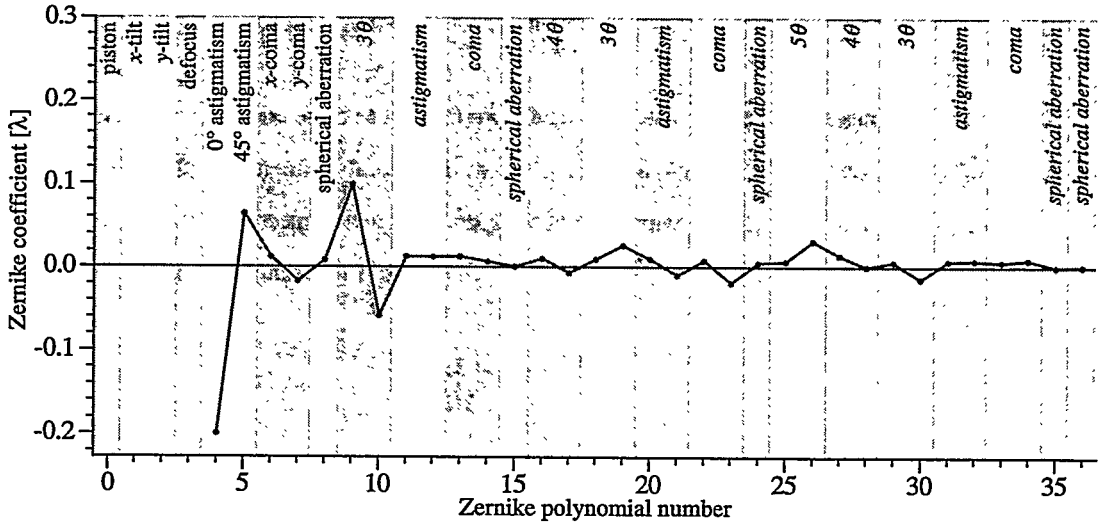

Figure 6. Key to Zernike coefficient plots. Here the named and unnamed components of a Zernike polynomial series are identified on the graph. Individual terms and pairs of terms that share radial dependence are identified by the grey vertical bands. The Zernike polynomials are described in Chapter 14. The line connecting the individual points of the discrete set has no physical significance.

References

Anderson, E. H. and D. Kern, "Nanofabrication of zone plates for X-ray microscopy," *Spring Series in Optical Sciences, Vol. 67, X-Ray Microscopy III*, A. Michette, G. Morrison, and C. Buckley, Eds., Springer-Verlag, Berlin, 1992, pp. 75-8.

Attwood, D., G. Sommargren, R. Beguiristain, *et al.*, "Undulator radiation for at-wavelength interferometry of optics for extreme-ultraviolet lithography," *Applied Optics* , **32** (34), 7022-31 (1993).

Babinet, A., *Compt. Rend.*, **4**, 638*ff* (1837).

Bathia, A. B. and E. Wolf, "The Zernike circle polynomials occuring in diffraction theory," *Proc. Phys. Soc.*, **B65**, 909-10 (1952).

Bathia, A. B. and E. Wolf, "On the circle polynomials of Zernike and related orthogonal tests," *Proc. Cambr. Phil. Soc.*, **50**, 40-48 (1954).

Beguiristain, R. *et al.*, "Characterization of thermal distortion effects on beamline optics for EUV interferometry and soft x-ray microscopy," *Rev. Sci. Instrumen.*, **67** (9), 1-9 (1996).

Bevington, P. R., *Data Reduction and Error Analysis for the Physical Sciences*, McGraw-Hill, New York, 1969.

Bjorkholm, J. E., A. A. MacDowell, O. R. Wood II, *et al.*, "Phase-measuring interferometry using extreme ultraviolet radiation," *Journal of Vacuum Science & Technology B*, **13** (6), 2919-22 (1995).

Bone, D. J., H.-A. Bachor, and R. J. Sandeman, "Fringe-pattern analysis using a 2-D Fourier transform," *Applied Optics*, **25** (10), 1653-60 (1986).

Born, M. and E. Wolf, *Principles of Optics*, 6th ed., Pergamon Press, New York, 1980.

Brophy, C. P., "Effect of intensity error correlation on the computed phase of phase-shifting interferometry," *J. Opt. Soc. Am. A*, **7**, 537*ff* (1990).

Bruning, J. H., D. R. Herriott, J. E. Gallagher, *et al.*, "Digital wavefront measuring interferometer for testing optical surfaces and lenses," *Applied Optics*, **13**, 2693*ff* (1974).

Carpio, M. and D. Malacara, "Closed cartesian representation of the Zernike polynomials," *Optical Communications*, **110**, 514-16 (1994).

Carre, P., "Installation et utilisation du comparateur photoelectrique et interferential du bureau international des poids et mesures," *Metrologia*, **2**, 13*ff* (1966).

Cerjan, C., "Scalar wave diffraction from a circular aperture," in *OSA Proceedings on Extreme Ultraviolet Lithography, Vol. 23*, F. Zernike and D. T. Attwood, Eds., Optical Society of America, Washington, D.C., 1994.

Charette, P. G. and I. W. Hunter, "Robust phase-unwrapping method for phase images with high noise content," *Applied Optics*, **35** (19), 3506-13 (1996).

Clarke, R. H. and J. Brown, *Diffraction Theory and Antennas*, John Wiley & Sons, New York, 1980.

Conte, S. D. and C. de Boor, *Elementary Numerical Analysis: An Algorithmic Approach*, 3rd ed., International Series in Pure and Applied Mathematics, McGraw-Hill, New York, 1980.

Crane, R., "Interference phase measurement," *Applied Optics*, **8**, 538*ff* (1969).

Creath, K., "Comparison of phase-measurement algorithms," *Proc. SPIE*, **680**, 19-28 (1986).

Crennell, K., "Introductory digital image processing," in *Interferogram Analysis: Digital Fringe Pattern Measurement Techniques*, D. W. Robinson and G. T. Reid, Eds., Institute of Physics Publishing, Bristol and Philadelphia, 1993, 1-22

de Groot, P. J., "Derivation of algorithms for phase-shifting interferometry using the concept of a data-sampling window," *Applied Optics*, **34** (22), 4723-30 (1995).

Fischer, D. J., J. T. O'Bryan, *et al.*, "Vector formulation for interferogram surface fitting," *Applied Optics*, **32** (25), 4738-43 (1993).

Foucault, L. M., "Description des procedees employes pour reconnaitre la configuration des surfaces optiques," *C. R. Acad. Sci. (Paris)*, **47**, 958*ff* (1858).

Foucault, L. M., "Memoire sur la construction des telescopes em verre argente," *Ann. Obs. Imp. Paris*, **5**, 197*ff* (1859).

Frieden, B. R., "Some statistical properties of the median window," *Proc. SPIE*, **373**, 219-24 (1981).

Goldberg, K. A., R. Beguiristain, J. Bokor, *et al.*, "Point diffraction interferometry at EUV wavelengths," in *OSA Proceedings on Extreme Ultraviolet Lithography, Vol. 23*, F. Zernike and D. T. Attwood, Eds., Optical Society of America, Washington, D.C., 1994, pp. 134-41.

Goldberg, K. A., R. Beguiristain, J. Bokor, H. Medecki, *et al.*, "At-wavelength testing of optics for EUV," *Proc. SPIE*, **2437**, 347-54, (1995a).

Goldberg, K. A., R. Beguiristain, and J. Bokor, *et al.*, "Progress towards λ/20 extreme ultraviolet interferometry," *Journal of Vacuum Science & Technology B*, **13** (6), 2923-27 (1995b).

Goldberg, K. A., E. Tejnil, and J. Bokor, "A 3-D numerical study of pinhole diffraction to predict the accuracy of EUV point diffraction interferometry," in *OSA Trends in Optics and Photonics, Vol. 4*, G. D. Kubiak and D. R. Kania, Eds., Optical Society of America, Washington, D.C., 1996, pp. 133-37.

Goldberg, K. A., E. Tejnil, S. H. Lee, *et al.*, "Characterization of an EUV Schwarzchild objective using phase-shifting point diffraction interferometry," *Proc. SPIE*, **3048**, 264-70 (1997).

Goodman, J. W., *Introduction to Fourier Optics*, reissued ed., McGraw-Hill, New York, 1988.

Greivenkamp, J. E., "Generalized data reduction for heterodyne interferometry," *Opt. Eng.*, **23**, 350*ff* (1984).

Greivenkamp, J. E., "Sub-Nyquist interferometry," *Appl. Opt.*, **26**, 5245*ff* (1987).

Greivenkamp, J. E. and J. H. Bruning, "Phase-shifting interferometry," in *Optical Shop Testing*, 2nd ed., D. Malacara, Ed., John Wiley & Sons, Inc., New York, 1992, pp. 501-98.

Han, G.-S. and S.-W. Kim, "Numerical correction of reference phases in phase-shifting interferometry by iterative least-squares fitting," *Applied Optics*, **33** (31), 7321-25 (1994).

Hariharan, P., B. F. Oreb, and T. Eiju, "Digital phase-shifting interferometry: A simple error-compensating phase calculation algorithm," *Applied Optics*, **26**, 2504*ff* (1987).

Hayes, J. B., "Compact Micromotion Translator," U.S. Patent 4,884,003 (1989).

Hecht, E., *Optics*, 2nd ed., Addison-Wesley Publishing Company, Reading, MA, 1987.

Henke, B. L., E. M. Gullikson, and J. C. Davis, "X-ray interactions: Photoabsorption, scattering, transmission, and reflection at E = 50-30,000 eV, Z = 1-92," *Atomic Data and Nuclear Data Tables*, **54** (2), 181-342 (1993).

Himel, M. D., "Optic fabrication and metrology for soft x-ray projection lithography," in *OSA Proceedings on Soft X-Ray Projection Lithography, Vol. 18,* A. M. Hawryluk and R. H. Stulen, Eds., Optical Society of America, Washington, D.C., 1993, pp. 108-9.

Huntley, J. M., "Noise-immune phase-wrapping algorithm," *Applied Optics*, **28** (15), 3268-71 (1989).

Kania, D. R., D. P. Gaines, D. S. Sweeney, G. E. Sommargren, *et al.*,"Precision optical aspheres for extreme ultraviolet lithography," *Journal of Vacuum Science & Technology B,* **14** (6), 3706-8 (1996).

Koliopoulos, C. L., "Interferometric optical phase measurement," Ph.D. Dissertation, Univ. Arizona, Tucson, 1981.

Kreis, T. M., "Digital holographic interference-phase measurement using the Fourier-transform method," *J. Opt. Soc. Am. A*, **3** (6), 847-55 (1986).

Kreis, T. M. and W. P. O. Juptner, "Fourier-transform evaluation of interference patterns: The role of filtering in the spatial frequency domain," *Proc. SPIE*, **1162**, 116-25 (1989).

Kubiak, G. D., Tichenor, D. A., Ray-Chaudhuri, A. K., *et al.*, "Characterization of an expanded-field Schwarzschild objective for extreme ultraviolet lithography," *Journal of Vacuum Science & Technology B,* **12** (6), 3820-25 (1994).

Linnik, W. P., "A simple interferometer for the investigation of optical systems," *Proceedings of the Academy of Sciences of the USSR,* **1**, 208 (1933).

Macy, W. W., Jr., "Two-dimensional fringe-pattern analysis," *Applied Optics*, **22** (23), 3898-901 (1983).

Mahajan, V. N., "Zernicke annular polynomials and optical aberrations of systems with annular pupils," *Optics and Photonics News*, **5** (11), Suppl. (1994).

Malacara, D., Ed., *Optical Shop Testing*, 2nd ed., John Wiley & Sons, Inc., New York, 1992.

Malacara, D. and S. L. DeVore, "Interferogram evaluation and wavefront fitting," in *Optical Shop Testing*, 2nd ed.,
D. Malacara, Ed., John Wiley & Sons, Inc., New York, 1992, pp. 455-99.

Medecki, H., E. Tejnil, K. A. Goldberg, J. Bokor, "Phase-shifting point diffraction interferometer," *Optics Letters*, **21** (19), 1526-28 (1996).

Melozzi, M. and L. Pezzati, "Interferometric testing of annular apertures," *Proc. SPIE*, **1781**, 241-48 (1992).

Mrowka, S., W. Harris, and R. J. Speer, "Short wavelength interferometric testing of x-ray optics," *Proc. SPIE*, **316**, 16-20 (1981).

Nugent, K. A., "Interferogram analysis using an accurate fully automatic algorithm," *Applied Optics,* **24** (18), 3101-5 (1985).

Nyquist, H. *AIEE Transactions*, **47**, 617-44 (1928).

Quiroga, J. A. and E. Bernabeu, "Phase-unwrapping algorithm for noisy phase-map processing," *Applied Optics*, **33** (29), 6725*ff* (1994).

Ray-Chaudhuri, A. K., W. Ng, *et al.*, "Soft X-ray Foucault test: a path to diffraction-limited imaging," *Nuclear Instruments & Methods in Physics Research, A,* **347** (1-3), 364-71 (1994).

Ray-Chaudhuri, A. K., W. Ng, F. Cerrina, *et al.*, "Alignment of a multilayer-coated imaging system using extreme ultraviolet Foucault and Ronchi interferometric testing," *Journal of Vacuum Science & Technology B,* **13** (6), 3089-93 (1995a).

Ray-Chaudhuri, A. K., R. P. Nissen, K. D. Krenz, *et al.,* "Development of compact extreme ultraviolet interferometry for on-line testing of lithography cameras," *Proc. SPIE,* **2536**, 99-104 (1995b).

Ray-Chaudhuri, A. K., K. D. Krenz, R. P. Nissen, *et al.,* "Development of extreme ultraviolet interferometry for laser plasma source operation." in *OSA Trends in Optics and Photonics, Vol. 4, Extreme Ultraviolet Lithography,* G. D. Kubiak and D. R. Kania, Eds., Optical Society of America, Washington, D.C., 1996a, pp. 128-32.

Ray-Chaudhuri, A. K., K. D. Krenz, R. P. Nissen, *et al.,* "Initial results from an extreme ultraviolet interferometer operating with a compact laser plasma source," *Journal of Vacuum Science & Technology B,* **14** (6), 3964-8 (1996b).

Robinson, D. W., "Phase-unwrapping methods," in *Interferogram Analysis: Digital Fringe Pattern Measurement Techniques*, D. W. Robinson and G. T. Reid, Eds., Institute of Physics Publishing, Bristol and Philadelphia, 1993, 194-229.

Roddier, C. and F. Roddier, "Interferogram analysis using Fourier transform techniques," *Applied Optics*, **26** (9), 1686-73 (1987).

Ronchi, V., *Ann. Sci. Norm. Super. Pisa,* **15** (1923).

Ronchi, V., "Forty years of history of a grating interferometer," *Applied Optics*, **3**, 437*ff* (1964).

Schmit, J. and K. Creath, "Spatial and temporal phase-measurement techniques: A comparison of major error sources in one-dimension," *Proc. SPIE*, **1755**, 202-11 (1992).

Smartt, R. N. and W. H. Steel, "Theory and application of point-diffraction interferometers (telescope testing)," *Japan. J. of Appl. Phys.* **14** (Suppl. **14-1**), 351 (1975).

Sommargren, G. E., "Phase shifting diffraction interferometry for measuring extreme ultraviolet optics," in *OSA Trends in Optics and Photonics, Vol. 4, Extreme Ultraviolet Lithography,* G. D. Kubiak and D. R. Kania, Eds., Optical Society of America, Washington, D.C., 1996a, pp. 108-12.

Sommargren, G. E., "Diffraction methods raise interferometer accuracy," *Laser Focus World,* **32** (8), 61-71 (1996b).

Sommargren, G. E.and R. Hostetler, in *OSA Proceedings on Soft X-Ray Projection Lithography, Vol. 18*, A.M. Hawryluk and R. H. Stulen, Eds., Optical Society of America, Washington, D.C., 1993, pp. 100-104.

Soobitsky, J. A., "Piezoelectric Micromotion Actuator," U.S. Patent 4,577,131 (1986).

Spallas, J. P., R. E. Hostetler, G. E. Sommargren, and D. R. Kania, "Fabrication of extreme-ultraviolet point-diffraction interferometer aperture arrays," *Applied Optics*, **34** (28), 6393-98 (1995).

Speer, R. J., M. Chrisp, D. Turner, *et al.*, "Grazing incidence interferometry: The use of the Linnik interferometer for testing image-forming reflection systems," *Applied Optics,* **18** (12), 2003-12 (1979).

Stearns, D. G., R. S. Rosen, and S. P. Vernon, "Multilayer mirror technology for soft-x-ray projection lithography," *Applied Optics*, **32** (34), 6952-60 (1993).

Stephenson, P., D. R. Burton, and M. J. Lalor, "Data validation techniques in a tiled phase unwrapping algorithm," *Optical Engineering*, **33** (11), 3703-8 (1994).

Sussman, M., "Elementary diffraction theory of zone plates," *Am. J. Phys.*, **28**, 394*ff* (1960).

Takeda, M., H. Ina, and S. Kobayashi, "Fourier-transform method of fringe-pattern analysis for computer-based topography and interferometry," *J. Opt. Soc. Am.*, **72** (1), 156-60 (1981).

Tejnil, E. "Characterization of extreme ultraviolet imaging systems," Ph.D. Dissertation, Univ. California, Berkeley, 1997.

Tejnil, E., K. A. Goldberg, H. Medecki, *et al.*, "Phase-shifting point diffraction interferometry for at-wavelength testing of lithographic optics," in *OSA Trends in Optics and Photonics, Vol. 4, Extreme Ultraviolet Lithography,* G. D. Kubiak and D. R. Kania, Eds., Optical Society of America, Washington, DC, 1996a, pp. 118-23.

Tejnil, E., K. A. Goldberg, E. H. Anderson, and J. Bokor, "Zonal placement errors in zone plate lenses" in *OSA Trends in Optics and Photonics, Vol. 4, Extreme Ultraviolet Lithography,* G. D. Kubiak and D. R.Kania, Eds., Optical Society of America, Washington, D.C., 1996b, pp. 138-42.

Tejnil, E., K. A. Goldberg, S. H. Lee, H. Medecki, *et al.*, "At-wavelength interferometry for EUV lithography," *Journal of Vacuum Science & Technology B,* to be published (1997).

Tichenor, D. A., *et al.*, "Development and characterization of a 10x Schwarzschild system for SXPL," in *OSA Proceedings on Soft X-Ray Projection Lithography, Vol. 18,* A. M. Hawryluk and R. H. Stulen, Eds., Optical Society of America, Washington, D.C., 1993, pp. 79-82.

Tichenor, D. A., A. K. Ray-Chaudhuri, G. D. Kubiak, *et al.*, "10x reduction imaging at 13.4 nm," *OSA Proceedings on Extreme Ultraviolet Lithography, Vol. 23*, F. Zernike and D. T. Attwood, Eds., Optical Society of America, Washington, D.C., 1994, pp. 89-97.

Tichenor, D.A., Kubiak, G.D., Malinowski, M.E., *et al.*, "Development of a laboratory extreme-ultraviolet lithography tool," *Proc. SPIE,* **2194**, 95-105 (1994).

Wang, J. Y. and D. E. Silva, "Wave-front interpretation with Zernike polynomials," *Applied Optics*, **19** (9), 1510-18 (1980).

Williamson, D. M., "The elusive diffraction limit," in *OSA Proceedings on Extreme Ultraviolet Lithography, Vol. 23*, F. Zernike and D. T. Attwood, Eds., Optical Society of America, Washington, D.C., 1994, pp. 68-76.

Wong, A. K. and A. R. Neureuther, "Rigorous three-dimensional time-domain finite-difference electromagnetic simulation for photolithographic applications," *IEEE Transactions on Semiconductor Manufacturing*, **8**, 419-31 (1995).

Wood, O. R., II, *et al., Journal of Vacuum Science & Technology B,* to be published (1997).

Wyant, J. C., "Use of an ac heterodyne lateral shear interferometer with real-time wavefront corrections systems," *Applied Optics*, **14**, 2622*ff* (1975).

Wyant, J. C. and R. N. Shagam, "Use of electronic phase measurement techniques in optical testing," *Proc. ICO, Vol. 11, Madrid,* 659*ff* (1978).

Yatagai, T., "Intensity based analysis methods," in *Interferogram Analysis: Digital Fringe Pattern Measurement Techniques*, D. W. Robinson and G. T. Reid, Eds., Institute of Physics Publishing, Bristol and Philadelphia, 1993, 72-93.

Zernike, F., "Begunstheorie des Schneidenver-Fahrens und Seiner Verbesserten Form. der Phasekontrast-methode," *Physica*, **1**, 689*ff* (1934).

Zernike, F. and B. R. A. Nijober, contribution to *La Théorie des Images Optiques*, Revue d'Optique, Paris, 1949, p. 227*ff*.

ADDITIONAL REFERENCES

Attwood, D., "Challenges for utilization of the new synchrotron facilities," *Nuclear Instruments and Methods in Physics Research*, **A291**, 1-7 (1990).

Bone, D. J., "Fourier fringe analysis: The two-dimensional phase unwrapping problem," *Applied Optics*, **30** (25), 3627-32 (1991).

Fields, C. H., W. G. Oldham, A. K. Ray-Chaudhuri, *et al.*, "Initial experiments on direct aerial image measurements in the extreme ultraviolet." in *OSA Trends in Optics and Photonics, Vol. 4, Extreme Ultraviolet Lithography,* G. D. Kubiak and D. R. Kania, Eds., Optical Society of America, Washington, D.C., 1996, pp. 124-27.

Fields, C. H., W. G. Oldham, A. K. Ray-Chaudhuri, *et al.*, "Direct aerial image measurements to evaluate the performance of an extreme ultraviolet projection lithography system," *Journal of Vacuum Science & Technology B,* **14** (6), 4000-3 (1996).

Guse, F. and J. Kross, "A new approach for quantitative interferogram analysis," *Proc. SPIE*, **1781**, 258-65 (1992).

Kujawinska, M. and J. Wojciak, "High accuracy Fourier transform fringe pattern analysis," *Optics and Lasers in Engineering*, **14**, 325-39 (1991).

Malacara, D., "A review of interferogram analysis methods," *Proc. SPIE*, **1332**, 678-89 (1990).

Mastin, G. A. and D. C. Ghiglia, "Digital extraction of interference fringe contours," *Applied Optics*, **24** (12), 1727-28 (1985).

Morimoto, Y. and M. Fujisawa, "Fringe pattern analysis by a phase-shifting method using Fourier transform," *Optical Engineering*, **33** (11), 3709-14 (1994).

Nguyen, K. B., G. F. Cardinale, D. A. Tichenor, *et al.*, "Fabrication of MOS devices with extreme ultraviolet lithography," in *OSA Trends in Optics and Photonics, Vol. 4, Extreme Ultraviolet Lithography,* G. D. Kubiak and D. R. Kania, Eds., Optical Society of America, Washington, D.C., 1996, pp. 208-11.

Nguyen, K. B., G. F. Cardinale, D. A. Tichenor., *et al.*, "Fabrication of metal-oxide-semiconductor devices with extreme ultraviolet lithography," *Journal of Vacuum Science & Technology B,* **14** (6), 4188-92 (1996).

Smith, H. I., S. D. Hector, M. L. Schatenburg, and E. H. Anderson, "A new approach to high fidelity e-beam and ion-beam lithography based on an in situ global-fiducial grid," *Journal of Vacuum Science & Technology B,* **9**, (6):2992-5 (1991).

Tichenor, D. A., G. D. Kubiak, S. J. Haney, *et al.*, "Recent results in the development of an integrated EUVL laboratory tool," *Proc. SPIE*, **2437**, 292-307 (1995).

Tichenor, D. A., A. K. Ray-Chaudhuri, G. D. Kubiak, *et al.*, "Progress in the development of EUV imaging systems," in *OSA Trends in Optics and Photonics, Vol. 4, Extreme Ultraviolet Lithography,* G. D. Kubiak, and D. R. Kania, Eds., Optical Society of America, Washington, D.C., 1996, pp. 2-8.

Towers, D. P., T. R. Judge and P. J. Bryanston-Cross, "Automatic interferogram analysis techniques applied to quasi-heterodyne holography and ESPI," *Optics and Lasers in Engineering*, **14**, 239-81 (1991).

Wang, G., A. Sun, J. Ren, and Z. Wang, "New method of fringe pattern trace and analysis," *Proc. SPIE*, **1704**, 293-301 (1992).

Womack, K. H., "Frequency domain description of interferogram analysis," *Optical Engineering*, **23** (4), 396-400 (1984).

Wyant, J. C., "Interferometric testing of aspheric surfaces," *Proc. SPIE*, **816**, 19*ff* (1987).

Xi, Y. and C. Ai, "Simple and effective phase unwrapping technique," *Proc. SPIE*, **2003**, 254-63 (1993).

Yu, Q., X. Liu, and K. Andresen, "New spin filters for interferometric fringe patterns and grating patterns," *Applied Optics*, **33** (17), 3705-11 (1994).

Zhengquan Tan, A. A.MacDowell, B. La Fontaine, *et al.*, "At-wavelength metrology of 13 nm lithography imaging optics," *Review of Scientific Instruments*, **66** (2-2), 2241-43 (1995).

Zweig, D. A. and R. E. Hufnagel, "A Hilbert transform algorithm for fringe-pattern analysis," *Proc. SPIE*, **1333**, 295-302 (1990).